A New Generator of One-Loop Scattering Amplitudes for Precision Multi-Particle Simulations at the LHC

Dissertation

zur

Erlangung der naturwissenschaftlichen Doktorwürde

(Dr. sc. nat.)

vorgelegt der

Mathematisch-naturwissenschaftlichen Fakultät

der

Universität Zürich

von

Fabio Cascioli

aus

Italien

Promotionskomitee

Prof. Dr. Stefano Pozzorini (Vorsitz)

Prof. Dr. Thomas Gehrmann

PD. Dr. Massimiliano Grazzini

Prof. Dr. Ben Kilminster

Zürich, 2014

Abstract

After the discovery of the Higgs boson, in the next two decades the Large Hadron Collider (LHC) will explore the interactions of fundamental particles by carrying out a vast programme of accurate measurements at unprecedented collision energies. In this context, precision tests of the current paradigm of particle interactions as well as the quest for new physics require precise theoretical predictions for a large variety of processes and theoretical models. In particular, next-to-leading-order (NLO) accuracy in perturbation theory is indispensable in order to achieve decent predictions and reliable estimates of residual theoretical uncertainties due to the truncation of the perturbative expansion.

One-loop scattering amplitudes are an essential ingredient of NLO calculations, and their complexity grows extremely fast with the number of scattering particles. In the context of LHC physics, the high collider energy results in the abundant production of multi-particle final states, which can require one-loop amplitudes of unmanageable complexity when applied to non-trivial multi-particle processes with six or more external particles. Traditional techniques for one-loop calculations can require huge CPU and human power on a process-by-process basis and are plagued by severe numerical instabilities.

In this thesis we present a new algorithm for the automated generation of one-loop scattering amplitudes called OpenLoops. It is based on a model- and process-independent numerical approach for the recursive construction of tree-level and one-loop Feynman diagrams. The building blocks of the recursion, called open-loops, are associated to the tensorial coefficients of the polynomial representation of the numerator of loop integrals as a function of the loop momentum. The unprecedented CPU efficiency of the OpenLoops algorithm, as well as its very high degree of flexibility, automation and numerical stability have been demonstrated in a series of technical studies.

OpenLoops has been interfaced with Monte Carlo event generators in a way that provides complete automation along the full chain of operations—from process definition to physical observables—that are required for NLO calculations at high energy colliders. The potential of this new NLO technology has been illustrated through a series of non-trivial multi-particle NLO simulations that play an important role for top-quark, Higgs-boson and electroweak phenomenology at the LHC.

In this thesis we will present state-of-the art predictions for the irreducible $\mu^+\nu_\mu \mathrm{e}^-\bar{\nu}_\mathrm{e}$ background to Higgs boson production in the $\mathrm{H} \to \mathrm{WW}^*$ decay channel. This calculation includes off-shell effects, gluon-induced contributions arising from squared quark loops, as well as a precise description of extra jet radiation based on parton shower matching and multi-jet merging techniques. As a second application we will present the NLO QCD corrections to $\mathrm{W}^+\mathrm{W}^-\mathrm{b}\bar{\mathrm{b}}$ production, including b-quark mass effects and off-shell W-boson decays into the $\nu_\mathrm{e}\mathrm{e}^+\mu^-\bar{\nu}_\mu\mathrm{b}\bar{\mathrm{b}}$ final state. This simulation—which provides the first consistent NLO description of $\mathrm{t}\bar{\mathrm{t}}$ and Wt production and decay, including their quantum interference—plays an important role in various areas of the top-quark

physics programme as well as for Higgs-boson analyses and new-physics searches with large top backgrounds and jet vetoes or jet bins.

The OpenLoops program will become publicly available in the next future and will be applicable to a multitude of phenomenological studies at the LHC.

Zusammenfassung

Nach der Entdeckung des Higgs-Bosons werden die Experimente am Large Hadron Collider (LHC) nun während der nächsten zwei Jahrzehnte ein gross angelegtes experimentelles Programm durchführen, um die Wechselwirkung der bekannten Elementarteilchen bei bisher unerreichten Kollisionsenergien zu untersuchen. Sowohl die dabei durchgeführten Präzisionstests des Standardmodells der Teilchenphysik, als auch die unnachgiebige Suche nach neuer Physik, bedürfen sehr präzise theoretische Vorhersagen für eine Vielzahl von Prozessen innerhalb verschiedener theoretischer Modelle. In diesen Vorhersagen ist die Berücksichtigung von Korrekturen in (mindestens) nächstführender Ordnung der Störungsrechnung unabdingbar. Nur so wird eine ausreichende Präzision der Vorhersagen erreicht, und es können verbleibende theoretische Unsicherheiten abgeschätzt werden.

Ein wichtiger Bestandteil von Rechnungen in nächstführender Ordnung der Störungsrechnung sind Ein-Schleifen-Streuamplituden, deren Komplexität extrem schnell mit der Anzahl der gestreuten Teilchen wächst. Speziell Prozessen mit sechs oder mehr externen Teilchen sind oft nur schwer zu beherrschen. Auf Grund der hohen Energien am LHC treten solche Vielteilchenendzustände jedoch vermehrt auf. Hergebrachte Berechnungsmethoden stoßen dabei schnell an ihre Grenzen. Unter anderem wachsen sowohl Rechenleistung als auch Arbeitsaufwand prohibitiv an und es können schwerwiegende numerische Instabilitäten auftreten.

In dieser Arbeit wird ein neuer Algorithmus, namens OpenLoops, zur automatisierten Berechnung von Ein-Schleifen-Streuamplituden vorgestellt. Er basiert auf einer modell- und prozessunabhängigen Methode zur rekursiven numerischen Konstruktion von Baum-level- und Ein-Schleifen-Feynmandiagrammen. Die Bausteine der zugrundeliegenden Rekursion werden "open-loops" genannt und stehen im Zusammenhang mit den Tensorkoeffizienten der Polynomialdarstellung der Schleifen-Integrale als Funktion der Schleifen-Impulse. Sowohl die beispiellose numerische Effizienz und Stabilität, als auch der hohe Grad an Flexibilität und Automatisierung, wurden in mehreren Präzisionsstudien gezeigt.

Das Programm OpenLoops wurde in verschiedenen Monte Carlo Generatoren eingebettet. So wird eine vollständige Automatisierung ermöglicht—von der Prozessdefinition bis zur Berechnung physikalischer Observablen. Unter Verwendung dieser entwickelten neuen Technologien konnte eine Vielzahl von hochgradig nicht-trivialen Vielteilchensimulationen durchgeführt werden, die alle eine wichtige Rolle in der phänomenologischen Untersuchung z.B. des Top-Quarks, des Higgs-Bosons oder verschiedener elektroschwacher Prozesse spielen.

In dieser Arbeit werden state-of-the-art Vorhersagen für den nicht reduzierbaren $\mu^+\nu_\mu e^-\bar{\nu}_e$-Hintergrund zur Higgs-Boson Produktion im $H \to WW^*$-Kanal vorgestellt. Unsere Rechnung beinhaltet neben off-shell Effekten auch von Gluonen induzierte Beiträge, die von quadrierten Quark-Schleifen herrühren, und ebenfalls eine präzise Beschreibung von zusätzlichen Jets, basierend auf Parton-Shower-Matching- und Multi-Jet-Merging-Methoden. Als zweite Anwendung wird die Produktion von $W^+W^-b\bar{b}$-

Endzuständen unter Berücksichtigung von QCD Strahlungskorrekturen zur nächstführenden Ordnung der Störungsrechnung vorgestellt. Speziell werden hier Effekte auf Grund von massiven b-Quarks und off-shell Zerfällen von W-Bosonen im $\nu_e e^+ \mu^- \bar{\nu}_\mu b\bar{b}$ Endzustand untersucht. Diese Simulation stellt damit die erste konsistente Beschreibung von Produktion und Zerfall von $t\bar{t}$- und Wt-Paaren inklusive Quanteninterferenzen dar. Diese Prozesse spielen eine sehr wichtige Rolle in verschiedenen Bereichen der Untersuchung des Top-Quarks, des Higgs-Bosons und auch bei der Suche nach neuer Physik.

Das Programm OpenLoops wird in naher Zukunft veröffentlicht werden und wird so für eine Vielzahl von weiteren phänomenologischen Studien am LHC zur Verfügung stehen.

Contents

Introduction

The Standard Model of particle physics (SM) is one of the greatest achievements of modern science [1–6]. It is a quantum gauge field theory of electromagnetic, weak and strong interactions of fundamental particles. Quantum field theory is a general framework for describing particle interactions. It is based on the hypothesis that each particle can be associated to quantized excitation modes of an underlying field in four dimensional spacetime. The observed interactions between particles are related to the interactions of the corresponding fields. The full dynamics is encoded in the Lagrangian density of the theory. The symmetry properties of the fields under the set of Lorentz transformations and spacetime translations define the basic quantum numbers of the field quanta, i.e. their mass and spin. The fundamental bosons and fermions of spin zero, one-half and one are associated respectively to scalar, spinor and vector fields. The symmetry properties of the fields with respect to transformations acting on possible extra internal degrees of freedom are known as gauge symmetries. Requiring the invariance of the scalar Lagrangian under a group of gauge transformations has the powerful consequence of naturally introducing vector fields and fixing the structure of the couplings between matter and gauge fields.

The Standard Model is built as a gauge theory based on the group $SU(3)_C \otimes SU(2)_L \otimes U(1)_Y$, associated to the colour, weak and hypercharge degrees of freedom, respectively. The matter fields are spin one-half fermions, i.e. quarks—subject to strong and electroweak forces—and leptons, interacting only via the electroweak force. The gauge bosons associated to the $SU(3)_C$ colour group are the gluons, mediators of the strong interactions. In the electroweak sector $SU(2)_L \otimes U(1)_Y$ the force carriers are the massive $W^{\pm}$ and Z^0 vector bosons, mediators of the weak interactions, and the massless photon associated to electromagnetic interactions [1–3]. The generation of non-zero mass terms for the weak gauge bosons is implemented in the SM through the mechanism of spontaneous symmetry breaking (SSB) [4–7]. In its minimal formulation, a colourless $SU(2)_L$ doublet of complex scalar fields is introduced in the Lagrangian. Through the interactions specified by its potential, one out of an infinite set of degenerate vacua (relative minima of the potential) is picked out as the physical ground state of the theory. The would-be Goldstone bosons associated to the broken generators of the $SU(2)_L \otimes U(1)_Y$ group are reabsorbed as longitudinal modes of the $W^{\pm}$ and Z^0 vector bosons, thus providing them with a mass term in a way that does not explicitly break the local gauge symmetry of the original Lagrangian. The remnant in the physical spectrum of the theory is the Higgs boson: a colourless and chargeless spin zero particle. The same scalar doublet can be exploited to write down gauge invariant interaction terms for the fermionic matter fields. After SSB, the non-zero vacuum expectation value of the Higgs field results in explicit mass terms for the quarks and

charged leptons. Furthermore, a new set of interactions of the Higgs boson with itself and with all other massive particles is generated.

Apart from an undeniable beauty of the underlying mathematical structure, the great success of the SM as the current paradigm of fundamental particle physics lies in its incontrovertible experimental confirmation [8]. The main probe to test its predictions consists in studying in a controlled environment the outcomes of scattering events of highly energetic particles like protons and electrons. The Large Hadron Collider (LHC) at CERN was designed to study collisions of protons up to center-of-mass energies of 14 TeV, with the main goal of investigating the mechanism through which elementary particles acquire a mass. This effort led on the 4th of July 2012 to the announcement, by the ATLAS and CMS collaborations, of the discovery of a scalar particle with a mass of around 125 GeV compatible with the Higgs boson predicted by the Standard Model [9, 10].

At a proton-proton collider like the LHC, scattering processes are dominated by the physics of strong interactions as described at the fundamental level by quantum chromodynamics (QCD) of quarks and gluons in the $SU(3)_C$ sector of the SM gauge group. Typical cross sections for Higgs production at the LHC are around ten orders of magnitude smaller than the total hadronic cross section and five orders of magnitude smaller than the cross sections for vector boson production. A further complication arises from the peculiar long-distance behaviour of strong interactions, reflected in the so called confinement property: quarks and gluons cannot be observed experimentally but only their bound states (hadrons) can. The high energy of the scattering protons results in complicated final states with hundreds of particles (hadrons, electrons, muons, photons) observed in the detectors. The physics programme of the LHC is based on the capacity of extracting signatures of small signals—not only of Higgs boson production but also of many other interesting SM processes, as well as possible hints or effects of beyond the Standard Model (BSM) physics—from a typically overwhelming background of other events. On the one hand, this pushes towards the development of more and more sophisticated technologies for handling experimental data, analysing them and extracting sensible results. In this respect, the incessant activity of designing and realising experimental detectors, trigger and data storage systems and advanced statistical analyses constantly shifts the frontiers of knowledge of the respective fields. On the other hand, this has to be accompanied by an equivalent effort from the theory community devoted to improving the theoretical predictions which have to be eventually confronted with experimental data.

From the theoretical point of view, the description of a scattering event at hadron colliders is a challenging problem which involves many different energy scales. The way to tackle it consists in identifying the correct variables and degrees of freedom that play the major role at each considered scale and ignoring, as a very good approximation, the others. In hadronic collisions, the crucial concept of factorization allows one to separate the treatment of the scattering event into different regimes, according to the scales of momentum transfer involved. At the highest scales, of the order of few to several hundred GeV up to the TeV scale, the constituent partons (quarks and gluons) of the incoming beams interact—in a so called *hard* scattering process—to produce energetic outgoing partons, leptons, gauge and Higgs bosons. The produced particles evolve towards lower energy scales. During this phase, hard partons progressively loose their

energy by multiple emissions of extra relatively softer partons in what appears to be as a *shower* of emitted particles. At scales of the order of 1 GeV the confinement properties of QCD come into play via the *hadronization* process that transforms bare coloured quarks and gluons in colourless bound states known as hadrons. Without loosing memory of the kinematic configuration of the original hard process and subsequent parton shower, hadrons evolve and propagate in collimated cones of particles called *jets*. Besides, the remnants of the initial-state scattered hadrons, from which the initial-state partons of the hard process have been extracted, interact via multiple low-energy scatterings—known as *underlying event*—producing extra activity mostly aligned to the beam direction, as compared to the hard, high transverse momentum particles.

As complicated as it might seem from the previous discussion, it is somehow astonishing how good and precise theoretical predictions can be computed, and how spectacular the agreement with experimental data turns out to be in some cases. In fact, altough many aspects of a hadronic scattering event—e.g. hadronization and underlying event—have to be described by rather simple phenomenological models, quantum field theory offers us the tools for a proper description of the hard scattering process. The genuinely quantum mechanical transition probability between well defined initial and final states is connected to the expectation values of a unitary operator—the scattering matrix S—between the corresponding quantum states. As discussed in some detail in Section 2.1, S-matrix elements can be computed via a perturbative expansion in powers of the coupling constant of the involved interaction in terms of vacuum expectation values of field operators known as Green's functions (see e.g. [11]). Whenever the expansion parameter proportional to the coupling is small enough, i.e. the strength of the interaction is sufficiently weak, truncating the series at a fixed perturbative order turns out to give sufficiently precise results for phenomenological predictions. When dealing with electromagnetic and weak interactions, the use of perturbation theory is justified by the fact that at the energy scales probed in current experiments the expansion parameter is $\lesssim \mathcal{O}\left(\frac{1}{100}\right)$. Perturbative calculations in QCD are justified by the property of asymptotic freedom [12, 13]. As a consequence of the non-abelian $SU(3)_C$ colour gauge group, the strength of strong interactions decreases when increasing the characteristic energy scale of the considered process. Roughly speaking, at the typical scales of hard scattering processes at the LHC, $\mathcal{O}(100\,\text{GeV})$, the strong coupling α_s is $\mathcal{O}\left(\frac{1}{10}\right)$.

The standard techniques to compute S-matrix elements exploit a one-to-one correspondence with a finite set of Feynman diagrams. As will be discussed in Section 2.1, Feynman diagrams represent all possible ways of connecting the initial- and final-state particles given the allowed set of interactions encoded in the Lagrangian density of the model. The first non-zero order usually corresponds to tree-level diagrams that can be computed quite straightforwardly. The corresponding leading-order (LO) theoretical predictions are usually not sufficient to meet the accuracy of experimental measurements. The next term in the expansion is associated to one-loop scattering amplitudes. They contribute to the next-to-leading-order (NLO) corrections to the hard scattering process that allow to give more reliable predictions and reduce the associated theoretical uncertainties. One-loop amplitudes represent the most involved aspect of NLO calculations, and their complexity grows extremely fast with the number of scattering particles. Moreover, until a few years ago, NLO predictions had to be specifically com-

puted on a process-by-process basis, and the calculation of a single nontrivial process could require up to a few years of man power. The vast physics programme of the LHC requires NLO predictions for a large variety of processes and theoretical models. In this context, the fairly large particle multiplicities resulting from the high collider energy can lead to one-loop amplitudes of unmanageable complexity, and addressing processes with more than five external particles with traditional NLO techniques is extremely challenging. For these reasons, in the recent years a considerable effort has been devoted to the development of completely new methods and techniques for the computation of one-loop amplitudes.

A big boost in this direction has come on the one hand with the introduction of on-shell methods based on so called generalized unitarity [14–25] and OPP integrand reduction [26–29]. On the other hand, diagram-based techniques also received a big boost thanks to new tensor-integral reduction methods [30–40]. These developments led to the calculation of NLO QCD corrections for several multi-particle processes with six or more external particles that few years before would have been considered an almost impossible task, paving the way to the so called NLO revolution (for recent reviews of the main results see e.g. [41,42]). One of the features that emerged from the first NLO QCD calculations of $2 \to 4$ processes about five years ago, was a trade-off between CPU efficiency and automation. While the tensor-reduction approach led to faster numerical codes, its large-scale applicability was limited by the occurrence of very large algebraic expressions. In contrast, the higher flexibility of the on-shell-based codes came at the price of a lower CPU efficiency.

This thesis presents a new, fully automated and highly efficient algorithm—that we called OpenLoops—for the calculation of tree-level and one-loop scattering amplitudes [43]. Originally inspired by the observation that multi-gluon amplitudes can be efficiently computed by combining tensor integrals with a one-loop Dyson-Schwinger recursion [44], OpenLoops is a numerical algorithm that generates one-loop amplitudes via recursive construction of Feynman diagrams. Promoting traditional tree-level algorithms to generators of loop-momentum polynomials, the OpenLoops approach naturally adapts to tensor-integral and OPP reduction, resulting in a high level of efficiency that does not depend on the employed reduction. The algorithm is formulated in a fully model- and process-independent way.

Integrating such a tool for the computation of one-loop matrix elements in the framework of general purpose Monte Carlo event generators, it becomes possible to reach the complete automation of the whole chain that goes from the process definition to a full simulation of hadronic scattering events. The accuracy given by computing NLO corrections to the hard process, combined with the inclusion of complementary effects such as parton shower, hadronization, underlying event etc., results in very accurate and realistic theoretical predictions. In the last few years, the different techniques for the computation of one-loop scattering amplitudes mentioned above have been implemented in various automated codes, such as Rocket [45], CutTools [46], Samurai [47], BlackHat [17], Helac-NLO [48], NJet [49], MadLoop [50], GoSam [51], Recola [52]. Some of them have also been interfaced with the main Monte Carlo generators, Sherpa [53], Herwig++ [54], aMC@NLO [55], Powheg-Box [56].

In combination with Sherpa, Herwig++ and an in-house Monte Carlo generator [57], OpenLoops has been successfully applied to several phenomenological studies

relevant for LHC physics [58–66]. They represent state-of-the-art predictions that show the efficiency and flexibility of the method.

The thesis is organised as follows. In Chapter 1 we discuss general concepts and techniques for computing theoretical predictions for observables at hadron colliders. The complementary approaches of fixed-order NLO calculations and parton shower algorithms will be presented, as well as methods to combine them. In Chapter 2, after a brief introduction to the diagrammatic expansion of the S-matrix, we will focus on one-loop scattering amplitudes and two alternative reduction techniques for their computation. A large part will be devoted to the detailed explanation of the OpenLoops algorithm and its practical implementation. Technical performance studies will be discussed in detail. Two phenomenological applications, based on [58,60], are presented in Chapter 3 and 4. After summarizing the main conclusions of this work, in Appendix A we show explicit examples of numerical routines used for the computation of tree-level and one-loop amplitudes.

Part I

Methods

Chapter 1

Next-to-leading-order Event Generators

In this chapter we will discuss general concepts and techniques for computing theoretical predictions for hadron colliders. In Section 1.1 we will outline the main steps needed to calculate the cross section of a hard partonic process at next-to-leading-order accuracy, introducing the idea of subtraction methods for the treatement of infrared divergences. The complementary approach of a parton shower for the description of soft and collinear QCD radiation will be presented in Section 1.2. In Section 1.3 we will discuss how to combine the two approaches to further improve the theoretical picture of scattering events.

1.1 Next-to-leading-order cross sections

The description of a scattering event at a hadron collider is a challenging theoretical problem. The crucial concept of factorization allows us to separate its treatment into different regimes, according to the scales of momentum transfer involved. At the highest scales, the constituent partons of the incoming beams interact to produce energetic outgoing partons, leptons, gauge and Higgs bosons. The matrix elements of these hard subprocesses are perturbatively computable. At lower scales, around $\Lambda_{\mathrm{QCD}} \sim 0.2\,\mathrm{GeV}$, the outgoing partons interact non-perturbatively to form the observed final-state hadrons. Due to QCD confinement, these soft processes cannot be calculated from first principles but have to be modelled using phenomenological approximations. The transition from the hard to the soft regime takes place by means of initial- and final-state parton showers through the emission of multiple soft and collinear partons which eventually participate in the low-scale process of hadron formation.

Let us consider the scattering of two protons h_1 and h_2 that interact to produce a configuration of final-state particles X. The previous picture is encoded in the following factorization formula for the hadronic cross section [67, 68],

$$\sigma = \sum_{i,j} \int_0^1 dx_i dx_j f_{i/h_1}(x_i, \mu_F) f_{j/h_2}(x_j, \mu_F) d\hat{\sigma}_{ij\to X}(\mu_F). \tag{1.1}$$

The physical cross section σ is a sum over all possible partonic cross sections $d\hat{\sigma}_{ij\to X}$ for two constituent partons i, j of the protons to interact and produce the final state

X. Each term of this sum is convoluted with the parton distribution functions (PDFs) $f_{i/h_1}(x_i, \mu_F)$, $f_{j/h_2}(x_j, \mu_F)$ that are associated to the probability of finding e.g. a parton of species i in the hadron h_1 with a momentum fraction x_i of the total momentum p. This factorized description is imposed at an arbitrary factorization scale μ_F with the underlying idea that the low-energy (long-distance) physics that describes the structure of the two hadrons and that is encoded in the PDFs is independent from the high-energy (short-distance) physics that describes the hard partonic scattering.

At the current stage of our knowledge the PDFs cannot be computed from first principles, but have to be extracted from experimental data using various fitting procedures. The crucial point that allows us to provide sensible predictions for scattering events is that they are independent from the particular process at hand. More precisely, once their functional dependence from the momentum fraction x has been extracted from some experimental data at a scale μ_0, their evolution with μ_F is governed by a set of differential equations that can be solved using a perturbative approach.

The other ingredient of the factorization formula (1.1), the partonic cross section $d\hat{\sigma}$, depends clearly on the process that we are interested in, but can be computed, at least in principle, in the established framework of perturbation theory. It can be written as

$$d\hat{\sigma}_{ij\to X} = \frac{1}{2x_i x_j s} \int d\Phi_n |\mathcal{M}_{ij\to X}|^2(\Phi_n; \mu_F), \tag{1.2}$$

where the squared matrix element $|\mathcal{M}_{ij\to X}|^2$ is averaged over the initial-state spin and colour quantum numbers and summed over the final-state ones. It must then be integrated over the n-body phase space of the final state X,

$$d\Phi_n = \prod_{l=1}^{n} \frac{d^3k_l}{(2\pi)^3 2E_l} (2\pi^4)\delta^{(4)}(p_i + p_j - \sum_{l=1}^{n} k_l). \tag{1.3}$$

The squared matrix element $|\mathcal{M}_{ij\to X}|^2$ is a genuinely quantum-mechanical probability that describes the transition from the initial quantum state of two incoming partons to the n-particle final state X. It can be computed in the framework of quantum field theory as a perturbative expansion in powers of the coupling constants of the theory. Given the finite set of allowed interactions of the model, expressed in terms of vertices and propagators of quantum fields associated to the particle content, at each fixed perturbative order one can consider the set of Feynman diagrams that contribute to the transition amplitude. This will be discussed in more detail in Chapter 2. The first non-zero leading-order (LO) amplitude is usually represented by tree-level diagrams that can be computed rather straightforwardly and correspond to classical interactions. At the next-to-leading order (NLO) of the expansion we have to take into account two different contributions: the extra power of the coupling can arise from the quantum interference of the tree-level amplitude with the *virtual* amplitude where a particle is emitted and reabsorbed at intermediate stages and does not appear as an external physical particle; or from a *real-emission* contribution where an extra unresolved particle is emitted in the final state. In terms of Feynman diagrams the virtual amplitude contains a closed loop with an arbitrary loop momentum flowing in it which is not fixed by the conservation of energy and momentum and which must be integrated over; whereas the real emission diagrams are tree-level-like with an extra

leg in the final state. At each increasing order of the expansion the complexity of the calculation increases, since we are led to consider not only diagrams with the highest number of loops or extra emissions but also mixed real-virtual contributions of diagrams with extra loops and extra legs compared to the LO amplitude. In the following we will focus on the case of QCD NLO calculations, which is the main topic of this thesis.

The loop integrals that enter the virtual corrections are usually divergent both in the ultraviolet (UV) regime of loop momenta going to infinity and in the infrared (IR) limit where a momentum becomes soft, i.e. closed to zero, or collinear to the momentum of another particle. To properly handle such divergences one has first to regularize the integrals to render them formally finite. The standard technique for this is dimensional regularization. It consists in shifting the number of space-time dimensions $d = 4$ by an infinitesimal amount, $d = 4 - 2\epsilon$, and then analytically continue the results to the standard four dimensions. In this limit, $\epsilon \to 0$, the divergences will reappear as $1/\epsilon$ poles. The UV divergences are reabsorbed through the *renormalization* procedure in a redefinition of the parameters of the theory (couplings, masses and fields). In the case of renormalizable theories like the SM this does not require the introduction of new parameters at each perturbative order, thus resulting in a very high predictive power. In practice this is achieved by splitting the original Lagrangian in a set of standard bare interactions and a new set of extra counterterm interactions with related Feynman rules. The latter produce in turn a new set of tree-level-like diagrams that, when summed with the one-loop amplitude, allow for the full cancellation of UV divergences. The renormalization procedure introduces at each order a spurious dependence of the full scattering amplitude on an arbitrary *renormalization scale* μ_R. The cancellation of IR divergences in the loop integrals comes instead from a peculiar interplay of the one-loop and real-emission amplitudes. At NLO the squared real-emission amplitude contains an extra final-state parton compared to the Born kinematics. Therefore, the phase space integration must be extended to a $3(n+1)$-dimensional integral, i.e. with an integration over all possible kinematical configurations of the unresolved extra parton. It turns out that the real-emission amplitude also diverges whenever the extra parton becomes soft or collinear to another external parton. The Kinoshita-Lee-Nauenberg (KLN) theorem [69, 70] states that, for so called IR-safe observables (to be discussed later in more detail), the IR divergences coming from the phase space integration of the real amplitude cancel exactly those present in the virtual amplitude. In hadronic collisions, this is still not sufficient to ensure a finite result. In fact, infrared divergences associated to initial-state collinear splittings remain uncancelled. Intuitively, this can be understood observing that the emission of a collinear parton off an initial-state leg changes the kinematic configuration of the hard process as compared to the virtual contribution evaluated with Born-like kinematics. Such initial-state singularities arising from the matrix elements are cancelled by a third contribution to the NLO cross section known as *collinear counterterm* and originating from the UV renormalization of the parton distribution functions. The NLO partonic cross section can be written as

$$\begin{aligned}\hat{\sigma}^{\mathrm{NLO}}_{ij\to X} = \frac{1}{2x_i x_j s}\Bigg(&\int d\Phi_n |\mathcal{M}^{\mathrm{tree}}_{ij\to X}|^2(\Phi_n;\mu_R) + \int d\Phi_n |\mathcal{M}^{\mathrm{virt}}_{ij\to X}|^2(\Phi_n;\mu_R) + \\ &+ \int d\Phi_n \, |\mathcal{M}^{\mathrm{tree}}_{ij\to X}|^2 \otimes \mathcal{C}(\Phi_n;\mu_F,\mu_R) + \int d\Phi_{n+1} |\mathcal{M}^{\mathrm{real}}_{ij\to X+1}|^2(\Phi_{n+1};\mu_R)\Bigg),\end{aligned} \tag{1.4}$$

where the squared tree-level amplitude, the virtual correction coming from the interference of tree-level and one-loop amplitudes,

$$|\mathcal{M}^{\text{virt}}_{ij\to X}|^2 = 2\,\mathfrak{Re}\left(\langle\mathcal{M}^{1-\text{loop}}_{ij\to X}|\mathcal{M}^{\text{tree}}_{ij\to X}\rangle\right), \tag{1.5}$$

and the convoluted collinear counterterm—dependent on the factorization scale μ_F—are integrated over the Born n-body phase space, whereas the real-emission squared amplitude is integrated over the $(n+1)$-particle phase space. Assuming that we know how to compute the needed scattering amplitudes in Eq.(1.4), the calculation of the NLO cross section for a $2 \to n$ particle process involves $3n$- and $3(n+1)$-dimensional phase space integrals. The NLO predictions needed for LHC physics can involve multiplicities of six or more external particles. Performing these integrals analytically is not possible. This is in parallel prevented by the fact that increasing the final-state multiplicity also the scattering amplitudes cannot be computed anymore in a closed analytic form. Furthermore, to produce sensible theoretical predictions, we should be able to put arbitrary cuts on specific variables while integrating over the phase space, mainly because they should reflect the geometry and acceptance of experimental detectors and adapt to the needs of progressively more refined experimental analysis that can have a rather sophisticated set of cuts and definitions of observables designed to highlight a particular physical effect. This would formally require computing Eq.(1.4) independently for each observable.

The solution for phenomenological applications is given by numerical calculations. On the one hand, the multidimensional phase space integration is perfectly suited for being tackled with Monte Carlo methods. On the other hand, the computation of scattering amplitudes can be formulated in an algorithmic way that allows it to be implemented in numerical codes. In doing this, one has to be careful that the computed quantity is defined properly as an *IR-safe observable*, i.e. one for which the cancellation of IR divergences holds. This is indeed the case for quantities sufficiently inclusive over the phase space—after summing over all degenerate final states [69, 70]—e.g. the total inclusive cross section as defined in Eq.(1.4). However, as soon as one starts imposing non-trivial cuts this is no longer guaranteed. An intuitive and operational definition of IR-safe observable consists in requiring that the latter should be insensitive to the appearence of soft and collinear kinematical configurations. More precisely, its value should not depend on the number of soft or collinear final-state partons, i.e. it should not change after collinear merging of two partons or the disappearence of one parton in the soft limit. For this class of observables the KLN theorem guarantees the finiteness of the result. At NLO the singularities appearing in the soft and collinear real-emission configurations must cancel those coming from the loop integrals of the virtual contribution. In a numerical approach though, the separately divergent integrals in Eq.(1.4) must also be computed separately, since they have different dimensionality. To cure the problem one has to rearrange the calculation in such a way that all possible divergences are cancelled locally at the integrand level, thus resulting in well defined finite integrals that can be numerically integrated. Several strategies have been developed to implement this idea. They can be broadly classified in two categories: phase-space slicing [71,72] and infrared subtraction methods [73–80]. The most widely used in current NLO QCD calculations are the latter.

Subtraction methods are based on the observation that in QCD the soft and collinear divergences appearing in the real-emission contribution possess a *universal* structure. They can be therefore investigated and classified once and for all through a set of process-independent functions. Their role is to approximate the generic scattering amplitude in the divergent limit as the factorized contribution of a finite Born-like matrix element and a splitting kernel that fully encodes the collinear or soft divergent kinematical configuration. The basic idea of the NLO subtraction algorithms is thus to rewrite the cross section by adding and subtracting a *ad hoc* contribution that allows to regularize the virtual and real corrections separately. Let us rewrite Eq.(1.4) in a more compact way as

$$\hat{\sigma}_{\rm NLO} = \int d\Phi_n \mathcal{B} + \int d\Phi_n \mathcal{V} + \int d\Phi_n \mathcal{B} \otimes \mathcal{C} + \int d\Phi_{n+1} \mathcal{R}, \tag{1.6}$$

where the four integrals represent respectively the Born, the virtual, the collinear counterterm and the real contributions. The subtraction terms can be written schematically as $\mathcal{B} \otimes \mathcal{S}$, i.e. as a convolution of a Born-like matrix element $\mathcal{B}$ and a set of universal splitting kernels $\mathcal{S}$. Each of these counterterms is associated to a particular soft, final-state collinear or initial-state collinear singular region with precise mapping relations from the real to the Born phase space. This allows to subtract the divergences in the real piece and integrate the infrared finite term $\mathcal{R} - \mathcal{B} \otimes \mathcal{S}$ over the $n+1$-particle phase space. The subtraction terms are added back to the virtual piece $\mathcal{V}$ after integration over the one-dimensional phase space of the unresolved extra parton. Given the relative simplicity of the universal splitting kernels, this extra integration can be performed analytically once and for all, resulting in the *integrated* subtraction terms that cancel now the divergences coming from the loop integrals. The divergences left over in the collinear counterterm are cancelled by corresponding initial-state subtraction terms, which introduce a dependence on the momentum fraction z of the incoming partons. Thus, the NLO cross section can be written as

$$\begin{aligned} \hat{\sigma}_{\rm NLO} = & \int d\Phi_n \mathcal{B} + \int d\Phi_n \left(\mathcal{V} + \mathcal{B} \otimes \mathbf{I}\right) + \\ & \int d\Phi_{n+1} \left(\mathcal{R} - \mathcal{B} \otimes \mathcal{S}\right) + \int_0^1 dz \int d\Phi_n \, \mathcal{B} \otimes \left(\mathbf{P}(z;\mu_F) + \mathbf{K}(z)\right), \end{aligned} \tag{1.7}$$

where $\mathbf{I}, \mathbf{P}, \mathbf{K}$ are universal insertion operators defined after integration of the subtraction terms over the one-dimensional singular phase space and after cancellation of the initial-state collinear singularities. Each piece is now well defined and finite in four dimensions and can therefore be numerically integrated.

Equation (1.7), when combined with the factorization formula (1.1), is well suited for a modular and algorithmic approach. In order to compute NLO QCD accurate theoretical predictions for cross sections and differential distributions, tree-level, one-loop and real-emission scattering amplitudes must be computed. They have then to be combined with the needed set of subtraction terms, integrated over the phase space and convoluted with the PDFs of the incoming protons. The different ingredients can be provided independently and then assembled to obtain the physical results. The tools that allow to perform these computations are called NLO event generators. They provide a general framework to simulate high-energy scattering events. By including

the modelling of other physical effects, such as parton shower, hadronization and underlying events, the idealized fixed-order parton-level picture is improved towards a more realistic hadron-level description.

1.2 Parton showers

In the previous section we discussed how to compute a next-to-leading-order accurate cross section at hadron colliders. Reminding the picture of a scattering event as a multi-scale problem, the next step is modelling how the hard partons evolve towards lower energy scales. In this downward evolution partons progressively loose their energy via emission of extra QCD radiation. This closely resembles the QED bremsstrahlung effect for which electrons and positrons emit multiple photons. Due to the non-abelian nature of strong interactions, both quarks and gluons, possessing a net colour charge, can emit other QCD partons.

The physical process for which highly energetic particles produce a cascade of extra radiation is called a parton shower (PS). In the factorized approach discussed at the beginning of the previous section, the degrees of freedom and physical variables which best describe the new regime turn out to be different from the ones used for the hard matrix element. The regions of phase space where emissions are particularly enhanced correspond to kinematic configurations where collinear or soft partons are emitted. In these limits amplitudes describing such splittings are divergent. The correct description of soft and collinear emissions catches the bulk of the whole spectrum of radiation and provides an approximated picture beyond the first few orders of perturbation theory whenever the latter is not applicable.

In this approximation a parton shower can be treated as a perturbative stochastic process that evolves the system from the high scales of the hard scattering to lower scales (typically of the order of few GeV) where non-perturbative effects become dominant. At the latter stage the scattering event consists of order hundred partons that represent the initial condition for the hadronization models that eventually connect partons with colourless hadrons observed in the detectors. Parton shower algorithms are based on the universal properties of factorization of collinear and soft singularities in QCD. In this respect, they can be treated as process-independent building blocks and can be used as very general tools to improve theoretical predictions. In the following we will discuss the main ideas behind the current implementations of parton shower algorithms. For a more detailed treatement, we refer to [81, 82] and references therein.

Let us consider first the collinear emission of an extra parton at small angles by an outgoing line of a n-parton final state. The cross section approximately factorizes as

$$d\sigma_{n+1} \approx \sum_{\text{partons } i,j} d\sigma_n \, \frac{\alpha_s}{2\pi} \frac{dq}{q} dz \, P_{ji}(z,\phi) d\phi, \tag{1.8}$$

i.e. as independent contributions where the i-th parton contributing to the $d\sigma_n$ cross section emits a new parton j as allowed by the Feynman rules. The variable q parameterizes the behaviour in the neighborhood of the singular region and can be chosen as the polar angle of the collinear splitting ($q = \theta^2$) or any other variable proportional to

it, e.g. the transverse momentum of the emitted parton with respect to the parent's direction. In the collinear limit different choices will all give the same result. $P_{ji}(z,\phi)$ is the DGLAP splitting function that describes the flavour-dependent splitting of a parent parton $i \to jk$ with longitudinal momentum fraction z at azimuthal angle ϕ. The above formula is completely general and consistent at the quantum level. In the range of validity of the approximations discussed so far, it takes into account all Feynman diagrams and quantum interferences that lead to the $n+1$-final state. The resulting picture is rather intuitive: when looking at collinear emissions, each parton behaves independently from the others. Iterating Eq.(1.8), each outgoing parton produces its own collinear shower. Through these multiple emissions we eventually approach the exactly collinear limit ($\theta = 0$) where the emission probability diverges. The way-out comes from the observation that any physical measurement can only deal with resolvable emissions. In other words, it is conceptually impossible to distinguish a pair of exactly collinear partons from a single parton whose momentum and quantum numbers are the sum of the pair. The divergence is therefore associated to an unphysical amplitude. In practice, the introduction of a transverse momentum cutoff Q_0 solves the problem. Emissions above this scale lead to resolvable partons with a finite probability distribution. Emissions below Q_0 are treated as unresolvable. The latter divergent contribution will in turn be cancelled by the corresponding virtual corrections to the (indistinguishable) non-emission hard process.

The non-emission probability is encoded in the so called Sudakov form factor. Its precise mathematical expression can be derived from a direct perturbative calculation, but the same result is obtained in a more intuitive way from unitarity-based arguments. Since the total probability for something to happen, i.e. emission or non-emission, must add to one, the non-emission probability can be computed as one minus the emission probability. More precisely, if Eq.(1.8) describes the emission probability between q and $q+dq$, it follows that the probability of zero emissions between the scales q_1 and $q_2 < q_1$ is given by

$$\Delta_i(q_1,q_2) = \exp\left[-\int_{q_2}^{q_1} \frac{\alpha_s(q)}{2\pi}\frac{dq}{q}\int_{z_0}^{1} P_{ji}(z)dz\right], \tag{1.9}$$

where $P_{ji}(z)$ is the splitting function averaged over the azimuthal angle ϕ and $z_0(q,Q_0)$ is the cutoff on z [1].

The discussion developed so far allows us to give already an idea of how a (final-state collinear) parton shower algorithm could be implemented using Monte Carlo methods. After choosing the starting scale Q of the parton shower, the scale of the first emission q_1 is found solving the equation $\Delta(Q,q_1) = R_1$, where R_1 is a pseudo-random number in the interval $[0,1]$. Subsequent emissions are generated iteratively by $\Delta(q_i,q_{i+1}) = R_{i+1}$ until the evolution reaches the cutoff scale Q_0. At every step each of the generated partons can emit new radiation following the same pattern. As already discussed, we end up with a large set of showered outgoing partons that represent the input of the subsequent hadronization phase.

So far we have only discussed final-state radiation (FSR), i.e. radiation originating from the outgoing final-state hard partons. When considering initial-state radiation

[1] This compact notation implies the contributions of all possible splittings $i \to jk$ of a parton of type i in what would be a matrix-valued quantity.

(ISR), altough the physics is essentially the same, the different kinematic configurations of the partons involved introduce some practical differences. The picture developed so far for FSR in fact would be very inefficient when applied to ISR. The incoming partons contained in the proton beams start their evolution at low scales (high x and low Q^2) and approach the hard scattering kinematics through a space-like evolution towards the hard scale (lower x and higher Q^2). Proceeding in this way one would generate all possible distributions of emitted radiation, but only very few of them would end up with having exactly the incoming partons with the correct kinematics of the hard process. For this reason parton shower algorithms implement ISR through a backward evolution of the well-defined initial state of the hard process. Radiation is generated according to the probability distribution for a parton at a given evolution scale and with a given momentum fraction to have been generated from one at a lower scale and a higher momentum fraction. The probability distribution follows very closely the one of FSR, but it turns out that it must be properly weighted by an extra factor given by the ratios of parton distribution functions, as they control the probability distribution of partons in the (x, Q^2)-plane. The Sudakov form factor for the non-emission probability for ISR takes the form

$$\Delta_i(q_1, q_2; x) = \exp\left[-\int_{q_2}^{q_1} \frac{\alpha_s(q)}{2\pi}\frac{dq}{q}\int_{z_0}^{1} P_{ij}(z)\frac{f_j(x/z, q)}{f_i(x, q)}dz\right]. \tag{1.10}$$

Let us now consider the other regime in which QCD scattering amplitudes diverge, namely the emission of soft radiation. Altough the pattern of soft divergences is also a universal feature of QCD, they differ from collinear divergences in a crucial aspect. The factorization property does not hold anymore at the cross section level but only at the amplitude level. To clarify this statement let us consider the emission of a soft gluon from a system consisting of a hard quark line and a extra (reasonably hard and collinear) gluon. The universality of soft divergences allows us to write the two independent amplitudes (Feynman diagrams) for the emission of the soft gluon respectively from the quark or the gluon line as the amplitude for the production of the hard quark-gluon pair times a universal factor describing the extra soft gluon emission. When computing the cross section by squaring the full amplitude we will naturally find interference terms between the different diagrams. This would indicate that the emission of soft radiation should be treated as a global property of the system, thus spoiling the picture of independent evolution of partons.

As it turns out looking at the explicit formulae, soft radiation happens to be emitted coherently, thus allowing it to be reconciled with collinear evolution. In fact, when the soft gluon is emitted at larger angles compared to the opening angle of the quasi-collinear hard pair, the interference is largely destructive and the cross section is identical to the one that would be obtained if the soft gluon had been emitted from a single on-shell quark line with total momentum and colour charge given by the combination of the quark-gluon pair. Analogously to the Chudakov effect in electrodynamics, wide-angle soft gluons only see the total colour charge of the system and cannot resolve the finer colour structure of the individual partons. On the other hand, when the soft gluon is emitted at smaller angles than the quark-gluon opening angle, the cross section receives contributions from the independent emissions off the two partons. In conclusion, soft gluon effects and colour-coherent radiation can be properly incorporated in

the independent collinear evolution by considering angular-ordered shower algorithms where the scale variable q is such that successive emissions are ordered with decreasing opening angles [83].

In this approach the first shower emission is not constrained to be the hardest, i.e. several wide-angle soft gluons might be emitted earlier in the evolution. This poses some subtle complications when trying to match the PS to a fixed-order matrix element computation. Alternative more recent PS algorithms that solve this problem and present some other technical advantages are based on the so called colour dipole model [84–86]. Starting from the large-N_C approximation, where gluons can be treated as colour-anticolour pairs, the system of partons can be decomposed in specific colour flow configurations where incoming and outgoing quarks, antiquarks and gluons are connected with their colour partners. Each colour line connecting a pair of partons emits independently as a colour-anticolour dipole following a universal pattern. In this approach one starts from soft emissions and then incorporates the collinear limits, resulting in the same formal accuracy of standard angular-ordered parton showers. The dipole PS algorithms are based on transverse momentum ordering, thus ensuring the first emission to be the hardest. Moreover, being based on $1 \to 2$ dipole splittings, and equivalently $2 \to 3$ parton splittings, they allow for explicit energy and momentum conservation with all partons being on-shell at each step of the recursion.

1.3 Matching and merging

In the previous sections we have discussed two different approaches for the description of multiparton final states. Matrix elements, computed at a fixed order of the coupling constant α_s, provide a consistent perturbative modelling of a limited number of highly energetic, well separated partons (as well as vector bosons and leptons) as produced in a well-defined hard scattering process. The inclusion of higher-order corrections improves the accuracy of the calculation and reduces the associated uncertainties. On the other hand, parton showers are very well suited for the description of multiple extra QCD radiation in the enhanced soft and collinear regions of phase space. Moreover, they evolve the hard process towards lower scales where non perturbative physics comes into play and bare coloured partons are recombined into colourless hadrons.

To get a more accurate and realistic description of scattering events it is clearly desirable to combine these two complementary approaches. The procedure that allows the combination of fixed-order matrix elements and parton showers is known as matching. To be fully consistent, the matching must be done in such a way to avoid possible double counting. In other words, one should take care that the whole phase space is smoothly and consistently filled with radiation, either coming from matrix elements or from the parton shower.

In this context many different solutions have been proposed, with the ultimate goal of improving the accuracy of the theoretical description of multi-jet final states. The matching of lowest multiplicity tree-level matrix elements with a parton shower was proposed originally in [87]. The MC@NLO [88] and POWHEG [89] methods have been developed to reach NLO accuracy for the inclusive cross section and correct the

first shower emission. A complementary approach consists in a unified description of different jet multiplicities with corresponding matrix elements matched to a parton shower. In general this requires the introduction of a merging scale that controls the interplay between showered and matrix-element corrected emissions, again taking care of possible double counting issues. At tree-level, the two main approaches to merge LO samples are known as CKKW [90] (and a similar procedure developed in [91]) and MLM [92, 93] merging. The current state of the art consists in merging algorithms based on NLO-accurate samples for each jet multiplicity [94–97]. In the rest of this section we will briefly review the main formulas and ideas related to matching and merging, focussing in particular on the methods used in the phenomenological applications discussed in Part II.

Let us start by introducing a more compact notation for the Sudakov form factor of Eq.(1.9). We rewrite it as follows,

$$\Delta(q_1, q_2) = \exp\left[-\int_{q_2}^{q_1} \frac{\alpha_s(q)}{2\pi}\frac{dq}{q}\int_{z_0}^{1} P_{ji}(z)dz\right] = \exp\left[-\int_{q_2}^{q_1} d\Phi_1 \mathcal{K}(\Phi_1)\right], \qquad (1.11)$$

i.e. as the exponentiation of a splitting kernel $\mathcal{K}(\Phi_1)$, encoding the universal properties of soft and collinear enhancements (in this case $\mathcal{K}(\Phi_1) \propto \frac{\alpha_s}{q}P(z)$), integrated over the one-emission phase space Φ_1. Given the probabilistic and unitary nature of shower algorithms, matching a fixed-order cross section to a shower cannot change the integrated normalization of the first. From this consideration the first shower emission will modify the inclusive LO cross section as follows,

$$\hat{\sigma}^{\rm PS}_{\rm LO} = \int d\Phi_B B(\Phi_B)\left[\Delta(t_0, \mu_Q^2) + \int_{t_0}^{\mu_Q^2} d\Phi_1 \mathcal{K}(\Phi_1)\Delta(t, \mu_Q^2)\right], \qquad (1.12)$$

where t_0 and μ_Q^2 are the infrared cutoff and the starting scale of the parton shower, respectively. The first term in the square bracket represents the probability of no-emission over the full range of the evolution scale q, whereas the second term gives the probability of one emission at the scale $t_0 < q < \mu_Q^2$. Given the unitarity constraint, by construction the square bracket integrates to one, thus maintaining the LO normalization but possibly modifying the shape of differential distributions sensible to extra emissions.

The next step consists in improving the fixed-order Born matrix element to include higher-order corrections and reach NLO accuracy for inclusive observables. As mentioned previously, NLO+PS matching is a non trivial problem because the parton shower will contribute with terms that are also present in the NLO computation, thus leading to possible double counting. Generally speaking the solution consists in removing from the NLO cross section the terms that will be added back by the shower. This is achieved modifying the NLO subtraction terms needed to cancel the divergences of the real and virtual contributions. Formally this translates in the introduction of extra subtraction terms that must match the pattern of soft and collinear divergences. The freedom inherent in these manipulations will eventually lead to different practical implementations that specifically differ on the choice of the subtraction terms.

To set the ground, let us consider the expression of a generic observable $\mathcal{O}$ computed at NLO accuracy. Starting from Eq.(1.7) for the inclusive partonic NLO cross section,

we simply recast it following the notation of Ref. [98],

$$\begin{aligned}\langle\hat{\mathcal{O}}\rangle_{\rm NLO} = &\int d\Phi_B \left[B(\Phi_B) + V(\Phi_B) + I(\Phi_B)\right] \mathcal{O}(\Phi_B) \\ &+ \int d\Phi_R \left[R(\Phi_R)\mathcal{O}(\Phi_R) - \sum_i D_i^{(S)}(\Phi_R)\mathcal{O}(\Phi_{B_i})\right].\end{aligned} \tag{1.13}$$

The subtraction terms $D_i^{(S)}$ approximate the real-emission matrix elements in the soft and collinear limits and are accompanied by kinematic mappings that associate for each divergent configuration i the real-like and Born-like parton configurations (i.e. momenta, colour, flavour, spin etc.). After integration over the extra-emission phase space they are added back as $I(\Phi_B)$ to cancel the corresponding divergences of the virtual piece. As mentioned above, we can now add and subtract a new arbitrary set of subtraction terms $D_i^{(A)}$ with the crucial constraint of having the same kinematic mappings and IR limits of the $D_i^{(S)}$. The previous equation becomes

$$\begin{aligned}\langle\hat{\mathcal{O}}\rangle_{\rm NLO} = &\int d\Phi_B \left[B(\Phi_B) + V(\Phi_B) + I(\Phi_B)\right] \mathcal{O}(\Phi_B) \\ &+ \int d\Phi_R \left[\sum_i D_i^{(A)}(\Phi_R)\mathcal{O}(\Phi_{B_i}) - \sum_i D_i^{(S)}(\Phi_R)\mathcal{O}(\Phi_{B_i})\right] \\ &+ \int d\Phi_R \left[R(\Phi_R) - \sum_i D_i^{(A)}(\Phi_R)\right] \mathcal{O}(\Phi_R) + \langle\hat{\mathcal{O}}\rangle_{\rm corr}^{(A)},\end{aligned} \tag{1.14}$$

where the correction term

$$\langle\hat{\mathcal{O}}\rangle_{\rm corr}^{(A)} = \int d\Phi_R \sum_i D_i^{(A)}(\Phi_R) \left[\mathcal{O}(\Phi_R) - \mathcal{O}(\Phi_{B_i})\right], \tag{1.15}$$

takes into account the mismatch generated by assuming in the second term of the square bracket of the last line the dependence of the observable on the full real-like kinematics. As we will see in a moment, this allows to set the path to a proper matching with the parton shower. Before moving to the matching, we can recast Eq.(1.14) in a more compact way. Given the one-to-one correspondence of the mappings and IR limits of the two sets of subtraction terms, we can consider a unique sum in the second line, interchange it with the integral, split the real-emission phase space in a Born-like configuration times the one-emission piece and define a new generalized integrated subtraction term, i.e. the second line of Eq.(1.14) would become

$$\begin{aligned}&\int d\Phi_R \left[\sum_i D_i^{(A)}(\Phi_R)\mathcal{O}(\Phi_{B_i}) - \sum_i D_i^{(S)}(\Phi_R)\mathcal{O}(\Phi_{B_i})\right] = \\ &\sum_i \int d\Phi_{B_i} d\Phi_1^i \left[D_i^{(A)}(\Phi_{B_i}, \Phi_1^i) - D_i^{(S)}(\Phi_{B_i}, \Phi_1^i)\right] \mathcal{O}(\Phi_{B_i}) = \\ &\int d\Phi_B \sum_i \int d\Phi_1^i \left[D_i^{(A)}(\Phi_{B_i}, \Phi_1^i) - D_i^{(S)}(\Phi_{B_i}, \Phi_1^i)\right] \mathcal{O}(\Phi_{B_i}).\end{aligned} \tag{1.16}$$

These manipulations allow us to recast the expression for the NLO-accurate observable as follows,

$$\begin{aligned}\langle\hat{\mathcal{O}}\rangle_{\rm NLO} = &\int d\Phi_B \bar{B}^{(A)}(\Phi_B)\mathcal{O}(\Phi_B) \\ &+ \int d\Phi_R \left[R(\Phi_R) - \sum_i D_i^{(A)}(\Phi_R)\right]\mathcal{O}(\Phi_R) + \langle\hat{\mathcal{O}}\rangle_{\rm corr}^{(A)},\end{aligned} \tag{1.17}$$

i.e. as a NLO-weighted Born-level contribution $\bar{B}^{(A)}$,

$$\bar{B}^{(A)} = B(\Phi_B)+V(\Phi_B)+I(\Phi_B)+\sum_i \int d\Phi_1^i \left[D_i^{(A)}(\Phi_{B_i},\Phi_1^i) - D_i^{(S)}(\Phi_{B_i},\Phi_1^i)\right], \tag{1.18}$$

plus a real-emission contribution with the new set of subtraction terms and the correction piece. The correction term (1.15) has the same structure as the first-order expansion of the LO+PS matching of Eq.(1.12),

$$\begin{aligned}\langle\hat{\mathcal{O}}\rangle_{\rm LO+PS} &= \int d\Phi_B B(\Phi_B)\left[\Delta^{(\mathcal{K})}(t_0,\mu_Q^2)\mathcal{O}(\Phi_B) + \int_{t_0}^{\mu_Q^2} d\Phi_1 \mathcal{K}(\Phi_1)\Delta^{(\mathcal{K})}(t,\mu_Q^2)\mathcal{O}(\Phi_R)\right] \\ &= \int d\Phi_B B(\Phi_B)\mathcal{O}(\Phi_B) + \langle\hat{\mathcal{O}}\rangle_{\rm corr}^{\mathcal{K}} + \mathcal{O}(\alpha_s^2),\end{aligned} \tag{1.19}$$

where the correction term is generated by the first shower emission and the first-order expansion of the Sudakov form factor $\Delta^{(\mathcal{K})}$ dependent on the splitting kernels $\mathcal{K}$,

$$\langle\hat{\mathcal{O}}\rangle_{\rm corr}^{\mathcal{K}} = \int_{t_0}^{\mu_Q^2} d\Phi_R\, B\cdot\mathcal{K}(\Phi_1)\left[\mathcal{O}(\Phi_R) - \mathcal{O}(\Phi_B)\right]. \tag{1.20}$$

The consistent matching of the NLO formula (1.17) and the first shower emission (1.19) is achieved by generating the correction term (1.15) through a parton shower with Sudakov factor

$$\Delta^{(A)}(t,t') = \exp\left[\int_t^{t'} d\Phi_1 D^{(A)}/B\right], \tag{1.21}$$

and by applying the shower to the NLO-weighted Born contribution (1.18). The resulting NLO+PS matching formula reads

$$\begin{aligned}\langle\hat{\mathcal{O}}\rangle_{\rm NLO+PS} = &\int d\Phi_B \bar{B}^{(A)}(\Phi_B)\left[\Delta^{(A)}(t_0,\mu_Q^2)\mathcal{O}(\Phi_B)\right. \\ &\left. + \int_{t_0}^{\mu_Q^2} d\Phi_1 \frac{D^{(A)}(\Phi_B,\Phi_1)}{B(\Phi_B)}\Delta^{(A)}(t,\mu_Q^2)\mathcal{O}(\Phi_R)\right] \\ &+ \int d\Phi_R \left[R(\Phi_R) - \sum_i D_i^{(A)}(\Phi_R)\right]\mathcal{O}(\Phi_R).\end{aligned} \tag{1.22}$$

The NLO accuracy is formally preserved up to the first emission given the correspondence between the splitting kernels of the shower and the terms $D_i^{(A)}$ that are subtracted from the real emission.

Different shower implementations correspond to different choices of the subtraction terms $D_i^{(A)}$ that are exponentiated in the Sudakov form factor. The POWHEG approach corresponds to the choice $D_i^{(A)} = \rho_i R$ with $\rho_i = D_i^{(S)} / \sum_i D_i^{(S)}$, i.e. the full radiative corrections are exponentiated. The MC@NLO method uses the splitting kernels $\mathcal{K}_i$ as subtraction terms, i.e. $D_i^{(A)} = B \cdot \mathcal{K}_i$. Alternatively, the kernels used in the IR subtraction terms of Eq.(1.13) can be used as parton evolution kernels [98], i.e. $D_i^{(A)} = D_i^{(S)}$, largely simplifying the $\bar{B}$ piece since the integral in the last line of Eq.(1.16) vanishes.

In the phenomenological applications discussed in Chapter 3 we use the MC@NLO implementation developed within the SHERPA event generator [53], which uses the Catani-Seymour dipoles both as subtraction terms and as splitting kernels. The latter are given by the spin-averaged dipoles taken in the large-N_C limit. In addition, the first shower emission is supplemented by exact spin and colour correlations.

Let us conclude this section with a brief discussion of merging algorithms. The main idea is to combine into a single sample matrix elements with different jet multiplicities up to a maximum number of jets $N_{\max}$, matching them in each case with a parton shower in such a way that formally both the LO(NLO) accuracy of the matrix element and the leading-logarithmic accuracy of the shower are preserved. This is achieved separating the phase space by means of a k_{T}-type jet measure into a hard region filled by matrix element emission and a softer region of intra-jet evolution. For each hard parton multiplicity the corresponding number of jets is described at the matrix-element level, whereas further shower emissions do not lead to any additional jets.

In the CKKW-based algorithm implemented in SHERPA and used in Chapter 3, multi-jet events are clustered into a core process using an inverse parton shower algorithm in such a way that clusterings are determined according to the parton shower branching probabilities [99]. Leading higher-order effects are taken into account by reweighting the strong coupling factors of the matrix element computed at the fixed scale μ_R with the factor $\alpha_s(k_{\mathrm{T}}^2)/\alpha_s(\mu_R^2)$. In this way the scale choice for α_s is adapted for each emission to the nodal scale k_{T} of the corresponding branching, thus improving the description of jet emission over the whole range of transverse momentum.

In LO multi-jet merging (MEPS@LO) two samples of n and $n+1$ parton multiplicity are matched to the shower introducing a cut Q_{cut} in the jet measure which should be chosen smaller than the minimum jet transverse momentum. The master equation reads,

$$\begin{aligned}\langle\hat{\mathcal{O}}\rangle_{\mathrm{MEPS@LO}} = &\int d\Phi_n B_n \left[\Delta_n^{(\mathcal{K})}(t_0,\mu_Q^2)\mathcal{O}_n + \int_{t_0}^{\mu_Q^2} d\Phi_1 \mathcal{K}_n \Delta_n^{(\mathcal{K})}(t_{n+1},\mu_Q^2)\Theta(Q_{\mathrm{cut}}-Q)\mathcal{O}_{n+1}\right] \\ &+ \int d\Phi_{n+1} B_{n+1} \Delta_n^{(\mathcal{K})}(t_{n+1},\mu_Q^2)\Theta(Q-Q_{\mathrm{cut}}) \\ &\times \left[\Delta_{n+1}^{(\mathcal{K})}(t_0,t_{n+1})\mathcal{O}_{n+1} + \int_{t_0}^{t_{n+1}} d\Phi_1 \mathcal{K}_{n+1}\Delta_{n+1}^{(\mathcal{K})}(t_{n+2},t_{n+1})\mathcal{O}_{n+2}\right].\end{aligned} \tag{1.23}$$

If we compare it with Eq.(1.19) for LO+PS matching, we see that the Θ-function restricts the shower emission for the n-jet process to the soft region $Q < Q_{\rm cut}$. In the hard region emission is corrected by the $n+1$ matrix element with an additional Sudakov factor $\Delta_n^{(\mathcal{K})}(t_{n+1}, \mu_Q^2)$ with respect to the n-jet process needed to implement the correct resummation behaviour of the inclusive sample. The procedure has been extended to NLO (MEPS@NLO) in [94, 95]. In this case MC@NLO simulations of different jet multiplicities up to $N_{\rm max}$ are combined into an inclusive sample. Again $Q_{\rm cut}$ is used to separate the phase space associated to QCD emissions into a soft and a hard region. The n-parton NLO+PS contribution from Eq.(1.22) is restricted below $Q_{\rm cut}$ with the function $\Theta(Q_{\rm cut} - Q)$ as follows,

$$\begin{aligned}\langle\hat{\mathcal{O}}_n\rangle_{\rm NLO+PS} = \int d\Phi_n \bar{B}_n^{(A)} \Bigg[& \Delta_n^{(A)}(t_0, \mu_Q^2)\mathcal{O}_n \\ & + \int_{t_0}^{\mu_Q^2} d\Phi_1 \frac{D_n^{(A)}}{B_n} \Delta_n^{(A)}(t_{n+1}, \mu_Q^2)\Theta(Q_{\rm cut} - Q)\mathcal{O}_{n+1} \Bigg] \\ & + \int d\Phi_{n+1} \left[R_n - D_n^{(A)}\right] \Theta(Q_{\rm cut} - Q)\mathcal{O}_{n+1},\end{aligned} \tag{1.24}$$

whereas the $n+1$-parton MC@NLO cross section fills the phase space above $Q_{\rm cut}$. Analogously to LO merging an extra Sudakov form factor $\Delta_n^{(\mathcal{K})}(t_{n+1}, \mu_Q^2)$ is needed in the $n+1$-contribution. Moreover, a shower counterterm of the form

$$1 + \frac{B_{n+1}}{\bar{B}_{n+1}} \int_{t_{n+1}}^{\mu_Q^2} d\Phi_1 \mathcal{K}_n, \tag{1.25}$$

is needed in order to avoid the double counting of Sudakov form factor contributions [94]. The master equation for MEPS@NLO merging reads,

$$\begin{aligned}\langle\hat{\mathcal{O}}\rangle_{\rm MEPS@NLO} = & \int d\Phi_n \bar{B}_n^{(A)} \Bigg[\Delta_n^{(A)}(t_0, \mu_Q^2)\mathcal{O}_n \\ & \qquad + \int_{t_0}^{\mu_Q^2} d\Phi_1 \frac{D_n^{(A)}}{B_n} \Delta_n^{(A)}(t_{n+1}, \mu_Q^2)\Theta(Q_{\rm cut} - Q)\mathcal{O}_{n+1} \Bigg] \\ & + \int d\Phi_{n+1} \left[R_n - D_n^{(A)}\right] \Theta(Q_{\rm cut} - Q)\mathcal{O}_{n+1} \\ & + \int d\Phi_{n+1} \bar{B}_{n+1}^{(A)} \left[1 + \frac{B_{n+1}}{\bar{B}_{n+1}} \int_{t_{n+1}}^{\mu_Q^2} d\Phi_1 \mathcal{K}_n\right] \Delta_n^{(\mathcal{K})}(t_{n+1}, \mu_Q^2)\Theta(Q - Q_{\rm cut}) \\ & \qquad \times \left[\Delta_{n+1}^{(A)}(t_0, t_{n+1})\mathcal{O}_{n+1} + \int_{t_0}^{t_{n+1}} d\Phi_1 \frac{D_{n+1}^{(A)}}{B_{n+1}} \Delta_{n+1}^{(A)}(t_{n+2}, t_{n+1})\mathcal{O}_{n+2}\right] \\ & + \int d\Phi_{n+2} \left[R_{n+1} - D_{n+1}^{(A)}\right] \Delta_n^{(\mathcal{K})}(t_{n+1}, \mu_Q^2)\Theta(Q - Q_{\rm cut})\mathcal{O}_{n+2}.\end{aligned} \tag{1.26}$$

To obtain the desired NLO accuracy for each jet multiplicity the separation cut $Q_{\rm cut}$ should be chosen smaller than the minimum jet transverse momentum. In this way the

soft region is filled by the parton shower alone, while the hard region is described in terms of fixed-order calculations matched to the parton shower. The smooth transition between parton-shower and matrix-element regimes at the merging scale Q_{cut} requires a consistent choice of the renormalisation scale at which the coupling constant α_s is evaluated. To this end multi-jet events are clustered into a core process by a clustering algorithm that corresponds to the inversion of the parton shower, such that clusterings are determined according to the parton-shower branching probabilities. The coupling factors resulting from the various QCD emissions are evaluated at the nodal scale t_i of the corresponding branching, $\alpha_s(t_i)$, while the α_s^k factor associated with the core process is computed at the global renormalisation scale μ_R. This implies the introduction of CKKW-like weight-correction factors $\alpha_s(t_i)/\alpha_s(\mu_R^2)$ for the hard emissions associated to higher-multiplicity matrix elements.

Chapter 2

One-loop Scattering Amplitudes

In this chapter we will present OpenLoops, a new highly efficient algorithm for the automated calculation of tree-level and one-loop scattering amplitudes. After introducing general aspects of perturbation theory and Feynman diagrams that are used to compute scattering amplitudes in quantum field theory, we will focus in Section 2.2 on the case of one-loop amplitudes, discussing two alternative approaches for the reduction of the amplitude to scalar integrals. In Section 2.3 and 2.4 we discuss the OpenLoops algorithm and its actual implementation, respectively.

2.1 Perturbation theory and Feynman diagrams

The basic objects that allow us to connect a quantum theory with experimental observations are transition amplitudes. They are associated to the probability for the system to go from an initial state $|i\rangle$ to a final state $|f\rangle$. In a quantum field theory of fundamental particles, we are more specifically interested in scattering amplitudes, i.e. the transition amplitudes for an initial state of two incoming particles $|p_1 p_2\rangle$ to interact and produce a well defined final state of n outgoing particles $|p'_1 p'_2 \dots p'_n\rangle$. They are formally computed as matrix elements of a unitary operator, the S-matrix. The squared matrix element $|\langle p'_1 p'_2 \dots p'_n|S|p_1 p_2\rangle|^2$ measures the probability for such a transition to occur. The actual computation of these matrix elements is a highly non trivial task that cannot be accomplished exactly. Nevertheless, they can be re-expressed through an iterative reduction technique (LSZ formula [100]) in terms of vacuum expectation values of fields operators. It turns out that these objects, known as Green's functions, are much more convenient to work with. Eventually it is possible to expand the field operators in a perturbation series and to construct an expansion of the S-matrix elements in terms of vacuum expectation values of products of free fields. Since this corresponds to an expansion in powers of the couplings which parametrize the strength of the interactions, this perturbative approach is physically justified only when the interactions are sufficiently weak. This is indeed the case for the electromagnetic and weak forces. At the energy scales probed in the hard scattering in particle colliders also the strong force can be treated perturbatively.

The perturbative expansion of the S-matrix has a very nice and intuitive graphical correspondence in terms of so called Feynman diagrams. At any fixed order the basic objects that appear in the calculation are propagators of free fields between two points

in spacetime and local interaction terms of three or more fields. If we associate lines to each propagating field and vertices where the lines meet to the interactions, the problem of writing all contributions to the scattering amplitude is reduced to a combinatorial problem of finding all possible ways of connecting the incoming and outgoing particles through vertices and propagators allowed by the theory. The finite set of building blocks is independent from the process at hand, but only depends on the theory, i.e. ultimately on the Lagrangian. From the latter one can derive a set of rules, dubbed Feynman rules, that associate a well defined mathematical expression to each propagator and vertex.

At each higher order of the perturbative expansion one has to consider the insertion of extra factors of field operators in the vacuum expectation value. Since the external states are fixed, the new contributions give rise to Feynman diagrams where the propagating fields have to be emitted and reabsorbed internally. The number of such closed loops in each diagram is fixed at each order of the expansion. They are interpreted as genuinely quantum mechanical effects associated to the emission and absorption of an increasing number of virtual particles at any point of spacetime.

Generally speaking, the S-matrix element is a function of the four-momenta of the external particles. The conservation of energy and momentum at each vertex fixes completely the kinematics of tree-level diagrams. This is no longer the case for loop diagrams. The momentum flowing in the loops is not constrained to have a fixed value, and one is left with an extra integration over the loop momentum for each loop. This fact can be interpreted by saying that the incoming and outgoing asymptotic states can be connected by virtual particles of arbitrary wavelenght emitted and reabsorbed between two arbitrary points of spacetime. The interplay between quantum mechanical and relativistic effects ensures that the propagator be non zero also for space-like intervals. It can be shown that as long as the field operators associated to a physical observable commute for space-like intervals, this does not violate the principle of causality. The picture discussed so far holds generally in the Feynman diagrammatic expansion of the S-matrix. Each order is in a one-to-one correspondence with a set of diagrams containing a fixed number of loops. Each loop is associated to an extra integration over the loop-momentum flowing in it. Altough the n-loop contribution to the scattering amplitude can always be written using the Feyman rules, the presence of loop integrals hugely complicates the actual computation of the amplitude.

Let us consider now in more detail the case of strong interactions. The hypothesis that QCD is a gauge theory based on the group $SU(3)_C$ with quark fields q having three different colour charges $i = r, g, b$ fixes the Lagrangian (at the classical level) to be

$$\mathcal{L} = -\frac{1}{4} F^a_{\mu\nu} F^{a\mu\nu} + \sum_q \bar{q}_i (\mathrm{i}\gamma^\mu D_\mu - m_q)_{ij} q_j, \tag{2.1}$$

where sums over repeated indices are implicitly understood. The field strength tensor $F^a_{\mu\nu}$ and the covariant derivative D_μ are given by

$$\begin{aligned} F^a_{\mu\nu} &= \partial_\mu A^a_\nu - \partial_\nu A^a_\mu - g_s f^{abc} A^b_\mu A^c_\nu, \\ (D_\mu)_{ij} &= \delta_{ij}\partial_\mu + \mathrm{i} g_s T^a_{ij} A^a_\mu, \\ (m_q)_{ij} &= m_q \delta_{ij}. \end{aligned} \tag{2.2}$$

The quanta of the gauge fields A^a_μ ($a = 1, \ldots, 8$) are the gluons, g_s is the strong coupling constant that fixes the strength of the interaction, f^{abc} and T^a_{ij} are the structure constants and the generators of the $SU(3)_C$ Lie group, respectively. The Lagrangian is invariant under arbitrary local gauge transformations. Via the covariant derivative the spin one-half quarks interact with the spin one gluons. Furthermore, because of the non-abelian gauge group, the field strength tensor gives rise to three- and four-gluon self interactions.

Altough specifying all interactions of quarks and gluons at the classical level, the previous Lagrangian is not sufficient to define a consistent quantum theory of QCD. The core of the problem lies in the fact that gauge invariance allows for an infinite set of equivalent configurations of the gauge fields. This in turn can introduce unphysical divergences in the definition of physical observables. This degeneracy is broken imposing a gauge-fixing condition through a formal procedure due to Faddeev and Popov [101]. To remove the extra degrees of freedom from the computation of the amplitudes, we are forced to introduce a set of unphysical ghost fields. They are scalar fields obeying the Fermi-Dirac statistics and transform, as the gluons, in the adjoint representation of the gauge group. The QCD quantum Lagrangian can be written (in the case of a covariant gauge-fixing) adding to Eq.(2.1) the two extra terms

$$\mathcal{L}_{\text{fix+ghost}} = -\frac{1}{2\xi}(\partial_\mu A^{a\mu})(\partial_\nu A^{a\nu}) + \partial_\mu \eta^{a\dagger}(\partial^\mu \delta^{ab} + g_s f_{abc} A^{c\mu})\eta^b, \tag{2.3}$$

where η^a are the ghost fields. From it one can derive the Feynman rules for the quark, gluon and ghost propagators, the quark-gluon and ghost-gluon vertices and the triple- and quartic-gluon vertices.

Now, the machinery of S-matrix perturbative expansion and Feynman diagrams can be applied to compute QCD scattering amplitudes. The external quarks and gluons are described by spinor wavefunctions and polarization vectors, respectively. The colour and Dirac algebra needed to manipulate the diagrams can be rather cumbersome. The computation of tree-level amplitudes does not pose particularly serious issues or obstacles. Algorithmic techniques exist for the fully automated calculation of generic tree amplitudes. For what concerns one-loop amplitudes, any loop integral can be reduced to a combination of a set of well-known one-, two-, three- and four-point scalar integrals.

As we discussed in the previous chapter, one-loop amplitudes are an essential ingredient of NLO calculations, as they enter the virtual corrections to the LO result. It turns out that they are actually the most involved aspect of such computations, and their complexity grows extremely fast with the number of external scattering particles. This observation can be understood on a purely combinatorial ground thinking that, after having fixed the external legs as for tree-level diagrams, the freedom of introducing a closed loop using the set of vertices and propagators allowed by the Feynman rules can greatly increase the number of one-loop topologies. In fact, the number of one-loop diagrams can be more than one order of magnitude bigger than the number of tree-level diagrams. In addition, due to the complexity of the loop-momentum integrals and their reduction to scalar integrals, in the case of multi-particle processes each single one-loop diagram can lead to gigantic algebraic expressions.

Until a few years ago, the computation of one-loop amplitudes required dedicated work on a process-by-process basis, and the calculation of a single nontrivial process

with more than five external particles could require up to a few years of man power. With the advent of the LHC, the theoretical community had to face the need of NLO predictions for a large variety of processes and theoretical models. In this context, the fairly large particle multiplicities resulting from the high collider energy can lead to one-loop amplitudes of unmanageable complexity, when addressed with traditional techniques. For these reasons, in recent years a considerable effort has been devoted to the development of new methods and techniques for the computation of one-loop amplitudes.

Based on the strategy to reduce the amplitudes to scalar integrals, one-loop methods can be broadly divided in two categories: tensor-integral reduction techniques [30–40], which have been traditionally used in combination with Feynman diagrams and their manipulation through computer algebra, and so-called on-shell methods, which allow one to circumvent tensor integrals and possibly also Feynman diagrams by means of OPP reduction [26–29] or in the generalized unitarity framework [14–25]. In the following, we will concentrate on the tensor-integral and OPP reduction techniques, which are strictly connected with the OpenLoops algorithm that we are going to introduce in Section 2.3.

Let us consider the following generic one-loop diagram which represents the basic building block of any one-loop scattering amplitude,

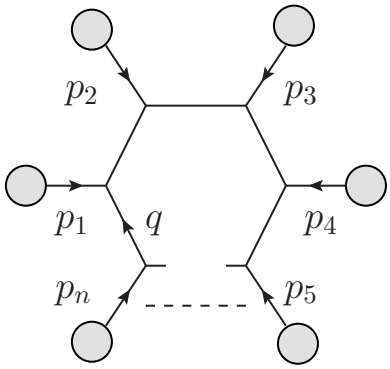

It consists of n legs attached to the loop with—by convention—ingoing momenta $p_1, \ldots, p_n$. The blobs represent possible tree-level structures that are connected to the external particles through vertices and propagators. The n loop propagators can be associated to different fields with masses $m_0, m_1, \ldots, m_{n-1}$ and momenta given by $q, p_1 + q, \ldots, p_1 + \ldots p_{n-1} + q$, where q is the loop momentum flowing by convention in the first propagator. If d is the label of the diagram, the associated amplitude $\delta\mathcal{M}^{(d)}$ can be written as

$$\delta\mathcal{M}^{(d)} = \mathcal{C}^{(d)} \int d^d q \frac{\mathcal{N}(q; p_1, p_2, \ldots, p_{n-1})}{D_0 D_1 \ldots D_{n-1}}, \tag{2.4}$$

where $\mathcal{C}^{(d)}$ is a colour factor that can be fully factorized at (sub)-diagram level (see Section 2.3.1). The denominator of the i-th loop propagator is defined as

$$D_i = \left(q + \sum_{j=0}^{i} p_j \right)^2 - m_i^2 + \mathrm{i}\epsilon; \qquad p_0 = 0. \tag{2.5}$$

The numerator $\mathcal{N}$ contains all other contributions from loop propagators, vertices and external tree structures. It is a polynomial of degree $R \leq n$ in the loop momentum q

$$\mathcal{N}(q; p_1, p_2, \ldots, p_{n-1}) = \sum_{r=0}^{R} \mathcal{N}_{\mu_1 \ldots \mu_r}(p_1, p_2, \ldots, p_{n-1}) q^{\mu_1} \cdots q^{\mu_r}. \tag{2.6}$$

In general, the loop integral can be divergent when the loop momentum tends to infinity (UV divergences) or whenever it becomes soft ($q \simeq 0$) or collinear to an external momentum (IR divergences). Both divergences are regularised via analytic continuation of the loop integration to $d = 4 - 2\epsilon$ dimensions. The UV divergences are reabsorbed via renormalisation of the parameters of the theory. This introduces a set of counterterm interactions and a dependence of the scattering amplitude on the arbitrary renormalization scale μ_R, which is formally of higher order and reflects the truncation of the perturbative series. As discussed in Section 1.1, the cancellation of IR divergences is achieved in physical observables by summing the contributions of one-loop virtual and real-emission amplitudes and by absorbing initial-state collinear singularities into the PDFs.

Using the decomposition (2.6) of the numerator, the diagram in Eq.(2.4) can be rewritten as

$$\delta\mathcal{M}^{(d)} = \mathcal{C}^{(d)} \sum_{r=0}^{R} \mathcal{N}_{\mu_1 \ldots \mu_r} \int d^d q \frac{q^{\mu_1} \ldots q^{\mu_r}}{D_0 D_1 \ldots D_{n-1}} \equiv \mathcal{C}^{(d)} \sum_{r=0}^{R} \mathcal{N}_{\mu_1 \ldots \mu_r} \mathcal{T}_n^{\mu_1 \ldots \mu_r}, \tag{2.7}$$

i.e., as a linear combination of tensor integrals

$$\mathcal{T}_n^{\mu_1 \ldots \mu_r} = \int d^d q \frac{q^{\mu_1} \ldots q^{\mu_r}}{D_0 D_1 \ldots D_{n-1}}. \tag{2.8}$$

The Feynman diagram (and eventually the full amplitude) is by definition a scalar quantity. As discussed in the following section, to simplify Eq.(2.7), the tensor integrals in Eq.(2.8) can be reduced to a combination of covariant tensor coefficients and scalar integrals with only one, two, three or four loop propagators. Alternatively, one can completely bypass the tensor integral representation by means of so-called integrand reduction methods, which permit a direct determination of the scalar-integral coefficients using the numerator $\mathcal{N}(q; \{p_i\})$.

2.2 Reduction of one-loop amplitudes

2.2.1 Tensor-integral reduction

Let us define the generic tensor integral in d dimensions, following the notation in [32], as follows,

$$\mathcal{T}_n^{\mu_1 \ldots \mu_r} = \frac{(2\pi\mu)^{4-d}}{i\pi^2} \int d^d q \frac{q^{\mu_1} \ldots q^{\mu_r}}{D_0 D_1 \ldots D_{n-1}}, \tag{2.9}$$

with the denominators

$$D_0 = q^2 - m_0^2 + \mathrm{i}\epsilon, \qquad D_i = (q + k_i)^2 - m_i^2 + \mathrm{i}\epsilon, \qquad i = 1, \ldots, n-1. \tag{2.10}$$

where we introduced the compact notation $k_i = \sum_{j=0}^{i} p_j$. The integrals are classified according to the number n of loop propagators and the rank r, i.e. the number of loop momenta q in the numerator. For $r + d - 2n \geq 0$ the integrals are UV-divergent. In renormalizable theories the property $r \leq n$ holds, thus ensuring a finite number of divergent integrals. It is a generally adopted convention to denote the integrals with the corresponding nth letter of the alphabet. Thus we set $T_n = A, B, C, D, E, F, \ldots$ for $n = 1, 2, 3, 4, 5, 6, \ldots$, respectively.

The tensor integrals are manifestly symmetric in the Lorentz indices μ_k. Using Lorentz covariance they can be decomposed into a combination of tensors constructed from the external momenta k_i and the metric tensor $g_{\mu\nu}$ with totally symmetric coefficients $\mathcal{T}_{n;i_1\ldots i_r}$ [32]. In order to have a schematic compact expression for this general decomposition one employs the extra "pseudo" momentum k_0, which is related to the $g_{\mu\nu}$ terms via

$$\begin{aligned} k_0^{\mu_1} k_0^{\mu_2} &\to g^{\mu_1\mu_2}, \\ k_0^{\mu_1} k_0^{\mu_2} k_0^{\mu_3} k_0^{\mu_4} &\to g^{\mu_1\mu_2} g^{\mu_3\mu_4} + g^{\mu_1\mu_3} g^{\mu_2\mu_4} + g^{\mu_1\mu_4} g^{\mu_2\mu_3}. \end{aligned} \tag{2.11}$$

In this way we can write

$$\mathcal{T}_n^{\mu_1\cdots\mu_r} = \sum_{i_1\ldots i_r=0}^{n-1} \mathcal{T}_{n;i_1\ldots i_r} k_{i_1}^{\mu_1} \cdots k_{i_r}^{\mu_r}. \tag{2.12}$$

Terms with an odd number of k_0's do not contribute. The explicit decompositions for the low-rank integrals read

$$\begin{aligned} B^\mu &= k_1^\mu B_1, \qquad C^\mu = \sum_{i=1}^{2} k_i^\mu C_i, \qquad D^\mu = \sum_{i=1}^{3} k_i^\mu D_i, \\ B^{\mu\nu} &= g^{\mu\nu} B_{00} + k_1^\mu k_1^\nu B_{11}, \qquad C^{\mu\nu} = g^{\mu\nu} C_{00} + \sum_{i,j=1}^{2} k_i^\mu k_j^\nu C_{ij}, \\ D^{\mu\nu\rho} &= \sum_{i=1}^{3} (g^{\mu\nu} k_i^\rho + g^{\nu\rho} k_i^\mu + g^{\mu\rho} k_i^\nu) D_{00i} + \sum_{i,j,k=1}^{3} k_i^\mu k_j^\nu k_k^\rho D_{ijk}. \end{aligned} \tag{2.13}$$

Through an iterative procedure the coefficients $\mathcal{T}_{n;i_1\ldots i_r}$ can be reduced to a combination of scalar integrals $\mathcal{T}_{n;0}$ [102]. The relevant reduction identities are obtained by contracting the tensor integral with the external momenta k_i^μ or with the metric tensor $g_{\mu\nu}$. These products can then be re-expressed as combinations of denominators of loop propagators. In this way one can progressively reduce the rank and the number of propagators in the tensor integral, eventually arriving at scalar integrals. In the following we will briefly sketch this procedure. Contracting the loop momentum q with the external momentum k_k yields

$$k_{k\mu} q^\mu = \frac{1}{2}(D_k - D_0 - f_k), \qquad f_k = k_k^2 - m_k^2 + m_0^2. \tag{2.14}$$

Multiplying the generic tensor integral (2.9) with k_k and inserting the previous identity

yields

$$\begin{aligned} k_{k\mu_r}\mathcal{T}_n^{\mu_1\dots\mu_r} &= \frac{1}{2}\frac{(2\pi\mu)^{4-d}}{i\pi^2}\int d^dq\left[\frac{q^{\mu_1}\dots q^{\mu_{r-1}}}{D_0\dots D_{k-1}D_{k+1}\dots D_{n-1}}\right. \\ &\qquad \left. -\frac{q^{\mu_1}\dots q^{\mu_{r-1}}}{D_1\dots D_{n-1}} - f_k\frac{q^{\mu_1}\dots q^{\mu_{r-1}}}{D_0\dots D_{n-1}}\right] \\ &= \frac{1}{2}[\mathcal{T}_{n-1}^{\mu_1\dots\mu_{r-1}}(k) - \mathcal{T}_{n-1}^{\mu_1\dots\mu_{r-1}}(0) - f_k\mathcal{T}_n^{\mu_1\dots\mu_{r-1}}], \end{aligned} \tag{2.15}$$

where in the last line we indicate in parenthesis the propagator that has been cancelled. Note that, after removing the propagator D_0, an external momentum appears in the first loop propagator. Therefore, one has to perform a shift of the loop momentum to bring it back to the standard form. The tensor integrals on the right-hand side have rank $r-1$; and the first two have also one propagator less. If the loop momentum enters the numerator at least to the second power, one obtains extra relations by contraction with the metric tensor

$$g_{\mu\nu}q^\mu q^\nu = q^2 = D_0 + m_0^2. \tag{2.16}$$

This gives

$$\begin{aligned} g_{\mu_{r-1}\mu_r}\mathcal{T}_n^{\mu_1\dots\mu_r} &= \frac{(2\pi\mu)^{4-d}}{i\pi^2}\int d^dq\left[\frac{q^{\mu_1}\dots q^{\mu_{r-2}}}{D_1\dots D_{n-1}} + m_0^2\frac{q^{\mu_1}\dots q^{\mu_{r-2}}}{D_0\dots D_{n-1}}\right] \\ &= [\mathcal{T}_{n-1}^{\mu_1\dots\mu_{r-2}}(0) + m_0^2\mathcal{T}_n^{\mu_1\dots\mu_{r-2}}]. \end{aligned} \tag{2.17}$$

Having these relations at disposal, the reduction proceeds schematically as follows. After inserting the covariant decomposition (2.12) into Eq.(2.15) and (2.17), one obtains a set of linear algebraic equations for the coefficients of the tensor integrals. Provided that the Gram determinant

$$\det Z_{n-1} = \begin{vmatrix} k_1k_1 & k_1k_2 & \dots & k_1k_{n-1} \\ k_2k_1 & k_2k_2 & \dots & k_2k_{n-1} \\ \vdots & \vdots & \ddots & \vdots \\ k_{n-1}k_1 & k_{n-1}k_2 & \dots & k_{n-1}k_{n-1} \end{vmatrix} \tag{2.18}$$

is non-zero, the system can be inverted and solved for the coefficients $\mathcal{T}_{n;i_1\dots i_r}$ in terms of coefficients of tensor integrals with lower rank and a lower number of propagators. The reduction stops when all tensor integrals are expressed in terms of scalar integrals $\mathcal{T}_{P;0}$ with $P \le n$. The scalar integrals with $n \ge 5$ can be further reduced to four-point integrals ($n = 4$) exploiting the four-dimensionality of spacetime [32]. For example, six-point and five-point scalars can be expressed respectively as a combination of six five-point and five four-point functions. In conclusion the basic integrals needed for one-loop calculations are scalar tadpoles, bubbles, triangles and boxes with $n = 1, 2, 3, 4$.

In phase-space regions where Gram determinants become very small, the reduction procedure outlined above leads to spurious singularities that can spoil the numerical stability of the calculation. For $2 \to 2$ processes, this happens only in some very small corners of phase space, e.g. for forward scattering or at thresholds. For more complicated processes, involving more than four external particles, Gram determinants can vanish or become small also within the allowed phase space. Consequently, techniques

for calculating tensor integrals have to be further refined. Various methods have been developed to cure or bypass these problems (see e.g. [35]). Here we will briefly discuss two alternatives that have been implemented in the tensor reduction library used for the phenomenological applications presented in this thesis [31, 32, 103]. One method consists in expanding the tensor coefficients around the limit of vanishing Gram determinants. It requires the calculation of $(n-1)$-point functions of higher rank compared to the standard Passarino-Veltman algorithm [102]. The convergence of the calculation can be controlled and improved by adding more terms to the expansions. In general the first few terms turn out to be sufficient. The tensor coefficients are expressed in terms of a reduced basis, since the scalar integrals themselves become linearly dependent in the limit of vanishing Gram determinants. The other method consists in a modified formulation of Passarino-Veltman reduction which avoids Gram determinants all together. One can evaluate a particular tensor coefficient and from this deduce algebraically all the others including the scalar integral, thus changing also the set of master integrals. In this approach the inverse of modified Cayley determinants $\det X$ appear. They are connected to the Gram matrix Z through the relations

$$X_{ij} = Z_{ij} - f_i - f_j + 2m_0^2, \quad X_{0i} = X_{i0} = -f_i + 2m_0^2, \qquad i,j = 1,\ldots,n. \tag{2.19}$$

This reduction can again become problematic if $\det X$ becomes small. If it vanishes exactly, extra analytical results allow for a stable evaluation and systematic expansions exist for the case of small Cayley determinants [32].

2.2.2 OPP reduction

Let us now discuss the OPP reduction method [26] starting from the n-point contribution to the scattering amplitude at the integrand level [33, 104]

$$A(\bar{q}) = \frac{\mathcal{N}(\bar{q})}{\bar{D}_0 \bar{D}_1 \ldots \bar{D}_{n-1}}, \tag{2.20}$$

where the bar denotes objects living in $d = 4 + 2\epsilon$ dimensions, i.e.,

$$\bar{q}^2 = q^2 + \tilde{q}^2, \quad \bar{D}_i = (\bar{q} + k_i)^2 - m_i^2 = D_i + \tilde{q}^2. \tag{2.21}$$

The external momenta p_i, entering via $k_i = \sum_{j=0}^{i} p_j$, are treated as four-dimensional objects. Let us neglect for the moment the ϵ-dimensional part of the numerator. The four-dimensional piece can be expressed—at the integrand level—in terms of the denominators as follows,

$$\begin{aligned}
\mathcal{N}(q) = &\sum_{i_0<i_1<i_2<i_3}^{n-1} \Big[d(i_0 i_1 i_2 i_3) + \tilde{d}(q; i_0 i_1 i_2 i_3)\Big] \prod_{i\neq i_0,i_1,i_2,i_3}^{n-1} D_i \\
&+ \sum_{i_0<i_1<i_2}^{n-1} [c(i_0 i_1 i_2) + \tilde{c}(q; i_0 i_1 i_2)] \prod_{i\neq i_0,i_1,i_2}^{n-1} D_i \\
&+ \sum_{i_0<i_1}^{n-1} \Big[b(i_0 i_1) + \tilde{b}(q; i_0 i_1)\Big] \prod_{i\neq i_0,i_1}^{n-1} D_i \\
&+ \sum_{i_0}^{n-1} [a(i_0) + \tilde{a}(q; i_0)] \prod_{i\neq i_0}^{n-1} D_i .
\end{aligned} \tag{2.22}$$

If inserted back into Eq.(2.20) this parameterization exposes the multi-pole structure of the amplitude. The residues of the poles consist of two parts. The spurious contributions $\tilde{d}, \tilde{c}, \tilde{b}, \tilde{a}$ depend on the loop momentum q and vanish upon integration. The constant parts of the residues d, c, b, a can be identified with the standard coefficients of the loop functions: $d(i_0 i_1 i_2 i_3)$ are the coefficients of the four-point functions associated to the denominators i_0, i_1, i_2, i_3. Similarly, $c(i_0 i_1 i_2)$, $b(i_0 i_1)$ and $a(i_0)$ are the coefficients of all possible three-, two- and one-point functions.

Starting from the parameterization (2.22) the problem of computing the amplitude is formally reduced to the algebraic problem of extracting all coefficients. This can be achieved by computing the numerator $\mathcal{N}(q)$ for a sufficient number of different values of q and then inverting the system of algebraic equations. To this end, the functional form of the q-dependence of the spurious terms has to be known. This can be extracted by decomposing q in terms of an external momentum and a set of massless momenta l_i built from linear combinations of p_i's,

$$q^\mu = -p_0^\mu + \sum_{i=1}^{4} G_i l_i^\mu, \qquad l_i^2 = 0. \tag{2.23}$$

For specific values of q the coefficients G_i either reconstruct some denominators D_i or vanish upon $d^d\bar{q}$ integration, thus giving rise respectively to the coefficients d, c, b, a or $\tilde{d}, \tilde{c}, \tilde{b}, \tilde{a}$. In this way the functional form of the spurious terms can be extracted and classified on a process-independent basis. In fact, it depends only on the maximum tensor rank appearing in the amplitude. In renormalizable gauges used in practical calculations the maximum rank cannot be higher than the number of loop denominators, thus leading to a limited number of spurious terms. Schematically, one can first recover the functional dependence of the spurious terms on q by singling out all terms that do not reconstruct denominators. At this stage the coefficients can be extracted choosing values of q resulting in multiple on-shell cuts for which a set of denominators D_i vanishes. This allows to simplify the system of equations and put it in a triangular form. It can then be solved iteratively first computing all possible four-point functions, then the three-point functions and so on. For example, one can pick up a value of q built as $q = -p_0 + \sum_i x_i l_i$ corresponding to a quadruple cut with

$$D_0 = D_1 = D_2 = D_3 = 0. \tag{2.24}$$

The associated system of equations in x_i admits two (complex) solutions $q_0^\pm$. Inserting them in the decomposition of the numerator, and knowing from the functional form of $\tilde{d}$ that it has only one unknown constant coefficient, one can extract the coefficients $d(0123)$ and $\tilde{d}(q_0^\pm; 0123)$ by solving the two equations

$$\mathcal{N}(q_0^\pm) = \Big[d(0123) + \tilde{d}(q_0^\pm; 0123) \Big] \prod_{i \neq 0,1,2,3} D_i(q_0^\pm). \tag{2.25}$$

This can be iterated until all coefficients have been determined.

The outlined procedure is numerically applicable in four dimensions. Since a dimensional shift is needed to regularize the divergent integrals, to be fully consistent it has to be formally carried out in d dimensions. The resulting mismatch between the

dimensionally regularized denominators $\bar{D}_i$ in Eq.(2.20) and the four-dimensional D_i in Eq.(2.22) gives rise to extra contributions known as R_1 rational terms [105]. By construction the two sets of denominators differ by the ϵ-dimensional piece of the loop momentum $\bar{q}^2 = q^2 + \tilde{q}^2$,

$$\bar{D}_i = D_i + \tilde{q}^2. \tag{2.26}$$

The required R_1 terms are generated introducing the $\tilde{q}^2$ dependence in the coefficients through mass shifts

$$m_i^2 \to m_i^2 - \tilde{q}^2. \tag{2.27}$$

After the expansion

$$\begin{aligned} d(ijkl;\tilde{q}^2) &= d(ijkl) + \tilde{q}^2 d^{(2)}(ijkl) + \tilde{q}^4 d^{(4)}(ijkl), \\ c(ijk;\tilde{q}^2) &= c(ijk) + \tilde{q}^2 c^{(2)}(ijk), \\ b(ij;\tilde{q}^2) &= b(ij) + \tilde{q}^2 b^{(2)}(ij), \end{aligned} \tag{2.28}$$

the extra contributions can be computed by solving the system of equations obtained from the evaluation of Eq.(2.28) for different values of $\tilde{q}^2$.

A further set of rational terms appears when considering the ϵ-dimensional part of the numerator in Eq.(2.20), i.e.

$$\mathcal{N}(\bar{q}) = \mathcal{N}(q) + \tilde{\mathcal{N}}(\tilde{q}^2, \epsilon; q). \tag{2.29}$$

They are called R_2-terms and are defined as [105]

$$R_2 \equiv \frac{1}{(2\pi)^4} \int d^d\bar{q} \frac{\tilde{\mathcal{N}}(\tilde{q}^2, \epsilon; q)}{\bar{D}_0 \bar{D}_1 \dots \bar{D}_{n-1}}. \tag{2.30}$$

In the calculation of these R_2 all ingredients of the numerator function have to be consistently split into four- and ϵ- dimensional pieces. This means that also Dirac γ matrices and the metric tensor have to be split,

$$\begin{aligned} \bar{q} &= q + \tilde{q}, \\ \bar{\gamma}_{\bar{\mu}} &= \gamma_\mu + \tilde{\gamma}_{\tilde{\mu}}, \\ \bar{g}^{\bar{\mu}\bar{\nu}} &= g^{\mu\nu} + \tilde{g}^{\tilde{\mu}\tilde{\nu}}. \end{aligned} \tag{2.31}$$

The R_2 terms depend on the gauge and the regularization scheme. They are generated only by the relatively small number of possible UV-divergent (sub)-graphs. Given the Lagrangian—and so the Feynman rules—of the theory at hand, starting from the definition (2.30) the R_2 terms can be computed using a special set of tree-level-like Feynman rules which can be derived once and for all. They are extracted considering all one-particle irreducible amplitudes with up to four external legs (enough to cover all possible UV-divergent contributions). R_2 terms can thus be computed in a straightforward way on the same footing as UV-counterterm diagrams. The R_2 Feynman rules have been derived for QCD [28], the full SM [106,107] and also for the QCD corrections in the minimal supersymmetric extension of the SM [108].

The methods discussed so far—as well as methods based on generalized unitarity [109]—permit to design and implement algorithms for the automated numerical

computation of one-loop amplitudes. In this respect, a high degree of automation is desirable to reduce as much as possible the needed man power on a process-by-process basis. This also reflects the possibility of enlarging the range of applicability of a one-loop generator to different classes of processes within different models. In fact, the physics programme of a hadron collider as the LHC requires precise simulations for highly non-trivial multiparticle processes not only in the framework of the Standard Model but also in many BSM extensions explored in the experimental searches.

Another crucial aspect of automated generators is the CPU efficiency. In fact, to achieve the mentioned large-scale applicability for processes with six or more external particles, it is crucial that the numerical evaluation of matrix elements be fast, not to represent a bottleneck in the complex chain of simulations of scattering events. Indeed, until few years ago, one-loop generators have represented exactly such a bottleneck that mainly hampered substantial improvements in this direction. The advent of unitarity-based methods and new techniques for Feynman diagram computation in the framework of tensor-integral and OPP reduction led to the calculation of NLO QCD corrections for several $2 \to 4(5)$ processes—notably the ones listed in the so called Les Houches wish list [110]—that few years before would have been considered an almost impossible task, paving the way to the so called NLO revolution (for recent reviews of the main results see e.g. [41,42]). One of the features that emerged from the first NLO QCD calculations of $2 \to 4$ processes, was a trade-off between CPU efficiency and automation. On the one hand, the tensor-reduction approach led to the fastest numerical codes, but its large-scale applicability was limited by the occurrence of very large algebraic expressions. On the other hand, on-shell techniques permit to construct one-loop amplitudes in terms of tree-level building blocks, which can be generated with fully automated tree algorithms, thereby obtaining a similar level of automation at one-loop level. However, as we will discuss in the following section, in original on-shell approaches based on conventional tree amplitudes, the high level of automation was obtained at a rather high price in terms of CPU efficiency.

2.3 The OpenLoops algorithm

In this section we will discuss OpenLoops [43], a fully automated generator of tree-level and one-loop scattering amplitudes, which represents the core of this PhD project. The OpenLoops algorithm is a Feynman-diagram based, numerical, recursive approach inspired by a Dyson-Schwinger recursion proposed by van Hameren for the construction of colour-ordered one-loop multi-gluon amplitudes [44].

The algorithm has been designed in a way that provides full automation and flexibility together with very high CPU efficiency. Its main features can be summarized as follows.

- For the first time, a similarly high level of automation as originally obtained with OPP reduction is achieved also in the tensor-integral framework.

- Similarly as in the OPP approach, one-loop amplitudes are generated with a tree-like numerical recursion; but instead of using conventional tree algorithms, the OpenLoops approach is based on new tensorial building blocks, which are

related to tensor integrals and encode the full loop-momentum dependence of cut-open loops.

- This approach yields unprecedented CPU efficiency, both in combination with tensor-integral or OPP reduction. As compared to original implementations of OPP reduction, a speed up of two orders of magnitude is achieved.
- The numerical and recursive nature of the algorithm permits to circumvent all bottlenecks encountered in pioneering one-loop generators based on computer algebra. In particular, the compactness of the code and its generation time are improved by orders of magnitude.

In the following we will adopt the notation of [43]. Leading-order transition amplitudes $\mathcal{M}$ and virtual NLO corrections $\delta\mathcal{M}$ are handled as sums of tree and one-loop Feynman diagrams d,

$$\mathcal{M} = \sum_d \mathcal{M}^{(d)}, \qquad \delta\mathcal{M} = \sum_d \delta\mathcal{M}^{(d)}. \tag{2.32}$$

They enter the computation of the cross section through the corresponding scattering probability densities

$$\mathcal{W} = \sum_{\text{hel,col}} |\mathcal{M}|^2, \qquad \delta\mathcal{W} = \sum_{\text{hel,col}} 2\mathfrak{Re}(\mathcal{M}^*\delta\mathcal{M}). \tag{2.33}$$

The sums run over the colour and helicity states of each external particle.

2.3.1 Colour treatement

An advantage of the diagrammatic approach, that balances the rapid growth in the number of graphs when increasing the particle multiplicity, is the possibility to perform colour sums very efficiently. This is a consequence of factorization of individual (sub)-diagrams into a colour factor $\mathcal{C}$ and a colour-stripped amplitude $\mathcal{A}$,

$$\mathcal{M}^{(d)} = \mathcal{A}^{(d)}\mathcal{C}^{(d)}, \qquad \delta\mathcal{M}^{(d)} = \delta\mathcal{A}^{(d)}\mathcal{C}^{(d)}. \tag{2.34}$$

In the special case of the quartic gluon vertex, the Feynman rule contains three independent colour structures. Thus if n_4 is the number of quartic gluon vertices in a diagram, it will actually give rise to 3^{n_4} colour-factorized terms, which are treated as separate sub-diagrams. For istance the following two 6-point diagrams, contributing to the amplitude $gg q\bar{q}q\bar{q} \to 0$, are splitted as

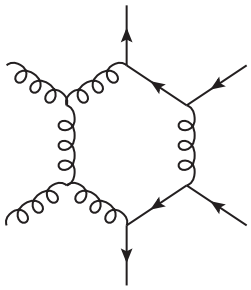

$$= \mathcal{A}^{(d)} f^{a_1 bd} f^{a_2 cd} \left(T^b T^e\right)_{i_3 i_4} \left(T^c T^e\right)_{i_5 i_6},$$

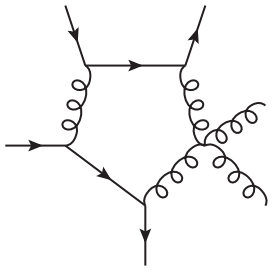

$$= \left[\mathcal{A}^{(d_1)} f^{a_1 bd} f^{a_2 cd} + \mathcal{A}^{(d_2)} f^{a_1 cd} f^{a_2 bd} + \mathcal{A}^{(d_3)} f^{a_1 a_2 d} f^{bcd}\right] \left(T^b T^e\right)_{i_3 i_4} \left(T^c T^e\right)_{i_5 i_6},$$

where a_1, a_2 and i_3, i_4, i_5, i_6 are the colour indices of the external gluons and quarks, respectively. A sum over repeated internal indices is implicitly understood. The colour factors can all be reduced fully algebraically to a standard colour basis $\{\mathcal{C}_i\}$ consisting of Kronecker symbols and Gell-Mann matrices $T^a = \lambda^a/2$ by using general identities of $\mathrm{SU}(N_c)$ Lie groups such as

$$f^{abc} T^c = -\mathrm{i}\left[T^a, T^b\right], \qquad T^a_{ij} T^a_{kl} = \frac{1}{2}\left(\delta_{il}\delta_{kj} - \frac{1}{N_c}\delta_{ij}\delta_{kl}\right). \tag{2.35}$$

After colour reduction the tree-level amplitude can be rewritten as a linear combination of the colour basis $\{\mathcal{C}_1, \ldots, \mathcal{C}_N\}$ in colour space,

$$\mathcal{M} = \sum_d \mathcal{C}^{(d)} \mathcal{A}^{(d)} = \sum_d \left(\sum_i c_i^{(d)} \mathcal{C}_i\right) \mathcal{A}^{(d)} = \sum_i \mathcal{C}_i \left(\sum_d c_i^{(d)} \mathcal{A}^{(d)}\right) = \sum_i \Gamma_i \mathcal{C}_i, \tag{2.36}$$

where the coefficients $c_i^{(d)}$ are rational functions of the number of colours N_c. The colour sum for the LO probability density is then easily computed as

$$\sum_{\mathrm{col}} \mathcal{M}^* \mathcal{M} = \sum_{\mathrm{col}} \left(\sum_i \Gamma_i \mathcal{C}_i\right)^\dagger \left(\sum_l \Gamma_l \mathcal{C}_l\right) = \sum_{i,l} \Gamma_i^* \left(\sum_{\mathrm{col}} \mathcal{C}_i^\dagger \mathcal{C}_l\right) \Gamma_l. \tag{2.37}$$

This requires a single evaluation of the colour-stripped amplitudes $\mathcal{A}^{(d)}$ and the construction, once and for all for a given process, of the colour-interference matrix

$$\mathcal{K}_{il} = \sum_{\mathrm{col}} \mathcal{C}_i^\dagger \mathcal{C}_l. \tag{2.38}$$

When considering loop diagrams, the reduction of the colour factors generally requires an extension of the colour basis. After constructing the interference of the tree-level amplitude with the elements of the basis,

$$\tilde{\mathcal{M}}_j = \sum_{\mathrm{col}} \mathcal{M}^* \mathcal{C}_j = \sum_i \mathcal{K}_{ij} \Gamma_i^*, \tag{2.39}$$

the colour sum for the Born-loop interference can be written as

$$\begin{aligned} \sum_{\mathrm{col}} 2\mathfrak{Re}(\mathcal{M}^* \delta\mathcal{M}) &= \sum_d 2\mathfrak{Re}\left\{\left(\sum_{\mathrm{col}} \mathcal{M}^* \mathcal{C}^{(d)}\right) \delta\mathcal{A}^{(d)}\right\} \\ &= \sum_d 2\mathfrak{Re}\left\{\left(\sum_j c_j^{(d)} \tilde{\mathcal{M}}_j\right) \delta\mathcal{A}^{(d)}\right\}. \end{aligned} \tag{2.40}$$

Colour sums are performed at zero cost from the trivial linear combination $\sum_j c_j^{(d)} \tilde{\mathcal{M}}_j$ once the one-loop colour-stripped amplitude $\delta\mathcal{A}^{(d)}$ is known.

2.3.2 Colour-stripped amplitudes

Colour-stripped tree diagrams $\mathcal{A}^{(d)}$ are built through an efficient recursive algorithm that merges previously computed building blocks called sub-trees. A sub-tree is a subdiagram obtained by cutting the propagator associated with an internal off-shell line. It can be seen as a generalized wavefunction described by a complex n-tuple $w^\beta(i)$, where β is the spinor, Lorentz or scalar index of the cut line. In this compact notation the label i represents the topology, momentum and particle content of the sub-tree. Pictorially a sub-tree is represented as

$w^\beta(i) =$ 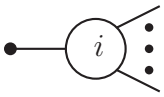

(2.41)

The recursive procedure consists in merging sub-trees by connecting them through vertices and propagators:

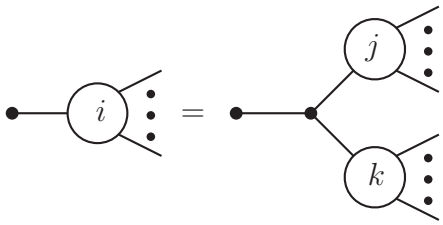

(2.42)

The sub-trees i, j and k represent *individual* sub-topologies that connect an off-shell line to a subset of the on-shell external lines. Note that (2.42) is different with respect to Berends–Giele or Dyson–Schwinger recursions [111–113], where off-shell currents effectively involve *all* diagrams that connect external and internal lines. The recursion makes use of the Feynman rules of the model at hand to build the new sub-tree as

$$w^\beta(i) = \frac{X^\beta_{\gamma\delta}(i,j,k) w^\gamma(j) w^\delta(k)}{p_i^2 - m_i^2 + \mathrm{i}\epsilon}, \tag{2.43}$$

where $X^\beta_{\gamma\delta}(i,j,k)/(p_i^2 - m_i^2 + \mathrm{i}\epsilon)$ describes a vertex connecting i, j, k and a propagator attached to i, as in the pictorial representation above. The treatement of quartic vertices proceeds straightforwardly in the very same way. Starting from the external wavefunctions of the scattering particles, the recursion terminates with the contraction through a propagator of the last two sub-trees to form a full tree-level diagram,

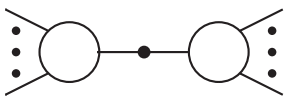
(2.44)

To clarify the procedure, let us show an explicit example of few recursion steps

needed to build the following sub-tree,

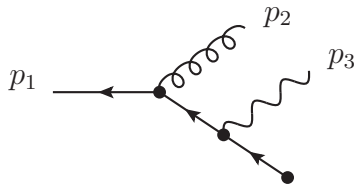

(2.45)

where the (incoming) momenta p_1, p_2 and p_3 are associated to an external quark, gluon and W boson, respectively. The wavefunctions of the external particles are fully specified by their momentum and helicity state,

$$\begin{aligned} w_\alpha(1) = & \quad = \bar{u}_\alpha(p_1,\lambda_1), \\ w_\mu(2) = & \quad = \epsilon_\mu(p_2,\lambda_2), \\ w_\nu(3) = & \quad = \epsilon_\nu(p_3,\lambda_3). \end{aligned} \tag{2.46}$$

The next steps in the recursion consist in merging the wavefunctions to build the internal line as $1+2 \to 12$ and $12+3 \to 123$,

$$w_\beta(12) = \quad = \frac{g_s[(-\not{p}_{12}+m)\gamma^\mu]_{\alpha\beta}}{p_{12}^2-m_{12}^2}\, w_\alpha(1) w_\mu(2), \tag{2.47}$$

$$w_\gamma(123) = \quad = \frac{e[(-\not{p}_{123}+m)\gamma^\nu(1-\gamma_5)]_{\beta\gamma}}{2\sqrt{2}s_w(p_{123}^2-m_{123}^2)}\, w_\beta(12) w_\nu(3). \tag{2.48}$$

where g_s and e are the strong and electromagnetic coupling constants and s_w is the sine of the weak mixing angle.

The basic building blocks are just wavefunctions, vertices and propagators. They are specified by the Feynman rules and depend only on the model at hand. The algorithm is in this sense fully general and model- and process-independent. Its main strength lies in the fact that pre-computed sub-trees shared by different diagrams can be reused without recomputing them, resulting in high CPU efficiency.

2.3.3 One-loop diagrams

Let us now consider one-loop amplitudes. A colour-stripped n-point loop diagram corresponds to an ordered set of n sub-trees, $\mathcal{I}_n = \{i_1, \ldots, i_n\}$, connected by loop

propagators

$$\delta\mathcal{A}^{(d)} = \int \frac{d^d q\, \mathcal{N}(\mathcal{I}_n;q)}{D_0 D_1 ... D_{n-1}} =$$

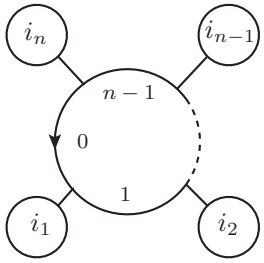

(2.49)

The particular ordering $\{i_1, \ldots, i_n\}$ of the external sub-trees describes the topology of the corresponding one-loop diagram. By considering the full set of diagrams, we automatically take into account all possible orderings allowed by the Feynman rules. Apart from the denominators, $D_i = (q+k_i)^2 - m_i^2 + \mathrm{i}\epsilon$, all other contributions from loop propagators, vertices and external sub-trees are contained in the numerator function $\mathcal{N}$. As discussed in the previous sections, the latter is a polynomial of degree $R \leq n$ in the loop momentum (see Eq.(2.6)).

In the framework of OPP reduction, the numerator function $\mathcal{N}(\mathcal{I}_n; q)$, which is needed as input of the reduction, can be built as a cut loop using a tree-level algorithm. Let us consider the cut loop that results from cutting the D_0 propagator in the generic n-point diagram above,

$$\mathcal{N}_\alpha^\beta(\mathcal{I}_n; q) =$$

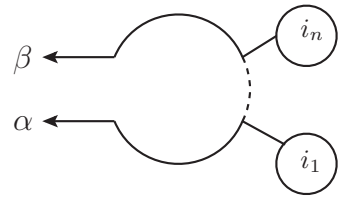

(2.50)

The indices α and β are associated to the field propagating in the cut line (i.e. spinor, vector, scalar). The trace of the cut loop corresponds to the full numerator

$$\sum_\alpha \mathcal{N}_\alpha^\alpha(\mathcal{I}_n; q) = \mathcal{N}(\mathcal{I}_n; q). \tag{2.51}$$

Generalizing the tree-level recursion (2.43), n-point cut loops can be constructed by recursively merging lower-point cut loops and sub-trees,

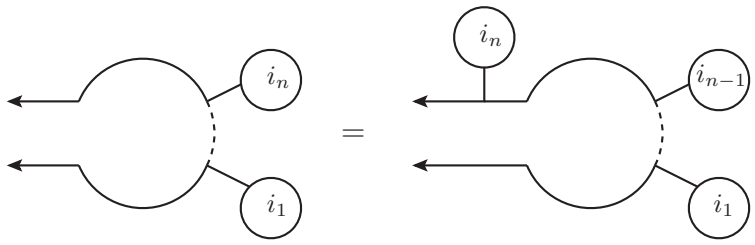

$$\mathcal{N}_\alpha^\beta(\mathcal{I}_n; q) = X_{\gamma\delta}^\beta(\mathcal{I}_n, i_n, \mathcal{I}_{n-1}) \mathcal{N}_\alpha^\gamma(\mathcal{I}_{n-1}; q) w^\delta(i_n), \tag{2.52}$$

where $X^{\beta}_{\gamma\delta}$ and w^{δ} are the same vertices and sub-trees that enter the tree algorithm. This approach allows to reduce the calculation of one-loop amplitudes to a tree-level problem. This permits to achieve a high level of automation by upgrading conventional tree algorithms such as HELAC [29] or MADGRAPH [50] to one-loop generators. However, for $2 \to n$ processes with $n \geq 4$ final-state particles, this approach does not allow to achieve very high CPU efficiency. The reason is that, to extract the coefficients of the scalar integrals, the OPP reduction requires repeated evaluations of the numerator function at multiple values of the loop momentum q, while tree algorithms are conceived for fixed momenta flowing in the diagrams. The nature of loop amplitudes, instead, requires the knowledge of the loop-momentum functional dependence of the numerator. The natural step is thus to introduce a new kind of loop-level algorithm which is designed to handle the building blocks of the recursion as polynomials in the loop momentum q.

Let us start by introducing what we call the open-loop representation of the cut numerator,

$$\mathcal{N}^{\beta}_{\alpha}(\mathcal{I}_n; q) = \sum_{r=0}^{R} \mathcal{N}^{\beta}_{\mu_1\dots\mu_r;\alpha}(\mathcal{I}_n) q^{\mu_1} \cdots q^{\mu_r}. \tag{2.53}$$

The coefficients $\mathcal{N}^{\beta}_{\mu_1\dots\mu_r;\alpha}(\mathcal{I}_n)$ of the polynomial are what we call open-loops. They are the objects that we want to build recursively. To this end, we split the tensor X in Eq.(2.52) into a constant and a part linear in q (this is always possible for renormalizable gauge theories),

$$X^{\beta}_{\gamma\delta} = Y^{\beta}_{\gamma\delta} + q^{\nu} Z^{\beta}_{\nu;\gamma\delta}. \tag{2.54}$$

Substituting this representation in (2.52), we obtain the master equation of the OPENLOOPS recursion,

$$\mathcal{N}^{\beta}_{\mu_1\dots\mu_r;\alpha}(\mathcal{I}_n) = \left[Y^{\beta}_{\gamma\delta} \mathcal{N}^{\gamma}_{\mu_1\dots\mu_r;\alpha}(\mathcal{I}_{n-1}) + Z^{\beta}_{\mu_1;\gamma\delta} \mathcal{N}^{\gamma}_{\mu_2\dots\mu_r;\alpha}(\mathcal{I}_{n-1}) \right] w^{\delta}(i_n). \tag{2.55}$$

Eq.(2.55) connects n-point, rank r open-loops on the left-hand side to $(n-1)$-point open-loops of rank r and $r-1$ on the right-hand side. At a given step of the recursion, interaction terms of type Y connect same-rank open-loops, while the Z_μ term gives rise—via the extra Lorentz index μ—to a new set of higher-rank coefficients. The recursion starts from the initial condition $\mathcal{N}^{\beta}_{\alpha}(\mathcal{I}_0) = \delta^{\beta}_{\alpha}$ associated to the D_0 propagator, and terminates by taking the trace over the open indices α and β after the last insertion for $n = N$,

$$\mathcal{N}_{\mu_1\dots\mu_r}(\mathcal{I}_n) = \sum_{\alpha} \mathcal{N}^{\alpha}_{\mu_1\dots\mu_r;\alpha}(\mathcal{I}_n). \tag{2.56}$$

In spite of the high tensor rank ($R = 6$) that can be reached in $2 \to 4$ amplitudes and the resulting large number of tensorial components that have to be evaluated, as shown in the next section, Eq.(2.55) can be implemented as a very fast numerical recursion. Once the coefficients $\mathcal{N}_{\mu_1\dots\mu_r}$ have been computed, multiple evaluations of the numerator

$$\mathcal{N}(q; \mathcal{I}_n) = \sum_{r=0}^{R} \mathcal{N}_{\mu_1\dots\mu_r}(\mathcal{I}_n) q^{\mu_1} \cdots q^{\mu_r}, \tag{2.57}$$

can be performed at a negligible CPU cost, resulting in a speed-up of orders of magnitude with respect to original implementations of OPP reduction based on standard tree-level algorithms.

The open-loops representation (2.53) can be used in combination with tensor integrals by writing the one-loop colour-stripped amplitude (2.49) as

$$\delta\mathcal{A}^{(d)} = \sum_{r=0}^{R} \mathcal{N}_{\mu_1\dots\mu_r}(\mathcal{I}_n) \int d^d q \frac{q^{\mu_1}\cdots q^{\mu_r}}{D_0 D_1 \dots D_{n-1}}. \tag{2.58}$$

In fact, the algorithm has been originally designed as a numerical recursion in the tensor-integral framework, and, as discussed in the next section, combining open-loops with tensor integrals results in the fastest and most stable approach, inheriting at the same time the high level of automation and flexibility of OPP-based generators. In this context, splitting the numerator into open-loops coefficients and loop-momentum monomials is the key point that leads to a very natural connection to both the tensor-integral and OPP-representation of one-loop diagrams.

The idea of recursively building the coefficients of the polynomial representation of the numerator has a series of extra consequences that allow to further improve the efficiency of the algorithm. The first one is the possibility of connecting sets of open-loops coefficients associated to equivalent intermediate sub-topologies shared by different loop diagrams. Once a specific set of open-loops has been computed, it can be shared and reused in the recursive calculation of other diagrams. Pinching the last loop propagator of a given recursion step links n-point parent diagrams to pre-computed parts of $(n-1)$-point child diagrams, as illustrated in the following schematic picture

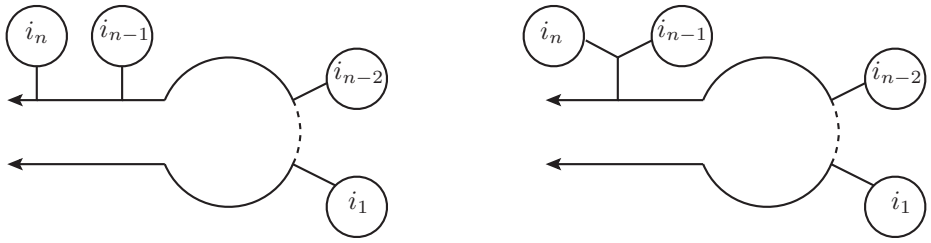

(2.59)

The parent diagram on the left can be constructed starting the recursion from the $\mathcal{I}_{n-2}$ open-loop of the child diagram on the right. To exploit this possibility the diagrams must be cut in the same way, namely starting from the loop propagator before the i_1 sub-tree. To this end we order the external sub-trees using a function $i_k \to S(i_k)$ that fulfills $S(i_k) > 0; S(i_k) \neq S(i_l)$ if i_k and i_l contain different external legs; $S(i_k \oplus i_l) > \max\{S(i_k), S(i_l)\}$ where $i_k \oplus i_l$ is the merged sub-tree resulting from i_k and i_l. This guarantees that—at least in QCD—each parent can be constructed from the $\mathcal{I}_{n-2}$ part of a previously computed child, allowing for an efficient recycling.

Another important feature of the open-loops approach is the possibility of performing highly efficient helicity sums. A particular helicity configuration is uniquely defined by the polarization states of the external wavefunctions. This information propagates through the diagram only via the coefficients of the numerator polynomial. This means that only the helicity-dependent open-loops have to be recomputed for each helicity configuration, whereas the reduction to scalar integrals can be performed only once

taking as input the unpolarised colour-summed interference between open-loops and tree amplitudes. This permits to bypass the operation of summing explicitly the full polarised amplitudes for each helicity configuration of the external particles, thereby largely avoiding the high CPU cost that can result from the exponential growth of the number of helicity configurations at large particle multiplicity. More explicitly, the contribution of a one-loop diagram $\delta\mathcal{M}^{(d)}$ to the helicity- and colour-summed interference with the Born amplitude can be rewritten, in the tensor-integral representation, as

$$\sum_{\text{hel,col}} \left[\mathcal{M}^* \delta\mathcal{M}^{(d)}\right] = \sum_{r=0}^{R} \delta\mathcal{W}^{(d)}_{\mu_1\dots\mu_r} \int \frac{d^d q\, q^{\mu_1}\dots q^{\mu_r}}{D_0 D_1 \dots D_{n-1}}, \tag{2.60}$$

where the reduction is done on top of the helicity- and colour-summed coefficients

$$\delta\mathcal{W}^{(d)}_{\mu_1\dots\mu_r} = \sum_{\text{hel,col}} \left[\mathcal{M}^* \mathcal{C}^{(d)} \mathcal{N}_{\mu_1\dots\mu_r}\right]. \tag{2.61}$$

In the OPP framework the starting point is the representation

$$\sum_{\text{hel,col}} \left[\mathcal{M}^* \delta\mathcal{M}^{(d)}\right] = \int \frac{d^d q\, \delta\mathcal{W}^{(d)}(q)}{D_0 D_1 \dots D_{n-1}}, \tag{2.62}$$

based on the unpolarised numerator function

$$\delta\mathcal{W}^{(d)}(q) = \sum_{r=0}^{R} \delta\mathcal{W}^{(d)}_{\mu_1\dots\mu_r} q^{\mu_1}\dots q^{\mu_r}. \tag{2.63}$$

The efficiency can be further improved by grouping, before reduction to scalar integrals, sets of diagrams with identical one-loop topologies but different external sub-trees, after Born interference and colour and helicity sums. For example, the following two diagrams can be combined at the coefficient level and reduced afterwards only once:

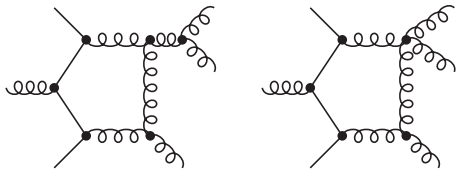

2.4 Implementation and performance

In this section we will describe the implementation of the open-loops algorithm in a fully automated computer program called OpenLoops. After sketching the general structure and main features of the program, we will show examples of the numerical routines for the construction of sub-trees and open-loops. We will then discuss extensive validation and performance studies, focussing on speed and numerical stability.

As discussed in the previous section, the open-loops algorithm is a model- and process-independent recursive approach based on Feynman diagrams. The basic building blocks are the off-shell sub-trees introduced in (2.41) and the open-loops coefficients

of Eq.(2.53). They are built starting from the external wavefunctions through the tensorial kernels X, Y, Z defined in Eq.(2.43) and (2.54). The kernels depend only on the vertices and propagators in the Feynman rules of the model at hand, and are implemented in numerical routines that are applicable to the calculation of any scattering amplitude.

The full generation chain is completely automatized. Starting from a process-definition file, the numerical code is generated in a few seconds or minutes depending on the particle multiplicity and number of diagrams. The internal structure of OpenLoops is the following: Feynman diagrams are generated with `FeynArts` [114], they are subsequently processed by a `Mathematica` program that handles the skeleton of the recursion, builds the set of sub-trees and open-loops, concatenates them to compute all diagrams, takes care of the colour algebra and generates `Fortran90` code. The latter returns, given a phase space point, the tree-level and one-loop amplitudes for a set of input parameters (couplings, masses, etc.). The reduction to scalar integrals can be performed in terms of tensor integrals using the Collier library by A. Denner, S. Dittmaier and L. Hofer [115], which implements the scalar integrals of [103] as well as various expansions in Gram determinants and other kinematic quantities [31, 32] in order to avoid numerical instabilities during tensor reduction.

Alternatively, OPP reduction is performed using either CutTools [46] or Samurai [47]. Ultraviolet and infrared divergences are dimensionally regularized. While loop denominators are consistently treated in $d = 4 - 2\epsilon$ dimensions, the momenta q^μ and the coefficients $\mathcal{N}_{\mu_1 \dots \mu_r}$ are handled in four dimensions. The R_2 rational terms are restored by computing an extra set of counter-term-like diagrams based on special Feynman rules as discussed in section 2.2. UV renormalization is performed generating the relevant set of standard counter-term diagrams. The strong coupling constant is renormalized in the $\overline{\text{MS}}$ scheme. Bottom and top quark masses are renormalized within the on-shell scheme.

The current implementation allows to generate one-loop QCD corrections to any SM process. It is also possible to compute squared one-loop amplitudes for processes for which no tree-level contribution exists. The complex-mass scheme [116] for the consistent description of intermediate unstable resonances, including finite width effects, is fully supported. The extension to full QCD+EW one-loop corrections—in particular the rather large set of extra Feynman rules for the R_2 contributions and the UV renormalization—has been already fully implemented and is presently being validated. Extensions to BSM or effective theories are also possible.

2.4.1 Tree-level amplitudes

For the detailed description of the OpenLoops algorithm implementation, let us start looking at the tree-level generator. We adopted for the Feynman rules of the Standard Model the conventions in [117] and [118]. The numerical routines are of three different types: external wavefunctions, vertices and propagators. The generic wavefunction routine has the form

```
subroutine wf_F(P, M, POL, J_F).
```

For an external particle of type `F=S,V,Q,A` (scalar, vector, fermion, antifermion) it takes as input the four-momentum `P`, the mass `M`, the helicity state `POL` and returns

as output an array `J_F` of length $n = 1$ for scalar and $n = 4$ for vector or spinor wavefunctions. For scalar particles one trivially obtains `J_S=1`, whereas for vectors and fermions we employ the formulae of [119, 120] . We use the chiral representation of the Dirac γ matrices in [121]. The numerical routines for vertices and propagators involve the products of γ matrices with spinor arrays and metric tensors with four-vector arrays. Introducing the following linear combinations of Dirac γ^μ matrices,

$$\tilde{\gamma}^1 = \gamma^0 - \gamma^3 = \begin{pmatrix} 0 & 0 & -2 & 0 \\ 0 & 0 & 0 & 0 \\ 0 & 0 & 0 & 0 \\ 0 & -2 & 0 & 0 \end{pmatrix}, \quad \tilde{\gamma}^2 = \gamma^0 + \gamma^3 = \begin{pmatrix} 0 & 0 & 0 & 0 \\ 0 & 0 & 0 & -2 \\ -2 & 0 & 0 & 0 \\ 0 & 0 & 0 & 0 \end{pmatrix},$$
$$\tilde{\gamma}^3 = -\gamma^1 - \mathrm{i}\gamma^2 = \begin{pmatrix} 0 & 0 & 0 & -2 \\ 0 & 0 & 0 & 0 \\ 0 & 2 & 0 & 0 \\ 0 & 0 & 0 & 0 \end{pmatrix}, \quad \tilde{\gamma}^4 = -\gamma^1 + \mathrm{i}\gamma^2 = \begin{pmatrix} 0 & 0 & 0 & 0 \\ 0 & 0 & -2 & 0 \\ 0 & 0 & 0 & 0 \\ 2 & 0 & 0 & 0 \end{pmatrix}, \tag{2.64}$$

allows to reduce the number of non-zero entries from four to two, thus reducing as well the number of basic operations that have to be performed in a subroutine. Motivated by this observation, we systematically express all Lorentz vectors and tensors in a light-cone representation related to the combinations of γ^μ matrices in (2.64). Given the contravariant components of a four-vector v^μ in the standard representation, the contravariant light-cone components $\tilde{v}^A$ are defined as

$$\begin{aligned} &v^\mu = (v^0, v^1, v^2, v^3), \\ &\tilde{v}^A = (v^0 - v^3, v^0 + v^3, -v^1 - \mathrm{i}v^2, -v^1 + \mathrm{i}v^2) \equiv (\tilde{v}^1, \tilde{v}^2, \tilde{v}^3, \tilde{v}^4). \end{aligned} \tag{2.65}$$

The contraction of two four-vectors gives

$$\begin{aligned} v^\mu w_\mu = v^\mu w^\nu g_{\mu\nu} &= v^0 w^0 - v^1 w^1 - v^2 w^2 - v^3 w^3 \\ &= \frac{1}{2}(\tilde{v}^1 \tilde{w}^2 + \tilde{v}^2 \tilde{w}^1 - \tilde{v}^3 \tilde{w}^4 - \tilde{v}^4 \tilde{w}^3) \\ &\equiv \tilde{v}^A \tilde{w}^B \tilde{g}_{AB} = \tilde{v}^A \tilde{w}_A, \end{aligned} \tag{2.66}$$

and allows to define the modified metric tensor as

$$\tilde{g}_{AB} = \frac{1}{2}\begin{pmatrix} 0 & 1 & 0 & 0 \\ 1 & 0 & 0 & 0 \\ 0 & 0 & 0 & -1 \\ 0 & 0 & -1 & 0 \end{pmatrix}, \quad \tilde{g}^{AB} = \begin{pmatrix} 0 & 2 & 0 & 0 \\ 2 & 0 & 0 & 0 \\ 0 & 0 & 0 & -2 \\ 0 & 0 & -2 & 0 \end{pmatrix}, \quad \tilde{g}^{AC}\tilde{g}_{CB} = \tilde{g}^A_B = \delta^A_B. \tag{2.67}$$

Starting from the input of external four-momenta defined as standard Lorentz vectors, all internal manipulations involving momenta, γ matrices, polarization vectors and more general tensors are performed in light-cone representation.

The routines that implement propagators are of the form

```
subroutine prop_F1_F2(J_F1, P, M, J_F2).
```

Here, an incoming bare sub-tree `J_F1` associated to the field `F1` is dressed with a propagator of momentum `P` and mass `M` to generate the outgoing sub-tree `J_F2`. The denominators of all propagators in a tree diagram can be factorized as a global scalar factor that multiplies the whole amplitude. Thus only the structure of the numerator needs to be explicitly implemented. In Feynman gauge, the only non-trivial numerator is associated to fermion and antifermion dressing [1]. Let us consider, for example, the fermion propagator. Using the Feynman rule we can write,

$$\psi_\alpha(i) = \frac{\mathrm{i}(\not{p}+m)_{\alpha\beta}}{p^2-m^2}\,\psi_\beta^{\mathrm{bare}}(i) = \qquad (2.68)$$

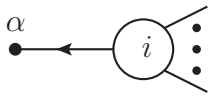

where p is the off-shell momentum flowing in the direction of the index α and $\psi_\beta^{\mathrm{bare}}(i)$ is the previously computed bare sub-tree. The factor $\mathrm{i}/(p^2-m^2)$ can be factorized and therefore we only need to compute the light-cone components of the expression $(\tilde{p}^A\tilde{\gamma}_A + m1)_{\alpha\beta}\psi_\beta$. The corresponding numerical routine is presented in Appendix A.1.

The last class of routines implements the three- and four-point vertices. Apart from the (two or three) incoming sub-trees, depending on the vertex, extra input arguments can be the different left- and right-handed chiral couplings and the momenta entering into the vertex. Let us consider two examples: the $Zq\bar{q}$ vertex and the triple vector boson vertex VVV. In the first case we have

$$Z^A(j+k) = \bar{\psi}_\alpha(k)[\tilde{\gamma}^A(g_R\omega_R + g_L\omega_L)]_{\alpha\beta}\psi_\beta(j) = \qquad (2.69)$$

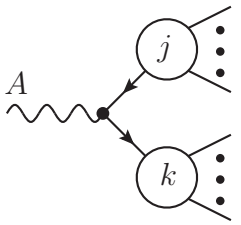

where $\bar{\psi}_\alpha(k)$ and $\psi_\beta(j)$ are pre-computed fermion sub-trees, $A = 1,2,3,4$ is the Lorentz index of the Z boson in light-cone representation, $g_{R,L}$ are the right and left couplings associated to the chirality projectors $\omega_{R,L} = (1 \pm \gamma_5)/2$. The corresponding numerical routine is presented in Appendix A.2.

The triple vector boson vertex reads

$$\epsilon^{A_3} = [\tilde{g}_{A_1A_2}(p_1-p_2)^{A_3} + \tilde{g}^{A_3}_{A_2}(p_1+2p_2)_{A_1} + \tilde{g}^{A_3}_{A_1}(-2p_1-p_2)_{A_2}]\epsilon^{A_1}\epsilon^{A_2} = \qquad (2.70)$$

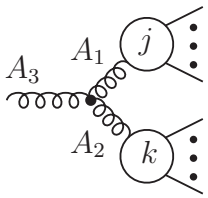

where $\epsilon^{A_1}(j)$ and $\epsilon^{A_2}(k)$ are the two sub-trees with incoming momenta p_1 and p_2, A_3 is the Lorentz index of the new sub-tree resulting from merging the two. The associated numerical subroutine is presented in Appendix A.3.

[1] For tree-level amplitudes the unitary gauge is also supported. In this case also the vector propagator contains a non trivial Lorentz structure in the numerator.

2.4.2 One-loop amplitudes

Let us now move to the case of one-loop amplitudes. Our goal is the recursive computation of the coefficients of the numerator polynomial (2.53), whose degree corresponds to the rank r of the loop integral, using the open-loops master equation (2.55). The coefficients $\mathcal{N}_{\mu_1\dots\mu_r}$ are contracted with the symmetric tensor $q^{\mu_1}\cdots q^{\mu_r}$ and can thus be symmetrised in the Lorentz indices $\mu_1\dots\mu_r$. In fact, the full algorithm is implemented in terms of symmetrised open-loops tensors, thereby avoiding the proliferation of the number of components at high tensor rank. We can rewrite the numerator of the loop integral as

$$\mathcal{N}(q) = \sum_{r=0}^{R} \mathcal{N}_{\mu_1\dots\mu_r} q^{\mu_1}\cdots q^{\mu_r} = \sum_{\substack{n_0\dots n_3=0 \\ n_0+n_1+n_2+n_3\leq R}}^{R} \mathcal{N}_{n_0\dots n_3} \underbrace{q^0\cdots q^0}_{n_0}\cdots\underbrace{q^3\cdots q^3}_{n_3}. \tag{2.71}$$

The independent $q^{\mu_1}\cdots q^{\mu_r}$ monomials and the corresponding coefficients are uniquely identified by counting the number of occurrences of the four possible values $\mu = 0,1,2,3$. The full set of components $\{n_0,n_1,n_2,n_3\}$ contributing to a fixed tensorial rank r satisfies the constraint $n_0+n_1+n_2+n_3 = r$. As noted in [44], this systematic symmetrisation allows for the tensor integral reduction to be competitive with unitarity methods up to particle multiplicities as high as $n\sim 10$. For a set of symmetrised tensors from rank $r=0$ up to maximum rank $r=R$, the total number of independent components is given by $\binom{R+4}{4}$. As illustrated in the following table,

R	0	1	2	3	4	5	6	7
$\binom{R+4}{4}$	1	5	15	35	70	126	210	330

(2.72)

for realistic LHC applications with up to 6 external particles we have to compute $\mathcal{O}(100)$ tensorial coefficients per diagram. This number grows mildly with the number of particles and roughly doubles when the tensor rank augments by one. All ingredients of the calculation, i.e. the coefficients $\mathcal{N}_{\mu_1\dots\mu_r}$ built with open-loops, the loop momentum tensor $q^{\mu_1}\cdots q^{\mu_r}$ needed for OPP reduction and the tensor integrals $\mathcal{T}_N^{\mu_1\dots\mu_r}$, are handled internally in their symmetrized form.

Let us rephrase the open-loops recursion (2.55) in terms of symmetrized coefficients $\mathcal{N}^{\beta}_{n_0n_1n_2n_3;\alpha}$. To this end, it is convenient to split the recursion in two terms,

$$\mathcal{N}^{\beta}_{n_0n_1n_2n_3;\alpha}(\mathcal{I}_n) = \mathcal{Y}^{\beta}_{n_0n_1n_2n_3;\alpha}(\mathcal{I}_n) + \mathcal{Z}^{\beta}_{n_0n_1n_2n_3;\alpha}(\mathcal{I}_n). \tag{2.73}$$

The first one connects $(n-1)$-point open-loops to n-point open-loops of the same rank r via

$$\mathcal{Y}^{\beta}_{n_0n_1n_2n_3;\alpha}(\mathcal{I}_n) = Y^{\beta}_{\gamma\delta}\mathcal{N}^{\gamma}_{n_0n_1n_2n_3;\alpha}(\mathcal{I}_{n-1})w^{\delta}(i_n). \tag{2.74}$$

The second term connects lower-point and lower-rank open-loops to higher-point and higher-rank open-loops as

$$\mathcal{Z}^{\beta}_{n_0n_1n_2n_3;\alpha}(\mathcal{I}_n) = \sum_{\mu=0}^{3} Z^{\beta}_{\mu;\gamma\delta}\mathcal{N}^{\gamma}_{n_0\dots(n_\mu-1)\dots n_3;\alpha}(\mathcal{I}_{n-1})w^{\delta}(i_n), \tag{2.75}$$

where the extra Lorentz index μ gives rise to four new contributions to the higher-rank coefficient $\mathcal{N}^{\beta}_{n_0\dots(n_\mu-1+1)\dots n_3;\alpha}$ for $\mu = 0,1,2,3$.

For an efficient bookkeeping of the symmetrized components in the numerical code we defined a mapping that associates the set $\{n_0, n_1, n_2, n_3\}$ to a unique integer l via

$$l = f(\{n_0, n_1, n_2, n_3\}) = N_3(r_3 - 1) + N_2(r_2 - 1) + N_1(r_1 - 1) + r_0 + 1, \tag{2.76}$$

where the function $N_i(r)$ and the sub-ranks r_i are defined as

$$\begin{gathered} N_i(r) = \sum_{k=0}^{r} \binom{k+i-1}{k} = \binom{r+i}{r}, \\ r_3 = n_3, \quad r_2 = r_3 + n_2, \quad r_1 = r_2 + n_1, \quad r_0 = r_1 + n_0. \end{gathered} \tag{2.77}$$

This allows to store the tensorial coefficients—as well as all other tensors—in a one-dimensional array with the ordering convention illustrated in the following table,

rank	$\mathcal{N}_{n_0n_1n_2n_3}$	l
0	$N[0,0,0,0]$	1
1	$N[1,0,0,0]$	2
	$N[0,1,0,0]$	3
	$N[0,0,1,0]$	4
	$N[0,0,0,1]$	5
2	$N[2,0,0,0]$	6
	$N[1,1,0,0]$	7
	$N[1,0,1,0]$	8
	$N[1,0,0,1]$	9
	$N[0,2,0,0]$	10
	$N[0,1,1,0]$	11
	$N[0,1,0,1]$	12
	$N[0,0,2,0]$	13
	$N[0,0,1,1]$	14
	$N[0,0,0,2]$	15

In this representation, the contraction of the tensor coefficients $\mathcal{N}_{\mu_1\ldots\mu_r}$ with the loop-momentum tensor $q^{\mu_1}\cdots q^{\mu_r}$ or the tensor integrals $\mathcal{T}_{\mu_1\ldots\mu_r}$ becomes just the product of the corresponding one-dimensional arrays,

$$\sum_{r=0}^{R} \mathcal{N}_{\mu_1\ldots\mu_r} \mathcal{T}^{\mu_1\ldots\mu_r} = \sum_{l} \mathcal{N}(l)\mathcal{T}(l). \tag{2.78}$$

The corresponding numerical function is presented in Appendix A.4.

The symmetrised open-loops are handled as three-dimensional arrays of the form

$$\mathcal{N}^{\beta}_{\mu_1\ldots\mu_r;\alpha} \to \mathcal{N}^{\beta}_{n_0n_1n_2n_3;\alpha} \to \mathcal{N}^{\beta}_{\alpha}(l) \to \texttt{G[1:4,:,1:4]}.$$

The first entry is associated to the active index $\beta = 1, 2, 3, 4$ of the open-loop that in each step is contracted with the free index of the attached sub-tree as in Eq.(2.74) and (2.75). The second one spans over the full set of tensor components up to the maximum rank (see Eq.(2.72)) and the last is the open index $\alpha = 1, 2, 3, 4$ from where the recursion started. This definition of the arrays follows from the observation that

in each step (numerical routine) we have to perform operations on the components of the array associated to the indices β and l, independently for each value of the index $\alpha = 1, 2, 3, 4$. Storing the components with this ordering allows, within `Fortran`, to access them more efficiently in the memory slots allocated to them.

Whenever in a recursion step a non-zero higher-rank contribution from Eq.(2.75) arises—ultimately because the involved Feynman rule contains a dependence on the loop momentum—the new set of coefficients has to be stored in the second entry of the array `G[1:4,:,1:4]` following the ordering convention introduced in Eq.(2.76). As already discussed, starting from a component $l = f(\{n_0, n_1, n_2, n_3\}$, we can increase the rank by increasing one of the indices n_i to $n_i + 1$, obtaining in this way four contributions to the $r + 1$ tensorial coefficients,

$$\mathcal{N}(l) : l = f(\{n_0, n_1, n_2, n_3\})) \xrightarrow{r \to r+1} \begin{cases} \mathcal{N}(l_1) : l_1 = f(\{n_0 + 1, n_1, n_2, n_3\}) \\ \mathcal{N}(l_2) : l_2 = f(\{n_0, n_1 + 1, n_2, n_3\}) \\ \mathcal{N}(l_3) : l_3 = f(\{n_0, n_1, n_2 + 1, n_3\}) \\ \mathcal{N}(l_4) : l_4 = f(\{n_0, n_1, n_2, n_3 + 1\}) \end{cases} \tag{2.79}$$

We define a function, called `HR(i,l)`, that given a tensor index l, returns the four higher-rank indices l_i that arise from the shifting $n_i \to n_i + 1$. It just consists of mapping relations that once implemented can be loaded and stored in memory once and for all. The case for maximum rank $R = 6$ is reported in Appendix A.5.

Let us now discuss two examples of numerical routines for the construction of open-loops. We first consider the following diagram,

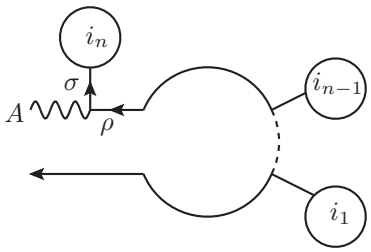

(2.80)

where a $(n-1)$-point open-loop with internal quark is connected to an anti-quark sub-tree i_n, resulting in a n-point open-loop with a propagating Z boson. ρ and σ are the spinor indices of the quark open-loop and antiquark sub-tree, respectively, A is the light-cone Lorentz index of the resulting Z boson. Inserting the Feynman rule for the $q\bar{q}Z$ vertex we get for the cut-open diagram,

$$\begin{aligned} &\sum_{r=0}^{R} \int \frac{d^d q\, q^{\mu_1} \cdots q^{\mu_r}}{D_0 D_1 \dots D_{n-1}} \mathcal{N}^{A}_{\mu_1 \dots \mu_r;\alpha}(\mathcal{I}_n) = \\ =&\sum_{r=0}^{R} \int \frac{d^d q\, q^{\mu_1} \cdots q^{\mu_r}}{D_0 D_1 \dots D_{n-1}} \mathcal{N}^{\rho}_{\mu_1 \dots \mu_r;\alpha}(\mathcal{I}_{n-1}) \bar{\psi}_\sigma(i_n) [\tilde{\gamma}^A (g_R \omega_R + g_L \omega_L)]_{\sigma\rho}. \end{aligned} \tag{2.81}$$

Since the vertex does not depend on any momentum the corresponding open-loops recursion step involves only a same-rank contribution of type (2.74), which reads

$$\mathcal{N}^{A}_{n_0 n_1 n_2 n_3;\alpha}(\mathcal{I}_n) = \mathcal{N}^{\rho}_{n_0 n_1 n_2 n_3;\alpha}(\mathcal{I}_{n-1}) \bar{\psi}_\sigma [\tilde{\gamma}^A (g_R \omega_R + g_L \omega_L)]_{\sigma\rho}. \tag{2.82}$$

This represents a generalization of the tree-level formula (2.69). Indeed, for each coefficient $\{n_0, n_1, n_2, n_3\}$, (2.82) is equivalent to a tree-level routine that has to be further evaluated for the four components $\alpha = 1, 2, 3, 4$.

The recursion step (2.82) is implemented through the numerical routines presented in Appendix A.6. The construction of the new open-loop proceeds in two steps. First, the generalization of the tree-level routine, `loop_QA_Z`, is called. It receives as input the pre-computed $(n-1)$-point open-loop, the anti-quark sub-tree, and the left- and right-couplings. As output it returns the n-point open-loop. Internally it consists of four independent calls for each value of α of the basic routine `vert_loop_QA_Z` that in turn, for each value of the tensor index $l = f(\{n_0, n_1, n_2, n_3\})$, builds the four components $A = 1, 2, 3, 4$ of the new open-loop.

Let us now consider the less trivial case of the triple vector boson vertex as depicted in the following diagram

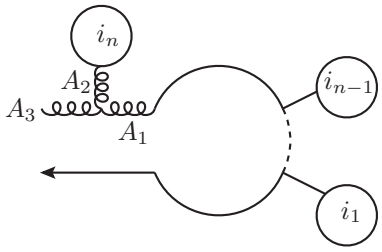

(2.83)

where a $(n-1)$-point open-loop with loop momentum $q + k_{n-1}$, where $k_i = \sum_{j=0}^{i} p_j$, interacts with the gluon sub-tree i_n with momentum p_n, resulting in the n-point open-loop with a propagating gluon. A_3, A_1 and A_2 are the light-cone Lorentz indices of the n-point open-loop, $(n-1)$-point open-loop and i_n sub-tree, respectively. All momenta are treated as incoming into the vertex. Inserting the Feynman rule the cut-open diagram reads,

$$\begin{aligned}
&\sum_{r=0}^{R+1} \int \frac{d^d q\, q^{\mu_1} \cdots q^{\mu_r}}{D_0 D_1 \dots D_{n-1}} \mathcal{N}^{A_3}_{\mu_1 \dots \mu_r;\alpha}(\mathcal{I}_n) = \\
&= \sum_{r=0}^{R+1} \int \frac{d^d q\, q^{\mu_1} \cdots q^{\mu_r}}{D_0 D_1 \dots D_{n-1}} \mathcal{N}^{A_1}_{\mu_1 \dots \mu_r;\alpha}(\mathcal{I}_{n-1}) [(q + k_{n-1} - p_n)^{A_3} \tilde{g}_{A_1 A_2} + \\
&\qquad + (q + k_{n-1} + 2p_n)_{A_1} \tilde{g}^{A_3}_{A_2} - (p_n + 2q + 2k_{n-1})_{A_2} \tilde{g}^{A_3}_{A_1}] \tilde{\epsilon}^{A_2}(i_n).
\end{aligned} \tag{2.84}$$

Separating the constant piece from the one dependent on the loop momentum, we get same-rank and rank-raising contributions that connect $(n-1)$- and n-point open-loops. Reminding Eq. (2.74) and (2.75), the same-rank piece reads

$$\begin{aligned}
&\mathcal{Y}^{A_3}_{n_0 n_1 n_2 n_3;\alpha}(\mathcal{I}_n) = \\
&\mathcal{Y}^{A_1}_{n_0 n_1 n_2 n_3;\alpha}(\mathcal{I}_{n-1}) \\
&\times [(k_n - p_{n+1})^{A_3} \tilde{g}_{A_1 A_2} + (k_n + 2p_{n+1})_{A_1} \tilde{g}^{A_3}_{A_2} - (p_{n+1} + 2k_n)_{A_2} \tilde{g}^{A_3}_{A_1}] \tilde{\epsilon}^{A_2}(i_n),
\end{aligned} \tag{2.85}$$

whereas the rank-raising contribution reads

$$\begin{aligned}
\mathcal{Z}^{A_3}_{n_0 n_1 n_2 n_3;\alpha}(\mathcal{I}_n) = &\sum_{i=0}^{3} \mathcal{Z}^{A_1}_{n_0 \dots (n_i - 1) \dots n_3;\alpha}(\mathcal{I}_{n-1}) \\
&\times [\tilde{g}_i^{A_3} \tilde{g}_{A_1 A_2} + \tilde{g}_{A_1 i} \tilde{g}^{A_3}_{A_2} - 2\tilde{g}_{A_2 i} \tilde{g}^{A_3}_{A_1}] \tilde{\epsilon}^{A_2}(i_n).
\end{aligned} \tag{2.86}$$

The corresponding routines are presented in Appendix A.7.

As discussed before, the last step to obtain the full set of tensor coefficients consists of taking the trace of the open-loops, $\mathcal{N}_{\mu_1\dots\mu_r} = \sum_\alpha \mathcal{N}^\alpha_{\mu_1\dots\mu_r;\alpha}$. This operation can be combined in a unique step with the last insertion to further optimize the recursion. Instead of computing first the full set of open-loops $\mathcal{N}^\beta_{\mu_1\dots\mu_r;\alpha}$ and then taking the trace, we implemented a dedicated set of routines that compute only the diagonal part of the last insertion and directly take the trace. For fermions the last step consists in dressing the loop line with the propagator, thus increasing the rank by one. For scalar and vector particles it is enough to consider the last vertex insertion, since the loop propagator does not contribute to the numerator but only with an extra loop denominator, similarly to the tree-level case. The optimized version of the numerical routine for the last step in the case of the $Zq\bar{q}$ vertex is shown in Appendix A.8.

2.4.3 Performance

To assess the flexibility and performance of OpenLoops, we considered the set of $2 \to 2,3,4$ processes $u\bar{u} \to W^+W^- + ng$, $u\bar{d} \to W^+g + ng$, $u\bar{u} \to t\bar{t} + ng$ and $gg \to t\bar{t} + ng$, with $n = 0,1,2$ gluons. This allows to test the code in a variety of processes relevant for LHC phenomenology, for different particle multiplicity and complexity of the calculation.

The high degree of automation is reflected in compact codes and fast code generation. Table 1 shows the size of the compiled process libraries and the time needed to generate and compile the `Fortran90` numerical code starting from the process definition file. For the considered set of twelve processes, the code size ranges from 100kB to a few MB. Code generation and compilation time ranges from a few seconds for simple $2 \to 2$ processes up to minutes for the most complicated $2 \to 4$ amplitudes. During the code generation phase the largest fraction of the time is actually spent in Feynman diagram generation by `FeynArts`. In this regard, adopting a more efficient diagram generator could lead to a further strong improvement. Comparing to the algebraic approaches used in [122, 123] for $pp \to t\bar{t}b\bar{b}$ and $pp \to WWb\bar{b}$, OpenLoops leads to a code compression of $\mathcal{O}(10^2 - 10^3)$ and a speed-up in code generation of three orders of magnitude.

The numerical code turns out to be also very fast in the actual computation of one-loop virtual amplitudes. The CPU cost for the evaluation of the full colour- and helicity-summed squared Born-loop interference is plotted versus the number of one-loop diagrams in Fig.1. For W bosons and top quarks, assuming decays into massless left-handed fermions, we include a single helicity. For the considered processes, involving $\mathcal{O}(10)$ to $\mathcal{O}(10^4)$ diagrams, the CPU cost scales almost linearly with the number of diagrams. This indicates that the increase of tensorial rank, when combined with the systematic symmetrization of the tensor coefficients, does not represent a penalty at large particle multiplicity. The upper frame displays results obtained with tensor-integral reduction. The runtime is below 1 ms for $2 \to 2$ processes and it never exceeds one second for the most complex $2 \to 4$ process. Extrapolating this trend we expect that $2 \to 5$ amplitudes and processes with $\mathcal{O}(10^5)$ diagrams are feasible. The lower frame shows the ratio of runtimes using tensor-integral and OPP reduction with CutTools [46]. Altough always slightly slower, when combined with open-loops OPP

Process	size[MB]	t_{code}[s]
$u\bar{u} \to t\bar{t}$	0.1	2.2
$u\bar{u} \to W^+W^-$	0.1	7.2
$u\bar{d} \to W^+g$	0.1	4.2
$gg \to t\bar{t}$	0.2	5.4
$u\bar{u} \to t\bar{t}g$	0.4	12.8
$u\bar{u} \to W^+W^-g$	0.4	39.8
$u\bar{d} \to W^+gg$	0.5	22.9
$gg \to t\bar{t}g$	1.2	52.9
$u\bar{u} \to t\bar{t}gg$	3.6	236
$u\bar{u} \to W^+W^-gg$	2.5	381.7
$u\bar{d} \to W^+ggg$	4.2	366.2
$gg \to t\bar{t}gg$	16.0	3005

Table 1: Size (in MB) of the compiled process library and time (in seconds) needed to generate and compile the numerical code starting from the process definition file.

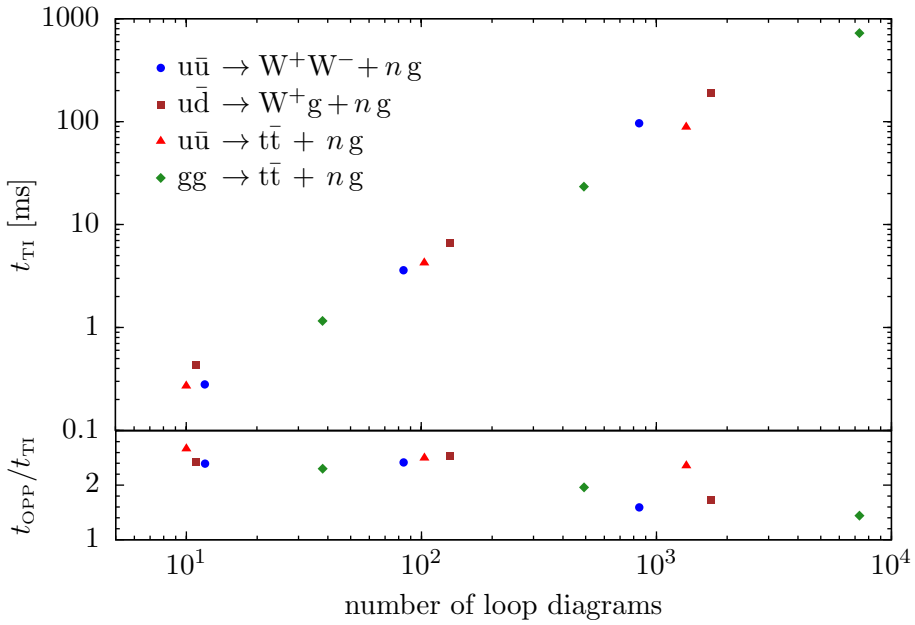

Figure 1: CPU cost of colour and helicity summed Born-loop interference amplitudes versus number of diagrams. Runtimes per phase space point with tensor-integral (t_{TI}) and OPP reduction (t_{OPP}), on a single Intel i5-750 core with ifort 10.1.

Process	$t^{\rm TI}_{\rm pol}$[ms]	$n_{\rm hel}$	$t^{\rm TI}_{\rm unpol}$[ms]
$u\bar{u} \to t\bar{t}$	0.25	2	0.27
$u\bar{u} \to W^+W^-$	0.25	2	0.28
$u\bar{d} \to W^+g$	0.39	2	0.43
$gg \to t\bar{t}$	0.89	4	1.16
$u\bar{u} \to t\bar{t}g$	3.5	4	4.2
$u\bar{u} \to W^+W^-g$	2.7	4	3.6
$u\bar{d} \to W^+gg$	5.3	4	6.7
$gg \to t\bar{t}g$	13.6	8	23.4
$u\bar{u} \to t\bar{t}gg$	56.2	8	88.4
$u\bar{u} \to W^+W^-gg$	65.6	8	96.4
$u\bar{d} \to W^+ggg$	134.5	8	190.5
$gg \to t\bar{t}gg$	335.0	16	725.0

Table 2: Speed of polarised ($t^{\rm TI}_{\rm pol}$) and unpolarised ($t^{\rm TI}_{\rm unpol}$) virtual amplitudes using tensor-integral reduction. $n_{\rm hel}$ is the number of independent helicity states of the external particles.

reduction reaches similar levels of efficiency as tensor-integral reduction. The difference in speed seems to reduce when increasing the particle multiplicity. Similar results are obtained using Samurai [47].

Table 2 compares the CPU cost for the computation of the colour-summed virtual corrections for one helicity configuration to the helicity-summed amplitude when using tensor reduction. One can clearly see that, when summing over the full set of helicity states $n_{\rm hel}$ (remind that we consider one helicity for W and t), the cost for the unpolarised amplitude is much lower than a naive factor $n_{\rm hel}$. This is the main benefit that comes from factorizing the helicity-dependent coefficients and reducing the helicity-independent tensor integral only once, as indicated in Eq.(2.61). This is further illustrated in Fig.2, where the runtime fractions needed for the evaluation of scalar integrals (blue, left), tensor reduction (green, center) and open-loops coefficients (red, right) are shown explicitly for the polarised and unpolarised virtual corrections for the class of processes $gg \to t\bar{t} + ng$. For a single helicity state the cost of the open-loops coefficients is only of the order of 10% of the helicity-independent remnant. The computation of the scalar integrals absorbs from 80% to 35% of the total runtime. They are the fundamental ingredients of one-loop amplitudes, which have to be calculated independently from the adopted reduction technique. Therefore, the fact that the scalar integrals represent the most consistent fraction of the total runtime is a further demonstration of the very high efficiency of the open-loops approach. For what concerns unpolarised amplitudes, only the open-loops coefficients have to be re-evaluated, which increases the related fraction of the total runtime to 30-60%.

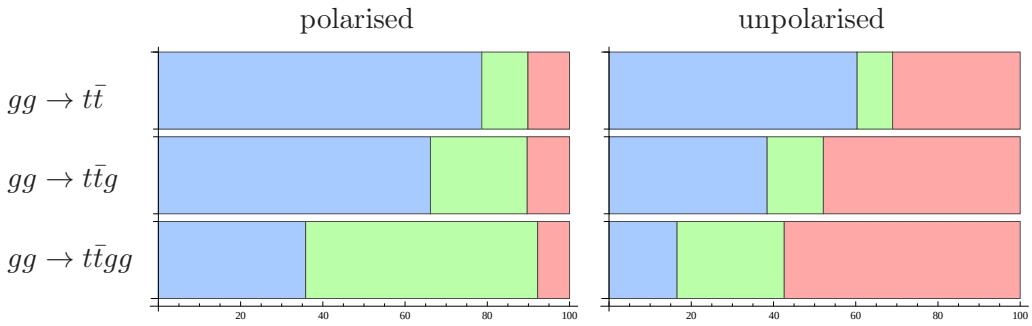

Figure 2: Runtime fractions for scalar integrals (blue, left), tensor reduction (green, center) and open-loops coefficients (red, right) for the computation of polarised and unpolarised virtual corrections for $gg \to t\bar{t} + ng$.

2.4.4 Numerical stability

Another important aspect that has been thoroughly investigated is the numerical stability of OpenLoops. When performing physical runs for the computation of cross sections and distributions, the appearence of numerical instabilities can spoil the convergence and, in some cases, lead to completely wrong results. For this reason it is crucial to assess how frequently instabilities can appear and, if needed, implement alternative strategies to ensure a sufficient level of stability. Numerical instabilities are mainly due to cancellations of several orders of magnitude that can happen internally during the reduction of one-loop amplitudes to scalar integrals. They are ultimately due to the linear dependence of the scalar integrals in exceptional phase-space regions and appear in each reduction method, but can be more or less pronounced depending on the particular technique.

As discussed in section 2.2, in the context of the tensor-reduction methods of [31,32], the appearence of small or zero Gram determinants can be systematically avoided switching to alternatives to the standard Passarino-Veltman reduction and thanks to analytic expansions in small Gram determinants. These methods are implemented in the tensor library Collier [115]. When using OPP reduction, the internal manipulations, needed to invert the systems of equation to extract the coefficients of scalar integrals, can lead to severe instabilities. In this case no analytic approach is available to cure such instabilities, and the only solution is provided by a re-evaluation in quadruple precision.

To investigate these issues, we studied the stability of the twelve processes considered above via rescaling of all dimensionful parameters entering in the computation. Starting from a standard setup we rescale momenta, masses, renormalization scale etc. with an arbitrary factor ξ, i.e. $\{p_i, m_i, \mu\} \to \{\xi p_i, \xi m_i, \xi\mu\}$. The total virtual correction $\delta\mathcal{W}$ computed with the original setup is expected to scale according to its mass dimension K as $\delta\mathcal{W} \to \delta\mathcal{W}' = \xi^K \delta\mathcal{W}$. The numerical accuracy of the result is reflected in the agreement between the original and the rescaled amplitudes, respectively $\delta\mathcal{W}$ and $\delta\mathcal{W}'$, normalized to the Born squared amplitude $\mathcal{W}$,

$$\Delta = \frac{\xi^{-K}\delta\mathcal{W}' - \delta\mathcal{W}}{\mathcal{W}}. \tag{2.87}$$

Results obtained with tensor integrals in double precision for all twelve processes are

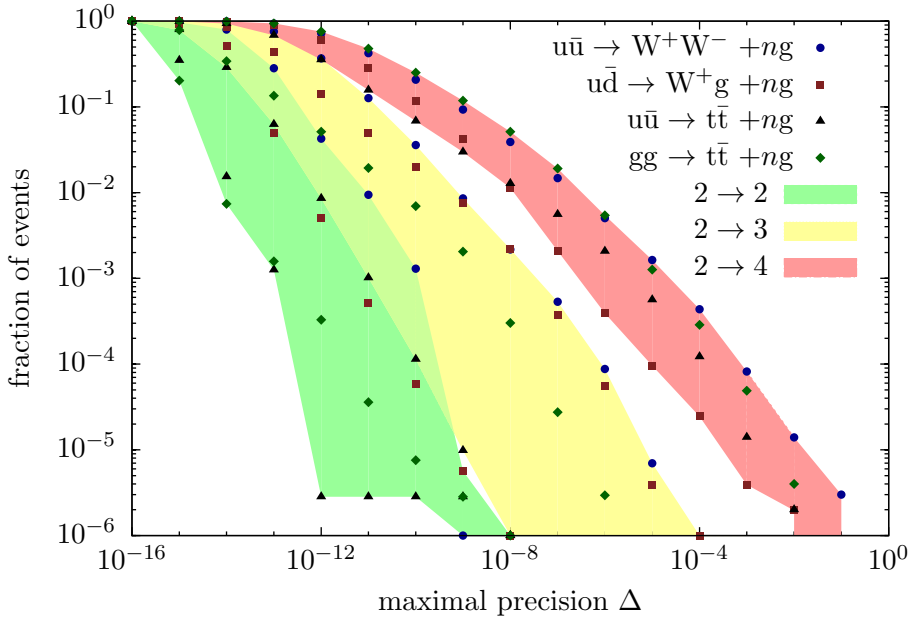

Figure 3: Accuracy of virtual corrections using tensor reduction in double precision. The probability of accuracy worse than Δ, in samples of 10^6 uniformly distributed phase-space points with $\sqrt{s} = 1$TeV, $p_T > 50$ GeV, $\Delta R_{ij} > 0.5$, is plotted versus Δ.

shown in Fig.3. In samples of 10^6 homogeneously distributed phase-space points with a standard set of cuts, the average number of correct digits for $\delta\mathcal{W}$ ranges from eleven to fifteen. For the most complicated processes, precision lower than 10^{-5} and 10^{-3} occurs with less than 2 and 0.1 permille probability, respectively. This demonstrates the robustness of the tensor reduction approach in double precision. In contrast, with OPP reduction, a small but non negligible fraction of points turns out to be not sufficiently stable in double precision.

For runs dedicated to the production of physical events a stability trigger has been implemented which monitors numerical instabilities on the fly. Starting from the observation that, in conjunction with tensor integrals, the probability of encountering very dangerous phase space points is very small, the trigger mechanism is based on the local K-factor, i.e. on the ratio of the virtual correction over the Born contribution. If the K-factor is above a predefined threshold with respect to the average value the point is considered "suspicious" and is further analysed by means of a second evaluation with an alternative reduction library or by performing a scaling test. The outcome is used to decide whether the point is sufficiently stable or not. In the latter case, a complete re-evaluation of the amplitude in quadruple precision can be performed.

2.4.5 Validation

A large effort has been devoted to the debugging and validation of the code. A series of internal consistency checks has been fully automatized through special routines. They allow to check the cancellation of UV divergences after renormalization, the cancellation of IR divergences when the virtual correction is combined with the Catani-Seymour integrated dipole operator [73] and the validity of the Ward identities

whenever the polarization vector of an external gluon or photon is replaced with its momentum. The correctness of the reduction is verified by comparing two independent versions of the COLLIER library for tensor integrals with the OPP reduction performed with CUTTOOLS or SAMURAI.

To further test the numerical routines for the construction of open-loops, as well as the correct implementation of the recursive algorithm and the recycling procedure, we developed an extra powerful check. First, the one-loop diagram is evaluated by building the open-loops coefficients up to the last n-point contribution, i.e. $\mathcal{N}^{\alpha}_{\mu_1\dots\mu_r;\beta}(\mathcal{I}_n)$. At this point, instead of closing the loop by taking the trace, the loop momentum q is fixed to an arbitrary value and a "pseudo-tree" amplitude is built attaching two fixed external wavefunctions ϵ^1_α and ϵ^2_β to the open-loops, i.e.

$$\mathcal{P} = \epsilon^1_\alpha \left(\mathcal{N}^{\alpha}_{\mu_1\dots\mu_r;\beta}\, q^{\mu_1}\cdots q^{\mu_r}\right) \epsilon^{2\beta} \tag{2.88}$$

The result can be compared with the one obtained using the tree-level generator and the routines for tree-level vertices and propagators.

In addition to such internal checks, an extensive validation programme has been pursued to check the correctness of the final virtual correction. Apart from comparing against known results in the literature for a few selected processes, we checked the agreement of OPENLOOPS with a completely independent in-house generator of one-loop amplitudes based on the algebraic approach used in [122, 123]. In samples of $\mathcal{O}(10^2)$ phase space points we have found an average agreement of 14-12 digits in more than one-hundred inequivalent partonic channels for many different classes of $2 \to 2, 3, 4$ processes.

The speed and efficiency of the code allowed us to perform also many detailed studies with high-statistics samples. Fig.4 shows, in a similar fashion as in Fig.3, for a sample of $6 \cdot 10^6$ points, the agreement for the process $\bar{u}d \to W^- g(g)$ between OPENLOOPS and the algebraic code compared to the intrinsic stability of the individual codes as a result of the scaling test. The results demonstrate that the scaling test is a good indicator of the number of correct digits. This is further confirmed in Fig.5. There, the conditional probability $P(\Delta_A|\Delta_S)$ to find an agreement Δ_A between the two codes, given the intrinsic stability Δ_S as outcome of the scaling test for OPENLOOPS, is plotted. From this plot we can conclude that the scaling test returns a good estimate of the instrinsic accuracy of the calculation, in this case with a one-two digits correlation at the 95% CL.

2.4.6 Interfacing with Monte Carlo generators

To arrive at a complete automation of NLO simulations from process definition to hadron-collider observables, matrix element generators must be interfaced with Monte Carlo event generators, which provide a general framework for infrared subtraction, real emission, phase space integration and matching to parton showers.

We developed a dedicated interface of OPENLOOPS to the SHERPA event generator [53], that, apart from fixed-order NLO calculations, supports fully automated matching to the SHERPA parton shower [98] in the MC@NLO formalism, as well as NLO multi-jet merging with the MEPS@NLO method [94, 95]. An application of

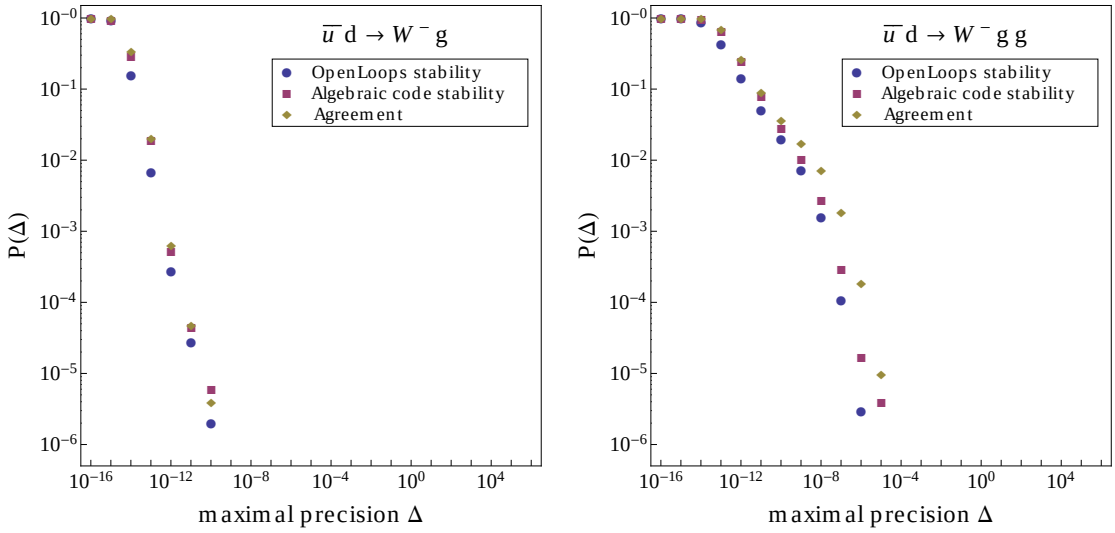

Figure 4: Probability to find precision worse than Δ when looking at the intrinsic stability of the two codes (scaling test) or at the agreement between them, for a sample of $6 \cdot 10^6$ uniformly distributed phase-space points.

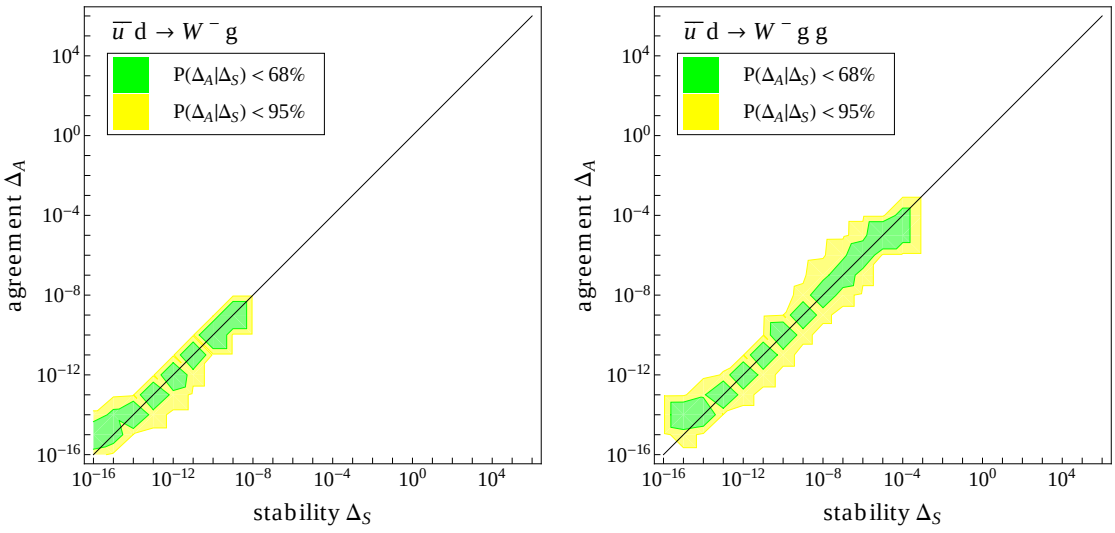

Figure 5: Conditional probability $P(\Delta_A|\Delta_S)$ to have agreement Δ_A between the two codes, given the stability Δ_S as outcome of the scaling test for OpenLoops. The green and yellow bands show the 68% and 95% CL regions, respectively.

Sherpa+OpenLoops to LHC phenomenology is presented in Chapter 3. A pre-release version of the Sherpa+OpenLoops framework has been made available to the Monte Carlo working groups of the ATLAS and CMS collaborations. It allows to simulate a wide range of $2 \to 2, 3, 4$ processes such as (multi)vector boson production, heavy quark, single-top, Higgs and photon production in association with multiple jets.

OpenLoops has also been interfaced to a parton-level Monte Carlo by S. Kallweit [57]. This tool is applicable to any Standard Model process at NLO QCD. Infrared singularities are handled with the Catani-Seymour dipole subtraction method [73, 74]. The phase-space integrator is based on the adaptive multi-channel technique [124] and implements dedicated channels for the dipole subtraction terms. Multiple scale variations in a single run are also supported. A phenomenological application based on OpenLoops in combination with this Monte Carlo framework is discussed in Chapter 4.

Finally, the standard Binoth-Les Houches interface [125] is also supported. This permits to link OpenLoops to any other Monte Carlo tool. Recently this has been applied for interfacing with the Herwig++ generator [54].

The first public release of OpenLoops will take place in the next future.

Part II

Applications

Introduction

The OpenLoops program has already been applied to a series of nontrivial multi-particle NLO simulations for the LHC, and also in the context of NNLO calculations. The MC@NLO simulation of $\mathrm{t\bar{t}b\bar{b}}$ production [59], obtained in the Sherpa+ OpenLoops framework, represents the first application of NLO matching to a process with four, massive, coloured, final-state particles. In this context, the inclusion of finite b-quark mass effects in combination with shower emissions led to the discovery of a new $\mathrm{t\bar{t}b\bar{b}}$ production mechanism, which proceeds via $\mathrm{t\bar{t}gg}$ production and double $g \to \mathrm{b\bar{b}}$ splittings and turns out to have a dramatic impact on ongoing $\mathrm{t\bar{t}}H$ searches at the LHC. The MEPS@NLO results for top-quark pair production in association with up to two jets, presented in [63], represent the current state of the art in multi-jet merging at NLO. This simulation will play an important role for a multitude of LHC searches based on leptons, missing energy, and multi-jet final states. Tri-lepton production, including up to one extra jet at NLO accuracy, has been studied in [64]. This simulation is relevant for the HZ and HW Higgs-strahlung signals in the $H \to W^+W^-$ decay channel, as well as various important backgrounds. Higgs pair production via gluon-gluon fusion, including finite top-mass effects and up to one extra jet, has been investigated in conjunction with Herwig++ in [62], by combining the relevant squared one-loop matrix elements with multi-jet merging.

OpenLoops is the first automated one-loop generator that has been applied in the context of $2 \to 2$ NNLO QCD calculations for the treatment of the $2 \to 3$ real-virtual contributions. Its high speed and numerical stability have proven to be very beneficial, especially for the consistent subtraction of infrared singularities in the soft and collinear regions of phase space. Preliminary NNLO results for top-pair production in the $q\bar{q}$ channel are reported in [65]. First complete results for NNLO QCD corrections to $Z\gamma$ and ZZ production at LHC have been presented in [61] and [66], respectively.

The Part II of this thesis is devoted to the simulations that have been published in [58] and [60]. In Chapter 3, based on [58], we present precise predictions for four-lepton plus jets production obtained within the fully automated Sherpa+OpenLoops framework. Off-shell intermediate vector bosons and related interferences are consistently included using the complex-mass scheme. Four-lepton plus 0- and 1-jet final states are described at NLO accuracy, and the precision of the simulation is further increased by squared quark-loop NNLO contributions in the $\mathrm{gg} \to 4\ell$, $\mathrm{gg} \to 4\ell + \mathrm{g}$, $\mathrm{g}q \to 4\ell + q$, and $q\bar{q} \to 4\ell + \mathrm{g}$ channels. These NLO and NNLO contributions are matched to the Sherpa parton shower, and the 0- and 1-jet final states are consistently merged using the Meps@Nlo technique. Thanks to Sudakov resummation, the parton shower provides improved predictions and uncertainty estimates for exclusive observables. This is important when jet vetoes or jet bins are used to separate

four-lepton final states arising from Higgs decays, diboson production, and top-pair production. Detailed predictions are presented for the ATLAS and CMS $H \to WW^*$ analyses at 8 TeV in the 0- and 1-jet bins. Assessing renormalisation-, factorisation- and resummation-scale uncertainties, which reflect also unknown subleading Sudakov logarithms in jet bins, we find that residual scale uncertainties are as small as a few percent.

In Chapter 4, based on [60], we present a NLO simulation of $W^+W^-b\bar{b}$ production with massive b-quarks. Off-shell and non-resonant contributions associated with top-pair and single-top channels and with leptonic W-boson decays are consistently taken into account using the complex-mass scheme. Thanks to the finite b-quark mass, $W^+W^-b\bar{b}$ predictions can be extended to the whole b-quark phase space, thereby including Wt-channel single-top contributions that originate from collinear $g \to b\bar{b}$ splittings in the four-flavour scheme. This provides the first consistent NLO description of $t\bar{t}$ and Wt production and decay, including quantum interference effects. The simulation is also applicable to exclusive 0- and 1-jet bins, which is of great importance for Higgs-boson studies in the $H \to W^+W^-$ channel and for any other analysis with large top backgrounds and jet vetoes or jet bins.

Chapter 3

Precise Higgs-background predictions: merging NLO QCD and squared quark-loop corrections to four-lepton + 0,1 jet production

3.1 Introduction

Final states involving four leptons played a key role in the discovery of the Higgs boson [9, 10] and will continue to be crucial in the understanding of its properties and coupling structure. There are two classes of final states of interest, namely those consistent with $H \to ZZ^*$ decays yielding four charged leptons and those related to $H \to WW^*$ resulting in two charged leptons and two neutrinos. They have quite different backgrounds, and for the latter, the dominant and large top-pair production background necessitates the introduction of jet vetoes to render the signal visible. More precisely, four-lepton final states consistent with $H \to WW^*$ decays are split into exclusive bins with 0, 1 and 2 jets. The separate analysis of the different jet bins permits to disentangle Higgs production via gluon fusion from the vector-boson fusion (VBF) production mode. In addition, data-driven determinations of the $H \to WW^*$ background take advantage of the fact that its two leading components—diboson and top-pair production—deliver final states of different jet multiplicity. While diboson production represents the leading background in the 0-jet bin, the top-production component becomes slightly more important in the 1-jet bin and clearly dominant in the 2-jet bin.

Due to the absence of a mass peak and the high background cross section, the experimental analyses suffer from signal-to-background ratios as low as around 10 percent. It is thus clear that the precision of the employed background-determination techniques, and the related error estimates, play a crucial role for any Higgs-boson measurement in this channel. In fact, with the statistics available at the end of the LHC run at 8 TeV, systematic errors resulting from the background subtraction already dominate the total uncertainty.

In the $H \to WW^*$ analyses by Atlas [126] and Cms [127] a data-driven approach is used to reduce uncertainties in the simulation of the two leading backgrounds. The top-production contribution is fitted to data in a top-enriched control sample. Using

Monte Carlo tools, the top background is extrapolated to the signal region and to an independent diboson-enriched control region. This latter region is used to normalise the diboson background after subtraction of the top contamination. The diboson background is then extrapolated to the signal region using Monte Carlo predictions. While this approach reduces theoretical uncertainties associated with the background normalisation, the extrapolations between the various control and signal sub-samples rely on Monte Carlo modelling of the background shapes.

Given that the accuracy of present Higgs-boson measurements requires extrapolation uncertainties at the percent level, it is clear that Monte Carlo simulations should include all available correction effects and appropriate error estimates. In this context, due to various nontrivial features of the $H \to WW^*$ analyses, the requirements in terms of theoretical precision go beyond the mere inclusion of higher-order corrections to inclusive four-lepton production. First, a reliable modelling of the various jets associated to the four-lepton final state requires higher-order QCD corrections up to the highest relevant jet multiplicity. Second, in order to describe potentially large Sudakov logarithms and related uncertainties, which arise from jet vetoes and exclusive jet bins, fixed-order predictions should be matched to parton showers or supplemented by appropriate resummations. Third, vector bosons are produced well below their mass shell in $H \to WW^* \to \ell\nu\ell\nu$ decays. Theoretical predictions for background processes should thus account for corresponding off-shell effects, including non-resonant channels and related interferences.

In this chapter we will concentrate on diboson production, which represents about 75 and 40 percent of the $H \to WW^* \to \ell\nu\ell\nu$ background in the 0- and 1-jet bins, respectively. While we are especially interested in the Higgs-boson analyses, diboson production plays an important role also for precision tests of the Standard Model, vector-boson scattering, searches for anomalous couplings, or as a background in numerous searches.

Higher-order QCD corrections to diboson production at hadron colliders have been extensively studied in the literature. Next-to-leading order (NLO) corrections to inclusive W-pair final states [128–133] amount to roughly 50% at the LHC and can be further enhanced in the tails of distributions or reduced by jet vetoes. Due to the gluon–(anti)quark channels, which start contributing to $pp \to W^+W^-$ only at NLO, the size of the corrections largely exceeds estimates based on leading-order (LO) scale variations. The matching of NLO predictions for WW production to parton showers was first studied in Ref. [88] using the MC@NLO method [88], while the POWHEG matching [134] for WW, WZ and ZZ production, including spin-correlated leptonic decays with non-resonant contributions, was presented in Ref. [135]. Similar predictions for ZZ production based on the MC@NLO method can be found in Ref. [136].

The NLO corrections to $pp \to W^+W^-j$ were presented in Refs. [137–139], including spin-correlated leptonic decays and off-shell effects associated with the Breit–Wigner distributions of the resonant W-bosons. At the 14 TeV LHC with rather inclusive cuts the corrections are slightly above 30%. Also in this case, due to the opening of the $gg \to W^+W^-q\bar{q}$ channel at NLO, the corrections largely exceed LO scale variations. This means that uncertainty estimates based on scale variations start to be meaningful only at NLO. The inclusion of QCD corrections is thus essential in order to improve both, theoretical predictions and error estimates. The matching of NLO $pp \to W^+W^-j$

calculations to parton showers remains to be addressed in the literature.

Higher-order QCD effects have been studied in quite some detail also for pp $\to$ WWjj in the VBF- and QCD-production modes. In the VBF case, NLO corrections including resonant and non-resonant leptonic decays [140] have been matched to parton showers [141]. For QCD-induced $\mathrm{W^+W^-}jj$ production, NLO predictions have been presented by two independent groups, including spin-correlated leptonic decays as Breit–Wigner resonances [142] or in narrow-width approximation [143]. Depending on the scale choice and the collision energy, NLO effects at the LHC can range from a few percent to tens of percent [142]. Up to date, only NLO QCD corrections to same-sign WWjj production [144, 145] have been matched to parton showers [146]. Recently, NLO predictions became available also for pp $\to WZjj$ [147].

While full NNLO corrections to diboson production are not yet available, the finite and gauge-invariant contribution from squared quark-loop gg $\to \mathrm{W^+W^-}$ amplitudes was studied in detail in Refs. [148–151]. Due to the large gluon flux, such NNLO terms increase the inclusive $\mathrm{W^+W^-}$ cross section by 3–5% at the LHC. Their relative importance is known to increase in the H $\to \mathrm{WW^*}$ analysis. While in presence of tight cuts it can reach up to 30% [148, 149], with the cuts currently applied by the LHC experiments it remains around 10% [150, 151], which corresponds to about half of the Higgs-boson signal. In spite of the tiny Higgs-boson width, the interference of the gg $\to 4\ell$ continuum with the signal can reach order 10% of the gg $\to 4\ell$ signal-plus-background cross section [149,150]. This interference contribution arises almost entirely above threshold, i.e. at invariant masses $M_{\mathrm{WW}} > 2M_{\mathrm{W}}$, and is strongly suppressed at small dilepton invariant mass as well as in the transverse-mass region $m_{\mathrm{T}} \lesssim M_{\mathrm{H}}$ [150, 152]. In Ref. [151] it was shown that also pp $\to \mathrm{W^+W^-}j$ receives a significant gg $\to \mathrm{W^+W^-g}$ contribution from squared quark-loop amplitudes, which can reach 6–9% when Higgs-search cuts are applied.

In this chapter we present new precise predictions for four-lepton plus 0- and 1-jet production,[1] obtained within the fully automated Sherpa+OpenLoops framework [43, 53]. The OpenLoops [43] algorithm is an automated generator of virtual QCD corrections to Standard-Model processes, which uses the Collier library [154] for the numerically stable evaluation of tensor integrals [31,32] and scalar integrals [103]. Thanks to a fully flexible interface of Sherpa with OpenLoops, the entire generation chain—from process definition to collider observables—is fully automated and can be steered through Sherpa run cards.

The simulation presented in this chapter is the first phenomenological application of Sherpa+OpenLoops. It comprises all previously known QCD contributions to pp $\to 4\ell$ and pp $\to 4\ell + 1j$, and extends them in various respects. For both processes, NLO corrections are matched to the Sherpa parton shower [53] using the fully colour-correct formulation [98, 155] of the Mc@Nlo method [88].[2] Using the recently developed multi-jet merging at NLO [94, 95], the two Mc@Nlo samples are consistently merged in a single simulation, which preserves the logarithmic accuracy of the shower and simultaneously guarantees NLO accuracy in the 0- and 1-jet bins. Also squared quark-

[1] First partial results of this study were anticipated in [153].

[2] In the following, Mc@Nlo refers to the algorithm of Refs. [98, 155], which is an extension of the original Mc@Nlo method by Frixione and Webber [88]. In particular, we never refer to the Mc@Nlo event generator.

loop contributions to pp $\to 4\ell + 0, 1$ jets are included. In addition to the pure gluonic channels, gg $\to 4\ell$ and gg $\to 4\ell +$ g, also the quark-induced $qg \to 4\ell + q$, $\bar{q}g \to 4\ell + \bar{q}$, and $q\bar{q} \to 4\ell +$g channels are taken into account. Moreover, the various squared quark-loop contributions are matched to the parton shower and merged in a single sample. To guarantee an exact treatment of spin correlations and off-shell vector bosons, the complex-mass scheme [156] is used, and all resonant and non-resonant four-lepton plus jets topologies are taken into account.

Detailed predictions are presented for the case of W-pair plus jets production as a signal, as well as for the irreducible background to the ATLAS and CMS H $\to$ WW* analyses in the 0- and 1-jet bins. To illustrate the relative importance of the various contributions, merged NLO predictions are contrasted with an inclusive MC@NLO simulation of pp $\to 4\ell$, with separate NLO results for four-lepton plus 0- and 1-jet production, and with squared quark-loop contributions. Residual perturbative uncertainties are assessed by means of scale variations. In addition to the usual renormalisation- and factorisation-scale variations, also the resummation scale of the SHERPA parton shower is varied. This reflects subleading Sudakov logarithms beyond the shower approximation, which renders error estimates more realistic in presence of jet vetoes.

The presented simulation involves various interesting improvements for the H $\to$ WW* analyses. The NLO matching and merging of pp $\to 4\ell + 0, 1$ jets provides NLO accurate predictions and Sudakov resummation in the first two exclusive jet bins. The inclusion of pp $\to 4\ell + 1j$ at NLO, which contributes, as a result of merging, both to the 0- and 1-jet bins, guarantees that all $q\bar{q}$, qg, $\bar{q}g$ and gg channels are open. In this situation scale variations can be regarded as more realistic estimates of theoretical uncertainties. Matching and merging render squared quark-loop gg $\to 4\ell$ contributions to exclusive jet bins more reliable. In fact, if not supplemented by shower emissions, the parton-level gg $\to 4\ell$ channel completely misses the Sudakov suppression induced by the jet veto. Matching gg $\to 4\ell$ to the parton shower automatically implies fermion-loop processes with initial-state quarks, like $qg \to 4\ell + q$, which result from $q \to qg$ shower splittings. The corresponding quark-induced matrix elements, which are included for the first time in this study, provide an improved description of hard jet emission.

Finally we point out that, while the presented simulation deals only with $\mu^+\nu_\mu e^-\bar{\nu}_e+$ jets final states, the employed tools allow for a fully automated generation of any other combination of charged leptons and neutrinos.

The chapter is organised as follows. In Section 3.2 we discuss the calculation of one-loop amplitudes with OPENLOOPS and COLLIER as well as NLO matching and merging in SHERPA. Details of the Monte Carlo simulations can be found in Section 3.3. In Section 3.4 we present results for inclusive WW-signal cuts, with emphasis on squared quark-loop contributions, merging aspects and jet-veto effects. Section 3.5 is devoted to a detailed discussion of the H $\to$ WW* analyses at the LHC. Our conclusions are presented in Section 3.6. Appendix B.1 describes the treatment of bottom- and top-quark contributions, and the H $\to$ WW* selection cuts are documented in Appendix B.2.

3.2 NLO, matching and merging with Sherpa and OpenLoops

This section is devoted to the automation of NLO calculations in Sherpa+ OpenLoops and to methodological aspects of matching and merging of NLO and squared quark-loop corrections.

3.2.1 Loop amplitudes with OpenLoops and Collier

For the calculation of virtual corrections we employ OpenLoops [43], a fully automated generator of Standard-Model scattering amplitudes at one loop. The OpenLoops method has been designed in order to break various bottlenecks in multi-particle one-loop calculations. The algorithm is formulated in terms of Feynman diagrams and tensor integrals, which allows for very high CPU efficiency to be achieved. While this was already known from $2 \to 4$ NLO calculations based on algebraic methods [122, 123, 157, 158], the idea behind OpenLoops is to replace algebraic manipulations of Feynman diagrams by a numerical recursion, which results in order-of-magnitude reductions both in the size of the numerical code and in the time needed to generate it. Thanks to these improvements, which are accompanied by a further speedup of loop amplitudes at runtime, OpenLoops is able to address large-scale problems, such as NLO simulations for classes of processes involving a large number of multi-leg partonic channels.

The OpenLoops recursion is based on the well known idea that one-loop Feynman diagrams can be cut-opened in such a way that the resulting tree-like objects can be generated with automated tree algorithms. However, rather than relying on conventional tree algorithms, the recursion is formulated in terms of loop-momentum polynomials called "open loops". An analogous idea was proposed in Ref. [44] in the framework of Dyson-Schwinger off-shell recursions. Diagrams involving N loop propagators are built by reusing components from related diagrams with $N-1$ loop propagators in a systematic way. Together with other techniques to speed up colour and helicity summations [43], this allows to handle multi-particle processes with up to $\mathcal{O}(10^4 - 10^5)$ one-loop diagrams.

The algorithm is completely general, since the kernel of the reduction depends only on the Feynman rules of the model at hand, and once implemented it is applicable to any process. Similarly, the so-called R_2 rational terms [28] are generated as counterterm-like diagrams from corresponding Feynman rules.

For the numerical evaluation of one-loop tensor integrals, OpenLoops is interfaced to the Collier library [154], which implements the Denner–Dittmaier reduction methods [31, 32] and the scalar integrals of Ref. [103]. Thanks to a variety of expansions in Gram determinants and other kinematic quantities [32], the Collier library systematically avoids spurious singularities in exceptional phase-space regions. This allows for a fast and numerically stable evaluation of tensor integrals in double precision. Alternatively, OPP reduction [26] can be used instead of tensor integrals.

The present implementation of OpenLoops can handle one-loop QCD corrections

to any Standard-Model process with up to six particles attached to the loops.[1] Virtual QCD corrections are computed exactly, and the full set of Feynman diagrams contributing to a given process is taken into account by default. For final states involving four leptons, the complex-mass scheme [156] is used for a consistent description of resonant and non-resonant vector-boson propagators and their interferences. OpenLoops can also be used to compute squared one-loop matrix elements, such as the various squared quark-loop amplitudes considered in this work. The correctness of one-loop amplitudes generated with OpenLoops has been tested systematically against an independent in-house generator for more than one hundred different parton-level processes, and agreement at the level of 12-14 digits on average was found.

3.2.2 Matching to parton shower and merging in Sherpa

The combination of fixed-order calculations and resummation is essential for the analysis of exclusive cross sections. Parton showers implement resummation in a simple, yet effective way. While formally only correct to leading-logarithmic accuracy, they include a number of features that are important for a realistic prediction of exclusive jet spectra. Firstly, the strong coupling factors associated to quark and gluon emissions are evaluated at scales set by the transverse momenta in the parton branchings. This choice sums higher-logarithmic corrections, originating in the enhanced probability for soft and collinear radiation. Secondly, modern parton showers naturally implement local four-momentum conservation in each individual parton emission, which leads to a realistic description of the kinematics in multi-particle final states. Thirdly, most parton showers include higher-logarithmic corrections in an effective approximation known as angular ordering. This method yields the correct jet rates in e^+e^- annihilation to hadrons [159], as well as the production of Drell–Yan lepton pairs in hadronic collisions [160].

Cross sections in jet bins as analysed here are strongly sensitive to real radiative corrections, or their suppression. Such corrections are dominated by Sudakov double logarithms of the jet-veto scale, which can have a large impact both on exclusive cross sections and related uncertainty estimates. A priori it is not clear if renormalisation- and factorisation-scale variations provide a meaningful estimate of NLO cross sections in jet bins. In fact conventional scale variations can turn out to be artificially small as a consequence of accidental cancellations between Sudakov-enhanced logarithms and contributions that do not depend on the jet veto [161]. In this respect, fixed-order calculations matched to a parton shower allow for more reliable predictions and error estimates. In particular, factorisation- and renormalisation-scale uncertainties can be supplemented by independent variations of the resummation scale, i.e. the scale that enters Sudakov logarithms and corresponds to the starting point of the parton-shower evolution. Resummation-scale variations reflect the uncertainties associated with subleading Sudakov logarithms beyond the shower approximation, and independent variations of the factorisation, renormalisation and resummation scales provide a more reliable assessment of theoretical errors in presence of jet bins.

The parton shower used for our calculation is based on Catani–Seymour dipole

[1] Final-state lepton pairs couple to QCD loops only via electroweak vector bosons and should thus be counted as a single particle.

subtraction [73]. It was described in detail in Refs. [86, 162]. Splitting kernels are given by the spin-averaged dipole-insertion operators, taken in the large-N_c limit. The momentum mapping in branching processes is defined by inversion of the kinematics in the dipole-subtraction scheme. The parameters of the parton shower are given by its infrared cutoff, by the resummation scale, and by the precise scale at which the strong coupling is evaluated. This latter scale must be proportional to the transverse momentum k_T in the splitting process, but it may be varied using a prefactor, b, of order one. In practice, the explicit form of k_T is dictated by the dipole kinematics, and different prefactors are used for final-state and initial-state evolution. The resummation scale can be chosen freely in principle, but at leading order it must be equal to the factorization scale.

The matching of NLO calculations and parton showers in the MC@NLO method [88] is based on the idea that $\mathcal{O}(\alpha_s)$ expansions of the parton shower can provide local subtraction terms (called MC counterterms), which cancel all infrared singularities in real-emission matrix elements. The subtracted result is a finite remainder. When combined with the parton shower it gives the correct $\mathcal{O}(\alpha_s)$ distribution of emissions in the radiative phase space. The total cross section is obtained to NLO accuracy by adding virtual corrections and integrated MC counterterms to the Born cross section and combining them into a common seed for the parton shower. The matching procedure effectively restricts the role of the parton shower to QCD emissions beyond NLO.

This method needs to be modified in processes with more than three coloured particles at Born level, because of non-factorisable soft-gluon insertions at real-emission level. Spin correlations further complicate the picture. This problem is solved by using a variant of the original MC@NLO technique [98, 155]. Like SHERPA's parton shower itself, this method is based on the dipole-subtraction formalism by Catani and Seymour [73], and it is implemented in SHERPA in a fully automated way. It supplements the parton shower with spin and colour correlations for the first emission and therefore extends it systematically beyond the large-N_c approximation.

We combine MC@NLO calculations of varying jet multiplicity into inclusive event samples using the MEPS@NLO method [94,95]. This technique is based on partitioning the phase space associated to QCD emissions into a soft and a hard regime. The soft region is filled by the parton shower alone, while the hard region is described in terms of fixed-order calculations, to which the parton shower has been matched. In case of the MC@NLO simulation with the highest jet multiplicity, $N_{\max}$, the parton shower is allowed to fill the entire phase space. The phase-space separation is achieved in terms of a kinematical variable analogous to the jet criterion in longitudinally-invariant k_T-clustering algorithms [99]. We will denote the separation cut by Q_{cut}. It should be chosen smaller than the minimum jet transverse momentum. In this manner, the prediction for inter-jet correlations involving up to $N_{\max}$ jets is always NLO accurate, and augmented by resummation as implemented in the parton shower.

The choice of the renormalisation scale in the MEPS@NLO approach is based on the CKKW technique, a multi-jet merging algorithm for tree-level matrix elements [90]. Each shower emission is associated with a factor $\alpha_s(b\,k_T^2)$, where the scale is dictated by the resummation. The smooth transition between parton-shower and matrix-element regimes at the merging scale Q_{cut} requires a similar scale choice also in matrix elements.

To this end, multi-jet events are clustered into a $2 \to 2$ core process. The clustering algorithm is defined as an exact inversion of the parton shower, such that clusterings are determined according to the parton-shower branching probabilities [99]. The coupling factors resulting from the various QCD emissions are then evaluated at scales $\mu^2 = b\,k_{\mathrm{T}}^2$, where k_{T} is the nodal scale of the corresponding branching, while the $\alpha_s^K(\mu^2)$ term associated with the core process is taken at the usual scale $\mu = \mu_{\mathrm{R}}$. This latter can be chosen freely as in fixed-order calculations.

In practice, in the MEPS@NLO algorithm all α_s terms are first evaluated at the scale μ_{R}, and the CKKW prescription is implemented via weight-correction factors,

$$\frac{\alpha_s(b\,k_{\mathrm{T}}^2)}{\alpha_s(\mu_{\mathrm{R}}^2)} \approx 1 - \frac{\alpha_s(\mu_{\mathrm{R}}^2)}{2\pi} b_0 \ln\left(\frac{b\,k_{\mathrm{T}}^2}{\mu_{\mathrm{R}}^2}\right), \tag{3.1}$$

for each branching. More precisely, in LO and NLO matrix elements the left- and right-hand sides of (3.1) are used, respectively. For the hard remainder function in the MC@NLO calculations contributing to the MEPS@NLO result the renormalisation scale is always evaluated according to the most likely underlying Born configuration, classified according to the branching probability in the parton shower.

The fact that the CKKW scale choice adapts to the jet kinematics can improve the description of jet emission also at high transverse momentum. In this region, where jet emission is typically associated to CKKW coupling factors $\alpha_s(p_{\mathrm{T}}^2)$, fixed-order calculations based on a global renormalisation scale μ_{R} involve a relative factor $\alpha_s(\mu_{\mathrm{R}}^2)/\alpha_s(p_{\mathrm{T}}^2)$, which can significantly overestimate the jet rate if μ_{R} does not adapt to the jet transverse momentum and $p_{\mathrm{T}} \gg \mu_{\mathrm{R}}$. This factor tends to be compensated by NLO corrections, but in MC@NLO simulations with fixed jet multiplicity N it remains uncompensated for the $(N+1)$-th jet, whose description relies on real-emission LO matrix elements. Within MEPS@NLO, if $N < N_{\max}$ such real-emission matrix elements are confined at transverse momenta below the merging scale and replaced by an MC@NLO simulation with $N+1$ jets above Q_{cut}. In this way NLO accuracy is ensured for the first $N_{\max}$ jets, and the problem remains present only for the subsequent jet. A simple solution consists of including $(N_{\max}+1)$-jet LO matrix elements in the merging procedure. In this way, also the $(N_{\max}+1)$-th jet receives a CKKW coupling factor $\alpha_s(p_{\mathrm{T}}^2)$ above the merging scale. As discussed in Section 3.3.3, for the MEPS@NLO simulation of $\mathrm{pp} \to 4\ell + 0, 1j$ we adopt a dynamical scale μ_{R} that depends only on the W-boson transverse energy and does not adapt to extra jet emissions. The above discussion is thus relevant for the high-p_{T} tail of the second jet, where it's likely that $\mu_{\mathrm{R}} \ll p_{\mathrm{T}}$, since the two jets typically recoil against each other and the transverse energy of the W bosons tends to remain of the order of M_{W}.

In order to guarantee a complete treatment of scale uncertainties, renormalisation-scale variations in the MEPS@NLO merging approach are performed simultaneously in the fixed-order calculation and in the parton shower. The same rescaling factors are applied to the CKKW scales and to the scale μ_{R} used in the α_s terms associated with the core process.

3.2.3 Merging of squared quark-loop contributions to four-lepton production

We present here, for the first time, a combination of the squared quark-loop contributions to pp $\to 4\ell + 0, 1j$ using the ME+PS merging technique of Ref. [99]. At matrix-element level we consider all squared one-loop amplitudes that involve a closed quark loop. While squared quark-loop corrections to 4ℓ final states involve only gg initial states, $4\ell + 1j$ production involves, in addition to gg $\to 4\ell + \mathrm{g}$, also $qg \to 4\ell + q$, $\bar{q}\mathrm{g} \to 4\ell + \bar{q}$ and $q\bar{q} \to 4\ell + \mathrm{g}$ contributions. For these quark-initiated channels we require that all final-state leptons are connected to the quark loop via vector-boson exchange, i.e. we exclude topologies where vector bosons couple to the external quark line. The inclusion of these quark-initiated channels is mandatory for a consistent merging of the $4\ell + 0, 1j$ samples. This is due to the fact that gluon- and quark-initiated channels are intimately connected via $q \to q\mathrm{g}$ and $\mathrm{g} \to q\bar{q}$ parton-shower splittings. Including the $q\mathrm{g}$ and $\bar{q}\mathrm{g}$ channels ensures that all splitting functions used in the shower are replaced by matrix elements in the hard-jet region. The finite contribution from the $q\bar{q} \to 4\ell + \mathrm{g}$ channel is added for consistency. While the gg-induced channels have already been discussed in the literature [148–151, 163], the squared quark-loop contributions to the $q\mathrm{g}$-, $\bar{q}\mathrm{g}$- and $q\bar{q}$-channels are investigated for the first time in this work.

To merge the $4\ell + 0, 1j$ final states we can use the tree-level techniques of Ref. [99] since all involved matrix elements are infrared and ultraviolet finite. In particular, the merging scale Q_{cut} acts as an infrared cutoff that avoids soft and collinear divergences of $4\ell + 1j$ matrix elements, and the phase-space region below Q_{cut} is filled by gg $\to 4\ell$ matrix elements plus shower emissions. As discussed in Section 3.3.3, while squared quark-loop corrections represent NNLO contributions to inclusive $4\ell + 0, 1j$ production, their intrinsic accuracy is only leading order. Consequently, as we will see in Sections 3.4–3.5, squared quark-loop terms are more sensitive to renormalisation- and resummation-scale variations as compared to MEPS@NLO predictions.

3.3 Monte Carlo simulations

In the following we discuss input parameters and theoretical ingredients of the Monte Carlo simulations presented in Sections 3.4 and 3.5.

3.3.1 Input parameters and process definition

The presented results refer to pp $\to \mu^+\nu_\mu \mathrm{e}^-\bar{\nu}_\mathrm{e} + X$ at a centre-of-mass energy of 8 TeV. Predictions at NLO and squared quark-loop corrections are evaluated using the five-flavour CT10 NLO parton distributions [164] with the respective running strong coupling α_s. At LO we employ the CT09MCS PDF set. For the vector-boson masses we use

$$M_\mathrm{W} = 80.399 \text{ GeV}, \qquad M_\mathrm{Z} = 91.1876 \text{ GeV}, \tag{3.2}$$

and in order to guarantee NLO accurate W $\to \ell\nu$ branching fractions we use NLO input widths

$$\Gamma_\mathrm{W} = 2.0997 \text{ GeV}, \qquad \Gamma_\mathrm{Z} = 2.5097 \text{ GeV}. \tag{3.3}$$

The electroweak mixing angle is obtained from the ratio of the complex W- and Z-boson masses as [156]

$$\cos^2\theta_\mathrm{w} = \frac{M_\mathrm{W}^2 - \mathrm{i}\Gamma_\mathrm{W} M_\mathrm{W}}{M_\mathrm{Z}^2 - \mathrm{i}\Gamma_\mathrm{Z} M_\mathrm{Z}}, \tag{3.4}$$

and the electromagnetic fine-structure constant is derived from the Fermi constant $G_\mu = 1.16637 \cdot 10^{-5}\ \mathrm{GeV}^{-2}$ in the so-called G_μ-scheme, which results in

$$\alpha^{-1} = \frac{\pi}{\sqrt{2}\, G_\mu M_\mathrm{W}^2} \left(1 - \frac{M_\mathrm{W}^2}{M_\mathrm{Z}^2}\right)^{-1} = 132.348905\,. \tag{3.5}$$

Since quark-mixing effects cancel almost completely [139], we set the CKM matrix equal to one.

Partonic channels with initial- and final-state b quarks are not included in order to avoid any overlap with $\mathrm{t\bar{t}}$ and tW production. At NLO this separation is nontrivial since $\mathrm{W^+W^-}+1j$ production receives $\mathrm{pp} \to \mathrm{W^+W^-b\bar{b}}$ real-emission contributions that involve top-quark resonances. At the same time, $\mathrm{W^+W^-b\bar{b}}$ final states are intimately connected to the virtual corrections to $q\bar{q} \to \mathrm{W^+W^-g}$ via cancellations of collinear singularities that arise from $\mathrm{g} \to \mathrm{b\bar{b}}$ splittings [139]. This is discussed in detail in Appendix B.1, where we introduce a prescription to separate $\mathrm{W^+W^-}$+jets from single-top and top-pair production processes in such a way that each contribution is infrared finite and free from large logarithms associated to $\mathrm{g} \to \mathrm{b\bar{b}}$ splittings. This prescription is not unique, and we estimate the related ambiguity to be of order 1%. It can be eliminated by a consistent matching of $\mathrm{W^+W^-}$+jets and $\mathrm{W^+W^-b\bar{b}}$ production as explained in Appendix B.1.

3.3.2 Fixed-order ingredients of the calculation

Sample Feynman diagrams contributing to the fixed-order building blocks of the calculation are shown in Figures 6 and 7. For brevity $\mu^+\nu_\mu\mathrm{e}^-\bar{\nu}_\mathrm{e}$ configurations are often denoted as $\ell\nu\ell\nu$ or 4ℓ final states in the following. The first figure illustrates NLO QCD corrections to $\mathrm{pp} \to 4\ell$ and $\mathrm{pp} \to 4\ell + 1j$, which involve various $\bar{q}q$, qg, $\bar{q}g$ and gg partonic channels. The complete set of Feynman diagrams and related interferences is taken into account, including single-resonant $\mathrm{Z}/\gamma^* \to \mathrm{e}^-\bar{\nu}_\mathrm{e}\mathrm{W}^+(\to \mu^+\nu_\mu)$ sub-topologies. Pentagons represent the most involved one-loop topologies.

In addition to NLO corrections also squared quark-loop contributions to the partonic channels $\mathrm{gg} \to 4\ell$, $\mathrm{gg} \to 4\ell + \mathrm{g}$, $\mathrm{g}q \to 4\ell + q$, $\mathrm{g}\bar{q} \to 4\ell + \bar{q}$, and $q\bar{q} \to 4\ell + \mathrm{g}$ are computed. Corresponding Feynman diagrams are shown in Fig. 7. The most involved diagrams are again pentagons. As discussed in Section 3.2.3, the inclusion of the quark-induced channels is mandatory for a correct description of the full spectrum of jet emission based on the merging of 4ℓ and $4\ell + j$ simulations. Contributions where the leptons are coupled to quark triangles via Z/γ^* exchange, like in the first two diagrams of Fig. 7, vanish due to electroweak Ward identities [133]. In contrast, related topologies with an extra gluon in the final state, like the last two diagrams in Fig. 7, yield non-vanishing contributions. The various NLO and squared quark-loop amplitudes generated for the present study comprise all relevant Higgs-boson contributions, including the interference of the Higgs signal with the four-lepton continuum.

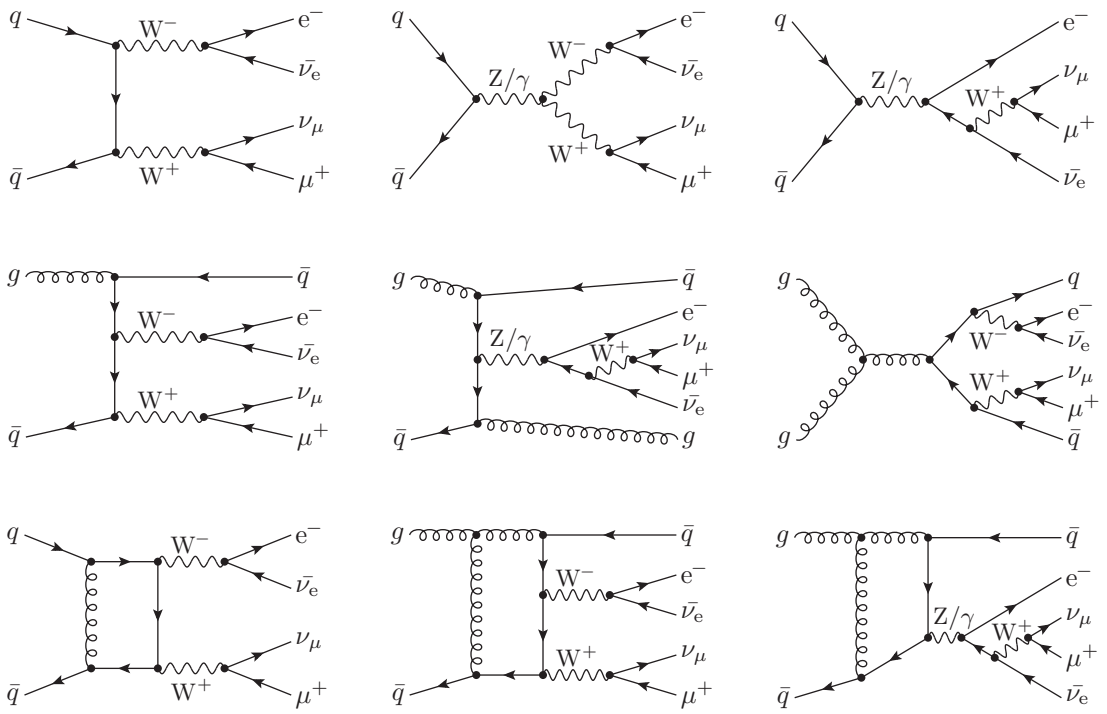

Figure 6: Sample Feynman diagrams contributing to $pp \to \mu^+\nu_\mu e^-\bar{\nu}_e$ and $pp \to \mu^+\nu_\mu e^-\bar{\nu}_e + 1j$ at NLO.

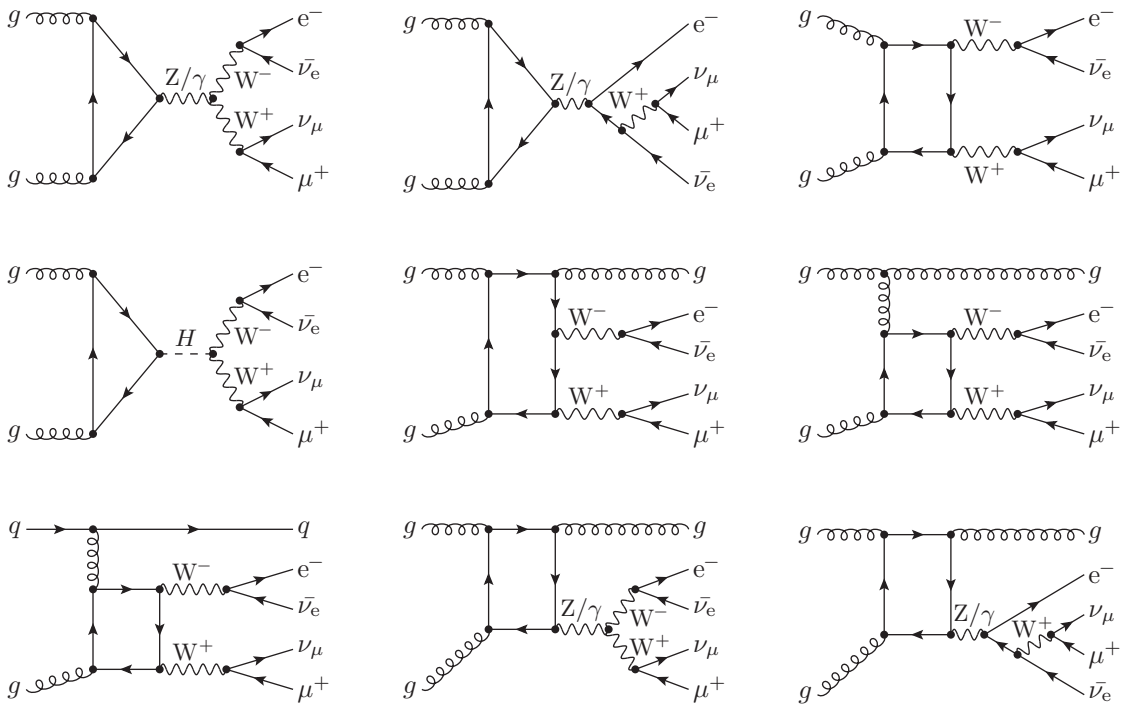

Figure 7: Sample Feynman diagrams involved in the squared quark-loop NNLO contributions to $pp \to \mu^+\nu_\mu e^-\bar{\nu}_e$ and $pp \to \mu^+\nu_\mu e^-\bar{\nu}_e + 1j$.

However, for the background predictions presented in Sections 3.4–3.5 all Higgs-boson contributions have been decoupled by setting $M_{\mathrm{H}} \to \infty$.

A series of checks has been performed to validate all ingredients of the QCD corrections. To check the correctness of the $q\bar{q} \to 4\ell + 0, 1\mathrm{g}$ OpenLoops matrix elements we used an independent computer-algebra generator, originally developed for the calculations of Refs. [122, 123]. The squared quark-loop $\mathrm{gg} \to 4\ell + 0, 1\mathrm{g}$ amplitudes have been checked against MCFM [165] and Ref. [151]. The NLO and squared quark-loop integrated cross sections for $\mathrm{pp} \to 4\ell + 0, 1j$ and $\mathrm{gg} \to 4\ell + 0, 1\mathrm{g}$ have been found to agree with various results in the literature [135, 149, 151]. Finally, the NLO cross sections for hadronic $4\ell + 0, 1j$ production have been reproduced with sub-permil statistical precision using an independent Monte Carlo generator, which was developed by S. Kallweit in the framework of the $\mathrm{pp} \to \mathrm{W^+W^-b\bar{b}}$ calculation of Ref. [123].

The calculation of tree-level matrix elements is performed either by the Amegic++ [166] or the Comix [167] matrix-element generator, where Comix is used only for $\mathrm{pp} \to 4\ell + 2j$ subprocesses. Integrated and real subtraction terms are computed with the method of Catani and Seymour [73], using the automated implementation in Amegic++ [168].

3.3.3 Matching to the parton shower, multi-jet NLO merging, and scale variations

The perturbative content of the various fixed-order, matched and merged simulations that are presented in Sections 3.4 and 3.5 is illustrated in Table 3. Parton-level NLO predictions for $\mathrm{pp} \to 4\ell + 0, 1j$ are denoted as Nlo 4ℓ and Nlo $4\ell + 1j$. Their NLO predictive power is restricted to the 0- and 1-jet bins, respectively.[1] In bins with one extra jet with respect to the simulated process, the precision decreases to LO, and higher-multiplicity bins are not populated at all.

This is overcome by matching Nlo 4ℓ or Nlo $4\ell+1j$ matrix elements to the parton shower. Corresponding predictions are denoted as Mc@Nlo 4ℓ and Mc@Nlo $4\ell + 1j$. The shower radiates an arbitrary number of extra jets, which effectively resums large Sudakov logarithms that arise when QCD radiation is constrained by tight cuts, such as in presence of jet vetoes. Similarly as the underlying NLO matrix elements, Mc@Nlo predictions provide NLO precision only for one particular jet multiplicity. In the following sections we will consider only Mc@Nlo 4ℓ predictions. This corresponds to the usual inclusive NLO+PS samples used in experimental studies, where observables involving one jet are only LO accurate, and the emission of additional jets is entirely based on the parton-shower approximation.

Our best NLO predictions are denoted as Meps@Nlo $4\ell + 0, 1j$ and result from merging Mc@Nlo 4ℓ and Mc@Nlo $4\ell + 1j$ samples. This provides shower-improved NLO precision in the first two jet bins. To ensure that the formal NLO accuracy is preserved in the 0- and 1-jet bins, the merging scale Q_{cut} should not exceed the p_{T}-threshold used for jet binning. On the other hand, in the limit of small Q_{cut} the fact that higher-logarithmic terms in the fixed-order Nlo $4\ell+1j$ calculation are not resummed in

[1] In this discussion of the perturbative accuracy we refer to jet bins in the inclusive sense. The 0-, 1- and 2-jet bins should namely be understood as final states with ≥ 0, ≥ 1 and ≥ 2 jets, or equivalently as observables that explicitly or implicitly involve a corresponding number of jets.

Nlo simulations	**0-jet**	**1-jet**	**2-jet**
NLO 4ℓ	NLO	LO	-
NLO $4\ell + 1j$	-	NLO	LO
MC@NLO 4ℓ	NLO+PS	LO+PS	PS
MC@NLO $4\ell + 1j$	-	NLO+PS	LO+PS
MEPS@NLO $4\ell + 0, 1j$	NLO+PS	NLO+PS	LO+PS
Loop^2 simulations	**0-jet**	**1-jet**	**2-jet**
LOOP^2 4ℓ	LO	-	-
LOOP^2 $4\ell + 1j$	-	LO	-
LOOP^2+PS 4ℓ	LO+PS	PS	PS
LOOP^2+PS $4\ell + 1j$	-	LO+PS	PS
MEPS@LOOP^2 $4\ell + 0, 1j$	LO+PS	LO+PS	PS

Table 3: Perturbative accuracy of various fixed-order, matched and merged simulations for final states with 0, 1 and 2 jets.

the Sudakov form factor gives rise to a logarithmic sensitivity to the merging scale. Such logarithms are beyond the shower accuracy but can be numerically non-negligible [96, 169]. Thus the merging scale should not be set too far below the jet-p_{T} threshold. Following this reasoning the value $Q_{\mathrm{cut}} = 20$ GeV has been used as merging scale, and the stability of the results with respect to this technical parameter has been tested using variations in the range 15 GeV $\leq Q_{\mathrm{cut}} \leq$ 35 GeV. The corresponding uncertainties are discussed in Section 3.5 for the case of the $\mathrm{H} \to \mathrm{WW}^*$ analysis, where they turn out to be at the percent level. The MEPS@NLO $4\ell + 0, 1j$ sample is further improved by including LO matrix elements with two jets in the merging procedure. As explained in Section 3.2.2, this guarantees a better (CKKW-type) scale choice for the α_s factor associated with the second jet emission.

In order to gain insights into the importance of parton-shower and merging effects, we will present systematic comparisons of NLO, MC@NLO and MEPS@NLO predictions. While Sudakov resummation effects due to the parton shower show up in the difference between NLO 4ℓ and MC@NLO 4ℓ, comparing MC@NLO 4ℓ to MEPS@NLO 4ℓ+ $0, 1j$ allows one to assess NLO corrections to the first emission.

As already mentioned, squared quark-loop terms included in our simulation represent NNLO contributions to $\mathrm{pp} \to 4\ell + (0)1j$. On the other hand, since NNLO is the first order at which the $\mathrm{gg} \to 4\ell + 0(1)\mathrm{g}$ channels start contributing to $4\ell + (0)1j$ production, these corrections can also be regarded as LO contributions. As indicated in Table 3, squared quark-loop terms behave as LO predictions also for what concerns the number of external QCD partons. In fact, fixed-order squared quark-loop predictions, which we denote as LOOP^2 4ℓ and LOOP^2 4ℓ+$1j$, populate only a single jet bin. In par-

ticular, LOOP^2 4ℓ predictions completely miss exclusive jet emission and suppression effects resulting from jet vetoes. A first realistic estimate of jet-veto effects is obtained by showering squared quark-loop contributions. The corresponding predictions are labelled as LOOP^2+PS 4ℓ and LOOP^2+PS $4\ell + 1j$, depending on the jet multiplicity of the underlying matrix elements. Merging the LOOP^2+PS simulations with 0 and 1 jets results in a single MEPS@LOOP^2 4ℓ+$0, 1j$ sample, which provides a reliable description of the full spectrum of jet emission, from soft to hard regions. This merged squared quark-loop simulation comprises also partonic channels with initial-state quarks. To assess their relative importance, in Section 3.4, full MEPS@LOOP^2 4ℓ+$0, 1j$ predictions are compared to corresponding predictions involving only initial-state gluons.

As a default renormalisation ($\mu_{\rm R}$), factorisation ($\mu_{\rm F}$) and resummation (μ_Q) scale we adopt the average W-boson transverse energy

$$\mu_0 = \frac{1}{2}\left(E_{\rm T,W^+} + E_{\rm T,W^-}\right), \tag{3.6}$$

where $E^2_{\rm T,W} = M^2_{\rm W} + (\vec{p}_{\rm T,\ell} + \vec{p}_{\rm T,\nu})^2$. As discussed in Section 3.4, motivated by the comparison of hard-jet emission from parton shower and matrix elements, in the case of squared quark-loop contributions we decided to reduce the resummation scale by a factor two, i.e. we set $\mu_Q = \mu_0/2$.

Renormalisation- and factorisation-scale uncertainties are assessed by applying independent variations $\mu_{\rm R} = \xi_{\rm R}\mu_0$ and $\mu_{\rm F} = \xi_{\rm F}\mu_0$, with factor-two rescalings $(\xi_{\rm R}, \xi_{\rm F}) = (2,2), (2,1), (1,2), (1,1), (1,0.5), (0.5,1), (0.5,0.5)$. The renormalisation scale is varied in all α_s terms that arise in matrix elements or from the shower. In NLO and MC@NLO predictions all α_s terms arising from matrix elements are evaluated at $\mu_{\rm R} = \xi_{\rm R}\mu_0$, while in MEPS@NLO the scale μ_0 is used only in tree and loop contributions to the $pp \to 4\ell$ core process, which results from 4ℓ+jets configurations via clustering of all hard jets. For the α_s factors associated with jet emissions a CKKW scale choice is applied, as discussed in Section 3.2.2. As a consequence, MEPS@NLO predictions are less sensitive to the choice of the central scale μ_0. Also in MEPS@LOOP^2 merging the scale of α_s factors associated to QCD emissions is dictated by the CKKW prescription. In this case the core process involves a term $\alpha_s^2(\mu_{\rm R})$, which renders squared quark-loop corrections more sensitive to the choice of the central scale μ_0.

In addition to usual QCD-scale studies, the SHERPA framework allows also for automated variations of the resummation scale μ_Q, which corresponds to the starting scale of the parton shower. This scale is varied by factors $\mu_Q/\mu_0 = 1/\sqrt{2}, 1, \sqrt{2}$, while keeping $\mu_{\rm R}$ and $\mu_{\rm F}$ fixed. As discussed in Section 3.2.2, this reflects uncertainties related to subleading logarithms beyond the shower approximation and yields more realistic error estimates for exclusive observables such as jet-vetoed cross sections. In order to quantify the total scale uncertainty we will regard $(\mu_{\rm R}, \mu_{\rm F})$ and μ_Q variations as uncorrelated and add them in quadrature.[1] Uncertainties related to the PDFs, $\alpha_s(M_{\rm Z})$, hadronisation, and underlying event are not considered in this study.

[1] Another natural way of combining these two sources of uncertainty is to consider simultaneous variations of $(\mu_{\rm R}, \mu_{\rm F}, \mu_Q)$, excluding rescalings in opposite directions as usual. The variations resulting from this alternative approach are likely to be even smaller than those obtained by adding QCD- and resummation-scale uncertainties in quadrature.

The presented results were obtained with a SHERPA 2.0 pre-release version[1]. First partial results of this simulation have been presented in Ref. [153]. In addition to the squared quark-loop contributions, which were not included in Ref. [153], in this work we investigate various new observables. Due to the difference between (3.6) and the scale choice $\mu_0 = M_{\ell\nu\ell\nu}$ in Ref. [153], results presented here should not be directly compared to those of Ref. [153].

3.4 Analysis of inclusive $\ell\nu\ell\nu + 0, 1$ jets production

As a first application of our simulation we study $\mu^+\nu_\mu e^-\bar{\nu}_e$ and $\mu^+\nu_\mu e^-\bar{\nu}_e + 1$ jet production without any Higgs-analysis specific cuts. To this end we adopt the cuts of the `MC_WWJETS` truth analysis provided with the Rivet Monte Carlo validation framework [170]. Specifically, we require charged leptons with $p_{T,\ell} > 25$ GeV and $|\eta_\ell| < 3.5$. Missing transverse energy is identified with the vector sum of the neutrino transverse momenta and required to fulfil $\not{E}_T > 25$ GeV. Jets are defined using the anti-k_T algorithm [171] with a distance parameter of $R = 0.4$. No jet-rapidity cuts are applied.

To illustrate the importance of the various corrections and the respective scale uncertainties, we present cross sections and distributions at the different levels of simulation introduced in Section 3.3.3. In Section 3.4.1 we compare fixed-order predictions to matched and merged NLO simulations. Squared quark-loop corrections are discussed in Section 3.4.2.

3.4.1 Fixed-order, matched and merged NLO simulations

Rates for the inclusive analysis and when requiring (at least) one jet with $p_T > 30$ GeV are shown in Table 4. Fixed-order LO and NLO predictions for $pp \to 4\ell$ or $4\ell+1j$, depending on the jet bin, are compared to the inclusive MC@NLO 4ℓ simulation and to the NLO merged simulation of $4\ell+0, 1j$. For 0- and 1-jet production we observe positive NLO corrections of 50% and 38%, respectively, consistent with the typical size of K-factors in the literature. At NLO, scale uncertainties range from 3 to 5 percent, which is twice as large as compared to our previous Higgs-background predictions in exclusive jet bins [153]. This can be attributed to the new scale choice (3.6) and to the fact that results in Table 4 correspond to inclusive jet bins. In fact, as shown in Ref. [139], the choice of the central scale and a jet veto can have a strong impact on scale uncertainties in $4\ell+1j$ production [139]. In this respect, we note that the central scale used in Ref. [153], i.e. the total four-lepton invariant mass, is more than a factor two higher than the transverse-energy scale (3.6) adopted for the present study.

Comparing the MC@NLO and NLO simulations we observe one-percent level agreement and rather similar uncertainties in the inclusive analysis. This agreement, as well as the tiny resummation-scale uncertainties of MC@NLO, reflect the unitarity of the parton shower for inclusive observables. In contrast, in the 1-jet bin MC@NLO

[1]This pre-release version corresponds to SVN revision 21825 and the main difference with respect to the final SHERPA 2.0 release version is the tuning of parton shower, hadronisation and multiple parton interactions to experimental data.

Analysis	**Lo** $4\ell\,(+1j)$	**Nlo** $4\ell\,(+1j)$	**Mc@Nlo** 4ℓ	**Meps@Nlo** $4\ell + 0, 1j$
≥ 0 jets	$217.99(2)\ ^{+1.9\%}_{-2.8\%}$	$328.08\ ^{+3.1\%}_{-2.4\%}$	$326.70(29)\ ^{+4.5\%\ +0.0\%}_{-2.8\%\ -0.2\%}$	$356.01(58)\ ^{+1.3\%\ +1.8\%}_{-0.8\%\ -0.0\%}$
≥ 1 jets	$73.61(1)\ ^{+14.5\%}_{-11.6\%}$	$101.70\ ^{+5.2\%}_{-4.9\%}$	$83.23(15)\ ^{+9.9\%\ +2.4\%}_{-9.0\%\ -4.6\%}$	$103.45(28)\ ^{+2.8\%\ +3.3\%}_{-3.7\%\ -0.5\%}$

Table 4: Cross-section predictions in femtobarns for the $\mu^+\nu_\mu \mathrm{e}^-\bar{\nu}_\mathrm{e}$ analyses requiring ≥ 0 and ≥ 1 jets. Fixed-order LO and NLO results for the ≥ 0-jet and ≥ 1-jet analyses correspond to 4ℓ and $4\ell + 1j$ production, respectively. They are compared to an inclusive MC@NLO 4ℓ simulation and to MEPS@NLO $4\ell + 0, 1j$ predictions. Uncertainties associated to variations of the QCD scales $(\mu_\mathrm{R}, \mu_\mathrm{F})$ and the resummation scale (μ_Q) are shown separately as $\sigma \pm \delta_\mathrm{QCD} \pm \delta_\mathrm{res}$. Statistical errors are given in parenthesis.

predictions exhibit a deficit of about 20% and much larger uncertainties as compared to NLO. This is due to the fact that the inclusive matched calculation is only LO accurate in the 1-jet bin.

The inclusive MEPS@NLO cross section is found to be roughly 30 fb larger as compared to the NLO calculation, which can be interpreted as a result of NLO corrections to the first emission in the merged sample. In fact, the shift of 30 fb is comparable to the difference between the NLO and MC@NLO cross sections with ≥ 1 jets, which corresponds to NLO effects in the 1-jet bin. Finally, variations of the QCD and resummation scales in MEPS@NLO amount to only 1–3% in both jet bins. As already mentioned, the fact that fixed-order NLO cross sections feature significantly larger scale variations is related to the choice of the central scale μ_0. This scale plays only a marginal role in MEPS@NLO, since the $\mathrm{pp} \to 4\ell$ core process does not depend on the strong coupling, and α_s terms resulting from jet emissions are controlled by the CKKW prescription.

Distributions in the hardest-jet transverse momentum and in the total transverse energy H_T—defined as the scalar sum of the transverse momenta of leptons, missing E_T, and all reconstructed jets—are displayed in Fig. 8. The bands are obtained by adding QCD- and resummation-scale variations in quadrature. The MC@NLO and MEPS@NLO p_T-distributions agree fairly well in the soft region, but MC@NLO develops an increasingly large deficit at higher p_T, which reaches 30% in the tail. Similarly as MC@NLO, also NLO predictions for inclusive four-lepton production are only LO accurate in the first-jet emission and tend to underestimate the tail. The shapes of the MC@NLO and NLO tails are however somewhat different. This is due to the fact that, in the MC@NLO method, the weights of the first shower emission and of its MC-subtraction counterpart differ by an $\mathcal{O}(\alpha_s)$ relative factor, which involves the $\alpha_s(p_\mathrm{T})/\alpha_s(\mu_\mathrm{R})$ ratio as well as unresolved NLO corrections. This difference disappears above the resummation scale, i.e. where the parton shower stops emitting. This is however not visible in the plot, since due to the dynamical nature of the resummation-scale choice (3.6), this transition takes place only far above the scale M_W. In the $p_\mathrm{T} \to 0$ limit, the NLO 4ℓ calculation involves an infrared singularity of the form $\mathrm{d}\sigma/\mathrm{d}p_\mathrm{T} \sim \alpha_s \ln(p_\mathrm{T})/p_\mathrm{T}$, which manifests itself as a linear rise if the distribution is plotted against $\ln(p_\mathrm{T})$ as in Fig. 8.a. This feature is qualitatively clearly visible but quantitatively very mild, and the corresponding enhancement does not exceed 20% down to $p_\mathrm{T} = 5$ GeV. This signifies that the effect of resumming Sudakov logarithms

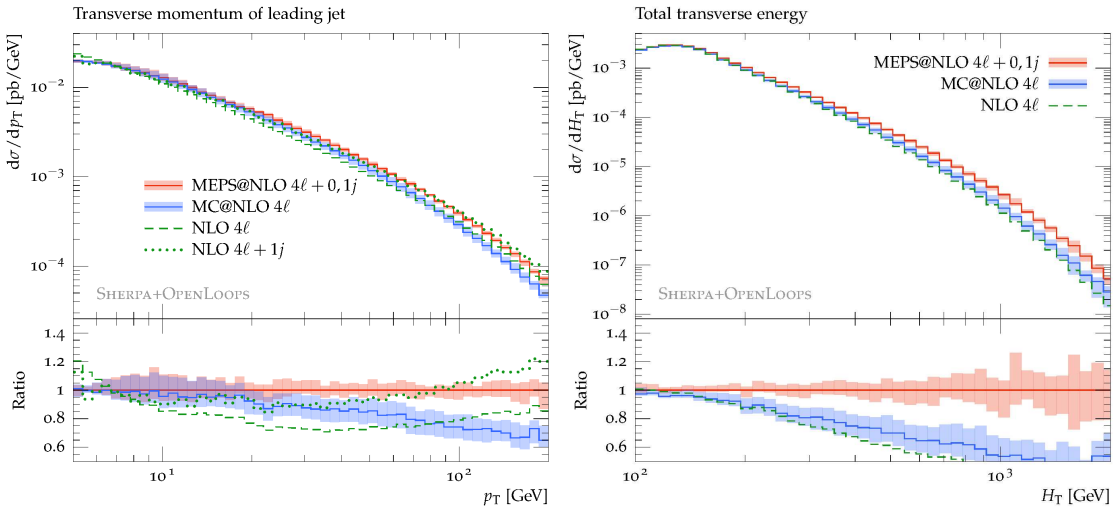

Figure 8: Leading-jet transverse momentum (left) and total transverse energy (right): NLO 4ℓ (green dashed) and NLO $4\ell + 1j$ (green dotted) results are compared to an inclusive MC@NLO 4ℓ simulation (blue) and to MEPS@NLO $4\ell + 0, 1j$ predictions (red). Uncertainty bands describe combined QCD- and resummation-scale uncertainties (added in quadrature).

is important but not dramatic in the considered p_T-range. Higher Sudakov logarithms are partially included in the NLO calculation of $4\ell + 1j$ production, which remains infrared divergent at $p_T \to 0$, but turns out to be in better agreement with MC@NLO and MEPS@NLO predictions for $p_T > 5$ GeV. The NLO $4\ell + 1j$ distribution has a higher tail with respect to inclusive NLO and MC@NLO predictions, as expected, but for $p_T \gtrsim M_W$ it starts to be above the MEPS@NLO curve as well. This can be explained by the fact that, in contrast to the MEPS@NLO approach, in fixed-order predictions the scale of α_s couplings associated with jet emission is not adapted to the jet-p_T (cf. discussion in Section 3.2.3).

The total transverse energy, plotted in Fig. 8.b, is dominated by hard multi-jet emissions that cannot be properly described neither by the inclusive NLO calculation nor by the MC@NLO approach and its parton-shower emissions. This starts to be visible at $H_T \sim 200$GeV and the deficit with respect to MEPS@NLO approaches 50% at 1 TeV.

Matching and merging effects in presence of a jet veto and jet binning are illustrated in Fig. 9, where the integrated cross sections in the exclusive 0-jet bin ($p_T < p_T^{max}$) and in the inclusive 1-jet bin ($p_T > p_T^{min}$) are plotted as a function of the corresponding upper and lower transverse-momentum bounds. In the 0-jet bin, MC@NLO and MEPS@NLO predictions agree well at small jet-veto scales and differ by less than 10% at large p_T^{max}. The respective uncertainties are as small as a few percent and nearly independent of p_T^{max}. For sufficiently inclusive jet-veto values, the NLO pp $\to 4\ell$ calculation is in excellent agreement with MC@NLO. In the $p_T^{max} \to 0$ limit, NLO predictions develop a double-logarithmic singularity of the form $-\alpha_s \ln^2(p_T^{max}/Q)$, while MC@NLO and MEPS@NLO vetoed cross sections consistently tend to zero as a result of the exponentiation of Sudakov logarithms. In this infrared regime, the exponentiation of double logarithms should manifest itself as a positive correction beyond NLO, while for $p_T^{max} \gtrsim 10$ GeV we observe that matched/merged predictions are still below the NLO jet-vetoed cross section. This is due to the fact that Sudakov logarithms are

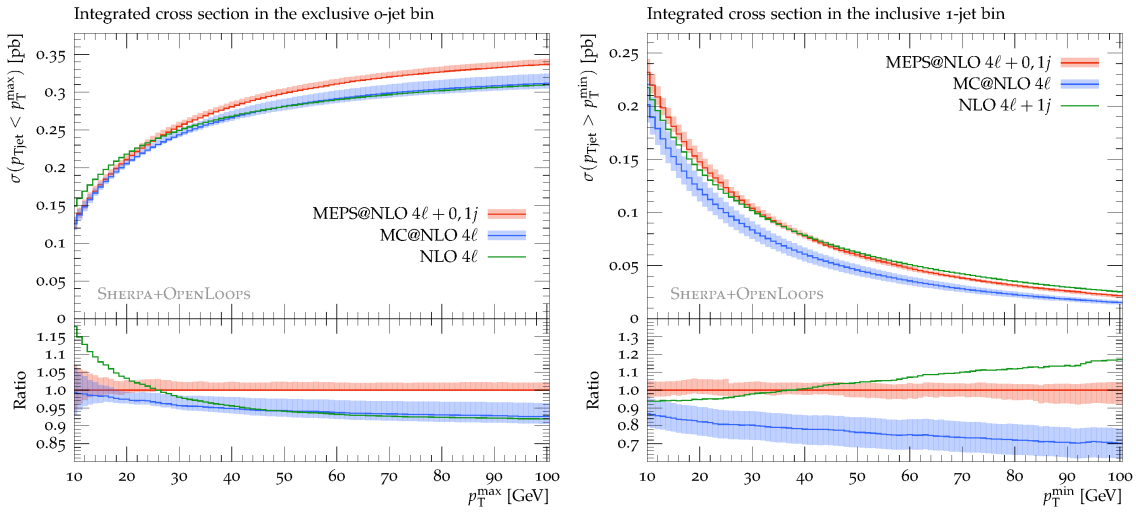

Figure 9: Integrated cross sections in the exclusive 0-jet bin (left) and in the inclusive 1-jet bin (right) as a function of the respective transverse-momentum bounds, $p_{\mathrm{T}}^{\mathrm{max}}$ and $p_{\mathrm{T}}^{\mathrm{min}}$. NLO results with appropriate jet multiplicity (green) are compared to MC@NLO 4ℓ (blue) and MEPS@NLO $4\ell + 0,1j$ (red) simulations. Uncertainty bands correspond to QCD-scale variations combined with the resummation-scale variations in quadrature.

relatively mild in this region (cf. Fig. 8.a), and parton-shower effects are dominated by subleading logarithms associated with the running of α_s in the $\alpha_s(p_{\mathrm{T}})\ln(p_{\mathrm{T}})/p_{\mathrm{T}}$ terms. Double logarithms become dominant at much smaller transverse momenta, and we checked that they drive the NLO cross sections into the negative range only at $p_{\mathrm{T}}^{\mathrm{max}} \sim 2$ GeV. For $p_{\mathrm{T}}^{\mathrm{max}} \simeq 25$–$30$ GeV, which corresponds to the jet-veto values in the $\mathrm{H} \to \mathrm{WW}^*$ analyses at the LHC, fixed-order and matched/merged results deviate by less than 5%. This represents the net effect of Sudakov logarithms beyond NLO, and its smallness is due to the moderate size of the logarithmic terms but also to cancellations between leading and subleading logarithms. The uncertainty due to subleading Sudakov logarithms that are not included in the MC@NLO and MEPS@NLO approximations are quantified via resummation-scale variations, which are reflected in the respective scale-variation bands, and turn out to be at the percent level.

As shown in Fig. 9.b, in the inclusive 1-jet bin the discrepancies between the various approximations become more sizable. The inclusive MC@NLO simulation underestimates the 1-jet cross section by 20–30% for 30 GeV $< p_{\mathrm{T}}^{\mathrm{min}} <$ 100 GeV. For transverse-momentum thresholds up to 50 GeV, the fixed-order $4\ell + 1j$ cross section is in quite good agreement with the MEPS@NLO prediction as expected. However, as already observed in Fig. 8.a, the NLO cross section develops a significant excess in the tail. The uncertainties of the MEPS@NLO and MC@NLO cross sections in the 1-jet bin are rather independent of the p_{T}-threshold and amount to about 5% and 10%, respectively.

3.4.2 Squared quark-loop contributions

Detailed results for the squared quark-loop cross sections in the inclusive analysis and requiring one or more jets with $p_{\mathrm{T}} > 30$ GeV are presented in Table 5. Fixed-order calculations for 4ℓ or $4\ell + 1j$ production, depending on the jet bin, are compared to an inclusive simulation obtained by showering four-lepton matrix elements

Analysis	**Loop**^{2} $4\ell\,(+1j)$	**Loop**^{2}**+PS** 4ℓ	**Meps@Loop**^{2} $\mathbf{pp} \to 4\ell + 0, 1j$	**Meps@Loop**^{2} $\mathbf{gg} \to 4\ell + 0, 1\mathbf{g}$
≥ 0 jets	$8.71(3)\ ^{+28\%}_{-20\%}$	$8.76(3)\ ^{+28\%\ +0.2\%}_{-21\%\ -0.1\%}$	$9.24(4)\ ^{+31\%\ +20\%}_{-20\%\ -14\%}$	$9.10(3)\ ^{+28\%\ +15\%}_{-21\%\ -12\%}$
≥ 1 jets	$3.98(7)\ ^{+48\%}_{-30\%}$	$1.75(1)\ ^{+32\%\ +55\%}_{-25\%\ -51\%}$	$2.75(3)\ ^{+40\%\ +5\%}_{-24\%\ -6\%}$	$2.01(2)\ ^{+35\%\ +1.4\%}_{-25\%\ -3.2\%}$

Table 5: Squared quark-loop predictions in femtobarns for the $\mu^+\nu_\mu \mathrm{e}^-\bar{\nu}_\mathrm{e}$ analyses requiring ≥ 0 jets and ≥ 1 jets. Fixed-order results (Loop^2) with a number of jets corresponding to the actual analysis are compared to an inclusive parton-shower simulation (Loop^2+PS 4ℓ) and to predictions from the merged Meps@Loop^2 $4\ell + 0, 1j$ simulation with and without the inclusion of quarks in the initial state. Scale variations and statistical errors are presented as in Table 4.

(Loop^2+PS 4ℓ) and to merged predictions (Meps@Loop^2 $4\ell + 0, 1j$). Additionally, to assess the importance of quark-induced channels, we show merged squared quark-loop results that involve only gluon–gluon partonic channels and, for consistency, only $\mathrm{g} \to \mathrm{gg}$ splittings in the parton shower.

As compared to the Meps@Nlo cross sections in Table 4, squared quark loops represent a correction of about 3%, both in the inclusive analysis and in the 1-jet bin. In the inclusive case, fixed-order and shower-improved predictions are in excellent agreement, as expected from the unitarity of the shower. In contrast, the Loop^2+PS simulation—which corresponds to the approach typically adopted in present experimental studies, where jet emission is entirely based on the shower approximation—underestimates the squared quark-loop cross section in the inclusive 1-jet bin by around 50%. Due to their LO α_s^2 and α_s^3 dependence, squared quark-loop corrections feature a QCD-scale dependence of 30–40%. The resummation-scale uncertainty of the Loop^2+PS simulation is close to zero in the inclusive case (due to unitarity), while in the 1-jet bin it is as large as 50%, due to the fact that the 1-jet bin is entirely filled by shower emissions.

Comparing Loop^2+PS predictions to the merged sample we observe that the matrix-element description of jet emission significantly increases the cross section, especially in the 1-jet bin. The QCD-scale uncertainty remains at 30–40% level, but resummation-scale variations change substantially: the 1-jet bin cross section becomes almost independent of the resummation scale, since, as a result of merging, 1-jet events are described in terms of matrix elements, and shower emissions induce only minor bin migrations. In contrast, in the inclusive analysis the merged simulation features a significantly higher resummation-scale dependence of approximately 15%, which can be attributed to unitarity violations induced by the merging procedure: the resummation-scale dependence that arises from the region below the merging cut, where 0-jet matrix elements are combined with the Sudakov suppression factor, is not compensated by an opposite dependence from above Q_cut, since the parton shower is superseded by 1-jet matrix elements in that region. We note that this kind of resummation-scale sensitivity is due to the LO nature of squared quark-loop merging and is strongly reduced in the case of NLO merging (cf. last column in Table 4). The fact that the Meps@Loop^2 cross section in the 1-jet bin is 30% below the fixed-order result can be attributed to the CKKW scale choice in the merging approach and is consistent with the size of renormalisation-scale variations. Finally, comparing the last two columns in Table 5,

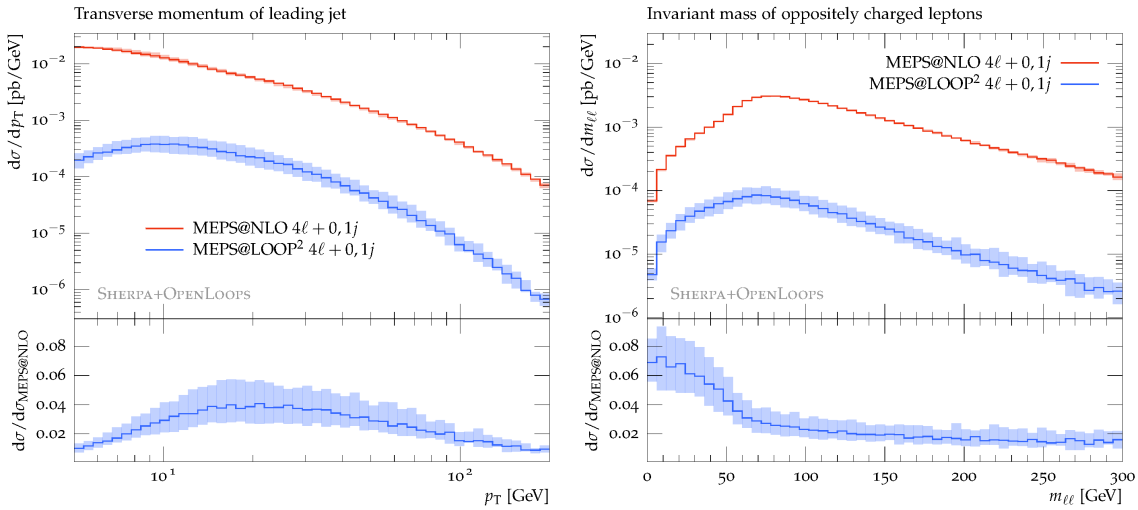

Figure 10: Comparison of merged squared quark-loop (blue) and NLO (red) predictions for $4\ell + 0, 1j$ production: transverse momentum of the leading jet (left) and invariant mass of the two charged leptons (right).

we observe that quark-induced channels account for roughly 1.5% and 30% of the squared quark-loop corrections in the 0- and 1-jet bins, respectively. This corresponds to about 0.5 permil and 1 percent of the total cross section in the respective jet bins. We note that the individual impact of quark channels at matrix-element or parton-shower level is significantly larger, i.e. a naive merging approach based on pure-gluon matrix elements plus a standard parton shower would lead to bigger deviations with respect to the MEPS@LOOP^2 results in Table 5.

Squared quark-loop corrections to differential observables are compared to NLO merged predictions in Fig. 10. As already found in Tables 4 and 5, their impact typically amounts to a few percent. Both for the leading-jet transverse momentum and for the dilepton invariant mass they feature a rather different kinematic dependence as compared to MEPS@NLO results. In the considered range their relative importance varies from one to seven percent, and the maximum lies in the region of small dilepton mass, which corresponds to the signal region of the $H \to WW^*$ analysis.

Merging effects are illustrated in the left plot of Fig. 11, where predictions from the inclusive squared quark-loop $gg \to 4\ell$ matrix element supplemented with a regular parton shower (LOOP^2+PS) are compared to the merged $pp \to 4\ell + 0, 1j$ simulation (MEPS@LOOP^2). The latter is decomposed into contributions from $4\ell + 0j$ and $4\ell + 1j$ matrix elements. In the region well below the merging cut, $Q_{\text{cut}} = 20$ GeV, merged predictions are dominated by 0-jet matrix elements and agree almost perfectly with the LOOP^2+PS curve. The agreement remains better than 10% up to $p_T \sim Q_{\text{cut}}$, where the MEPS@LOOP^2 sample is characterised by the transition from the 0-jet to the 1-jet matrix-element regime. This supports the use of the 0-jet plus shower approximation up to the merging scale. Starting from $p_T \gtrsim 40$ GeV, where 1-jet matrix elements dominate and render MEPS@LOOP^2 predictions more reliable, the parton-shower results feature a sizable deficit and are also strongly sensitive to the resummation scale.

Setting the resummation scale equal to the default scale (3.6), we found that the slight excess of the parton shower at $p_T \sim Q_{\text{cut}}$ propagates to higher transverse mo-

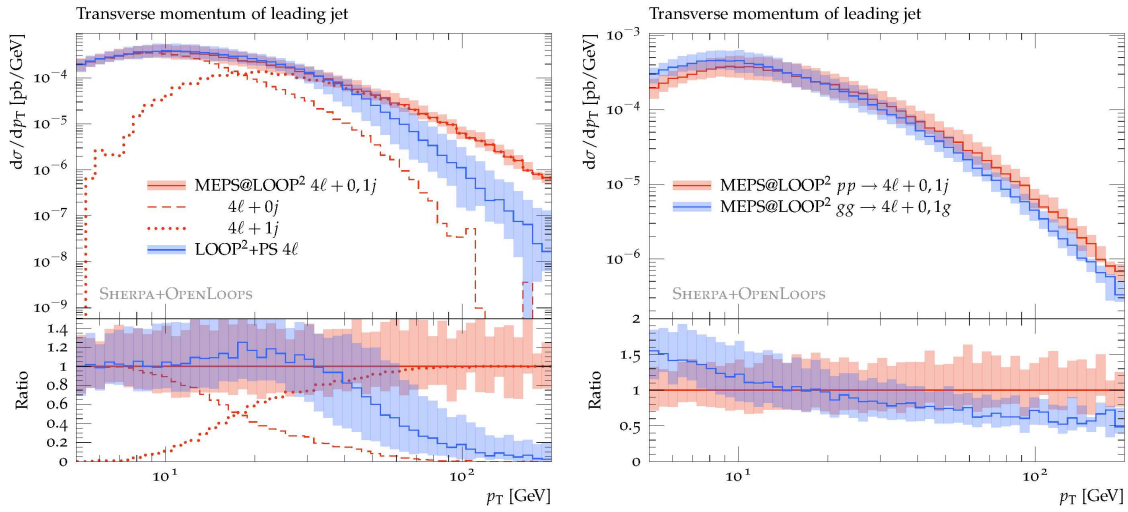

Figure 11: Squared quark-loop corrections to the leading-jet p_T-distribution: (a) a simulation based on 4ℓ matrix elements plus parton shower (blue) is compared to complete merged predictions (red solid). The latter are split into the contributions from $4\ell + 0j$ (red dashed) and $4\ell + 1j$ (red dotted) matrix elements; (b) full merged predictions (red) are compared to a corresponding simulation involving only gluon contributions (blue). Uncertainty bands correspond to the combination (in quadrature) of QCD- and resummation-scale variations.

menta reaching up to 40% at $p_T \gtrsim 100$ GeV. In order to avoid such an unnatural parton-shower excess at high p_T, and a corresponding excess in the Sudakov suppression at low p_T, as anticipated in Section 3.4.1 we decided to evaluate squared quark-loop contributions using a smaller resummation scale, $\mu_Q = \mu_0/2$. Of course the small value of μ_Q amplifies the natural deficit of the shower at large p_T and yields a quite small LOOP^2+PS cross section in the 1-jet bin (cf. Table 5). However this side-effect is compensated by 1-jet matrix elements in the MEPS@LOOP^2 simulation. The bands describe the total scale uncertainty, obtained by adding QCD- and resummation-scale variations in quadrature. Apart from the suppressed high-p_T tail of the LOOP^2+PS distribution, we find a rather constant uncertainty of about 30%.

The right plot in Fig. 11 illustrates the impact of quark-channel contributions on the leading-jet p_T-distribution. Plotted are full MEPS@LOOP^2 results and corresponding predictions involving only gg-induced matrix elements and g $\to$ gg shower splittings. As is clearly visible from the ratio plot, the quark channels enhance hard-jet emissions and induce a related Sudakov suppression at low p_T. The resulting distortion in the jet-p_T distribution amounts to $\pm 50\%$. When looking at Table 5, such opposite behaviour in the hard and soft regions explains why the quark-channel contribution reaches 30% in the 1-jet bin but goes down to 1.5% in the inclusive case.

Jet-veto and jet-binning effects on squared quark-loop contributions are shown in Fig. 12, where the integrated cross sections in the exclusive 0-jet bin ($p_T < p_T^{\max}$) and in the inclusive 1-jet bin ($p_T > p_T^{\min}$) are plotted as a function of $p_T^{\max}$ and $p_T^{\min}$. In the 0-jet bin, apart from the minor excess around 30 GeV, LOOP^2+PS predictions agree quite well with MEPS@LOOP^2 ones for any jet-veto scale up to 100 GeV. The corresponding scale uncertainties are in the 20–40% range. As in Table 5, MEPS@LOOP^2 uncertainties tend to be larger in the inclusive limit. Fixed-order gg $\to 4\ell$ contributions are inherently inclusive and independent of $p_T^{\max}$. Comparing them to the MEPS@LOOP^2

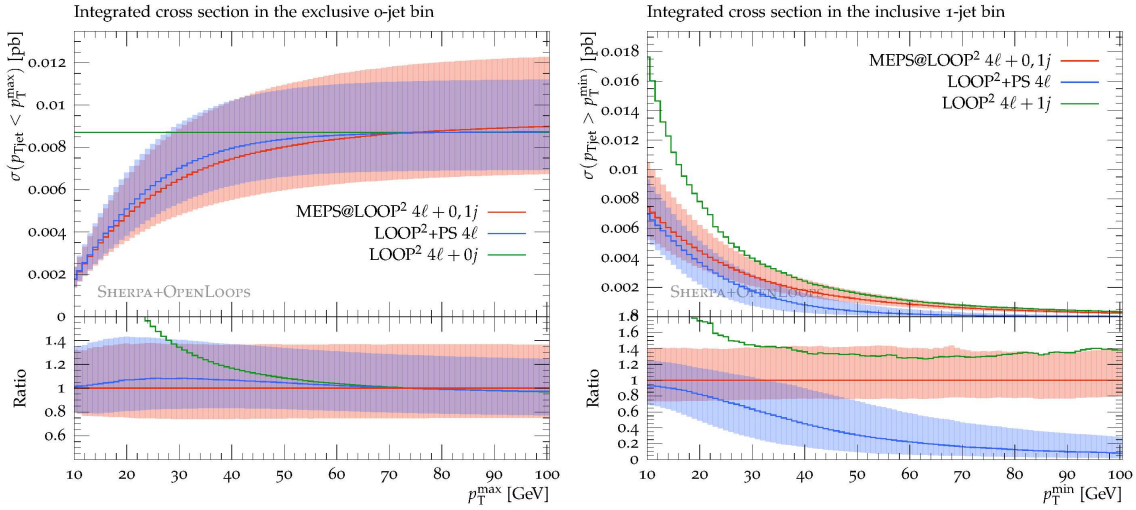

Figure 12: Integrated squared quark-loop cross sections in the exclusive 0-jet bin (left) and in the inclusive 1-jet bin (right) as a function of the respective transverse-momentum bounds, $p_{\mathrm{T}}^{\mathrm{max}}$ and $p_{\mathrm{T}}^{\mathrm{min}}$. Fixed-order LOOP^2 $4\ell\,(+1j)$ results (green) are compared to LOOP^2+PS 4ℓ (blue) and MEPS@LOOP^2 $4\ell + 0, 1j$ (red) simulations. Uncertainty bands correspond to QCD-scale variations combined with resummation-scale variations in quadrature.

and LOOP^2+PS curves we observe that jet-veto scales of 25–30 GeV, as those used in the experimental H $\to$ WW* analyses, correspond to a moderate cross-section suppression of approximately 30%. In this regime the parton shower should provide a sufficiently reliable resummation of Sudakov logarithms.

The right plot of Fig. 12 compares fixed-order, shower-improved and merged predictions in the inclusive 1-jet bin. For a jet threshold of 30 GeV, the various approximations agree only marginally within the respective errors, while higher and smaller values of $p_{\mathrm{T}}^{\mathrm{min}}$ lead to very large discrepancies. As compared to MEPS@LOOP^2 predictions, at large p_{T} we observe a dramatic deficit of the shower approximation, while the fixed-order squared quark-loop calculation yields a rather constant 40% excess as in Table 5. The resummation of Sudakov logarithms becomes relevant only for transverse-momentum thresholds below 30 GeV, where the excess of the fixed-order prediction grows up to 150% at 10 GeV.

3.5 ATLAS and CMS H$\to$WW* analyses in the 0- and 1-jet bins

In this section we study the irreducible four-lepton background to the ATLAS [126] and CMS [127] $H \to \mathrm{WW}^* \to \mu^+\nu_\mu \mathrm{e}^-\bar{\nu}_\mathrm{e}$ analyses at 8 TeV. We restrict ourselves to the exclusive 0- and 1-jet bins, which contain the bulk of the four-lepton background associated with diboson production, and focus on opposite-flavour $\mu^+\nu_\mu \mathrm{e}^-\bar{\nu}_\mathrm{e}$+jets final states, which provide the highest sensitivity to the Higgs-boson signal. Technically, within the automated SHERPA+OPENLOOPS framework, the simulation of $\ell\nu\ell\nu$+jets production with same lepton flavour is almost equivalent to the opposite-flavour case. Also for what concerns QCD corrections and uncertainties we do not expect any important difference between opposite- and same-flavour channels.

In the following we apply the cuts listed in Appendix B.2, which correspond to the ATLAS [126] and CMS [127] analyses at 8 TeV. Let us remind that the two experiments employ different definitions of the WW transverse mass, reported in eq. (B.6), and different anti-k_T jet radii. Note also that ATLAS employs a lower transverse-momentum threshold for central jets. After a pre-selection, which basically requires two hard leptons and large missing energy, two complementary selections based on $p_{T,\ell\ell'}$, $\Delta\phi_{\ell\ell'}$, $m_{\ell\ell'}$ and m_T, are used to define a signal and a control region. The latter is exploited to normalise WW-background simulations to data. Separate analyses are performed in the 0-, 1-, and 2-jet bins in order to improve the sensitivity to the Higgs-boson signal and the data-driven normalisation of the various background components.

In Section 3.5.1 we investigate kinematic distributions that are relevant for the experimental selection after pre-selection cuts. In Section 3.5.2 we consider the control and signal regions and discuss the observables that are exploited in the final stage of the Higgs analyses, namely the WW transverse mass and the dilepton invariant mass. Finally, in Section 3.5.3 we present predictions for the 0- and 1-jet bin cross sections in the signal and control regions, as well as uncertainties associated with variations of renormalisation, factorisation, resummation, and merging scales.

For each observable we present results for the ATLAS and CMS analyses in the exclusive 0- and 1-jet bins and, to provide insights into the convergence of the perturbative expansion and the size of Sudakov logarithms in jet bins, we compare NLO, MC@NLO, MEPS@NLO and squared quark-loop predictions. As discussed in Section 3.3, in NLO predictions for the 0- and 1-jet bins we always include the corresponding number of jets at matrix-element level. In contrast, MC@NLO results refer as usual to a single simulation of inclusive $\mu^+\nu_\mu e^-\bar{\nu}_e$ production, which is NLO accurate in the 0-jet bin and only LO accurate in the 1-jet bin. Only MEPS@NLO predictions are consistently matched to the parton shower and NLO accurate in both jet bins.

3.5.1 Kinematic distributions after pre-selection cuts

In Figures 13–15 we present jet and lepton observables after pre-selection cuts. The curves for MEPS@NLO, MC@NLO, NLO, and MEPS@LOOP^2 correspond to the central scale choice (3.6). The middle and lower panels show relative MC@NLO and NLO deviations from MEPS@NLO, and squared quark-loop contributions normalised to the central MEPS@NLO result. Scale-variation bands are shown only for MEPS@LOOP^2 and MEPS@NLO. In the latter case, renormalisation- and factorisation-scale variations $\Delta_{\rm QCD}$ (red band), resummation-scale variations $\Delta_{\rm res}$ (blue band), and their combination in quadrature $\Delta_{\rm tot} = (\Delta^2_{\rm QCD} + \Delta^2_{\rm res})^{1/2}$ (yellow band), are displayed as colour-additive regions. The various band regions assume different colours corresponding to the various possible overlaps. The band boundary, corresponding to variations δ in the range $\Delta_{\rm QCD}, \Delta_{\rm res} < \delta < \Delta_{\rm tot}$, is yellow. Orange areas appear in kinematic regions dominated by QCD-scale variations ($\Delta_{\rm res} < \delta < \Delta_{\rm QCD}$), while green areas reflect dominant resummation-scale variations ($\Delta_{\rm QCD} < \delta < \Delta_{\rm res}$), and the central band area ($\delta < \Delta_{\rm res}, \Delta_{\rm QCD}$), where all three colours overlap, is brown. Note that scale-variation bands are somewhat distorted by statistical fluctuations, which tend to increase in the tails of some distributions.

Before splitting the event sample into exclusive jet bins, in Fig. 13 we show the

transverse momenta of the hardest (upper plots) and second-hardest (lower plots) jet. Here all NLO curves correspond to $4\ell + 1$ jet production. In the case of the first jet, MC@NLO predictions are only LO accurate and significantly underestimate the tail of the p_{T} distribution. On the other hand, NLO predictions feature a 20% excess at high p_{T}. As already observed in Fig. 8.a, this behaviour can be explained by the fact that the scale (3.6) used in the fixed-order calculation does not adapt to the transverse momentum of the jet.

In the case of the second-jet p_{T}, NLO and MEPS@NLO results are both only LO accurate, and the shape differences at large p_{T} are more pronounced but qualitatively similar as for the first jet. The excess of the NLO distribution below 10 GeV reveals the presence of the infrared singularity at $p_{\mathrm{T}} \to 0$. The MC@NLO prediction for the second jet is entirely based on the shower approximation. It remains low over the entire spectrum, and above 30 GeV the deficit starts to be considerable.

The increase of MEPS@NLO scale variations from a few percent for the first jet to 10% for the second one, is due to the transition from NLO to LO accuracy. The abundance of orange and brown areas in the MEPS@NLO bands indicates that the uncertainty tends to be dominated by QCD-scale variations. Green band areas, which correspond to larger resummation-scale uncertainties, show up less frequently and only in the leading-jet p_{T} distribution. Even in the small-p_{T} region, where Sudakov logarithms have the highest possible impact, QCD- and resummation-scale variations do not exceed 10%. This suggests that subleading-logarithmic corrections beyond the MEPS@NLO accuracy should be rather modest.

Squared quark-loop corrections range from 1 to 6 percent and feature a more pronounced dependence on the jet p_{T} as compared to the inclusive analysis (cf. Fig. 10). The largest effects arise around $p_{\mathrm{T}} \simeq 20$ GeV, which corresponds to the 0-jet bin of the $\mathrm{H} \to \mathrm{WW}^*$ analysis.

Let us now switch to leptonic observables in the exclusive 0- and 1-jet bins of the $\mathrm{H} \to \mathrm{WW}^*$ analyses. Distributions in the azimuthal dilepton separation $\Delta\phi_{\ell\ell'}$ and in the dilepton invariant mass $m_{\ell\ell'}$ are displayed in Figures 14 and 15. These observables play an important role for the description of the background acceptance and for the optimisation of the Higgs-boson sensitivity in the experimental analyses. The corresponding MEPS@NLO distributions are NLO accurate in both jet bins. This is very well reflected by the MEPS@NLO uncertainty bands, which do not exceed the few-percent level. Also here, resummation-scale variations tend to be slightly subdominant with respect to QCD-scale variations. Comparing NLO, MC@NLO and MEPS@NLO distributions in the 0-jet bin, where none of these approximations loses NLO accuracy, we find overall agreement at the few-percent level. In the 1-jet bin, the agreement between NLO and MEPS@NLO remains, as expected, quite good. Due to the lack of NLO accuracy, inclusive MC@NLO predictions feature the characteristic 10–15% deficit in the 1-jet bin, which is accompanied by minor shape distortions. Given the good agreement with NLO within the small uncertainty band, the shape of MEPS@NLO distributions seems to be very well under control.

In the 0-jet bin, MEPS@LOOP^2 corrections are very sensitive both to the azimuthal separation and to the invariant mass of the dilepton system. At small $\Delta\phi_{\ell\ell'}$ and $m_{\ell\ell'}$, which corresponds to the Higgs-signal region, they reach up to 8% and 6%, respectively. A similar but weaker sensitivity is visible also in the 1-jet bin.

Inspecting the transverse-momentum distributions of the harder and softer charged lepton (not shown here) we found that the various NLO corrections behave very similarly as for $\Delta\phi_{\ell\ell'}$ and $m_{\ell\ell'}$, while squared quark-loop corrections are less sensitive to the lepton-p_{T} and vary between 2% and 4% only.

3.5.2 Kinematic distributions in control and signal regions

We now turn to the control (C) and signal (S) regions of the experimental analyses (see Table 11) and discuss the distributions in the WW transverse mass, m_{T}, and in the dilepton invariant mass, $m_{\ell\ell'}$. These observables are sensitive to the Higgs-boson signal, and their shape permits to increase the signal-to-background discrimination in the final fit. Separate distributions for the exclusive 0- and 1-jet bins and for the two experiments are shown in Figures 16–18.

In the signal and control regions, as well as in both jet bins, the size of the various corrections and the MEPS@NLO uncertainties behave fairly similar to what observed at pre-selection level. The NLO, MC@NLO and MEPS@NLO distributions agree at few-percent level in the 0-jet bin, while in the 1-jet bin discrepancies between MC@NLO and MEPS@NLO on the 10–15% level and little MC@NLO shape distortions appear. The size of the corrections and the scale uncertainties for the two experimental analyses are qualitatively and quantitatively similar. Obviously, due to the different cuts, absolute background predictions for ATLAS and CMS behave differently. The shapes of MEPS@NLO distributions are again in excellent agreement with NLO, suggesting moderate Sudakov logarithms beyond NLO. This is consistent with the small scale uncertainty of the merged simulation.

Squared quark-loop corrections feature a nontrivial sensitivity to m_{T} and $m_{\ell\ell'}$, which varies depending on the experimental analysis, the selection region, and the jet bin. The largest squared quark-loop corrections arise in the 0-jet bin, at small $m_{\ell\ell'}$ and at large m_{T}. The corrections to the transverse-mass distribution start growing at $m_{\mathrm{T}} = 100$–150 GeV and for the ATLAS (CMS) analysis they reach 10-20%(5-10%) in the tail. The largest effects arise in the signal region and in the ATLAS analysis, which implements tighter $m_{\ell\ell'}$ and $\Delta\phi_{\ell\ell'}$ cuts. For what concerns the $m_{\ell\ell'}$ distribution, Fig. 18 shows that in the 0-jet bin of the CMS signal region squared quark-loop corrections behave similarly as in the inclusive case (cf. Fig. 10). The fact that the characteristic enhancement at small $m_{\ell\ell'}$ is not visible in the ATLAS signal region, is simply due to the cut on $m_{\ell\ell'}$ at 50 GeV. For what concerns the 1-jet bin, MEPS@LOOP^2 corrections are generally slightly smaller and less dependent on m_{T} and $m_{\ell\ell'}$.

3.5.3 Exclusive 0- and 1-jet bin cross sections in control and signal regions

A precise quantitative assessment of the various correction effects and residual uncertainties is provided in Tables 6 and 7, where we present exclusive 0- and 1-jet bin cross sections in the signal and control regions of the two experimental analyses. The NLO and MEPS@NLO predictions at the central scale differ by only 1.5–3% and 4–6% in the 0-jet and 1-jet bins, respectively. This confirms that the discrepancy of order 5% observed in the inclusive 0-jet bin (cf. Table 4) is due the NLO corrections to the first

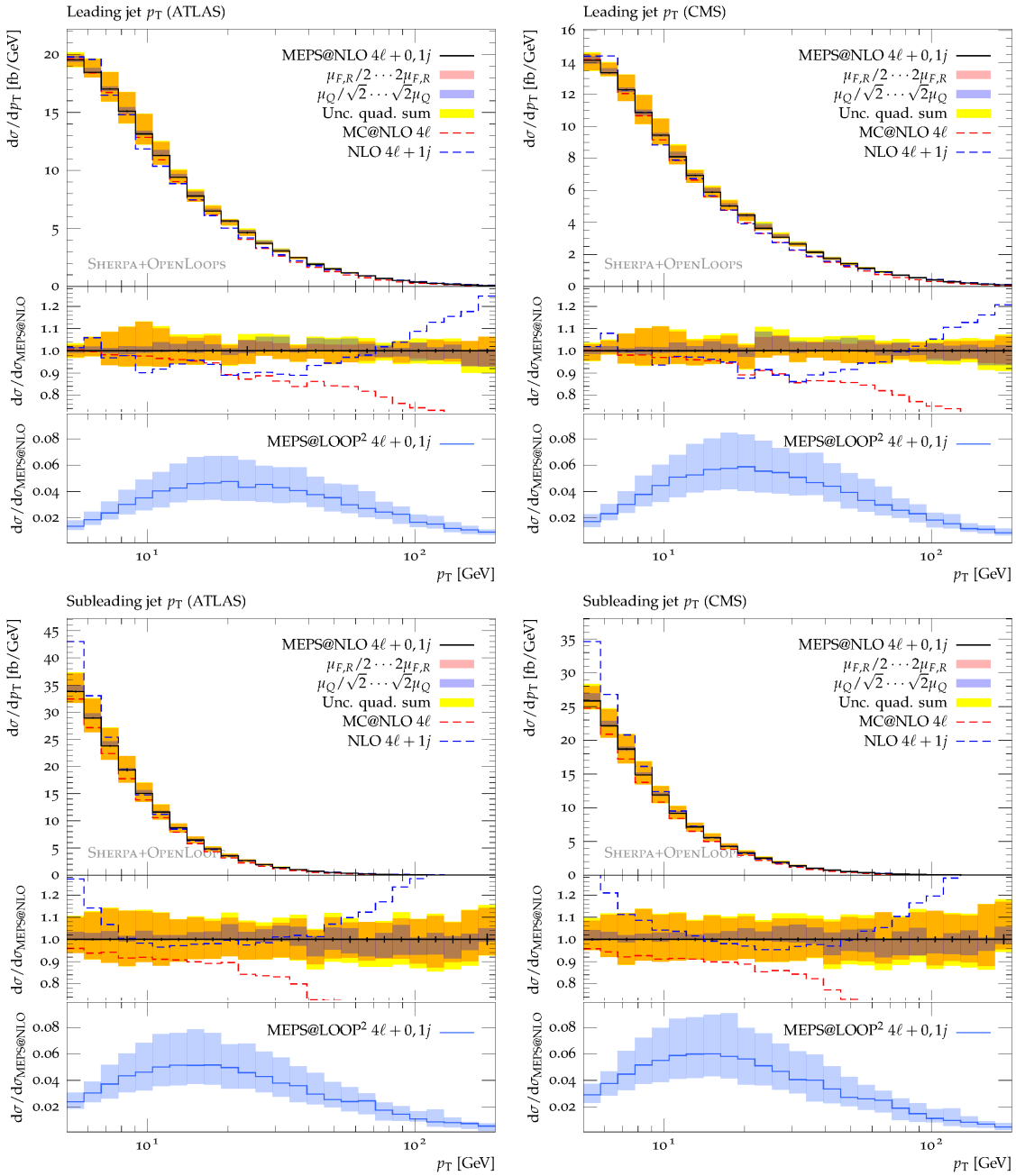

Figure 13: ATLAS (left) and CMS (right) analysis at 8 TeV after pre-selection cuts: transverse-momentum distributions of the first (top) and second (bottom) jet. MEPS@NLO (black solid), inclusive MC@NLO (red dashed), and NLO (blue dashed) predictions at the central scale. The ratio plots in the middle panels show relative uncertainties as well as MC@NLO and NLO deviations with respect to MEPS@NLO. The lower panels display relative MEPS@LOOP^2 corrections and uncertainties normalised to MEPS@NLO at the central scale. The factor-two variations of μ_R and μ_F (red band), and factor-$\sqrt{2}$ variations of μ_Q (blue band), are combined in quadrature (yellow band). Scale-variation bands are colour additive, i.e. yellow+blue=green, yellow+red=orange, and yellow+red+blue=brown.

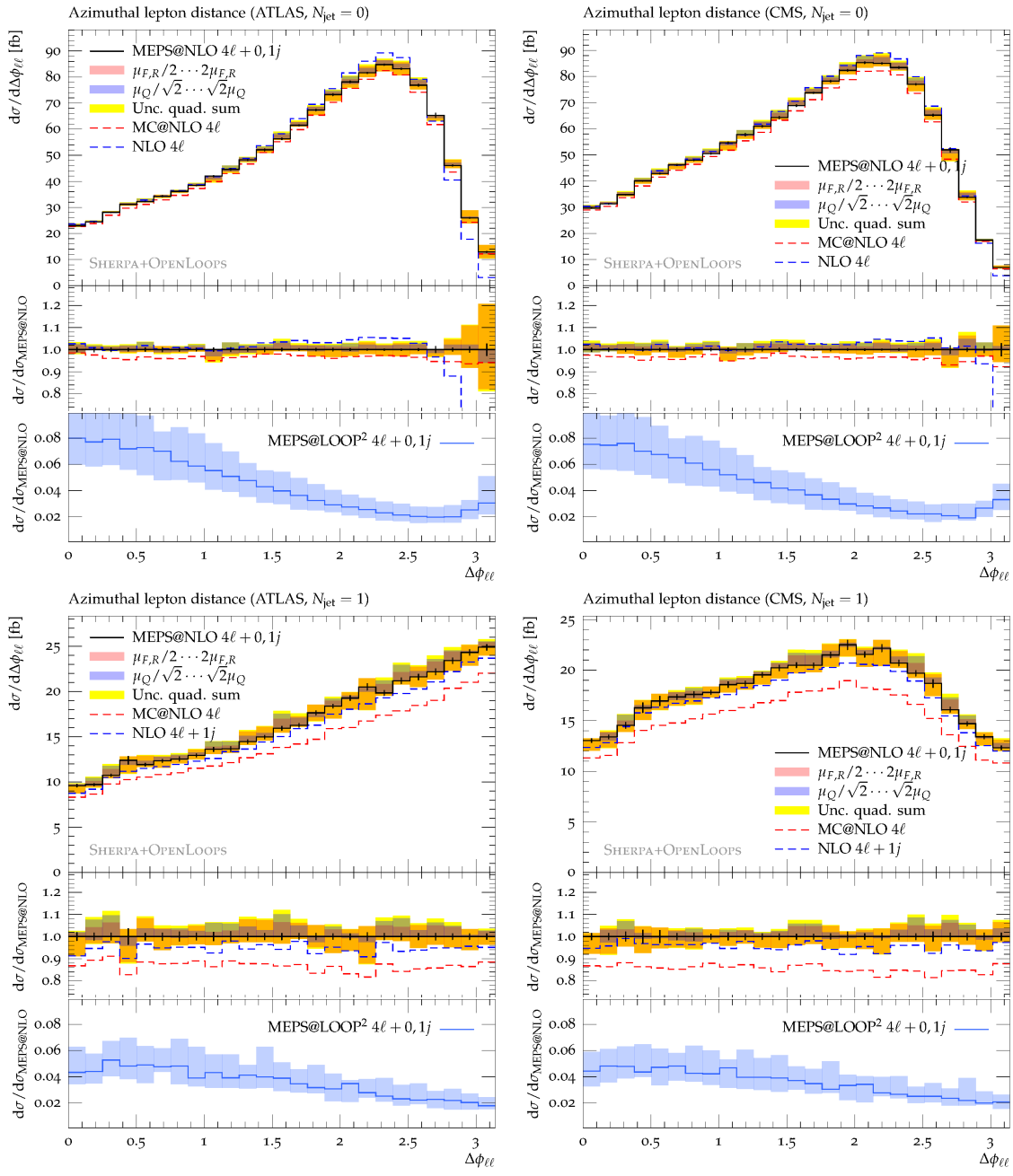

Figure 14: ATLAS (left) and CMS (right) analysis at 8 TeV after pre-selection cuts: azimuthal separation of the charged leptons in the 0-jet (top) and 1-jet (bottom) bins. Similar predictions and uncertainty bands as in Fig. 13.

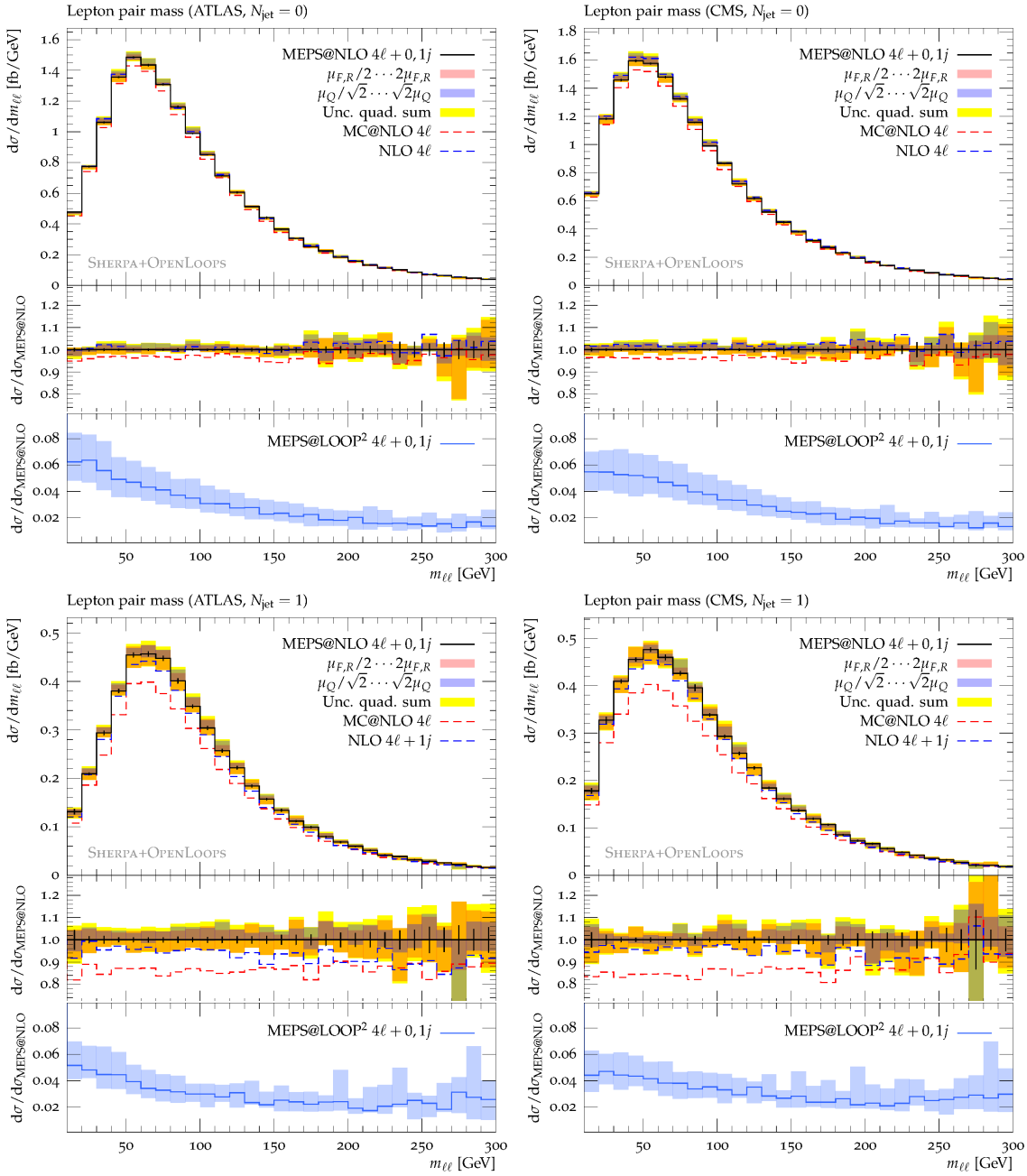

Figure 15: ATLAS (left) and CMS (right) analysis at 8 TeV after pre-selection cuts: dilepton invariant mass distribution in the 0-jet (top) and 1-jet (bottom) bins. Similar predictions and uncertainty bands as in Fig. 13.

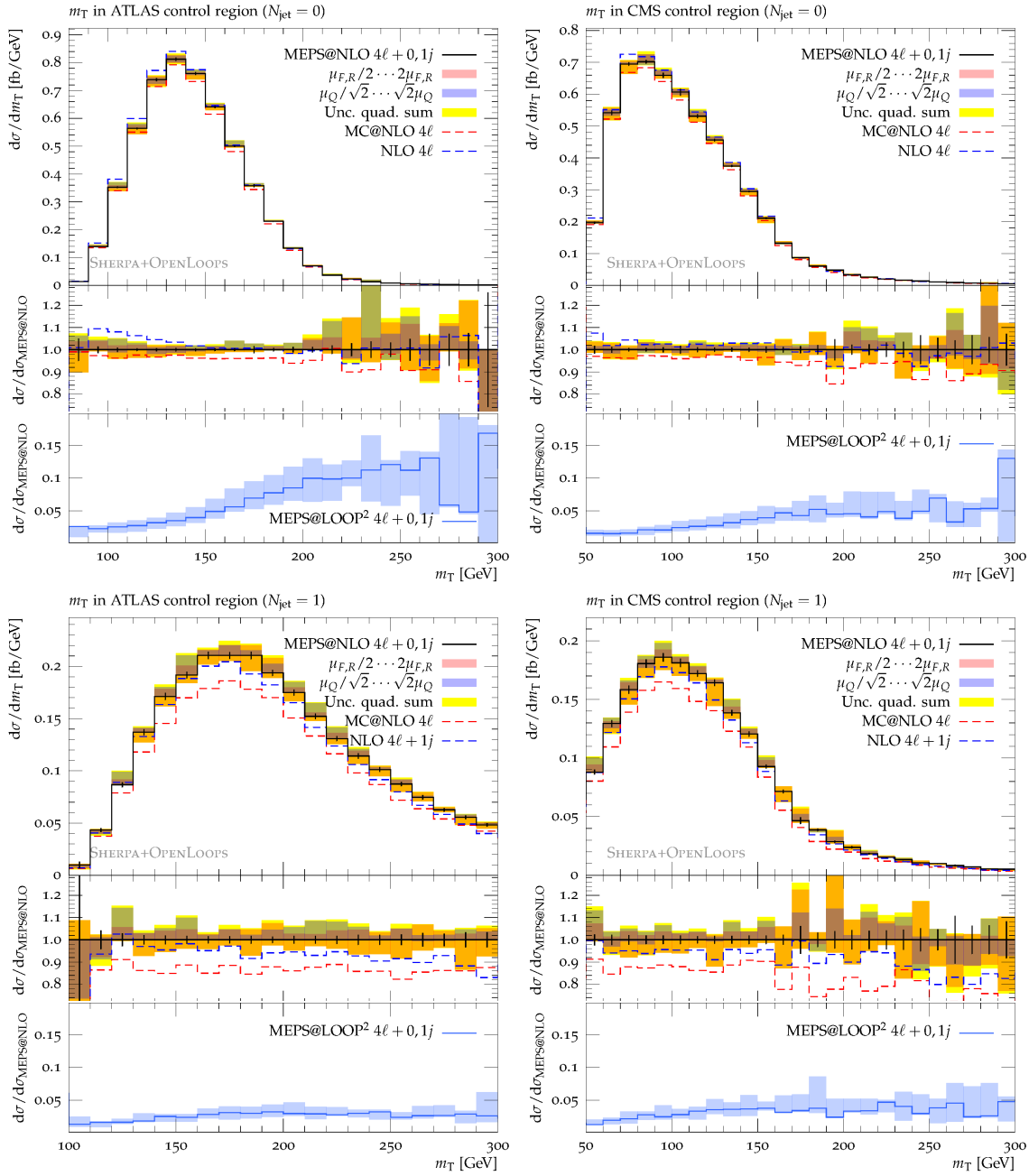

Figure 16: Control region of the ATLAS (left) and CMS (right) analysis at 8 TeV: transverse-mass distribution in the 0-jet (top) and 1-jet (bottom) bins. Similar predictions and uncertainty bands as in Fig. 13.

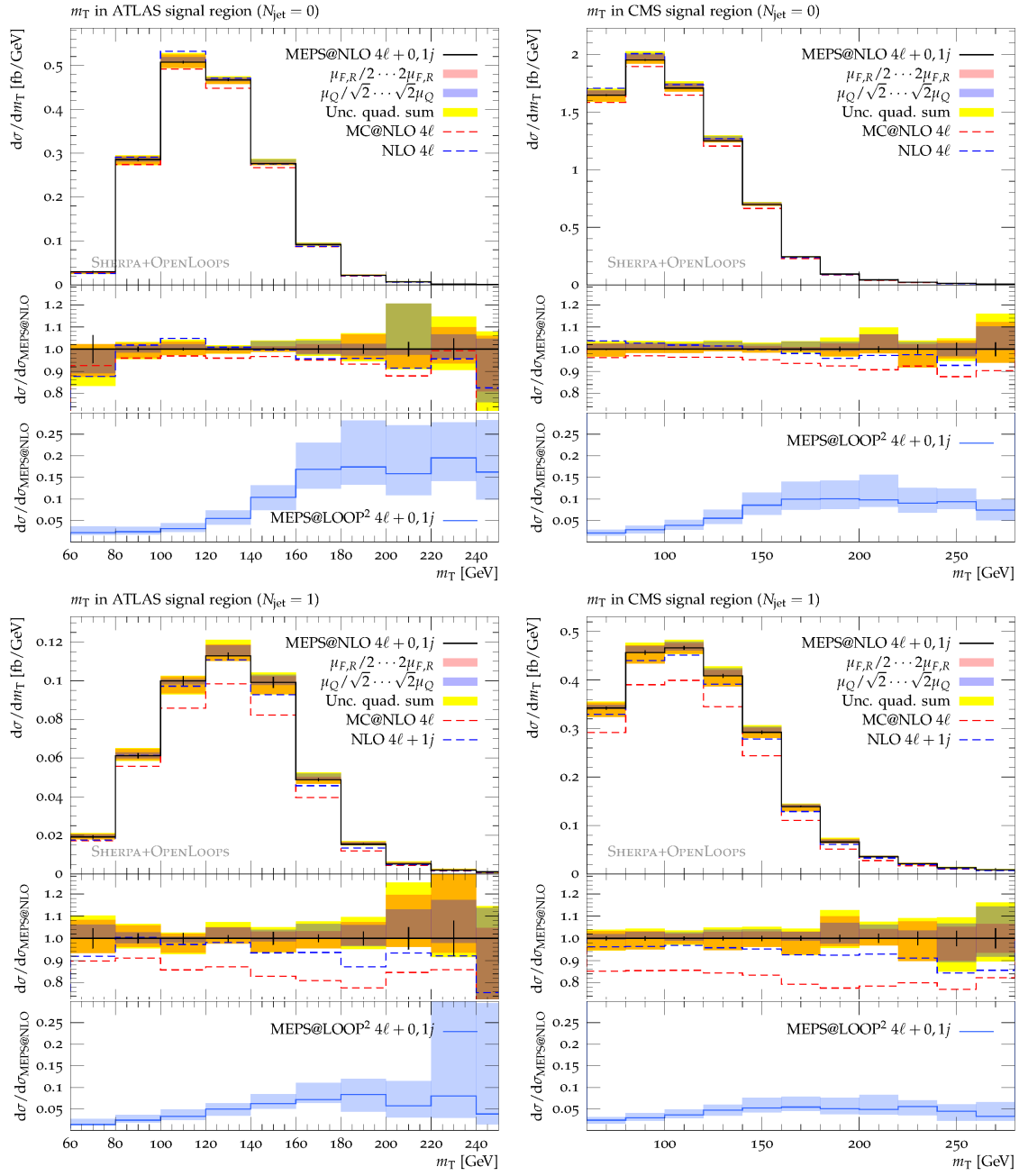

Figure 17: Signal region of the ATLAS (left) and CMS (right) analysis at 8 TeV: transverse-mass distribution in the 0-jet (top) and 1-jet (bottom) bins. Similar predictions and uncertainty bands as in Fig. 13.

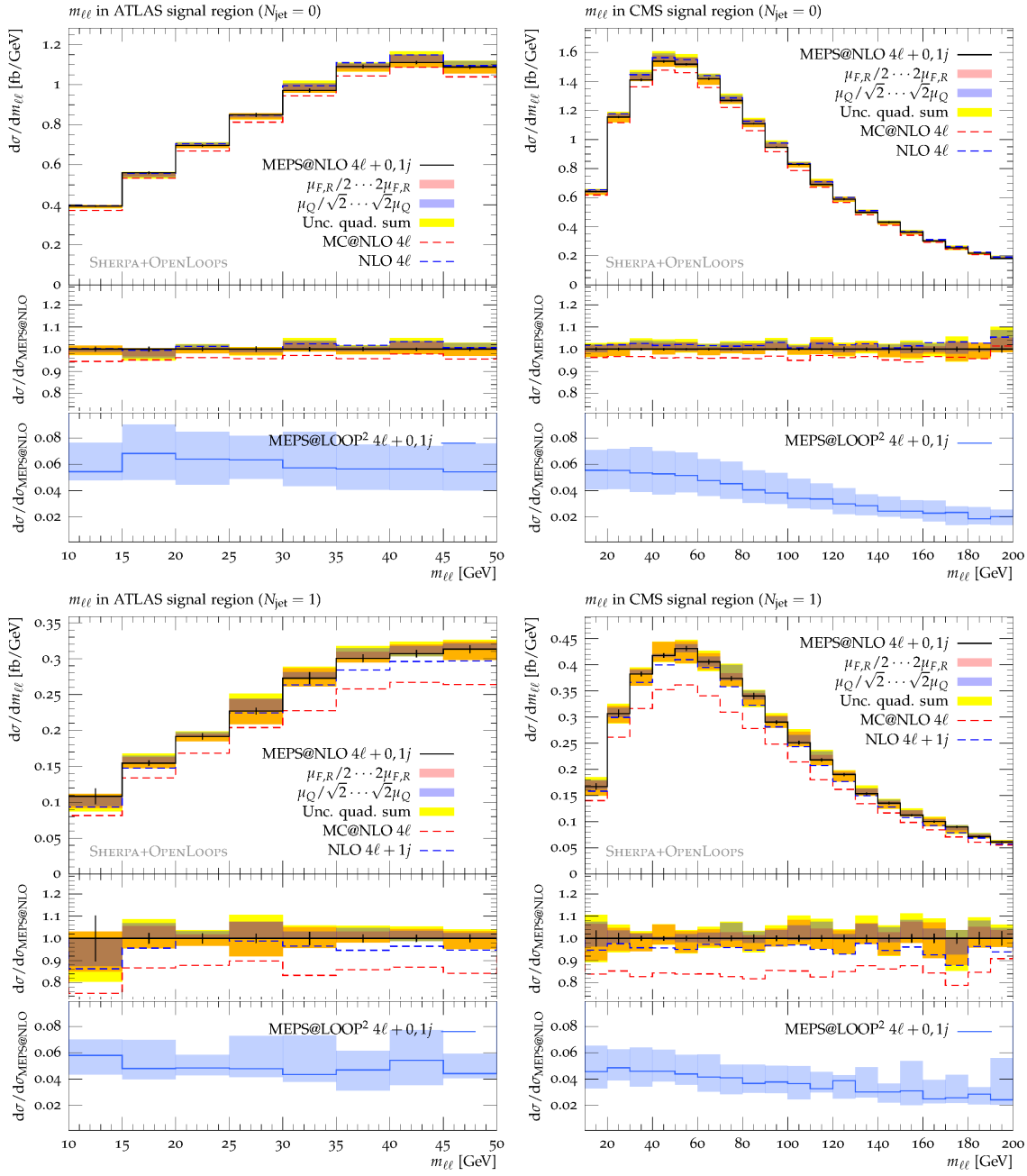

Figure 18: Signal region of the ATLAS (left) and CMS (right) analysis at 8 TeV: dilepton invariant-mass distribution in the 0-jet (top) and 1-jet (bottom) bins. Similar predictions and uncertainty bands as in Fig. 13.

0-jet bin	NLO $4\ell\,(+1j)$	MC@NLO 4ℓ	MEPS@NLO $4\ell+0,1j$	MEPS@LOOP^2 $4\ell+0,1j$
$\sigma_{\rm S}$ [fb]	$34.28(9)\ ^{+2.1\%}_{-1.6\%}$	$32.52(8)\ ^{+2.1\%\ +1.2\%}_{-0.8\%\ -0.7\%}$	$33.81(12)\ ^{+1.4\%\ +2.0\%\ +1.6\%}_{-2.2\%\ -0.4\%\ -1.7\%}$	$1.98(2)\ ^{+23\%\ \ +27\%}_{-16.5\%\ -20\%}$
$\sigma_{\rm C}$ [fb]	$55.76(9)\ ^{+2.0\%}_{-1.7\%}$	$52.28(9)\ ^{+1.4\%\ +1.4\%}_{-0.7\%\ -1.1\%}$	$54.18(15)\ ^{+1.4\%\ +2.5\%\ +1.7\%}_{-1.9\%\ -0.4\%\ -2.0\%}$	$2.41(2)\ ^{+22\%\ +27\%}_{-17\%\ -18\%}$
1-jet bin	NLO $4\ell\,(+1j)$	MC@NLO 4ℓ	MEPS@NLO $4\ell+0,1j$	MEPS@LOOP^2 $4\ell+0,1j$
$\sigma_{\rm S}$ [fb]	$8.99(4)\ ^{+4.9\%}_{-9.5\%}$	$8.02(4)\ ^{+8.5\%\ +0\%}_{-6.4\%\ -3.1\%}$	$9.37(9)\ ^{+2.6\%\ +2.5\%\ -0.1\%}_{-2.7\%\ -0.0\%\ -4.1\%}$	$0.46(1)\ ^{+40\%\ +2.2\%}_{-18\%\ -6.3\%}$
$\sigma_{\rm C}$ [fb]	$26.50(8)\ ^{+6.4\%}_{-12.5\%}$	$24.58(8)\ ^{+6.1\%\ +1.2\%}_{-6.5\%\ -3.0\%}$	$28.32(13)\ ^{+3.1\%\ +4.1\%\ +0.6\%}_{-4.7\%\ -0.0\%\ -2.7\%}$	$0.79(1)\ ^{+33\%\ +15\%}_{-20\%\ -7\%}$

Table 6: Exclusive 0- and 1-jet bin $\mu^+\nu_\mu e^-\bar{\nu}_e$+jets cross sections in the signal (S) and control (C) regions of the ATLAS analysis at 8 TeV. Fixed-order NLO results (with appropriate jet multiplicity) are compared to MC@NLO and MEPS@NLO predictions. Squared quark-loop contributions (MEPS@LOOP^2) are presented separately. Scale uncertainties are shown as $\sigma \pm \delta_{\rm QCD} \pm \delta_{\rm res} \pm \delta_{Q_{\rm cut}}$, where $\delta_{\rm QCD}$, $\delta_{\rm res}$ and $\delta_{Q_{\rm cut}}$ correspond respectively to variations of the QCD $(\mu_{\rm R}, \mu_{\rm F})$, resummation (μ_Q) and merging $(Q_{\rm cut})$ scales. Statistical errors are given in parenthesis.

0-jet bin	NLO $4\ell\,(+1j)$	MC@NLO 4ℓ	MEPS@NLO $4\ell+0,1j$	MEPS@LOOP^2 $4\ell+0,1j$
$\sigma_{\rm S}$ [fb]	$156.65(18)\ ^{+1.7\%}_{-1.6\%}$	$147.8(2)\ ^{+1.3\%\ +1.2\%}_{-0.6\%\ -1.0\%}$	$153.6(3)\ ^{+2.1\%\ +2.8\%\ +1.6\%}_{-1.9\%\ -0.0\%\ -2.2\%}$	$6.65(4)\ ^{+22\%\ +26\%}_{-17\%\ -18\%}$
$\sigma_{\rm C}$ [fb]	$59.26(15)\ ^{+1.3\%}_{-1.3\%}$	$55.92(11)\ ^{+0.8\%\ +0.5\%}_{-0.2\%\ -0.9\%}$	$58.06(21)\ ^{+2.1\%\ +2.2\%\ +1.5\%}_{-2.0\%\ -0.2\%\ -2.1\%}$	$1.47(2)\ ^{+26\%\ +28\%}_{-17\%\ -16\%}$
1-jet bin	NLO $4\ell\,(+1j)$	MC@NLO 4ℓ	MEPS@NLO $4\ell+0,1j$	MEPS@LOOP^2 $4\ell+0,1j$
$\sigma_{\rm S}$ [fb]	$43.01(9)\ ^{+3.3\%}_{-7.4\%}$	$37.87(9)\ ^{+7.6\%\ +0.9\%}_{-6.8\%\ -3.6\%}$	$44.99(18)\ ^{+2.5\%\ +2.9\%\ +0.5\%}_{-4.2\%\ -0.0\%\ -2.5\%}$	$1.83(2)\ ^{+34\%\ +6\%}_{-20\%\ -7\%}$
$\sigma_{\rm C}$ [fb]	$20.48(6)\ ^{+4.8\%}_{-10.3\%}$	$18.90(7)\ ^{+7.4\%\ +1.8\%}_{-7.3\%\ -3.3\%}$	$21.70(11)\ ^{+3.2\%\ +3.4\%\ +0.5\%}_{-4.1\%\ -0.0\%\ -1.6\%}$	$0.62(1)\ ^{+39\%\ +16\%}_{-16\%\ -6\%}$

Table 7: Exclusive 0- and 1-jet bin $\mu^+\nu_\mu e^-\bar{\nu}_e$+jets cross sections in the signal (S) and control (C) regions of the CMS analysis at 8 TeV. Similar predictions and conventions as in Table 6.

jet emission in MEPS@NLO. The differences between MC@NLO and MEPS@NLO in the exclusive 0- and 1-jet bins reach 2–4% and 13–16%, respectively, and the discrepancy in the 1-jet bin is consistent with the deficit of MC@NLO observed in differential distributions. Deviations between the NLO, MC@NLO and MEPS@NLO approximations are fairly similar in the various analyses and kinematic regions. As compared to corresponding results in Ref. [153], the various cross sections in Tables 6 and 7 differ by 1-5% and 1-10% in the 0- and 1-jet bins, respectively. These shifts are consistent with scale-variation uncertainties and can be attributed, as observed in Section 3.4.1, to the new scale choice (3.6) used in the present study.

Adding $(\mu_{\rm R}, \mu_{\rm F})$, μ_Q and $Q_{\rm cut}$ variations in quadrature, the combined scale uncertainties of MEPS@NLO cross-section predictions do not exceed 4(6)% in the 0(1)-jet bin. Renormalisation-, factorisation-, resummation- and merging-scale variations yield comparable contributions to the total scale uncertainty. In the 1-jet bin, MEPS@NLO results feature smaller QCD-scale variations as compared to the NLO calculation. This can be attributed to the variation of extra α_s terms originating from the shower and to the CKKW scale choice in MEPS@NLO.

Comparing NLO and MC@NLO cross sections in the 0-jet bin we observe a rather constant difference of about 5% that can be interpreted as the contribution from resummed Sudakov logarithms beyond NLO. On the one hand, this indicates that matching to the parton shower is essential in order to reach few-percent precision. On the other hand, the rather mild impact of Sudakov resummation suggests that subleading Sudakov logarithms beyond the shower approximation should not have a large impact on the $\rm H \to WW^*$ analysis. This is confirmed by the fact that resummation-scale variations of MC@NLO and MEPS@NLO cross sections do not exceed 2-3% in the various jet bins.

The relative impact of squared quark-loop corrections as compared to merged NLO predictions varies between 2.5 and 6 percent, depending on the experiment, the kinematic selection region, and the jet bin. In both experiments and jet bins, squared quark-loop effects increase when moving from control to signal regions. In the case of CMS they grow from 2-3.5% to 4%, while in the ATLAS analysis, due to the tighter $\Delta\phi_{\ell\ell'}$ and $m_{\ell\ell'}$ cuts, the effects are more pronounced and increase from 3-4.5% to 5-6%. Squared quark-loop uncertainties amount to 30–40%, similarly as for the inclusive analysis of Section 3.4.

Detailed results for the ratios of signal- to control-region cross sections, $\sigma_{\rm S}/\sigma_{\rm C}$, are presented in Table 8. These ratios and the related uncertainties play an important role for the extrapolation from control to signal regions in data-driven WW-background determinations. In addition to NLO, MC@NLO and MEPS@NLO ratios, we also present results obtained from the combination of NLO and squared quark-loop merging. These latter are denoted as MEPS@NLO+LOOP^2 and represent our best predictions. Upper and lower variations are obtained from corresponding QCD-, resummation- and merging-scale variations in Tables 6 and 7. More precisely, the ratios are evaluated at different scales,

$$R(\xi_{\rm R}, \xi_{\rm F}, \xi_Q, Q_{\rm cut}) = \frac{\sigma_{\rm S}(\xi_{\rm R}\mu_{\rm R}, \xi_{\rm F}\mu_{\rm F}, \xi_Q\mu_Q, Q_{\rm cut})}{\sigma_{\rm C}(\xi_{\rm R}\mu_{\rm R}, \xi_{\rm F}\mu_{\rm F}, \xi_Q\mu_Q, Q_{\rm cut})}, \tag{3.7}$$

applying correlated variations in signal and control regions. As shown in Table 8, due

ATLAS	NLO $4\ell\,(+1j)$	MC@NLO 4ℓ	MEPS@NLO $4\ell + 0,1j$	MEPS@NLO+LOOP^2	$\delta_{S/C}$
σ_S/σ_C 0-jet	$0.615\ ^{-0.1\%}_{-0.1\%}$	$0.622\ ^{-0.7\%\ +0.2\%}_{+0.1\%\ -0.4\%}$	$0.624\ ^{+0\%\ \ +0.5\%\ +0.1\%}_{-0.3\%\ -0\%\ \ -0.3\%}$	$0.632\ ^{-0.3\%\ +0.2\%}_{+0.5\%\ +0.3\%}$	1.3%
σ_S/σ_C 1-jet	$0.339\ ^{+1.4\%}_{-3.4\%}$	$0.326\ ^{-2.3\%\ +1.2\%}_{-0.1\%\ +0.1\%}$	$0.331\ ^{+0.5\%\ +1.5\%\ +0.7\%}_{-2.1\%\ -0\%\ \ +1.4\%}$	$0.338\ ^{-0.4\%\ +1.8\%}_{-1.8\%\ +0.1\%}$	2.1%
CMS	NLO $4\ell\,(+1j)$	MC@NLO 4ℓ	MEPS@NLO $4\ell + 0,1j$	MEPS@NLO+LOOP^2	$\delta_{S/C}$
σ_S/σ_C 0-jet	$2.64\ ^{-0.4\%}_{+0.3\%}$	$2.64\ ^{-0.5\%\ -0.7\%}_{+0.4\%\ +0.1\%}$	$2.65\ ^{+0\%\ \ -0.6\%\ -0.1\%}_{-0.1\%\ -0.2\%\ +0.1\%}$	$2.69\ ^{-0.2\%\ -0.9\%}_{+0.2\%\ +0.2\%}$	1.5%
σ_S/σ_C 1-jet	$2.10\ ^{+1.4\%}_{-3.2\%}$	$2.00\ ^{-0.2\%\ +0.9\%}_{-0.5\%\ +0.3\%}$	$2.07\ ^{+0.7\%\ +0.5\%\ +0\%}_{+0.1\%\ -0\%\ \ +0.9\%}$	$2.10\ ^{+0.4\%\ +0.7\%}_{+0.4\%\ +0.1\%}$	1.4%

Table 8: Ratios of signal- to control-region cross sections in the 0- and 1-jet bins of the two experimental analyses. Fixed-order NLO results (with appropriate jet multiplicity) are compared to MC@NLO and MEPS@NLO predictions. The combination of NLO and squared quark-loop merged results, denoted as MEPS@NLO+LOOP^2, represents the best prediction. Upper and lower variations are obtained from corresponding QCD-, resummation- and merging-scale uncertainties in Tables 6 and 7 assuming correlated σ_S and σ_C variations. The last column shows the relative difference between MEPS@NLO and full MEPS@NLO+LOOP^2 predictions, which corresponds to the shift induced by squared quark-loop corrections.

to almost complete cancellations between σ_S and σ_C variations this naive approach results in typical σ_S/σ_C shifts at the sub-percent level, which cannot be regarded as realistic estimates of uncertainties due to unknown higher-order corrections. On the other hand, applying uncorrelated scale variations to σ_S and σ_C would tend to overestimate σ_S/σ_C uncertainties. This becomes clear if one considers the ideal limit of identical signal and control regions, where $\sigma_S/\sigma_C = 1$ and the uncertainty must vanish. The reason why scale variations are not adequate to quantify theory uncertainties associated to the extrapolation between different kinematic regions, is that they tend to shift the normalisation of scattering amplitudes without altering their kinematic dependence. In this respect, squared quark-loop corrections provide much more useful insights into kinematic effects associated to higher-order corrections. As shown in the last column of Table 8, their impact on the σ_S/σ_C ratios amounts to $\delta_{S/C} \simeq 1.5\%$, which largely exceeds the typical scale variations of MEPS@NLO and MEPS@NLO+LOOP^2 predictions. This is due to the fact that squared quark-loop effects induce genuine NNLO kinematic distortions. Moreover, squared quark loops constitute only a subset of the full NNLO corrections, and their impact on σ_S/σ_C can be assumed to be quantitatively similar to the still unknown NNLO contributions. With other words, the $\delta_{S/C}$ shifts in Table 8 can be considered as a realistic estimate of the MEPS@NLO+LOOP^2 uncertainty of the σ_S/σ_C ratios.

3.6 Conclusions

In this chapter we have presented the first results for the simulation of hadronic four-lepton plus jets production using the novel MEPS@NLO multi-jet merging technology at NLO, and including also NNLO contributions from squared quark loops. This was also the first phenomenological application of the fully automated approach provided by the combination of the SHERPA Monte Carlo with the OPENLOOPS generator of one-loop amplitudes. The OPENLOOPS algorithm is based on a new numerical approach

for the recursive construction of cut-opened loop diagrams, which allows for a very fast evaluation of NLO matrix elements within the Standard Model. For the calculation of tensor integrals it relies on the COLLIER library, which implements the numerically stable reduction algorithms by Denner–Dittmaier.

Four-lepton plus jets final states are of large topical interest due to their implications on ongoing Higgs-boson studies, and in this chapter we discussed detailed predictions for the ATLAS and CMS $H \to WW^*$ analyses at 8 TeV in the 0- and 1-jet bins. For a thorough description of four-lepton production—including off-shell vector-boson effects, non-resonant topologies, and related interferences—the complex-mass scheme was applied. The use of exclusive jet bins, which is mandatory in order to suppress the background provided by top-quark production and decay, introduces potentially large theory uncertainties and ultimately requires a very robust modelling of jet-production properties and related errors. This requires an NLO accurate description of jet radiation, with a careful assessment of the uncertainties stemming from the usual perturbative scale variations, but also a resummation of Sudakov logarithms arising from jet vetoes, and an analysis of the related uncertainties. The MEPS@NLO approach as implemented in SHERPA allows to carry out this program in a fully automated way. In particular, the resummation of Sudakov logarithms is effectively implemented by matching NLO matrix elements to the SHERPA parton shower, and uncertainties related to subleading Sudakov logarithms beyond the shower approximation can be assessed through resummation-scale variations.

In order to allow precise statements on the impact of jet vetoes and jet binning on the $H \to WW^*$ analyses, we merged matrix elements for four leptons plus up to one jet at NLO accuracy, thus arriving at a simulation of the WW background with unprecedented accuracy. As a result of this calculation the residual scale uncertainty is reduced to about 5% on observables related to the hardest jet up to transverse momenta of the order of 200 GeV. We note large differences of up to 40% with respect to NLO or MC@NLO simulations of the $pp \to 4\ell$ process. These differences typically manifest themselves in regions of large jet momentum, where inclusive NLO or MC@NLO predictions are bound to undershoot the QCD activity. This of course is even more pronounced for observables related to the subleading jet. As compared to NLO predictions for $pp \to 4\ell + 1j$, apart from a generally good agreement, multi-jet merging yields quite significant corrections in the tail of the first-jet p_T distribution. This effect can be attributed to the fact that the CKKW-merging approach implemented in MEPS@NLO consistently adapts the renormalisation scale to the transverse momenta of the emitted jets.

The multi-jet merging thus improves the quality and stability of the perturbative series, especially for jet observables. This holds for hard phase-space regions as well as for low jet momentum, where fixed-order calculations start to suffer from the missing resummation of potentially large logarithms. Studying the case of a jet veto, we found that for veto scales around 30(10) GeV resummation effects beyond NLO amount to about 5(20)% of the vetoed four-lepton cross section. Their relatively small magnitude can be attributed to the limited size of Sudakov logarithms but also to cancellations between leading- and subleading-logarithmic contributions.

In the case of the inclusive four-lepton cross section, as a result of NLO corrections to the first QCD emission, MEPS@NLO results turn out to be 9% higher as compared

to inclusive NLO and MC@NLO calculations. Moreover, the CKKW scale choice in MEPS@NLO leads to a milder renormalisation-scale dependence as compared to fixed-order and MC@NLO predictions evaluated at a scale of the order of the W-boson transverse mass. For leptonic observables in the exclusive jet bins of the $H \to WW^*$ analyses, typically NLO and MC@NLO provide a good description in the 0-jet bin, but MC@NLO exhibits a deficit of about 10–15% in the 1-jet bin. It is notable that, for these observables, we find scale uncertainties of only a few percent in our best NLO prediction, i.e. MEPS@NLO. Our analysis indicates that also the uncertainties related to the choice of resummation scale, and thus due to the parton shower and its resummation properties, are at the percent level. This is consistent with the observation that Sudakov logarithms beyond NLO have a rather moderate impact on the jet bins of the $H \to WW^*$ analysis, and it suggests that subleading logarithmic corrections beyond the MEPS@NLO accuracy should not be important.

In addition to matched and merged NLO simulations, we also studied NNLO contributions to four-lepton plus jets production that emerge through squared one-loop amplitudes involving closed quark loops. These contributions are dominated by the gluon–gluon channel, which is enhanced by the high partonic flux. Moreover, squared quark-loop corrections are quite sensitive to lepton–lepton correlations that play a key role in the $H \to WW^*$ analysis. Their relative impact as compared to the full NLO contributions amounts to only 3% in the inclusive case, but grows to 6% if Higgs-analysis cuts are applied. This corresponds to about 50% of the Higgs-boson signal in the relevant analysis regions, which calls for a detailed theoretical investigation of squared quark-loop terms and of their nontrivial kinematic features. To this end we considered all relevant squared quark-loop matrix elements for the production of four leptons plus up to one jet. In particular, in addition to the well-known gluon–gluon fusion contributions, for the first time we also studied the $gq \to 4\ell + q$, $g\bar{q} \to 4\ell + \bar{q}$, and $q\bar{q} \to 4\ell + g$ channels. In order to merge squared quark-loop corrections with different jet multiplicity, we extended the tree-level multi-jet merging in SHERPA to include also purely loop-induced processes. In this context, the inclusion of the quark channels is indispensable for a consistent merging. The net effect of this merging is a visibly harder tail in the jet transverse momentum distribution with respect to the one obtained from only taking the leading $gg \to 4\ell$ contribution supplemented with the parton shower. To the best of our knowledge this has not been studied before.

In the $H \to WW^*$ analyses, the size of squared quark-loop corrections turns out to vary from 2% to 6%, depending on the jet bin, on the kinematic region and on the experiment. The merging approach is especially important in order to guarantee decent predictions in the 1-jet bin. Due to their nontrivial kinematic dependence, squared quark-loop corrections have a quite significant impact on the extrapolation of the WW-background from control to signal regions. The resulting shift in the relevant cross-section ratios is of order 1.5%, and we argued that these corrections can be regarded as a realistic estimate of unknown higher-order effects in the data-driven determination of the WW-background at the LHC.

At this point it should be stressed that all the studies reported here are at the parton level only, with one choice of PDFs to facilitate a clear and direct comparison between the different approaches. It is, however, a straightforward exercise to allow for different PDFs or to go from the parton to the hadron level in a simulation like the

one presented here: switching on hadronisation and the underlying event modelling allows to assess these effects automatically. As a further extension, it is possible to extend the current study to cases including all possible other four-lepton final states or to study in more detail the two-jet bin of the simulation, which is crucial for the vector-boson fusion signatures. For the latter case, the simulation could be extended to the production of four leptons in association with two jets at next-to leading order accuracy. It can be anticipated that a simulation on the level presented here would certainly lead to a similarly relevant reduction of QCD uncertainties for this important channel of Higgs physics.

Chapter 4

A unified NLO description of top-pair and associated Wt production

4.1 Introduction

Top quarks are the heaviest known fundamental particles, and the precise theoretical understanding of their production and decay mechanism, within or beyond the Standard Model, has deep implications on countless aspects of the LHC physics programme. At the LHC, top quarks are mainly produced as $t\bar{t}$ pairs and via single-top production in the t-channel or in the associated Wt mode. At 8 TeV these latter single-top channels amount to 40% and 10% of the $t\bar{t}$ cross section, respectively. In spite of their smaller cross sections, they play an important role as direct probes of top-quark weak interactions and of their flavour structure. The separation of top-production into individual top-pair and single-top contributions poses non-trivial experimental and theoretical challenges, which are mainly due to the similarity among the final states associated with the various mechanisms of top-production and decay. In particular, the definition of $t\bar{t}$ and Wt production involves notorious and quite subtle theoretical issues [172].

In the five-flavour (5F) scheme, Wt production proceeds via b-quark induced partonic channels like $gb \to W^-W^+b$, and the presence of a single b-jet represents a clearly distinctive feature with respect to $W^+W^-b\bar{b}$ final states associated with $t\bar{t}$ production. However, beyond LO this separation ceases to exist, since $gg \to W^+W^-b\bar{b}$ enters also the next-to-leading order (NLO) corrections to Wt production. The resulting $t\bar{t}$ contamination represents a huge NLO correction, which jeopardises the perturbative convergence of the Wt cross section in the 5F scheme. To circumvent this problem within the 5F scheme, various approaches have been proposed aimed at subtracting the contribution of a second top resonance in $pp \to Wt + X$ [172]. However, these prescriptions either break gauge invariance or are not applicable to a realistic experimental setup. Moreover they neglect the quantum interference between top-pair and single-top contributions.

A theoretically more rigorous approach consists of adopting the four-flavour (4F) scheme, where initial-state b-quarks result from gluons via explicit $g \to b\bar{b}$ splittings.

In this framework, the process $pp \to W^+W^-b\bar{b} + X$ provides a unified description of Wt and $t\bar{t}$ production [173], and the presence of the $t\bar{t}$–Wt interference at LO stabilises the perturbative expansion. In the 4F scheme, treating finite-top-width effects in the complex-mass scheme [156] ensures a consistent off-shell continuation of top-quark propagators and allows one to include double-, single-, and non-resonant contributions to $pp \to W^+W^-b\bar{b} + X$ with all relevant interferences. Moreover, the ill-defined separation of top-pair and Wt production can be replaced by a gauge-invariant separation of $pp \to W^+W^-b\bar{b}$ into its narrow-top-width limit, which corresponds to on-shell top-pair production and decay, and a finite-width remainder that includes off-shell $t\bar{t}$ effects as well as single-top and non-resonant contributions plus related interferences.

The presence of four final-state particles and intermediate top-quark resonances render the simulation of $W^+W^-b\bar{b}$ production quite challenging beyond LO. First NLO calculations with massless b-quarks have been presented in [123, 158, 174]. For $W^+W^-b\bar{b}$ production with two hard b-jets, apart from a few noticeable exceptions [158], most observables turn out to be completely dominated by the on-shell $t\bar{t}$ contribution. In phase-space regions with unresolved b-quarks, the importance of off-shell and single-top contributions is expected to increase quite substantially. However, due to the presence of collinear singularities, such regions are not accessible in the massless b-quark approximation of [123, 158, 174]. To fill this gap, in this chapter we present a complete NLO $W^+W^-b\bar{b}$ calculation including off-shell W-boson decays and massive b-quarks in the 4F scheme. A similar calculation has been presented very recently in [175]. These simulations provide NLO accurate $W^+W^-b\bar{b}$ predictions in the full phase space and allow one to investigate, for the first time, top-pair and single-top production in presence of jet vetoes or jet bins, such as in the case of the $H \to W^+W^-$ analysis. An important advantage of NLO $W^+W^-b\bar{b}$ predictions in the 4F scheme is that they provide a fully differential NLO description of both final-state b-jets and a correspondingly accurate modelling of jet vetoes, while in the 5F scheme a similar level of accuracy for spectator b-quarks in Wt production would require an NNLO calculation.

4.2 Technical tools and ingredients of the calculation

We will focus on NLO predictions for $pp \to \nu_e e^+ \mu^- \bar{\nu}_\mu b\bar{b}$, which comprises $t\bar{t}$ production and decay in the opposite-flavour di-lepton channel. For brevity we will denote this reaction as $W^+W^-b\bar{b}$ production, keeping in mind that all off-shell and interference effects related to the $\nu_e e^+ \mu^- \bar{\nu}_\mu$ final state are consistently handled in the complex-mass scheme [156], where finite-width effects are systematically absorbed in the imaginary part of the renormalised pole mass. The complex-mass scheme is used also for the off-shell continuation of top-quark resonances [158]. Examples of tree diagrams involving two, one and no top-quark resonances are illustrated in Figures 19 and 20. The second diagram in Fig. 19 is the 4F-scheme analogon of t-channel $gb \to tW^-$ production in the 5F scheme, and the initial-state $g \to b\bar{b}$ splitting is related to the b-quark parton distribution in 5F PDFs. At NLO we include the full set of tree, one-loop and real-emission diagrams that contribute to $\nu_e e^+ \mu^- \bar{\nu}_\mu b\bar{b}$ production without applying

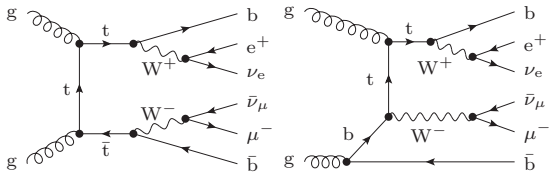

Figure 19: Representative $t\bar{t}$-like (left) and Wt-like (right) tree diagrams.

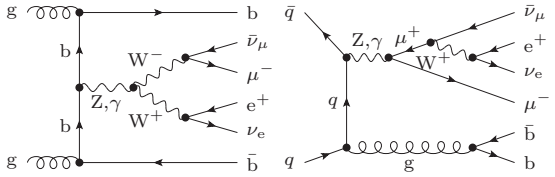

Figure 20: Representative tree topologies without top resonances and with two (left) or only one (right) resonant W-boson.

any approximation. In particular non-resonant $Z/\gamma \to \nu_e e^+ \mu^- \bar{\nu}_\mu$ sub-topologies like in the second diagram of Fig. 20 are included also in the virtual and real corrections. The bottom- and top-quark masses are renormalised in the on-shell scheme, and their contributions are retained everywhere.

The entire calculation has been performed with highly flexible and automated NLO programs, and the high complexity resulting from the presence of multiple top- and W-resonances, as well as from the wide spectrum of involved scales, render $pp \to W^+W^-b\bar{b}$ an excellent technical benchmark to test the performance of the employed tools. To evaluate tree, virtual, and real-emission amplitudes, we employed OpenLoops [43], a new one-loop generator that will become public in the next future. The OpenLoops program is based on a novel numerical recursion, which is formulated in terms of loop-momentum polynomials called "open loops" and allows for a fast evaluation of scattering amplitudes with many external particles. It uses the Collier library [154] for the numerically stable evaluation of tensor integrals [31,32] and scalar integrals [103]. Together with [58,59], the present study is one of the very first applications of OpenLoops. Phase-space integration and infrared subtractions are performed with an in-house NLO Monte-Carlo framework [57], which is interfaced with OpenLoops and provides full automation along the entire chain of operations that are required for NLO calculations. This tool is applicable to any Standard-Model process at NLO QCD. Infrared singularities are handled with dipole subtraction [73,74], and since collinear $g \to b\bar{b}$ splittings are regularised by the finite b-quark mass, corresponding subtraction terms are not included. The phase-space integrator is based on the adaptive multi-channel technique [124] and implements dedicated channels for the dipole subtraction terms, which improve the convergence, especially for multi-resonance processes. Multiple scale variations in a single run are also supported. This tool has been validated in several NLO processes and, in combination with OpenLoops and Collier, it is also applicable to NNLO calculations [61]. The correctness of the results is supported by various checks: OpenLoops has been validated against an independent in-house generator for more than hundred partonic processes, including $W^+W^-b\bar{b}$ production with massless b-quarks and various processes with massive heavy-quarks. For

the process at hand we checked the cancellation of infrared and ultraviolet singularities. The correctness of phase-space integration and dipole subtraction was tested by means of a second calculation based on OpenLoops in combination with Sherpa [53, 168] and Amegic++ [166].

4.3 Input parameters, cuts and jet definition

In the following, we present NLO results for $\mathrm{W^+W^-b\bar{b}}$ production at the 8 TeV LHC. For the heavy-quark and gauge-boson masses we use

$$\begin{aligned} m_\mathrm{t} = 173.2\ \mathrm{GeV}, \quad m_\mathrm{b} = 4.75\ \mathrm{GeV}, \\ M_\mathrm{Z} = 91.1876\ \mathrm{GeV}, \quad M_\mathrm{W} = 80.385\ \mathrm{GeV}. \end{aligned} \tag{4.1}$$

The electroweak coupling is derived from the Fermi constant, $G_\mu = 1.16637{\times}10^{-5}\mathrm{GeV}^{-2}$, in the G_μ-scheme,

$$\alpha = \frac{\sqrt{2}}{\pi} G_\mu M_\mathrm{W}^2 \left(1 - \frac{M_\mathrm{W}^2}{M_\mathrm{Z}^2}\right). \tag{4.2}$$

In the complex-mass scheme the electroweak mixing angle is evaluated as

$$\cos^2\theta_\mathrm{w} = \frac{M_\mathrm{W}^2 - \mathrm{i}\Gamma\mathrm{W} M_\mathrm{W}}{M_\mathrm{Z}^2 - \mathrm{i}\Gamma\mathrm{Z} M_\mathrm{Z}}, \tag{4.3}$$

and for the widths we use the NLO QCD values

$$\Gamma\mathrm{W} = 2.09530\ \mathrm{GeV}, \qquad \Gamma\mathrm{Z} = 2.50479\ \mathrm{GeV} \tag{4.4}$$

everywhere, i.e. for LO as well as for NLO matrix elements. The Higgs-boson mass and width are set to $M_\mathrm{H} = 126$ GeV and $\Gamma\mathrm{H} = 4.21$ MeV. To guarantee consistent top-decay branching fractions, matrix elements and top-width input parameters must be taken at the same perturbative order. For the LO and NLO top-quark widths we use the values

$$\Gamma_\mathrm{t}^\mathrm{LO} = 1.47451\ \mathrm{GeV}, \qquad \Gamma_\mathrm{t}^\mathrm{NLO} = 1.34264\ \mathrm{GeV}, \tag{4.5}$$

which are computed with massive b-quarks and off-shell W-bosons [176]. Consistently with the use of massive b-quarks we employ 4F parton distributions. Specifically, at NLO the LHApdf implementation of the 4F NNPDF2.3 parton distributions [177] and the corresponding running strong coupling are used. More precisely, we use a reference set[1] that is obtained from a variable-flavour set with $\alpha_s^{(5)}(M_\mathrm{Z}) = 0.118$ via inverse 5F evolution down to $\mu_\mathrm{F} = m_\mathrm{b}$ and subsequent upward evolution with four active flavours. Since the NNPDF2.3 release does not include LO parton distributions, for LO predictions we adopt the NNPDF21_lo_nf4_100 4F set, which corresponds to a reference strong-coupling value $\alpha_s^{(5)}(M_\mathrm{Z}) = 0.119$. While the 4F running of α_s misses heavy-quark-loop effects, corresponding $\mathcal{O}(\alpha_s)$ contributions are consistently included in the virtual corrections via zero-momentum subtraction of the top- and bottom-quark loops in the renormalisation of α_s.

[1] NNPDF23_nlo_FFN_NF4_as_0118

To investigate NLO corrections to top-pair and Wt production we select events with two oppositely charged leptons, $\ell = e^+, \mu^-$, with

$$p_{T,\ell} \;>\; 20\,\text{GeV}, \quad |\eta_\ell| < 2.5, \quad p_{T,\text{miss}} > 20\text{GeV}, \tag{4.6}$$

where $p_{T,\text{miss}}$ is obtained from the vector sum of the neutrinos' transverse momenta. Final-state QCD partons, including b-quarks, are recombined into IR-safe jets using the anti-k_T algorithm [171] with jet-resolution parameter $R = 0.4$. Events are categorised according to the total number, N_j, of jets with $p_T > 30$ GeV and $|\eta| < 2.5$ and the number of b-jets, N_b, within the same acceptance region. We classify as b-jet any jet involving at least a b-quark, which includes also the case of collimated $b\bar{b}$ pairs resulting from the splitting of energetic gluons. In fixed-order calculations the implementation of this b-jet definition is possible only in presence of massive b-quarks, while collimated $b\bar{b}$ pairs must be handled as "gluon-jets" in the massless case.

4.4 Scale choice for top-pair and single-top production

In order to isolate off-shell and single-top effects associated with the finite top-quark width (FtW) we decompose the differential $W^+W^-b\bar{b}$ cross section as

$$d\sigma_{W^+W^-b\bar{b}} = d\sigma_{t\bar{t}} + d\sigma^{\text{FtW}}_{W^+W^-b\bar{b}}, \tag{4.7}$$

where the $t\bar{t}$ term represents on-shell top-pair production and decay in spin-correlated narrow-width approximation. The $t\bar{t}$ contribution is obtained from the numerical extrapolation of the full $W^+W^-b\bar{b}$ cross section in the narrow-width limit [158],

$$d\sigma_{t\bar{t}} = \lim_{\Gamma_t \to 0} d\tilde{\sigma}_{W^+W^-b\bar{b}}(\Gamma_t), \tag{4.8}$$

with

$$d\tilde{\sigma}_{W^+W^-b\bar{b}}(\Gamma_t) = \left(\frac{\Gamma_t}{\Gamma_t^{\text{phys}}}\right)^2 d\sigma_{W^+W^-b\bar{b}}(\Gamma_t), \tag{4.9}$$

where the factor $(\Gamma_t/\Gamma_t^{\text{phys}})^2$ compensates the $1/\Gamma_t^2$ scaling of the cross section in such a way that top-decay branching fractions remain constant when $\Gamma_t \to 0$. By construction the $d\sigma^{\text{FtW}}_{W^+W^-b\bar{b}}$ remainder in (4.7) contains all finite-top-width effects, including off-shell $t\bar{t}$ production as well as single-top and non-resonant contributions.

As compared to $W^+W^-b\bar{b}$ production with two hard b-jets, the fully inclusive case involves a much wider spectrum of scales, ranging from m_b to $m_{t\bar{t}}$. This renders theoretical calculations significantly more involved. In particular, given that the $t\bar{t}$ and Wt contributions to $W^+W^-b\bar{b}$ production are characterised by very different scales, it is a priori not clear if a conventional QCD scale choice can ensure a perturbatively stable description of both contributions. For $t\bar{t}$ production, a scale of the order of the geometric average of the top-quark transverse energies,

$$\mu^2_{t\bar{t}} = E_{T,t}E_{T,\bar{t}} \quad \text{with} \quad E^2_{T,i} = m_i^2 + p^2_{T,i}, \tag{4.10}$$

is known to ensure a good perturbative convergence [158]. In the case of the single-top $\mathrm{W^-t}$ contribution one has to deal with two sub-processes: a collinear $g \to \mathrm{b\bar{b}}$ initial-state splitting followed by $\mathrm{gb} \to \mathrm{W^-t}$ hard scattering.[1] The respective characteristic scales are the bottom- and the top-quark transverse energies, $E_{\mathrm{T,b}} \ll E_{\mathrm{T,t}}$, and a QCD scale of type

$$\mu^2_{\mathrm{tW^-}} = E_{\mathrm{T,t}} E_{\mathrm{T,\bar{b}}} \tag{4.11}$$

should represent an appropriate choice, since

$$\alpha_s^2(\mu^2_{\mathrm{tW^-}}) \simeq \alpha_s(E^2_{\mathrm{T,t}})\alpha_s(E^2_{\mathrm{T,\bar{b}}}) \tag{4.12}$$

guarantees that the α_s factor associated with the collinear $\mathrm{g} \to \mathrm{b\bar{b}}$ splitting is effectively evaluated at the scale $E_{\mathrm{T,b}}$, similarly as in the resummation of initial-state b-quark emissions in the evolution of 5F PDFs. Vice versa, using a global QCD scale of the order m_t might underestimate the single-top component of $\mathrm{pp} \to \mathrm{W^+W^-b\bar{b}}$ by up to a factor $\alpha_s(m_\mathrm{b})/\alpha_s(m_\mathrm{t}) \sim 2$ at LO. This would be compensated by $\ln(m_\mathrm{b})$-enhanced higher-order corrections, resulting in a poor perturbative convergence. For an accurate description of the single-top contribution, the above considerations motivate a dynamic QCD scale that interpolates between (4.10) and (4.11) in $\mathrm{t\bar{t}}$- and Wt-dominated regions, respectively. Such a scale can be defined as

$$\mu^2_{\mathrm{WWbb}} = \mu_{\mathrm{W^+b}}\, \mu_{\mathrm{W^-\bar{b}}}, \tag{4.13}$$

with

$$\mu_{\mathrm{Wb}} = P_\mathrm{b}(p_\mathrm{W}, p_\mathrm{b})\, E_{\mathrm{T,b}} + P_\mathrm{t}(p_\mathrm{W}, p_\mathrm{b})\, E_{\mathrm{T,t}}, \tag{4.14}$$

where Wb represents either $\mathrm{W^+b}$ or $\mathrm{W^-\bar{b}}$, and the functions P_b and $P_\mathrm{t} = 1 - P_\mathrm{b}$ describe the probability that the b-quark of a given Wb pair arises from an initial-state $\mathrm{g} \to \mathrm{b\bar{b}}$ splitting or from a $\mathrm{t} \to \mathrm{Wb}$ decay, respectively. Their approximate functional form can be obtained from the leading matrix-element singularities associated with the $\mathrm{g} \to \mathrm{b\bar{b}}$ and $\mathrm{t} \to \mathrm{Wb}$ sub-processes,[2]

$$\chi_\mathrm{b} = \frac{m_\mathrm{t}^2}{E^2_{\mathrm{T,b}}}, \quad \chi_\mathrm{t} = \frac{m_\mathrm{t}^4}{[(p_\mathrm{W} + p_\mathrm{b})^2 - m_\mathrm{t}^2]^2 + \Gamma_\mathrm{t}^2 m_\mathrm{t}^2}, \tag{4.15}$$

by requiring that $P_\mathrm{b}/P_\mathrm{t} \propto \chi_\mathrm{b}/\chi_\mathrm{t}$. This yields

$$P_\mathrm{b} = 1 - P_\mathrm{t} = \frac{\chi_\mathrm{b}}{\chi_\mathrm{b} + R\chi_\mathrm{t}}. \tag{4.16}$$

The constant R can be derived from the condition

$$\int \mathrm{d}\sigma^{\mathrm{FtW}}_{\mathrm{W^+W^-\,b\bar{b}}} = \int \mathrm{d}\Phi\, [1 - P_\mathrm{t}(\Phi) P_\mathrm{t}(\Phi)]\, \frac{\mathrm{d}\sigma_{\mathrm{W^+W^-\,b\bar{b}}}}{\mathrm{d}\Phi}, \tag{4.17}$$

i.e. by requiring that finite-top-width corrections to the inclusive $\mathrm{W^+W^-b\bar{b}}$ cross section correspond to the contribution from non-$\mathrm{t\bar{t}}$ events according to the probability

[1] The charge-conjugate channels are implicitly understood.

[2] The χ_b and χ_t distributions are defined as dimensionless functions by introducing m_t-terms in the numerator. This convention is however irrelevant, since the probabilities resulting from (4.16) and (4.17) are independent of the normalisation of χ_b and χ_t.

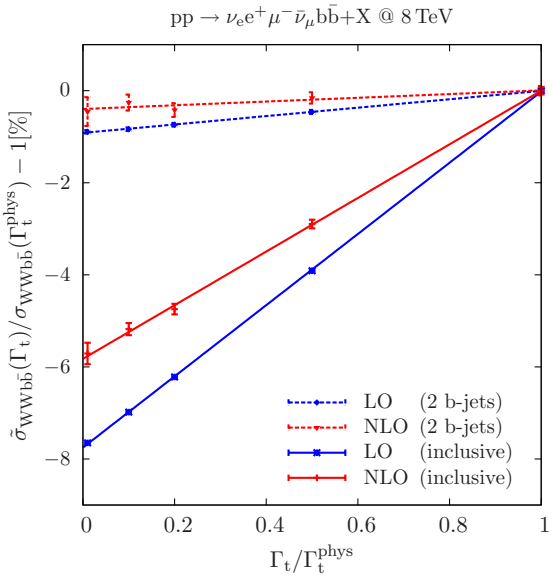

Figure 21: Numerical extrapolation of the LO and NLO $W^+W^-b\bar{b}$ cross section with leptonic cuts in the narrow-top-width limit, $\Gamma_t \to 0$. Results are shown as relative deviations (in percent) with respect to the $W^+W^-b\bar{b}$ cross section with $\Gamma_t = \Gamma_t^{\text{phys}}$. Results with inclusive jet emission are compared to a $t\bar{t}$-signal analysis with two b-jets.

distributions P_b and P_t.[1] The tuning of R is performed in LO approximation on the fully inclusive level and yields $R = 7.96$. At NLO, the kinematic quantities that enter μ_{WWbb} are defined in terms of b- and $\bar{b}$-jet momenta that are constructed with a modified jet algorithm where $b\bar{b}$ pairs are not clustered and light partons with $|\eta| > 4.5$ are excluded from the recombination procedure. The latter prescription guarantees the collinear safety of the reconstructed top mass, $(p_W + p_b)^2$, with respect to collinear light-parton emission from the initial state. In the reconstruction of the top and anti-top masses $(p_W + p_b)^2$ that enter (4.15), remaining hard jets are clustered with the t- or $\bar{t}$- system if the resulting invariant mass turns out to be closer to m_t. Top-jet clusterings are applied only if they yield $P_t > 0.5$. If that holds for t- and $\bar{t}$- system, the clustering to maximise the $t\bar{t}$ probability, $P_t P_{\bar{t}}$, is chosen.

4.5 Predictions for the LHC at 8 TeV

In the following we present predictions for $pp \to W^+W^-b\bar{b}$ at 8 TeV in presence of the leptonic cuts (4.6). If not stated otherwise, the renormalisation and factorisation scales are set to

$$\mu_{R,F} = \xi_{R,F}\mu_0 \quad \text{with} \quad \mu_0 = \mu_{WWbb}, \tag{4.18}$$

where $\xi_R = \xi_F = 1$ corresponds to the default scale choice. Theoretical uncertainties are assessed by applying the scale variations $(\xi_R, \xi_F) = (2,2), (2,1), (1,2), (1,0.5), (0.5,1), (0.5,0.5)$.

[1] Here we assume that finite-top-width effects are dominated by non-$t\bar{t}$ contributions. Note also that the finite-top-width term on the left-hand side of (4.17) must be extracted through $\Gamma_t \to 0$ extrapolation by keeping Γ_t and R fixed in (4.15)–(4.16).

Figure 21 illustrates the extrapolation of the $W^+W^-b\bar{b}$ cross section in the narrow-top-width limit (4.7)–(4.8). The results are well consistent—at the few-permil level—with the expected linear convergence of the NLO cross section in the $\Gamma_t \to 0$ limit. This provides a non-trivial check of the consistency of the calculation, since the narrow-width limit involves delicate cancellations of logarithmic singularities that arise from virtual and real soft-gluon corrections to the resonant top-quark propagators. Finite-width effects turn out to be at the sub-percent level if one requires the presence of two b-jets, like in a typical $t\bar{t}$-signal analysis. For the total cross section they are instead clearly more important. Their net effect, which results from the interplay of negative off-shell corrections and positive single-top contributions, amounts to about +6%(8%) at NLO(LO).

	μ_0	σ[fb]	σ_0[fb]	σ_1[fb]	σ_{2^+}[fb]
LO	μ_{WWbb}	$1232^{+34\%}_{-24\%}$	$37^{+38\%}_{-25\%}$	$367^{+36\%}_{-24\%}$	$828^{+33\%}_{-23\%}$
NLO	μ_{WWbb}	$1777^{+10\%}_{-12\%}$	$41^{+3\%}_{-8\%}$	$377^{+1\%}_{-6\%}$	$1359^{+14\%}_{-14\%}$
K	μ_{WWbb}	1.44	1.09	1.03	1.64
LO	m_t	$1317^{+35\%}_{-24\%}$	$35^{+37\%}_{-25\%}$	$373^{+36\%}_{-24\%}$	$909^{+35\%}_{-24\%}$
NLO	m_t	$1817^{+8\%}_{-11\%}$	$40^{+4\%}_{-8\%}$	$372^{+1\%}_{-8\%}$	$1405^{+13\%}_{-13\%}$
K	m_t	1.38	1.14	1.0	1.55
	μ_0	σ^{FtW}[fb]	σ_0^{FtW}[fb]	σ_1^{FtW}[fb]	$\sigma_{2^+}^{FtW}$[fb]
LO	μ_{WWbb}	$91^{+41\%}_{-27\%}$	$13^{+42\%}_{-27\%}$	$71^{+40\%}_{-27\%}$	$7^{+45\%}_{-29\%}$
NLO	μ_{WWbb}	$107^{+6\%}_{-11\%}$	$13^{+1\%}_{-7\%}$	$61^{+2\%}_{-16\%}$	$33^{+51\%}_{-31\%}$
K	μ_{WWbb}	1.18	0.99	0.86	4.70
LO	m_t	$63^{+36\%}_{-25\%}$	$8^{+36\%}_{-25\%}$	$49^{+36\%}_{-24\%}$	$6^{+46\%}_{-29\%}$
NLO	m_t	$100^{+17\%}_{-16\%}$	$13^{+14\%}_{-14\%}$	$65^{+9\%}_{-12\%}$	$23^{+42\%}_{-28\%}$
K	m_t	1.58	1.47	1.32	3.89

Table 9: LO and NLO predictions for $pp \to W^+W^-b\bar{b}$ at 8 TeV with scale variations and corrections, $K = \sigma_{NLO}/\sigma_{LO}$, for different scale choices: total cross section with leptonic cuts and partial contributions with 0,1 and ≥ 2 jets. Full $W^+W^-b\bar{b}$ predictions (σ) are compared to finite-top-width contributions (σ^{FtW}).

Predictions for the integrated cross section and in exclusive jet bins are listed in Table 9. To assess the influence of the scale choice, results based on $\mu_0 = \mu_{WWbb}$ are compared to the case of the conventional scale $\mu_0 = m_t$. For the total cross section we find positive corrections of about 40%.[1] Scale uncertainties decrease from about 30% at LO to 10% at NLO, and the differences between the two scale choices are consistent

[1]We note that these results are not directly comparable to those of [158], which reports a significantly smaller K-factor. In particular, while we apply the same cuts on leptons, missing energy and jets, here we do not restrict ourselves to the case of two b-jets, we adopt a smaller jet-resolution parameter and a different QCD scale choice. Moreover we employ a 4F PDF set, which implies an enhancement of the gluon density due to the absence of $g \to b\bar{b}$ splittings in the PDF evolution. The LO PDF sets used in [158] and in the present study feature also significantly different values of α_s,

within scale variations. The last three columns of Table 9 display jet cross sections in bins with $N_j = 0, 1$ and $N_j \geq 2$ jets, where N_j refers to the total number of b-jets and light jets. The different bins receive quite different corrections, and the relative weight of the individual bins in percent changes from 3:30:67 at LO to 2:21:76 at NLO. This indicates that a significant fraction of the 0- and 1-jet bin cross sections migrates to the inclusive 2-jet bin. We attribute this feature to the rather high probability of light-jet emissions with $p_{\mathrm{T}} \gtrsim 30\,\mathrm{GeV}$. While NLO scale uncertainties turn out to be fairly small in all jet bins, matching to the parton shower is certainly important for a more reliable description of such radiative processes. Comparing the two scale choices, also in jet bins we do not observe any dramatic difference: absolute LO and NLO results are well consistent within scale variations, and also K-factors and scale variations themselves turn out to be quite similar.

Finite-top-width (FtW) contributions are shown in the lower part of Table 9. For what concerns the total $\mathrm{W^+W^-b\bar{b}}$ cross section their impact is around 6%, and the scale μ_{WWbb} guarantees a good perturbative convergence: FtW contributions receive only minor NLO corrections, and the residual scale dependence is about 10%, while setting $\mu_0 = m_{\mathrm{t}}$ yields larger corrections and scale uncertainties. As compared to complete $\mathrm{W^+W^-b\bar{b}}$ predictions, FtW contributions are distributed in a completely different way among jet bins. The relative weight in percent of the 0-, 1- and 2-jet bins is 14:78:8 at LO and 12:57:31 at NLO. These results suggest that FtW effects are dominated by a single-top Wt component, which is concentrated in the 1-jet bin at LO and tends to migrate to the 2-jet bin due to light-jet emissions at NLO. The fact that the FtW part of the 2-jet bin features a 40–50% NLO uncertainty is irrelevant, since this contribution represents less than 3% of the complete cross section in the 2-jet bin. In the 0- and 1-jet bins, whose FtW components amount to 32% and 16%, respectively, NLO scale uncertainties are as small as 10% or so.

In Table 10 we report analogous results for the $\mathrm{W^+W^-b\bar{b}}$ cross section and its FtW contribution in b-jet bins. As compared to the case of generic jets, we observe that $\mathrm{W^+W^-b\bar{b}}$ K-factors feature a less pronounced dependence on the b-jet multiplicity if the μ_{WWbb} scale is used. This is due to the fact that NLO emissions consist of light jets and are thus less likely to induce bin migrations in the case of b-jet bins. Scale uncertainties at NLO are at the 20%, 15% and 10% level in the bins with 0, 1, and ≥ 2 b-jets, respectively. Finite-top-width contributions turn out to be even more stable than full $\mathrm{W^+W^-b\bar{b}}$ results with the scale μ_{WWbb}, while the scale m_{t} tends to give larger uncertainties. Using the μ_{WWbb} scale, FtW effects in the 0-, 1-, and 2-b-jet bins turn out to be 31, 14 and 0.4 percent of the respective $\mathrm{W^+W^-b\bar{b}}$ cross sections at NLO. Employing $\mu_0 = m_{\mathrm{t}}$ these percentages become 25, 13 and 0.5, respectively. In general, jet- and b-jet-bin results indicate that the conventional scale $\mu_0 = m_{\mathrm{t}}$ yields a similarly good perturbative convergence as $\mu_0 = \mu_{\mathrm{WWbb}}$. However, it is a priori not clear if this holds also for more exclusive observables. For what concerns theoretical uncertainties in jet and b-jet bins, we checked that NLO scale variations remain similarly small as in Tables 9–10 if the jet-rapidity acceptance is increased up to $|\eta| < 4.5$.

To illustrate jet-veto and jet-binning effects in more detail, in Fig. 22 we plot the integrated $\mathrm{W^+W^-b\bar{b}}$ cross section in exclusive bins with $N_j = 0$ and $N_j = 1$ jets versus

which influences LO results and K-factors. Finally, in addition to uniform scale variations considered in [158], here also independent μ_{R} and μ_{F} variations are taken into account.

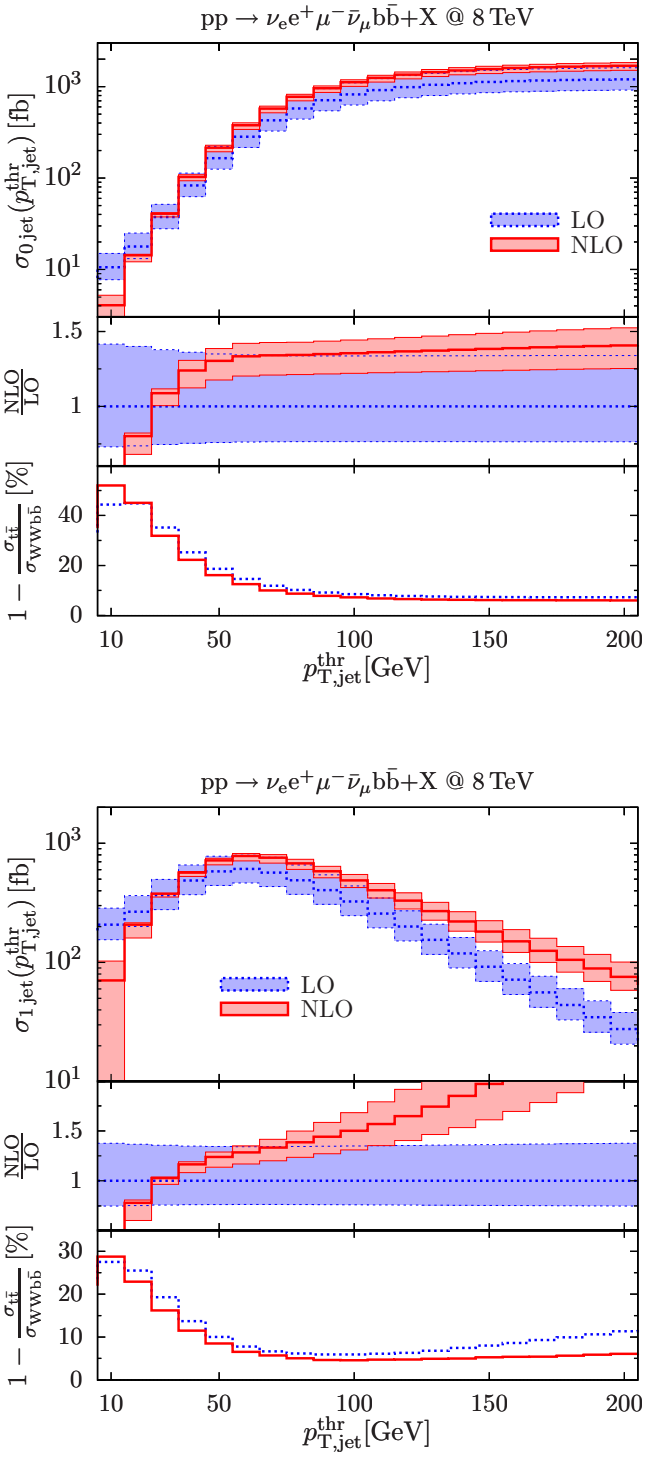

Figure 22: LO and NLO $\mathrm{W^+W^-b\bar{b}}$ cross sections in the exclusive bins with $N_j = 0$ (left) and $N_j = 1$ (right) jets as functions of the jet-p_{T} threshold, $p_{\mathrm{T,jet}}^{\mathrm{thr}}$. The middle of each bin corresponds to the actual value of $p_{\mathrm{T,jet}}^{\mathrm{thr}}$. The central and lower frames show the K-factor and the relative impact in percent of finite-top-width contributions. Where depicted, bands correspond to independent scale variations of $\mu_{\mathrm{R,F}}$ by a factor of two around the central scale μ_{WWbb}, not taking into account antipodal variations.

	μ_0	σ[fb]	σ_0[fb]	σ_1[fb]	σ_{2^+}[fb]
LO	μ_{WWbb}	$1232^{+34\%}_{-24\%}$	$37^{+38\%}_{-25\%}$	$367^{+36\%}_{-24\%}$	$828^{+33\%}_{-23\%}$
NLO	μ_{WWbb}	$1777^{+10\%}_{-12\%}$	$65^{+20\%}_{-17\%}$	$571^{+14\%}_{-14\%}$	$1140^{+7\%}_{-10\%}$
K	μ_{WWbb}	1.44	1.73	1.56	1.38
LO	m_{t}	$1317^{+35\%}_{-24\%}$	$35^{+37\%}_{-25\%}$	$373^{+36\%}_{-24\%}$	$909^{+35\%}_{-24\%}$
NLO	m_{t}	$1817^{+8\%}_{-11\%}$	$63^{+20\%}_{-17\%}$	$584^{+14\%}_{-14\%}$	$1170^{+5\%}_{-9\%}$
K	m_{t}	1.38	1.80	1.56	1.29
	μ_0	σ^{FtW}[fb]	σ_0^{FtW}[fb]	σ_1^{FtW}[fb]	$\sigma_{2^+}^{\mathrm{FtW}}$[fb]
LO	μ_{WWbb}	$91^{+41\%}_{-27\%}$	$13^{+42\%}_{-27\%}$	$71^{+40\%}_{-27\%}$	$7^{+45\%}_{-29\%}$
NLO	μ_{WWbb}	$107^{+6\%}_{-11\%}$	$20^{+18\%}_{-17\%}$	$82^{+4\%}_{-10\%}$	$5^{+2\%}_{-10\%}$
K	μ_{WWbb}	1.18	1.49	1.16	0.77
LO	m_{t}	$63^{+36\%}_{-25\%}$	$8^{+36\%}_{-25\%}$	$49^{+36\%}_{-24\%}$	$6^{+46\%}_{-29\%}$
NLO	m_{t}	$100^{+17\%}_{-16\%}$	$16^{+22\%}_{-18\%}$	$77^{+16\%}_{-15\%}$	$6^{+12\%}_{-16\%}$
K	m_{t}	1.58	1.89	1.58	1.10

Table 10: Full $\mathrm{W^+W^-b\bar{b}}$ predictions and finite-top-width contributions for bins with 0,1 and ≥ 2 b-jets. Same conventions as in Table 9.

the p_{T}-threshold that defines jets. The 0-jet bin corresponds to the integrated cross section in presence of a jet veto, $p_{\mathrm{T,jet}} < p_{\mathrm{T,jet}}^{\mathrm{thr}}$. At large $p_{\mathrm{T,jet}}^{\mathrm{thr}}$ the K-factor and the FtW contributions converge quite smoothly towards their inclusive limit. In contrast, the region of small transverse momentum features a very pronounced dependence on $p_{\mathrm{T,jet}}^{\mathrm{thr}}$: FtW corrections grow from 6% up to more than 40%, and the K-factor decreases very fast due to the presence of a soft singularity at $p_{\mathrm{T,jet}}^{\mathrm{thr}} \to 0$. For a jet veto with $p_{\mathrm{T,jet}}^{\mathrm{thr}} = 30\,\mathrm{GeV}$ we observe a 98% suppression of the $\mathrm{W^+W^-b\bar{b}}$ cross section. Yet the moderate size of the K-factor and NLO scale variations indicates that the perturbative expansion is still rather stable in this regime. In the 1-jet bin, the limit of small $p_{\mathrm{T,jet}}^{\mathrm{thr}}$ is driven by the effect of the veto on the second jet, and NLO and FtW corrections behave rather similarly as for the 0-jet bin in this region. In the opposite regime, $p_{\mathrm{T,jet}}^{\mathrm{thr}}$ mainly acts as a lower p_{T} bound for the first jet, and $\mathrm{t\bar{t}}$ production with LO on-shell kinematics turns out to be kinematically disfavoured at large $p_{\mathrm{T,jet}}^{\mathrm{thr}}$, while the relative importance of NLO jet emission and FtW effects increases quite dramatically.

Analogous results for exclusive bins with $N_{\mathrm{b}} = 0$ and $N_{\mathrm{b}} = 1$ b-jets are displayed in Fig. 23. In this case the reduced sensitivity of b-jet bins to NLO real emission is clearly reflected in the much better stability of the K-factor with respect to variations of $p_{\mathrm{T,bjet}}^{\mathrm{thr}}$. Similarly as for jet bins, FtW corrections are strongly enhanced at small p_{T}. This effect can be attributed to the single-top Wt channels, and the inclusion of $\mathrm{t\bar{t}}$–Wt interferences, as in the present $\mathrm{W^+W^-b\bar{b}}$ calculation, is clearly advisable in this regime.

Finally, in Fig. 24 we show distributions in the azimuthal-angle-separation and in the invariant mass of charged leptons in the 0-jet bin. These observables play a key role

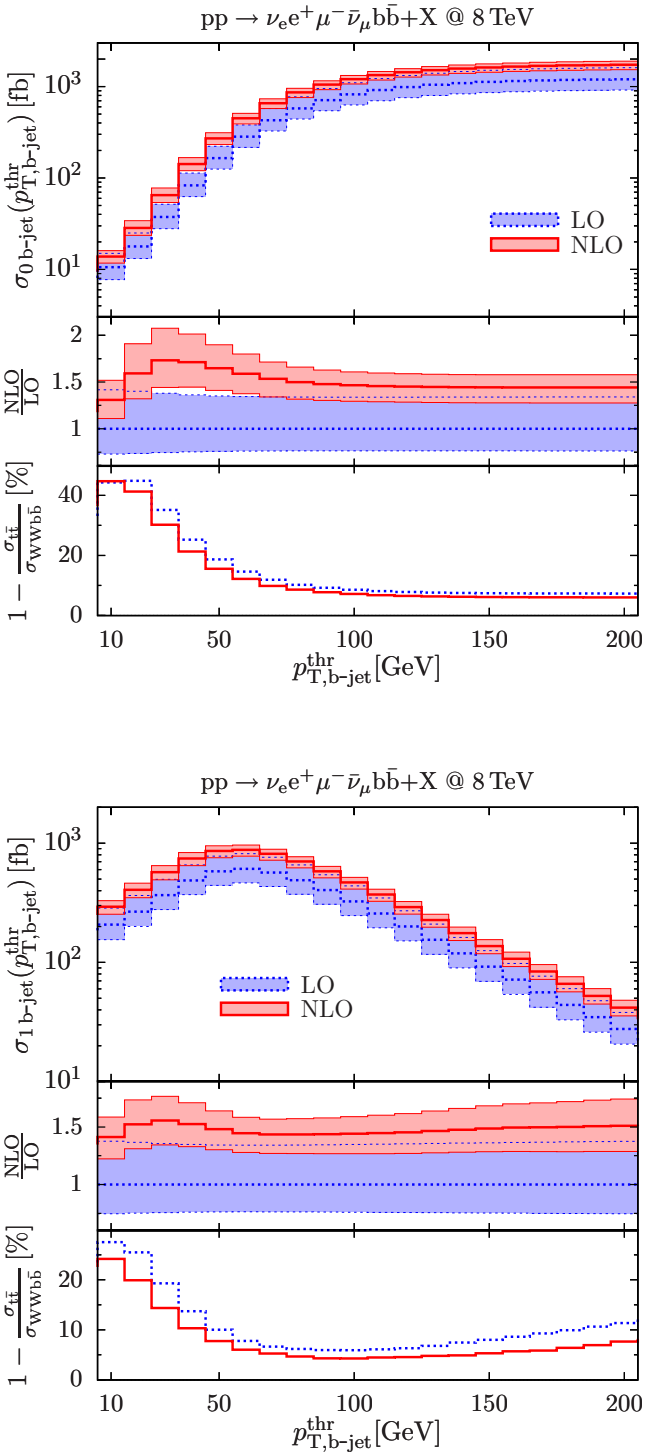

Figure 23: LO and NLO $W^+W^- b\bar{b}$ cross sections in the exclusive bins with $N_b = 0$ (left) and $N_b = 1$ (right) b-jets versus the b-jet-p_T threshold. Same conventions as in Fig. 22.

for the measurement of the $H \to W^+W^-$ signal at the LHC, and the accurate modelling of top-backgrounds is very important for the experimental analyses. In this context, Fig. 24 shows that NLO and FtW effects are quite significant. In particular, the impact of FtW contributions reaches up to 40%. Shape distortions due to the kinematic dependence of FtW and NLO contributions are at the 10% level, and scale variations do not exceed 10% at NLO. The fact that FtW corrections are fairly stable with respect to NLO corrections provides further evidence of the stability of the perturbative description.

4.6 Conclusions

We have presented a complete NLO simulation of $W^+W^-b\bar{b}$ production at the LHC, including W-boson decays in the opposite-flavour di-lepton channel, finite W- and top-width effects, and massive b-quarks in 4F scheme. The finite b-quark mass acts as a regulator of collinear singularities and allows one to describe the full b-quark phase space, including single-top contributions that arise from initial-state $g \to b\bar{b}$ splittings followed by $gb \to Wt$ scattering. This yields a gauge-invariant description of top-pair, single-top, and non-resonant $W^+W^-b\bar{b}$ production including all interferences at NLO QCD. We introduced a dynamical scale choice aimed at an improved perturbative stability of initial-state $g \to b\bar{b}$ splittings in single-top contributions. Using this scale, the NLO $W^+W^-b\bar{b}$ cross section in bins with 0, 1 and 2 jets features NLO scale uncertainties at the 10–15% level. The more conventional choice $\mu_0 = m_t$ yields similarly small NLO uncertainties in jet bins. While providing further evidence of the good convergence of the perturbative expansion, this means that a sophisticated dynamical scale is unnecessary for the rather inclusive observables considered in this chapter. However, such a dynamical scale might become important for more exclusive observables, like jet-p_T distributions.

Finite-top-width corrections mainly originate from single-top and off-shell $t\bar{t}$ contributions. They represent 6% of the integrated cross section and are strongly sensitive to the jet multiplicity. In the 2-jet bin they are as small as 2%, while in the 1- and 0-jet bins they reach the 16% and 32% level, respectively. Also NLO corrections vary quite strongly with the jet multiplicity. Moreover, finite-top-width contributions receive quite different corrections as compared to on-shell $t\bar{t}$ production.

The non-trivial interplay of NLO and finite-width effects is especially relevant for the 0- and 1-jet bins. It plays an important role for the accurate description of associated Wt production, as well as for top-backgrounds to $H \to W^+W^-$ and to other searches based on leptons, large missing energy and jet vetoes. All employed tools are fully automated and can be easily exploited to extend the present results to the like-flavour di-lepton channel or to simulate any other Standard-Model process at NLO QCD.

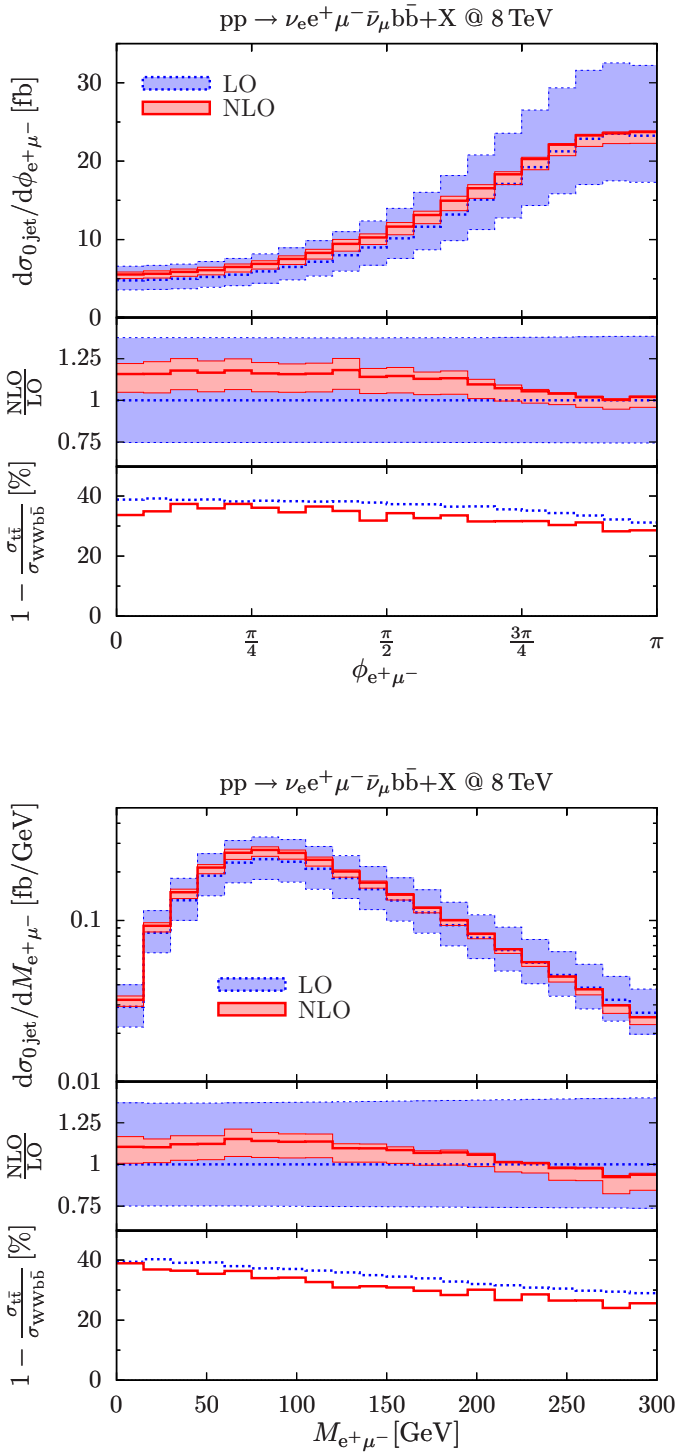

Figure 24: Differential distributions in the 0-jet bin: azimuthal-angle separation (left) and invariant mass (right) of the two charged leptons. Same conventions as in Fig. 22.

Summary and Conclusions

In this thesis we presented the OpenLoops algorithm for the generation of tree-level and one-loop scattering amplitudes [43]. It is a fully model- and process-independent method based on a numerical recursive construction of Feynman diagrams. Thanks to the diagrammatic approach, colour sums are performed efficiently by factorizing on a diagram-by-diagram basis the colour structures and reducing them algebraically to a standard basis. Tree-level colour-stripped amplitudes are computed by recursively merging sub-trees, i.e. complex n-tuples associated to subdiagrams resulting from cutting a line. Sub-trees are merged by connecting their cut lines through numerical routines associated to vertices and propagators of the Feynman rules of the model at hand. The systematic sharing of previously computed sub-trees in different diagrams boosts the efficiency of the calculation.

A colour-stripped one-loop diagram is handled as an ordered set of sub-trees connected by loop propagators. The open-loops representation is based on the polynomial nature of the numerator of one-loop integrands as a function of the loop momentum. The tensorial coefficients of the various loop-momentum monomials are the building blocks of the OpenLoops recursion. They are built via numerical routines that return higher-point (higher-rank) open-loops in terms of lower-point (lower-rank) open-loops and external sub-trees. Thanks to parent-child relations that arise from pinching loop propagators, the most involved high-point diagrams can be efficiently obtained starting from pre-computed lower-point diagrams. Working with symmetrized tensorial indices allows to keep the number of open-loops components under control when increasing the particle multiplicity and the tensorial rank. The open-loops representation naturally adapts to both tensor-integral and OPP reduction frameworks, in a way that combines the higher efficiency of the first with the flexibility of the second. The efficiency of OPP reduction is strongly enhanced by the fact that the multiple evaluations of the numerator function needed to extract the coefficients of the scalar integrals can be performed at a negligible cost in the open-loops representation. High speed in the numerical evaluations is obtained by sharing pre-computed open-loops coefficients in equivalent subtopologies of different diagrams and by performing helicity sums before reduction to scalar integrals.

The OpenLoops algorithm has been implemented in a computer program for the numerical computation of scattering amplitudes which automates the full chain of operations, from process definition to generation of `Fortran90` numerical code. OpenLoops has been thoroughly tested and validated for the computation of NLO QCD corrections to Standard Model processes. The extension to one-loop electroweak corrections—including ultraviolet renormalization and rational terms—has been recently completed. The high level of flexibility and efficiency of the algorithm has been

demonstrated in a series of technical studies. The time required for the generation of numerical code and the compactness of the latter have been improved by orders of magnitude with respect to previous approaches based on algebraic manipulations of Feynman diagrams. The speed of the numerical evaluation of the amplitudes has been further improved. In conjunction with the tensor integral reduction library Collier, which avoids spurious singularities due to small Gram determinants, we find excellent numerical stability. In physical runs with large samples of phase space points, instabilities are monitored on the fly by a trigger mechanism that allows to cure possible unstable points by double evaluations using different reduction libraries, scaling test or switching to quadruple precision. OpenLoops has been interfaced to Monte Carlo generators for the computation of physical NLO cross sections. In particular, we developed a dedicated interface to the Sherpa Monte Carlo which has been used for a series of state-of-the-art NLO simulations and which allows the automated matching to a MC@NLO parton shower and the NLO multi-jet merging in the MEPS@NLO framework. The standard Binoth-Les Houches interface for linking one-loop generators to Monte Carlo programs has also been implemented.

OpenLoops has proven to be very flexible and efficient, and has been used in a wide range of multi-particle NLO simulations [58–60, 62–64], including matching to the parton shower and multi-jet merging, as well as in the context of NNLO calculations [61, 65, 66]. In this thesis, we have presented a detailed study of the irreducible $\mu^+\nu_\mu \mathrm{e}^-\bar{\nu}_\mathrm{e}$ background to Higgs boson production in the $H \to W^+W^-$ channel [58]. Matrix elements for $\mathrm{pp} \to \mu^+\nu_\mu \mathrm{e}^-\bar{\nu}_\mathrm{e}+0,1$ jet production have been matched to the Sherpa parton shower, and the different jet multiplicities have been consistently merged with the MEPS@NLO technique. Loop-induced gluon-initiated contributions with up to one extra jet are also included via a consistent matching and merging. All contributions to four-lepton production, including off-shell intermediate vector bosons, non-resonant channels and related quantum interferences, are consistently taken into account using the complex-mass scheme. The parton shower provides improved predictions and uncertainty estimates for exclusive observables in the 0- and 1-jet bins of the ATLAS and CMS analyses. Assessing renormalisation-, factorisation- and resummation-scale uncertainties, we find that residual scale uncertainties are as small as a few percent.

We also discussed NLO QCD corrections to $\mathrm{W^+W^-b\bar{b}}$ final states including b-quark mass effects and all interferences leading to the $\nu_\mathrm{e}\mathrm{e}^+\mu^-\bar{\nu}_\mu \mathrm{b\bar{b}}$ final state [60]. This provides the first consistent NLO description of $\mathrm{t\bar{t}}$ and Wt production and decay, including quantum interference effects. The finite b-quark mass permits to describe the whole b-quark phase space with NLO accuracy and renders the simulation applicable to exclusive 0- and 1-jet bins, which is of great importance for Higgs-boson studies in the $\mathrm{H} \to \mathrm{W^+W^-}$ channel and for any other analysis with large top backgrounds and jet vetoes or jet bins. In contrast to previous, more exclusive, $\mathrm{W^+W^-b\bar{b}}$ calculations with massless bottom quarks, this simulation involves very large finite-width corrections to the naive on-shell description of $\mathrm{t\bar{t}}$ production and decay.

A pre-release version of OpenLoops, which allows to simulate a wide range of $2 \to 2,3,4$ LHC processes, has been distributed to the Monte Carlo working groups of the ATLAS and CMS collaborations. The first public version of the OpenLoops generator is going to be released very soon.

Acknowledgements

I would like to thank Stefano, my supervisor, for giving me the opportunity four years ago of joining him in this project. Starting from a nice idea and a blank blackboard, we arrived at a stage which is way beyond my—and I bet also his—best expectations. All of this would have been hardly possible without the valuable and unique collaboration of Philipp. I thank him for his patience whenever I knocked at his door and for having taught me how to properly use a computer, altough I am sure he would agree with me that I still have not learned it. I thank Jonas for the courage of going through my code and for carefully reading this manuscript.

Thanks to all the people that in these years made the "Institut für Theoretische Physik" a great place to work. Being now the wise old guy, they would be too many to mention them. A special thank to our secretaries, Regina and Esther, which always promptly helped me whenever I needed some bureaucratic assistance.

I can't help thanking all the friends that contributed making these four years such a beautiful and unforgettable experience. Among them special thanks go to Andrea, Davide, Benoit, Sandra, Daniela, Elena, Valentina and Lorenzo. The latter has been a colleague, a flatmate and a friend without whom it would definitely not have been the same.

Infine, ringrazio la mia famiglia, i miei genitori e mio fratello per l'incondizionato e costante supporto, e per non avermi mai fatto sentire veramente lontano.

Appendix A

Numerical routines

We collect here some examples of `Fortran90` subroutines for the numerical computation of tree-level and one-loop amplitudes as discussed in Section 2.4.

A.1 Subroutine prop_Q_A

Numerical subroutine for the dressing of an anti-fermion sub-tree with the corresponding propagator as described in Eq.(2.68).

```
subroutine prop_Q_A(J_Q, P, M, J_A)
  intent(in)  :: J_Q(4), P(4), M
  intent(out) :: J_A(4)

  J_A(1) = - P(2)*J_Q(3) + P(4)*J_Q(4)
  J_A(2) = - P(1)*J_Q(4) + P(3)*J_Q(3)
  J_A(3) = - P(1)*J_Q(1) - P(4)*J_Q(2)
  J_A(4) = - P(2)*J_Q(2) - P(3)*J_Q(1)
  J_A = J_A + M*J_Q

end subroutine prop_Q_A
```

A.2 Subroutine vert_QA_Z

Numerical subroutine for the computation of a tree-level Z-boson sub-tree that results from the merging of a quark and an anti-quark sub-tree as described in Eq.(2.69).

```
subroutine vert_QA_Z(g_RL, J_Q, J_A, J_Z)
  intent(in)  :: g_RL(2), J_Q(4), J_A(4)
  intent(out) :: J_Z(4)

  J_Z(1) = - g_RL(2)*J_A(1)*J_Q(3) - g_RL(1)*J_A(4)*J_Q(2)
  J_Z(2) = - g_RL(2)*J_A(2)*J_Q(4) - g_RL(1)*J_A(3)*J_Q(1)
  J_Z(3) = - g_RL(2)*J_A(1)*J_Q(4) + g_RL(1)*J_A(3)*J_Q(2)
  J_Z(4) = - g_RL(2)*J_A(2)*J_Q(3) + g_RL(1)*J_A(4)*J_Q(1)
  J_Z = J_Z + J_Z
```

```
end subroutine vert_QA_Z
```

A.3 Subroutine vert_UV_W

Numerical subroutine for the computation of a gluonic sub-tree that results from the merging of two gluonic sub-trees as described in (2.70). It makes use of the function `cont_VV(V1,V2)` for the contraction of two four-vectors in the light-cone representation.

```
subroutine vert_UV_W(J_V1, P1, J_V2, P2, Jout_V)
  intent(in)  :: J_V1(4), P1(4), J_V2(4), P2(4)
  intent(out) :: Jout_V(4)
  J1J2, P1J2, P2J1

  J1J2 = cont_VV(J_V1,J_V2)
  P1J2 = cont_VV(P1+P1+P2,J_V2)
  P2J1 = cont_VV(P1+P2+P2,J_V1)
  Jout_V = J1J2 * (P1 - P2) + P2J1 * J_V2 - P1J2 * J_V1

end subroutine vert_UV_W

function cont_VV(A,B)
  intent(in) :: A(4), B(4)
  cont_VV = A(1)*B(2) + A(2)*B(1) - A(3)*B(4) - A(4)*B(3)
  cont_VV = 0.5 * cont_VV
end function cont_VV
```

A.4 Function tensor_contract

Contraction of two symmetrized tensors stored as one-dimensional arrays `G` and `TI` as in Eq.(2.78), up to the maximum rank of `G`.

```
function tensor_contract(G, TI)
  intent(in) :: G(:), TI(:)
  tensor_contract = sum(G*TI(1:size(G)))
end function tensor_contract
```

A.5 Subroutine raise_rank_init

Subroutine for the initialization of the function HR(i,l). Given a tensor index l, it returns the four higher-rank indices l_i that arise from shifting $n_i \to n_i+1$ (see Eq.(2.76) and (2.79)).

```
subroutine raise_rank_init

  HR(:,   1) = [   2,   3,   4,   5 ]
  HR(:,   2) = [   6,   7,   8,   9 ]
```

```
HR(:,   3) = [   7,  10,  11,  12 ]
HR(:,   4) = [   8,  11,  13,  14 ]
HR(:,   5) = [   9,  12,  14,  15 ]
HR(:,   6) = [  16,  17,  18,  19 ]
HR(:,   7) = [  17,  20,  21,  22 ]
HR(:,   8) = [  18,  21,  23,  24 ]
HR(:,   9) = [  19,  22,  24,  25 ]
HR(:,  10) = [  20,  26,  27,  28 ]
HR(:,  11) = [  21,  27,  29,  30 ]
HR(:,  12) = [  22,  28,  30,  31 ]
HR(:,  13) = [  23,  29,  32,  33 ]
HR(:,  14) = [  24,  30,  33,  34 ]
HR(:,  15) = [  25,  31,  34,  35 ]
HR(:,  16) = [  36,  37,  38,  39 ]
HR(:,  17) = [  37,  40,  41,  42 ]
HR(:,  18) = [  38,  41,  43,  44 ]
HR(:,  19) = [  39,  42,  44,  45 ]
HR(:,  20) = [  40,  46,  47,  48 ]
HR(:,  21) = [  41,  47,  49,  50 ]
HR(:,  22) = [  42,  48,  50,  51 ]
HR(:,  23) = [  43,  49,  52,  53 ]
HR(:,  24) = [  44,  50,  53,  54 ]
HR(:,  25) = [  45,  51,  54,  55 ]
HR(:,  26) = [  46,  56,  57,  58 ]
HR(:,  27) = [  47,  57,  59,  60 ]
HR(:,  28) = [  48,  58,  60,  61 ]
HR(:,  29) = [  49,  59,  62,  63 ]
HR(:,  30) = [  50,  60,  63,  64 ]
HR(:,  31) = [  51,  61,  64,  65 ]
HR(:,  32) = [  52,  62,  66,  67 ]
HR(:,  33) = [  53,  63,  67,  68 ]
HR(:,  34) = [  54,  64,  68,  69 ]
HR(:,  35) = [  55,  65,  69,  70 ]
HR(:,  36) = [  71,  72,  73,  74 ]
HR(:,  37) = [  72,  75,  76,  77 ]
HR(:,  38) = [  73,  76,  78,  79 ]
HR(:,  39) = [  74,  77,  79,  80 ]
HR(:,  40) = [  75,  81,  82,  83 ]
HR(:,  41) = [  76,  82,  84,  85 ]
HR(:,  42) = [  77,  83,  85,  86 ]
HR(:,  43) = [  78,  84,  87,  88 ]
HR(:,  44) = [  79,  85,  88,  89 ]
HR(:,  45) = [  80,  86,  89,  90 ]
HR(:,  46) = [  81,  91,  92,  93 ]
HR(:,  47) = [  82,  92,  94,  95 ]
HR(:,  48) = [  83,  93,  95,  96 ]
HR(:,  49) = [  84,  94,  97,  98 ]
HR(:,  50) = [  85,  95,  98,  99 ]
HR(:,  51) = [  86,  96,  99, 100 ]
```

```
HR(:,  52) = [  87,  97, 101, 102 ]
HR(:,  53) = [  88,  98, 102, 103 ]
HR(:,  54) = [  89,  99, 103, 104 ]
HR(:,  55) = [  90, 100, 104, 105 ]
HR(:,  56) = [  91, 106, 107, 108 ]
HR(:,  57) = [  92, 107, 109, 110 ]
HR(:,  58) = [  93, 108, 110, 111 ]
HR(:,  59) = [  94, 109, 112, 113 ]
HR(:,  60) = [  95, 110, 113, 114 ]
HR(:,  61) = [  96, 111, 114, 115 ]
HR(:,  62) = [  97, 112, 116, 117 ]
HR(:,  63) = [  98, 113, 117, 118 ]
HR(:,  64) = [  99, 114, 118, 119 ]
HR(:,  65) = [ 100, 115, 119, 120 ]
HR(:,  66) = [ 101, 116, 121, 122 ]
HR(:,  67) = [ 102, 117, 122, 123 ]
HR(:,  68) = [ 103, 118, 123, 124 ]
HR(:,  69) = [ 104, 119, 124, 125 ]
HR(:,  70) = [ 105, 120, 125, 126 ]
HR(:,  71) = [ 127, 128, 129, 130 ]
HR(:,  72) = [ 128, 131, 132, 133 ]
HR(:,  73) = [ 129, 132, 134, 135 ]
HR(:,  74) = [ 130, 133, 135, 136 ]
HR(:,  75) = [ 131, 137, 138, 139 ]
HR(:,  76) = [ 132, 138, 140, 141 ]
HR(:,  77) = [ 133, 139, 141, 142 ]
HR(:,  78) = [ 134, 140, 143, 144 ]
HR(:,  79) = [ 135, 141, 144, 145 ]
HR(:,  80) = [ 136, 142, 145, 146 ]
HR(:,  81) = [ 137, 147, 148, 149 ]
HR(:,  82) = [ 138, 148, 150, 151 ]
HR(:,  83) = [ 139, 149, 151, 152 ]
HR(:,  84) = [ 140, 150, 153, 154 ]
HR(:,  85) = [ 141, 151, 154, 155 ]
HR(:,  86) = [ 142, 152, 155, 156 ]
HR(:,  87) = [ 143, 153, 157, 158 ]
HR(:,  88) = [ 144, 154, 158, 159 ]
HR(:,  89) = [ 145, 155, 159, 160 ]
HR(:,  90) = [ 146, 156, 160, 161 ]
HR(:,  91) = [ 147, 162, 163, 164 ]
HR(:,  92) = [ 148, 163, 165, 166 ]
HR(:,  93) = [ 149, 164, 166, 167 ]
HR(:,  94) = [ 150, 165, 168, 169 ]
HR(:,  95) = [ 151, 166, 169, 170 ]
HR(:,  96) = [ 152, 167, 170, 171 ]
HR(:,  97) = [ 153, 168, 172, 173 ]
HR(:,  98) = [ 154, 169, 173, 174 ]
HR(:,  99) = [ 155, 170, 174, 175 ]
HR(:, 100) = [ 156, 171, 175, 176 ]
```

```
  HR(:, 101) = [ 157, 172, 177, 178 ]
  HR(:, 102) = [ 158, 173, 178, 179 ]
  HR(:, 103) = [ 159, 174, 179, 180 ]
  HR(:, 104) = [ 160, 175, 180, 181 ]
  HR(:, 105) = [ 161, 176, 181, 182 ]
  HR(:, 106) = [ 162, 183, 184, 185 ]
  HR(:, 107) = [ 163, 184, 186, 187 ]
  HR(:, 108) = [ 164, 185, 187, 188 ]
  HR(:, 109) = [ 165, 186, 189, 190 ]
  HR(:, 110) = [ 166, 187, 190, 191 ]
  HR(:, 111) = [ 167, 188, 191, 192 ]
  HR(:, 112) = [ 168, 189, 193, 194 ]
  HR(:, 113) = [ 169, 190, 194, 195 ]
  HR(:, 114) = [ 170, 191, 195, 196 ]
  HR(:, 115) = [ 171, 192, 196, 197 ]
  HR(:, 116) = [ 172, 193, 198, 199 ]
  HR(:, 117) = [ 173, 194, 199, 200 ]
  HR(:, 118) = [ 174, 195, 200, 201 ]
  HR(:, 119) = [ 175, 196, 201, 202 ]
  HR(:, 120) = [ 176, 197, 202, 203 ]
  HR(:, 121) = [ 177, 198, 204, 205 ]
  HR(:, 122) = [ 178, 199, 205, 206 ]
  HR(:, 123) = [ 179, 200, 206, 207 ]
  HR(:, 124) = [ 180, 201, 207, 208 ]
  HR(:, 125) = [ 181, 202, 208, 209 ]
  HR(:, 126) = [ 182, 203, 209, 210 ]

end subroutine raise_rank_init
```

A.6 Subroutine loop_QA_Z

Subroutines for the computation of the coefficients of a Z-boson open-loop that is generated from an anti-quark open-loop and a quark sub-tree via a $q\bar{q}Z$ vertex as described in Eq.(2.82).

```
subroutine loop_QA_Z(G_Q, J_A, G_Z, g_RL)
  intent(in)  :: g_RL(2), G_Q(:,:,:), J_A(4)
  intent(out) :: G_Z(:,:,:)
  rank_in, rank_out
  rank_in  = size(G_Q,2)
  rank_out = size(G_Z,2)

  call vert_loop_QA_Z(rank_in, rank_out, g_RL, G_Q(:,:,1), J_A, G_Z(:,:,1))
  call vert_loop_QA_Z(rank_in, rank_out, g_RL, G_Q(:,:,2), J_A, G_Z(:,:,2))
  call vert_loop_QA_Z(rank_in, rank_out, g_RL, G_Q(:,:,3), J_A, G_Z(:,:,3))
  call vert_loop_QA_Z(rank_in, rank_out, g_RL, G_Q(:,:,4), J_A, G_Z(:,:,4))

end subroutine loop_QA_Z

subroutine vert_loop_QA_Z(rank_in, rank_out, g_RL, G_Q, J_A, G_Z)
  intent(in)  :: rank_in, rank_out
  intent(in)  :: G_Q(4,rank_in), J_A(4), g_RL(2)
```

```
  intent(out) :: G_Z(4,rank_out)

  do l = 1, rank_in
    G_Z(1,l) = - g_RL(2)*G_Q(3,l)*J_A(1) - g_RL(1)*G_Q(2,l)*J_A(4)
    G_Z(2,l) = - g_RL(2)*G_Q(4,l)*J_A(2) - g_RL(1)*G_Q(1,l)*J_A(3)
    G_Z(3,l) = - g_RL(2)*G_Q(4,l)*J_A(1) + g_RL(1)*G_Q(2,l)*J_A(3)
    G_Z(4,l) = - g_RL(2)*G_Q(3,l)*J_A(2) + g_RL(1)*G_Q(1,l)*J_A(4)
    G_Z(:,l) = G_Z(:,l) + G_Z(:,l)
  end do

end subroutine vert_loop_QA_Z
```

A.7 Subroutine loop_UV_W

Subroutines for the computation of the open-loops coefficients of a gluonic open-loop that is generated from a gluonic open-loop and a gluonic sub-tree via a triple-vector-boson vertex. The top-level routine, `loop_UV_W`, consists just of four identical calls for each value of the index α. It takes as input the incoming open-loop, the sub-tree and their momenta and returns the outgoing open-loop. The internal routine, `vert_loop_UV_W`, implements Eq.(2.85) and (2.86).

```
subroutine loop_UV_W(Gin_V, Ploop, J_V, Ptree, Gout_V)
  intent(in)  :: Gin_V(:,:,:), J_V(4), Ploop(4), Ptree(4)
  intent(out) :: Gout_V(:,:,:)
  rank_in  = size(Gin_V,2)
  rank_out = size(Gout_V,2)

  call vert_loop_UV_W(rank_in,rank_out,Gin_V(:,:,1),Ploop,J_V,Ptree,Gout_V(:,:,1))
  call vert_loop_UV_W(rank_in,rank_out,Gin_V(:,:,2),Ploop,J_V,Ptree,Gout_V(:,:,2))
  call vert_loop_UV_W(rank_in,rank_out,Gin_V(:,:,3),Ploop,J_V,Ptree,Gout_V(:,:,3))
  call vert_loop_UV_W(rank_in,rank_out,Gin_V(:,:,4),Ploop,J_V,Ptree,Gout_V(:,:,4))

end subroutine loop_UV_W


subroutine vert_loop_UV_W(rank_in, rank_out, Gin_V, Ploop, J_V, Ptree, Gout_V)
  intent(in)  :: rank_in, rank_out
  intent(in)  :: Gin_V(4,rank_in), J_V(4), Ploop(4), Ptree(4)
  intent(out) :: Gout_V(4,rank_out)

  Gout_V = 0
  Ptmp(:,1) = Ploop + 2*Ptree
  Ptmp(:,2) = Ptree + 2*Ploop
  Ptmp(:,3) = Ploop - Ptree
  C = cont_VV(Ptmp(1,2),J_V)
  Jhalf = 0.5_rp * J_V
  Jtwo(1) =  J_V(2)
  Jtwo(2) =  J_V(1)
  Jtwo(3) = -J_V(4)
  Jtwo(4) = -J_V(3)

  do l = 1, rank_in
    Ac = cont_VV(Gin_V(1,l), J_V)
    Bc = cont_VV(Gin_V(1,l), Ptmp(1,1))

    Gout_V(1, HR(1,l)) = Gout_V(1, HR(1,l)) + Ac + Gin_V(2,l)*Jhalf(1) - Gin_V(1,l)*Jtwo(1)
    Gout_V(2, HR(1,l)) = Gout_V(2, HR(1,l))      + Gin_V(2,l)*Jhalf(2) - Gin_V(2,l)*Jtwo(1)
    Gout_V(3, HR(1,l)) = Gout_V(3, HR(1,l))      + Gin_V(2,l)*Jhalf(3) - Gin_V(3,l)*Jtwo(1)
    Gout_V(4, HR(1,l)) = Gout_V(4, HR(1,l))      + Gin_V(2,l)*Jhalf(4) - Gin_V(4,l)*Jtwo(1)

    Gout_V(1, HR(2,l)) = Gout_V(1, HR(2,l))      + Gin_V(1,l)*Jhalf(1) - Gin_V(1,l)*Jtwo(2)
    Gout_V(2, HR(2,l)) = Gout_V(2, HR(2,l)) + Ac + Gin_V(1,l)*Jhalf(2) - Gin_V(2,l)*Jtwo(2)
```

```
    Gout_V(3, HR(2,l)) = Gout_V(3, HR(2,l))      + Gin_V(1,l)*Jhalf(3) - Gin_V(3,l)*Jtwo(2)
    Gout_V(4, HR(2,l)) = Gout_V(4, HR(2,l))      + Gin_V(1,l)*Jhalf(4) - Gin_V(4,l)*Jtwo(2)

    Gout_V(1, HR(3,l)) = Gout_V(1, HR(3,l))      - Gin_V(4,l)*Jhalf(1) - Gin_V(1,l)*Jtwo(3)
    Gout_V(2, HR(3,l)) = Gout_V(2, HR(3,l))      - Gin_V(4,l)*Jhalf(2) - Gin_V(2,l)*Jtwo(3)
    Gout_V(3, HR(3,l)) = Gout_V(3, HR(3,l)) + Ac - Gin_V(4,l)*Jhalf(3) - Gin_V(3,l)*Jtwo(3)
    Gout_V(4, HR(3,l)) = Gout_V(4, HR(3,l))      - Gin_V(4,l)*Jhalf(4) - Gin_V(4,l)*Jtwo(3)

    Gout_V(1, HR(4,l)) = Gout_V(1, HR(4,l))      - Gin_V(3,l)*Jhalf(1) - Gin_V(1,l)*Jtwo(4)
    Gout_V(2, HR(4,l)) = Gout_V(2, HR(4,l))      - Gin_V(3,l)*Jhalf(2) - Gin_V(2,l)*Jtwo(4)
    Gout_V(3, HR(4,l)) = Gout_V(3, HR(4,l))      - Gin_V(3,l)*Jhalf(3) - Gin_V(3,l)*Jtwo(4)
    Gout_V(4, HR(4,l)) = Gout_V(4, HR(4,l)) + Ac - Gin_V(3,l)*Jhalf(4) - Gin_V(4,l)*Jtwo(4)

    do beta = 1, 4
      Gout_V(beta,l) = Gout_V(beta,l) + Ac*Ptmp(beta,3) + Bc*J_V(beta) - C*Gin_V(beta,l)
    end do
  end do

end subroutine vert_loop_UV_W
```

A.8 Subroutine last_QA_Z

Optimized version of the routine for the last step in the case of the $Zq\bar{q}$ vertex. By comparison with `vert_loop_QA_Z` in A.6 we see that only the diagonal components `G[beta,l,beta]` are computed and summed in one step to return the final `Gtensor` array.

```
subroutine last_QA_Z(g_RL, G_Q, J_A, Gtensor)
  intent(in)  :: G_Q(:,:,:), J_A(4), g_RL(2)
  intent(out) :: Gtensor(size(G_Q,2))
  do l = 1, size(G_Q,2)
    Gtensor(l) = (- g_RL(1)*(G_Q(2,l,1)*J_A(4)  &
                           + G_Q(1,l,2)*J_A(3)  &
                           - G_Q(2,l,3)*J_A(3)  &
                           - G_Q(1,l,4)*J_A(4)) &
                 - g_RL(2)*(G_Q(3,l,1)*J_A(1)  &
                           + G_Q(4,l,2)*J_A(2)  &
                           + G_Q(4,l,3)*J_A(1)  &
                           + G_Q(3,l,4)*J_A(2)))
  end do
  Gtensor = Gtensor + Gtensor

end subroutine last_QA_Z
```

Appendix B

Four-lepton + 0,1 jet production

In this appendix for the Chapter 3, we discuss the treatment of bottom- and top-quark contributions, and document the cuts of the ATLAS and CMS analyses.

B.1 Treatment of bottom- and top-quark contributions

Consistently with the five-flavour evolution of PDFs and α_s, for bottom quarks we adopt the massless approximation. Top quarks are thus the only QCD partons that we treat as massive. They can contribute to $pp \to W^+W^-$+jets through closed quark loops, but also via resonant top propagators in sub-processes with external b quarks, such as $gb \to W^+W^-b$ and $gg \to W^+W^-b\bar{b}$. Partonic channels of this type are dominated by Wt and $t\bar{t}$ production, and are more conveniently handled as separate processes. Therefore, as operational definition of W^+W^-+jets production, we consider only partonic channels that do not involve b quarks in the initial or final state. As pointed out in Ref. [139], when excluding external b quarks, care must be taken to avoid NLO infrared singularities in $pp \to W^+W^-j$. This issue is related to the renormalisation of the external-gluon wave function, which receives a b-quark contribution

$$\delta Z_A^{(b)} = \frac{\alpha_s}{6\pi}\left[\mu^{2\varepsilon}\Delta_{IR} - \mu^{2\varepsilon}\Delta_{UV}\right] = 0, \tag{B.1}$$

where μ is the scale of dimensional regularisation, and infrared (IR) and ultraviolet (UV) singularities in $D = 4 - 2\varepsilon$ dimensions yield

$$\Delta_{IR,UV} = \frac{(4\pi)^\varepsilon}{\Gamma(1-\varepsilon)}\frac{1}{\varepsilon}, \qquad \mu^{2\varepsilon}\Delta_{IR,UV} = \Delta_{IR,UV} + \ln\mu^2 + \mathcal{O}(\varepsilon). \tag{B.2}$$

The renormalisation constant (B.1) vanishes due to an exact IR–UV compensation. However, while its UV pole $\mu^{2\varepsilon}\Delta_{UV}$ cancels in renormalised $q\bar{q} \to W^+W^-g$ amplitudes,[1] the compensation of the IR pole $\mu^{2\varepsilon}\Delta_{IR}$ requires a $q\bar{q} \to W^+W^-b\bar{b}$ real-emission counterpart involving collinear $g \to b\bar{b}$ splittings. The inclusion of $W^+W^-b\bar{b}$ final

[1] Here we discuss only partonic processes with gluons in the final state. Similar arguments apply also to the crossing-related $qg \to W^+W^-q$ and $\bar{q}g \to W^+W^-\bar{q}$ channels.

states—at least in the collinear region—is thus indispensable for an infrared-safe NLO definition of $\mathrm{W^+W^-}j$ production in the five-flavour scheme.

In Ref. [139], the IR cancellation was achieved by including the contribution of $\mathrm{g} \to \mathrm{b\bar{b}}$ splittings to the Catani–Seymour $\mathcal{I}$-operator [73],

$$\mathcal{I}^{(\mathrm{b})} = -\frac{\alpha_s}{6\pi}\left[\Delta_{\mathrm{IR}} + \frac{1}{2}\left(\ln\frac{\mu^2}{2p_q p_{\mathrm{g}}} + \ln\frac{\mu^2}{2p_{\bar{q}} p_g}\right) + \frac{8}{3}\right], \tag{B.3}$$

where $p_q, p_{\bar{q}}$ and p_{g} are the quark, anti-quark and gluon momenta, respectively. Combining $\delta Z_A^{(\mathrm{b})} + \mathcal{I}^{(\mathrm{b})}$ yields an IR-finite and $\ln\mu$-independent result. The $\mathcal{I}$-operator contribution (B.3) results from dipole-subtraction terms, which approximate $\mathrm{g} \to \mathrm{b\bar{b}}$ splittings in the collinear limit, upon integration over the entire $\mathrm{b\bar{b}}$ phase space. In principle, it should be combined with a subtracted real-emission counterpart, which is free from singularities but depends on the cuts applied to the $\mathrm{b\bar{b}}$ pair. In Ref. [139], this finite real-emission part was omitted, arguing that its contribution should be small if $\mathrm{b\bar{b}}$ pairs are confined in a jet cone. This kinematic restriction of the $\mathrm{b\bar{b}}$ phase space would also suppress $\mathrm{t\bar{t}}$ and tW contributions. However, confining $\mathrm{b\bar{b}}$ pairs in narrow jets would introduce potentially large logarithms of the jet radius. Moreover, the consistent inclusion of the real-emission part would exactly cancel the 8/3 term in (B.3), which results from the unphysical dipoles, and replace it by an unknown cut-dependent contribution. The inclusion of $\mathcal{I}$-operator terms (B.3) without corresponding real-emission parts should thus be regarded as a regularisation *prescription*, which guarantees the correct cancellation of poles and large logarithms corresponding to inclusive $\mathrm{b\bar{b}}$ emission, but involves ad-hoc constant parts. This ambiguity can be removed only upon inclusion of the dipole-subtracted $\mathrm{W^+W^-b\bar{b}}$ remnant.

Based on these considerations, we adopt a splitting approach similar to Ref. [139], but we prefer to subtract only the singular and logarithmically-enhanced terms arising from inclusive $\mathrm{g} \to \mathrm{b\bar{b}}$ emissions. More precisely, instead of the subtraction term (B.3) we use[1]

$$\mathcal{I}^{(\mathrm{b})}_{\mathrm{mod}} = -\frac{\alpha_s}{6\pi}\left(\Delta_{\mathrm{IR}} + \ln\frac{\mu^2}{\mu_{\mathrm{R}}^2}\right). \tag{B.4}$$

Since the renormalisation scale μ_{R} is typically of the same order of the kinematic invariants in (B.3), the main difference between (B.3) and (B.4) amounts to

$$\mathcal{I}^{(\mathrm{b})} - \mathcal{I}^{(\mathrm{b})}_{\mathrm{mod}} = -\frac{\alpha_s}{6\pi}\left[\frac{1}{2}\left(\ln\frac{\mu_{\mathrm{R}}^2}{2p_q p_{\mathrm{g}}} + \ln\frac{\mu_{\mathrm{R}}^2}{2p_{\bar{q}} p_g}\right) + \frac{8}{3}\right] \simeq -\frac{4\alpha_s}{9\pi} \simeq -1.7\%, \tag{B.5}$$

and can be regarded as the typical ambiguity inherent in the separation of the $\mathrm{W^+W^-}j$ and $\mathrm{W^+W^-b\bar{b}}$ cross sections. Note that, in order to reflect this kind of uncertainty in standard scale-variation studies, we intentionally introduce a fake $\ln\mu_{\mathrm{R}}$ dependence in the IR-subtraction term (B.4).

This small ambiguity is due to the absence of the dipole-subtracted $\mathrm{W^+W^-b\bar{b}}$ emission, which is supposed to be included in a separate calculation of $\mathrm{W^+W^-b\bar{b}}$

[1] Technically, we circumvent the explicit implementation of the subtraction term (B.4) by assigning the values $\Delta_{\mathrm{IR}} \to 0$ and $\mu \to \mu_{\mathrm{R}}$ to the dimensional-regularisation parameters.

production, i.e. of $t\bar{t}$ and Wt off-shell production. It can be removed by combining the W^+W^-+jets and $W^+W^-b\bar{b}$ calculations in a single simulation. For a consistent matching of the two processes, the $\mathcal{I}$-operator term (B.3) in the $pp \to W^+W^-b\bar{b}$ calculation should be replaced by the finite shift[1] (B.5).

In summary, due to collinear $g \to b\bar{b}$ singularities, the splitting of $pp \to W^+W^-j$ and $pp \to W^+W^-b\bar{b}$ is not unique, and the subtraction term (B.4) corresponds to a natural matching prescription, which is free from large logarithms and ad-hoc constants.

B.2 Cuts of the ATLAS and CMS H→WW* analyses in 0- and 1-jet bins

The cuts of the ATLAS [126] and CMS [127] $H \to WW^* \to \mu^+\nu_\mu e^-\bar{\nu}_e$ analyses at 8 TeV in the exclusive 0- and 1-jet bins are listed in Table 11. To be close to the experimental definitions of both ATLAS and CMS, lepton isolation is implemented at the particle level. The scalar sum of the transverse momenta of all visible particles within a $R = 0.3$ cone around the lepton candidate is not allowed to exceed 15% of the lepton p_T. Partons are recombined into jets using the anti-k_T algorithm [171]. The different WW transverse-mass definition employed in ATLAS and CMS is consistently taken into account,

$$m_T^2 = \begin{cases} \left(\sqrt{p_{T,\ell\ell'}^2 + m_{\ell\ell'}^2} + \not{E}_T\right)^2 - \left|p_{T,\ell\ell'} + \not{E}_T\right|^2 & \text{for ATLAS} \\ 2|p_{T,\ell\ell'}|\,|\not{E}_T|\,(1 - \cos\Delta\phi_{\ell\ell',\not{E}_T}) & \text{for CMS} \end{cases}, \tag{B.6}$$

where $p_{T,\ell\ell'}$ and $m_{\ell\ell'}$ are the transverse momentum and the mass of the di-lepton system, respectively, $\not{E}_T$ is the missing transverse momentum, and $\Delta\phi_{\ell\ell',\not{E}_T}$ is the difference in azimuth between $\not{E}_T$ and $p_{T,\ell\ell'}$. After a pre-selection (P), additional cuts are applied that define a signal (S) and a control (C) region. The latter is exploited to normalise background simulations to data in the experimental analyses in each jet bin. In the ATLAS analysis, different cuts are applied in the 0- and 1-jet bins. All cuts have been implemented in form of a RIVET [170] analysis.

[1] Here we assume that $pp \to W^+W^-b\bar{b}$ is computed using dipole subtraction, but the matching procedure can be obviously adapted to any other subtraction method.

anti-k_T jets		ATLAS	CMS
R	=	0.4	0.5
$p_{\mathrm{T},j}(\lvert\eta_j\rvert)$	>	25 GeV ($\lvert\eta_j\rvert < 2.4$)	30 GeV ($\lvert\eta_j\rvert < 4.7$)
		30 GeV ($2.4 < \lvert\eta_j\rvert < 4.5$)	
P selection		**ATLAS**	**CMS**
$p_{\mathrm{T},\{\ell_1,\ell_2\}}$	>	25, 15 GeV	20, 10 GeV
$\lvert\eta_{\{\mathrm{e},\mu\}}\rvert$	<	2.47, 2.5	2.5, 2.4
$\lvert\eta_\mathrm{e}\rvert$	$\notin$	[1.37, 1.57]	
$p_{\mathrm{T},\ell\ell'}$	>	see S, C	30 GeV
$m_{\ell\ell'}$	>	10 GeV	12 GeV
$\not{E}_T^{(proj)}$	>	25 GeV	20 GeV
S region		**ATLAS**	**CMS**
$\Delta\phi_{\ell\ell',\not{E}_T}$	>	$\pi/2$ (0 jets only)	
$p_{\mathrm{T},\ell\ell'}$	>	30 GeV (0 jets only)	
$\Delta\phi_{\ell\ell'}$	<	1.8 rad	
$m_{\ell\ell'}$	<	50 GeV	200 GeV
m_T	$\in$		[60 GeV, 280 GeV]
C region		**ATLAS**	**CMS**
$\Delta\phi_{\ell\ell',\not{E}_T}$	>	$\pi/2$ (0 jets only)	
$p_{\mathrm{T},\ell\ell'}$	>	30 GeV (0 jets only)	
$m_{\ell\ell'}$		$\in [50, 100]$ GeV (0 jets only)	> 100 GeV
		> 80 GeV (1 jet only)	

Table 11: Jet definitions and selection cuts in the ATLAS and CMS analyses of $\mathrm{H} \to \mathrm{WW}^* \to \mu^+\nu_\mu \mathrm{e}^-\bar{\nu}_\mathrm{e}$ at 8 TeV. The cuts refer to various levels and regions, namely event pre-selection (P cuts), the signal region (P and S cuts) and the control region (P and C cuts). The projected missing transverse energy $\not{E}_T^{(proj)}$ is defined as $\not{E}_\mathrm{T}^{(proj)} = \not{E}_\mathrm{T} \cdot \sin(\min\{\Delta\phi_\mathrm{near}, \pi/2\})$, where $\Delta\phi_\mathrm{near}$ denotes the angle between the missing transverse momentum $\not{E}_\mathrm{T}$ and the nearest lepton in the transverse plane.

Bibliography

[1] S. Glashow, *Partial Symmetries of Weak Interactions*, *Nucl.Phys.* **22** (1961) 579–588.

[2] S. Weinberg, *A Model of Leptons*, *Phys.Rev.Lett.* **19** (1967) 1264–1266.

[3] A. Salam, *Weak and Electromagnetic Interactions*, *Conf.Proc.* **C680519** (1968) 367–377.

[4] F. Englert and R. Brout, *Broken Symmetry and the Mass of Gauge Vector Mesons*, *Phys.Rev.Lett.* **13** (1964) 321–323.

[5] P. W. Higgs, *Broken Symmetries and the Masses of Gauge Bosons*, *Phys.Rev.Lett.* **13** (1964) 508–509.

[6] G. Guralnik, C. Hagen, and T. Kibble, *Global Conservation Laws and Massless Particles*, *Phys.Rev.Lett.* **13** (1964) 585–587.

[7] P. W. Higgs, *Broken symmetries, massless particles and gauge fields*, *Phys.Lett.* **12** (1964) 132–133.

[8] **Particle Data Group** Collaboration, J. Beringer et al., *Review of Particle Physics (RPP)*, *Phys.Rev.* **D86** (2012) 010001.

[9] **ATLAS** Collaboration, G. Aad et al., *Observation of a new particle in the search for the Standard Model Higgs boson with the ATLAS detector at the LHC*, *Phys.Lett.* **B716** (2012) 1–29, [arXiv:1207.7214].

[10] **CMS** Collaboration, S. Chatrchyan et al., *Observation of a new boson at a mass of 125 GeV with the CMS experiment at the LHC*, *Phys.Lett.* **B716** (2012) 30–61, [arXiv:1207.7235].

[11] J. Bjorken and S. Drell, *Relativistic Quantum Fields*. Mcgraw-Hill College, 1965.

[12] D. J. Gross and F. Wilczek, *Ultraviolet Behavior of Nonabelian Gauge Theories*, *Phys.Rev.Lett.* **30** (1973) 1343–1346.

[13] H. D. Politzer, *Reliable Perturbative Results for Strong Interactions?*, *Phys.Rev.Lett.* **30** (1973) 1346–1349.

[14] Z. Bern, L. J. Dixon, D. C. Dunbar, and D. A. Kosower, *Fusing gauge theory tree amplitudes into loop amplitudes*, *Nucl.Phys.* **B435** (1995) 59–101, [hep-ph/9409265].

[15] C. F. Berger, Z. Bern, L. J. Dixon, D. Forde, and D. A. Kosower, *Bootstrapping One-Loop QCD Amplitudes with General Helicities*, *Phys.Rev.* **D74** (2006) 036009, [hep-ph/0604195].

[16] Z. Bern, L. J. Dixon, and D. A. Kosower, *On-Shell Methods in Perturbative QCD*, *Annals Phys.* **322** (2007) 1587–1634, [arXiv:0704.2798].

[17] C. Berger, Z. Bern, L. Dixon, F. Febres Cordero, D. Forde, et al., *An Automated Implementation of On-Shell Methods for One-Loop Amplitudes*, *Phys.Rev.* **D78** (2008) 036003, [arXiv:0803.4180].

[18] R. Britto, F. Cachazo, and B. Feng, *Generalized unitarity and one-loop amplitudes in N=4 super-Yang-Mills*, *Nucl.Phys.* **B725** (2005) 275–305, [hep-th/0412103].

[19] A. Brandhuber, S. McNamara, B. J. Spence, and G. Travaglini, *Loop amplitudes in pure Yang-Mills from generalised unitarity*, *JHEP* **0510** (2005) 011, [hep-th/0506068].

[20] R. Britto, B. Feng, and P. Mastrolia, *The Cut-constructible part of QCD amplitudes*, *Phys.Rev.* **D73** (2006) 105004, [hep-ph/0602178].

[21] D. Forde, *Direct extraction of one-loop integral coefficients*, *Phys.Rev.* **D75** (2007) 125019, [arXiv:0704.1835].

[22] S. Badger, E. N. Glover, and K. Risager, *One-loop phi-MHV amplitudes using the unitarity bootstrap*, *JHEP* **0707** (2007) 066, [arXiv:0704.3914].

[23] C. Anastasiou, R. Britto, B. Feng, Z. Kunszt, and P. Mastrolia, *Unitarity cuts and Reduction to master integrals in d dimensions for one-loop amplitudes*, *JHEP* **0703** (2007) 111, [hep-ph/0612277].

[24] W. T. Giele, Z. Kunszt, and K. Melnikov, *Full one-loop amplitudes from tree amplitudes*, *JHEP* **0804** (2008) 049, [arXiv:0801.2237].

[25] R. K. Ellis, W. T. Giele, Z. Kunszt, and K. Melnikov, *Masses, fermions and generalized D-dimensional unitarity*, *Nucl.Phys.* **B822** (2009) 270–282, [arXiv:0806.3467].

[26] G. Ossola, C. G. Papadopoulos, and R. Pittau, *Reducing full one-loop amplitudes to scalar integrals at the integrand level*, *Nucl.Phys.* **B763** (2007) 147–169, [hep-ph/0609007].

[27] P. Mastrolia, G. Ossola, C. Papadopoulos, and R. Pittau, *Optimizing the Reduction of One-Loop Amplitudes*, *JHEP* **0806** (2008) 030, [arXiv:0803.3964].

[28] P. Draggiotis, M. Garzelli, C. Papadopoulos, and R. Pittau, *Feynman Rules for the Rational Part of the QCD 1-loop amplitudes*, *JHEP* **0904** (2009) 072, [arXiv:0903.0356].

[29] A. van Hameren, C. Papadopoulos, and R. Pittau, *Automated one-loop calculations: A Proof of concept*, *JHEP* **0909** (2009) 106, [arXiv:0903.4665].

[30] A. Ferroglia, M. Passera, G. Passarino, and S. Uccirati, *All purpose numerical evaluation of one loop multileg Feynman diagrams*, *Nucl.Phys.* **B650** (2003) 162–228, [hep-ph/0209219].

[31] A. Denner and S. Dittmaier, *Reduction of one loop tensor five point integrals*, *Nucl.Phys.* **B658** (2003) 175–202, [hep-ph/0212259].

[32] A. Denner and S. Dittmaier, *Reduction schemes for one-loop tensor integrals*, *Nucl.Phys.* **B734** (2006) 62–115, [hep-ph/0509141].

[33] F. del Aguila and R. Pittau, *Recursive numerical calculus of one-loop tensor integrals*, *JHEP* **0407** (2004) 017, [hep-ph/0404120].

[34] W. Giele and E. N. Glover, *A Calculational formalism for one loop integrals*, *JHEP* **0404** (2004) 029, [hep-ph/0402152].

[35] W. Giele, E. N. Glover, and G. Zanderighi, *Numerical evaluation of one-loop diagrams near exceptional momentum configurations*, *Nucl.Phys.Proc.Suppl.* **135** (2004) 275–279, [hep-ph/0407016].

[36] R. K. Ellis, W. Giele, and G. Zanderighi, *Semi-numerical evaluation of one-loop corrections*, *Phys.Rev.* **D73** (2006) 014027, [hep-ph/0508308].

[37] T. Binoth, J. P. Guillet, G. Heinrich, E. Pilon, and C. Schubert, *An Algebraic/numerical formalism for one-loop multi-leg amplitudes*, *JHEP* **0510** (2005) 015, [hep-ph/0504267].

[38] T. Binoth, J. P. Guillet, and G. Heinrich, *Algebraic evaluation of rational polynomials in one-loop amplitudes*, *JHEP* **0702** (2007) 013, [hep-ph/0609054].

[39] T. Diakonidis, J. Fleischer, J. Gluza, K. Kajda, T. Riemann, et al., *A Complete reduction of one-loop tensor 5 and 6-point integrals*, *Phys.Rev.* **D80** (2009) 036003, [arXiv:0812.2134].

[40] T. Diakonidis, J. Fleischer, T. Riemann, and J. Tausk, *A Recursive reduction of tensor Feynman integrals*, *Phys.Lett.* **B683** (2010) 69–74, [arXiv:0907.2115].

[41] S. Hoeche, *Applications of higher order QCD*, arXiv:1403.0037.

[42] G. Ossola, *Automated computation of scattering amplitudes*, arXiv:1310.3214.

[43] F. Cascioli, P. Maierhofer, and S. Pozzorini, *Scattering Amplitudes with Open Loops*, *Phys.Rev.Lett.* **108** (2012) 111601, [arXiv:1111.5206].

[44] A. van Hameren, *Multi-gluon one-loop amplitudes using tensor integrals*, *JHEP* **0907** (2009) 088, [arXiv:0905.1005].

[45] W. Giele and G. Zanderighi, *On the Numerical Evaluation of One-Loop Amplitudes: The Gluonic Case*, *JHEP* **0806** (2008) 038, [arXiv:0805.2152].

[46] G. Ossola, C. G. Papadopoulos, and R. Pittau, *CutTools: A Program implementing the OPP reduction method to compute one-loop amplitudes*, *JHEP* **0803** (2008) 042, [arXiv:0711.3596].

[47] P. Mastrolia, G. Ossola, T. Reiter, and F. Tramontano, *Scattering AMplitudes from Unitarity-based Reduction Algorithm at the Integrand-level*, *JHEP* **1008** (2010) 080, [arXiv:1006.0710].

[48] G. Bevilacqua, M. Czakon, M. Garzelli, A. van Hameren, A. Kardos, et al., *HELAC-NLO*, *Comput.Phys.Commun.* **184** (2013) 986–997, [arXiv:1110.1499].

[49] S. Badger, B. Biedermann, P. Uwer, and V. Yundin, *Numerical evaluation of virtual corrections to multi-jet production in massless QCD*, *Comput.Phys.Commun.* **184** (2013) 1981–1998, [arXiv:1209.0100].

[50] V. Hirschi, R. Frederix, S. Frixione, M. V. Garzelli, F. Maltoni, et al., *Automation of one-loop QCD corrections*, *JHEP* **1105** (2011) 044, [arXiv:1103.0621].

[51] G. Cullen, N. Greiner, G. Heinrich, G. Luisoni, P. Mastrolia, et al., *Automated One-Loop Calculations with GoSam*, *Eur.Phys.J.* **C72** (2012) 1889, [arXiv:1111.2034].

[52] S. Actis, A. Denner, L. Hofer, A. Scharf, and S. Uccirati, *Recursive generation of one-loop amplitudes in the Standard Model*, *JHEP* **1304** (2013) 037, [arXiv:1211.6316].

[53] T. Gleisberg, S. Hoeche, F. Krauss, M. Schonherr, S. Schumann, et al., *Event generation with SHERPA 1.1*, *JHEP* **0902** (2009) 007, [arXiv:0811.4622].

[54] J. Bellm, S. Gieseke, D. Grellscheid, A. Papaefstathiou, S. Platzer, et al., *Herwig++ 2.7 Release Note*, arXiv:1310.6877.

[55] J. Alwall, R. Frederix, S. Frixione, V. Hirschi, F. Maltoni, et al., *The automated computation of tree-level and next-to-leading order differential cross sections, and their matching to parton shower simulations*, arXiv:1405.0301.

[56] S. Alioli, P. Nason, C. Oleari, and E. Re, *A general framework for implementing NLO calculations in shower Monte Carlo programs: the POWHEG BOX*, *JHEP* **1006** (2010) 043, [arXiv:1002.2581].

[57] A fully automated C++ Monte-Carlo generator for NLO QCD by S. Kallweit. Under development.

[58] F. Cascioli, S. Hoeche, F. Krauss, P. Maierhoefer, S. Pozzorini, et al., *Precise Higgs-background predictions: merging NLO QCD and squared quark-loop corrections to four-lepton + 0,1 jet production*, *JHEP* **1401** (2014) 046, [arXiv:1309.0500].

[59] F. Cascioli, P. Maierhoefer, N. Moretti, S. Pozzorini, and F. Siegert, *NLO matching for ttbb production with massive b-quarks*, *Phys.Lett.* **B734** (2014) 210–214, [arXiv:1309.5912].

[60] F. Cascioli, S. Kallweit, P. Maierhfer, and S. Pozzorini, *A unified NLO description of top-pair and associated Wt production*, *Eur.Phys.J.* **C74** (2014) 2783, [arXiv:1312.0546].

[61] M. Grazzini, S. Kallweit, D. Rathlev, and A. Torre, *$Z\gamma$ production at hadron colliders in NNLO QCD*, *Phys.Lett.* **B731** (2014) 204–207, [arXiv:1309.7000].

[62] P. Maierhoefer and A. Papaefstathiou, *Higgs Boson pair production merged to one jet*, *JHEP* **1403** (2014) 126, [arXiv:1401.0007].

[63] S. Hoeche, F. Krauss, P. Maierhoefer, S. Pozzorini, M. Schonherr, et al., *Next-to-leading order QCD predictions for top-quark pair production with up to two jets merged with a parton shower*, arXiv:1402.6293.

[64] S. Hoeche, F. Krauss, S. Pozzorini, M. Schoenherr, J. Thompson, et al., *Triple vector boson production through Higgs-Strahlung with NLO multijet merging*, arXiv:1403.7516.

[65] G. Abelof, A. Gehrmann-De Ridder, P. Maierhofer, and S. Pozzorini, *NNLO QCD corrections to top-antitop production in the $q\bar{q}$ channel*, arXiv:1404.6493.

[66] F. Cascioli, T. Gehrmann, M. Grazzini, S. Kallweit, P. Maierhfer, et al., *ZZ production at hadron colliders in NNLO QCD*, arXiv:1405.2219.

[67] J. C. Collins, D. E. Soper, and G. F. Sterman, *Factorization for Short Distance Hadron - Hadron Scattering*, *Nucl.Phys.* **B261** (1985) 104.

[68] J. C. Collins, D. E. Soper, and G. F. Sterman, *Soft Gluons and Factorization*, *Nucl.Phys.* **B308** (1988) 833.

[69] T. Kinoshita, *Mass singularities of Feynman amplitudes*, *J.Math.Phys.* **3** (1962) 650–677.

[70] T. Lee and M. Nauenberg, *Degenerate Systems and Mass Singularities*, *Phys.Rev.* **133** (1964) B1549–B1562.

[71] W. Giele and E. N. Glover, *Higher order corrections to jet cross-sections in e+ e- annihilation*, *Phys.Rev.* **D46** (1992) 1980–2010.

[72] W. Giele, E. N. Glover, and D. A. Kosower, *Higher order corrections to jet cross-sections in hadron colliders*, *Nucl.Phys.* **B403** (1993) 633–670, [hep-ph/9302225].

[73] S. Catani and M. Seymour, *A General algorithm for calculating jet cross-sections in NLO QCD*, *Nucl.Phys.* **B485** (1997) 291–419, [hep-ph/9605323].

[74] S. Catani, S. Dittmaier, M. H. Seymour, and Z. Trocsanyi, *The Dipole formalism for next-to-leading order QCD calculations with massive partons*, *Nucl.Phys.* **B627** (2002) 189–265, [hep-ph/0201036].

[75] D. A. Kosower, *Antenna factorization of gauge theory amplitudes*, *Phys.Rev.* **D57** (1998) 5410–5416, [hep-ph/9710213].

[76] D. A. Kosower, *Antenna factorization in strongly ordered limits*, *Phys.Rev.* **D71** (2005) 045016, [hep-ph/0311272].

[77] A. Gehrmann-De Ridder, T. Gehrmann, and E. N. Glover, *Antenna subtraction at NNLO*, *JHEP* **0509** (2005) 056, [hep-ph/0505111].

[78] A. Daleo, T. Gehrmann, and D. Maitre, *Antenna subtraction with hadronic initial states*, *JHEP* **0704** (2007) 016, [hep-ph/0612257].

[79] S. Frixione, Z. Kunszt, and A. Signer, *Three jet cross-sections to next-to-leading order*, *Nucl.Phys.* **B467** (1996) 399–442, [hep-ph/9512328].

[80] S. Frixione, *A General approach to jet cross-sections in QCD*, *Nucl.Phys.* **B507** (1997) 295–314, [hep-ph/9706545].

[81] A. Buckley, J. Butterworth, S. Gieseke, D. Grellscheid, S. Hoche, et al., *General-purpose event generators for LHC physics*, *Phys.Rept.* **504** (2011) 145–233, [arXiv:1101.2599].

[82] P. Nason and B. Webber, *Next-to-Leading-Order Event Generators*, *Ann.Rev.Nucl.Part.Sci.* **62** (2012) 187–213, [arXiv:1202.1251].

[83] G. Marchesini and B. Webber, *Simulation of QCD Jets Including Soft Gluon Interference*, *Nucl.Phys.* **B238** (1984) 1.

[84] G. Gustafson and U. Pettersson, *Dipole Formulation of QCD Cascades*, *Nucl.Phys.* **B306** (1988) 746.

[85] Z. Nagy and D. E. Soper, *Matching parton showers to NLO computations*, *JHEP* **0510** (2005) 024, [hep-ph/0503053].

[86] S. Schumann and F. Krauss, *A Parton shower algorithm based on Catani-Seymour dipole factorisation*, *JHEP* **0803** (2008) 038, [arXiv:0709.1027].

[87] M. Bengtsson and T. Sjostrand, *Coherent Parton Showers Versus Matrix Elements: Implications of PETRA - PEP Data*, *Phys.Lett.* **B185** (1987) 435.

[88] S. Frixione and B. R. Webber, *Matching NLO QCD computations and parton shower simulations*, *JHEP* **0206** (2002) 029, [hep-ph/0204244].

[89] P. Nason, *A New method for combining NLO QCD with shower Monte Carlo algorithms*, *JHEP* **0411** (2004) 040, [hep-ph/0409146].

[90] S. Catani, F. Krauss, R. Kuhn, and B. Webber, *QCD matrix elements + parton showers*, *JHEP* **0111** (2001) 063, [hep-ph/0109231].

[91] L. Lonnblad, *Correcting the color dipole cascade model with fixed order matrix elements*, *JHEP* **0205** (2002) 046, [hep-ph/0112284].

[92] M. L. Mangano, M. Moretti, and R. Pittau, *Multijet matrix elements and shower evolution in hadronic collisions: $Wb\bar{b}$ + n jets as a case study*, *Nucl.Phys.* **B632** (2002) 343–362, [hep-ph/0108069].

[93] J. Alwall, S. Hoche, F. Krauss, N. Lavesson, L. Lonnblad, et al., *Comparative study of various algorithms for the merging of parton showers and matrix elements in hadronic collisions*, *Eur.Phys.J.* **C53** (2008) 473–500, [arXiv:0706.2569].

[94] S. Hoeche, F. Krauss, M. Schonherr, and F. Siegert, *QCD matrix elements + parton showers: The NLO case*, *JHEP* **1304** (2013) 027, [arXiv:1207.5030].

[95] T. Gehrmann, S. Hoche, F. Krauss, M. Schonherr, and F. Siegert, *NLO QCD matrix elements + parton showers in $e^+e^- \to$ hadrons*, *JHEP* **1301** (2013) 144, [arXiv:1207.5031].

[96] L. Lonnblad and S. Prestel, *Merging Multi-leg NLO Matrix Elements with Parton Showers*, *JHEP* **1303** (2013) 166, [arXiv:1211.7278].

[97] R. Frederix and S. Frixione, *Merging meets matching in MC@NLO*, *JHEP* **1212** (2012) 061, [arXiv:1209.6215].

[98] S. Hoeche, F. Krauss, M. Schonherr, and F. Siegert, *A critical appraisal of NLO+PS matching methods*, *JHEP* **1209** (2012) 049, [arXiv:1111.1220].

[99] S. Hoeche, F. Krauss, S. Schumann, and F. Siegert, *QCD matrix elements and truncated showers*, *JHEP* **0905** (2009) 053, [arXiv:0903.1219].

[100] H. Lehmann, K. Symanzik, and W. Zimmermann, *On the formulation of quantized field theories*, *Nuovo Cim.* **1** (1955) 205–225.

[101] L. Faddeev and V. Popov, *Feynman Diagrams for the Yang-Mills Field*, *Phys.Lett.* **B25** (1967) 29–30.

[102] G. Passarino and M. Veltman, *One Loop Corrections for e+ e- Annihilation Into mu+ mu- in the Weinberg Model*, *Nucl.Phys.* **B160** (1979) 151.

[103] A. Denner and S. Dittmaier, *Scalar one-loop 4-point integrals*, *Nucl.Phys.* **B844** (2011) 199–242, [arXiv:1005.2076].

[104] R. Pittau, *Formulae for a numerical computation of one-loop tensor integrals*, hep-ph/0406105.

[105] G. Ossola, C. G. Papadopoulos, and R. Pittau, *On the Rational Terms of the one-loop amplitudes*, *JHEP* **0805** (2008) 004, [arXiv:0802.1876].

[106] M. Garzelli, I. Malamos, and R. Pittau, *Feynman rules for the rational part of the Electroweak 1-loop amplitudes*, *JHEP* **1001** (2010) 040, [arXiv:0910.3130].

[107] H.-S. Shao, Y.-J. Zhang, and K.-T. Chao, *Feynman Rules for the Rational Part of the Standard Model One-loop Amplitudes in the 't Hooft-Veltman γ_5 Scheme*, *JHEP* **1109** (2011) 048, [arXiv:1106.5030].

[108] H.-S. Shao and Y.-J. Zhang, *Feynman Rules for the Rational Part of One-loop QCD Corrections in the MSSM*, *JHEP* **1206** (2012) 112, [arXiv:1205.1273].

[109] R. K. Ellis, Z. Kunszt, K. Melnikov, and G. Zanderighi, *One-loop calculations in quantum field theory: from Feynman diagrams to unitarity cuts*, *Phys.Rept.* **518** (2012) 141–250, [arXiv:1105.4319].

[110] **SM and NLO Multileg Working Group** Collaboration, J. Andersen et al., *The SM and NLO Multileg Working Group: Summary report*, arXiv:1003.1241.

[111] F. A. Berends and W. Giele, *Recursive Calculations for Processes with n Gluons*, *Nucl.Phys.* **B306** (1988) 759.

[112] F. Caravaglios and M. Moretti, *An algorithm to compute Born scattering amplitudes without Feynman graphs*, *Phys.Lett.* **B358** (1995) 332–338, [hep-ph/9507237].

[113] P. Draggiotis, R. H. Kleiss, and C. G. Papadopoulos, *On the computation of multigluon amplitudes*, *Phys.Lett.* **B439** (1998) 157–164, [hep-ph/9807207].

[114] T. Hahn, *Generating Feynman diagrams and amplitudes with FeynArts 3*, *Comput.Phys.Commun.* **140** (2001) 418–431, [hep-ph/0012260].

[115] A. Denner, S. Dittmaier, and L. Hofer, in preparation.

[116] A. Denner and S. Dittmaier, *The Complex-mass scheme for perturbative calculations with unstable particles*, *Nucl.Phys.Proc.Suppl.* **160** (2006) 22–26, [hep-ph/0605312].

[117] R. Ellis, W. Stirling, and B. Webber, *QCD and Collider Physics*. Cambridge University Press, 2003.

[118] M. Boehm, A. Denner, and H. Joos, *Gauge Theories of the Strong and Electroweak Interaction*. Vieweg+Teubner Verlag, 2001.

[119] A. Kanaki and C. G. Papadopoulos, *HELAC: A Package to compute electroweak helicity amplitudes*, *Comput.Phys.Commun.* **132** (2000) 306–315, [hep-ph/0002082].

[120] S. Dittmaier, *Weyl-van der Waerden formalism for helicity amplitudes of massive particles*, *Phys.Rev.* **D59** (1998) 016007, [hep-ph/9805445].

[121] C. Itzykson and J. Zuber, *Quantum Field Theory*. Dover Publications, 2006.

[122] A. Bredenstein, A. Denner, S. Dittmaier, and S. Pozzorini, *NLO QCD corrections to $pp \to t\bar{t}b\bar{b} + X$ at the LHC*, *Phys.Rev.Lett.* **103** (2009) 012002, [arXiv:0905.0110].

[123] A. Denner, S. Dittmaier, S. Kallweit, and S. Pozzorini, *NLO QCD corrections to WWbb production at hadron colliders*, *Phys.Rev.Lett.* **106** (2011) 052001, [arXiv:1012.3975].

[124] R. Kleiss and R. Pittau, *Weight optimization in multichannel Monte Carlo*, *Comput. Phys. Commun.* **83** (1994) 141–146.

[125] T. Binoth, F. Boudjema, G. Dissertori, A. Lazopoulos, A. Denner, et al., *A Proposal for a standard interface between Monte Carlo tools and one-loop programs*, *Comput.Phys.Commun.* **181** (2010) 1612–1622, [arXiv:1001.1307].

[126] **ATLAS** Collaboration, *Measurements of the properties of the Higgs-like boson in the $WW^* \to \ell\ell\nu\nu$ decay channel with the ATLAS detector using 25 fb^{-1} of proton-proton collision data*. ATLAS-CONF-2013-030.

[127] **CMS** Collaboration, *Evidence for a particle decaying to W^+W^- in the fully leptonic final state in a standard model Higgs boson search in pp collisions at the LHC*. CMS-PAS-HIG-13-003.

[128] J. Ohnemus, *An Order α_s calculation of hadronic W^-W^+ production*, *Phys.Rev.* **D44** (1991) 1403–1414.

[129] S. Frixione, *A Next-to-leading order calculation of the cross-section for the production of W+ W- pairs in hadronic collisions*, *Nucl.Phys.* **B410** (1993) 280–324.

[130] J. Ohnemus, *Hadronic ZZ, W^-W^+, and $W^\pm Z$ production with QCD corrections and leptonic decays*, *Phys.Rev.* **D50** (1994) 1931–1945, [hep-ph/9403331].

[131] L. J. Dixon, Z. Kunszt, and A. Signer, *Vector boson pair production in hadronic collisions at order α_s: Lepton correlations and anomalous couplings*, *Phys.Rev.* **D60** (1999) 114037, [hep-ph/9907305].

[132] J. M. Campbell and R. K. Ellis, *An Update on vector boson pair production at hadron colliders*, *Phys.Rev.* **D60** (1999) 113006, [hep-ph/9905386].

[133] J. M. Campbell, R. K. Ellis, and C. Williams, *Vector boson pair production at the LHC*, *JHEP* **1107** (2011) 018, [arXiv:1105.0020].

[134] S. Frixione, P. Nason, and C. Oleari, *Matching NLO QCD computations with Parton Shower simulations: the POWHEG method*, *JHEP* **0711** (2007) 070, [arXiv:0709.2092].

[135] T. Melia, P. Nason, R. Rontsch, and G. Zanderighi, *W+W-, WZ and ZZ production in the POWHEG BOX*, *JHEP* **1111** (2011) 078, [arXiv:1107.5051].

[136] R. Frederix, S. Frixione, V. Hirschi, F. Maltoni, R. Pittau, et al., *Four-lepton production at hadron colliders: aMC@NLO predictions with theoretical uncertainties*, *JHEP* **1202** (2012) 099, [arXiv:1110.4738].

[137] J. M. Campbell, R. K. Ellis, and G. Zanderighi, *Next-to-leading order predictions for $WW + 1$ jet distributions at the LHC*, *JHEP* **0712** (2007) 056, [arXiv:0710.1832].

[138] S. Dittmaier, S. Kallweit, and P. Uwer, *NLO QCD corrections to WW+jet production at hadron colliders*, *Phys.Rev.Lett.* **100** (2008) 062003, [arXiv:0710.1577].

[139] S. Dittmaier, S. Kallweit, and P. Uwer, *NLO QCD corrections to $pp/p\bar{p} \to WW + jet + X$ including leptonic W-boson decays*, *Nucl.Phys.* **B826** (2010) 18–70, [arXiv:0908.4124].

[140] B. Jaeger, C. Oleari, and D. Zeppenfeld, *Next-to-leading order QCD corrections to W+W- production via vector-boson fusion*, *JHEP* **0607** (2006) 015, [hep-ph/0603177].

[141] B. Jaeger and G. Zanderighi, *Electroweak W+W-jj prodution at NLO in QCD matched with parton shower in the POWHEG-BOX*, *JHEP* **1304** (2013) 024, [arXiv:1301.1695].

[142] T. Melia, K. Melnikov, R. Rontsch, and G. Zanderighi, *NLO QCD corrections for W^+W^- pair production in association with two jets at hadron colliders*, *Phys.Rev.* **D83** (2011) 114043, [arXiv:1104.2327].

[143] N. Greiner, G. Heinrich, P. Mastrolia, G. Ossola, T. Reiter, et al., *NLO QCD corrections to the production of W+ W- plus two jets at the LHC*, *Phys.Lett.* **B713** (2012) 277–283, [arXiv:1202.6004].

[144] T. Melia, K. Melnikov, R. Rontsch, and G. Zanderighi, *Next-to-leading order QCD predictions for W^+W^+jj production at the LHC*, *JHEP* **1012** (2010) 053, [arXiv:1007.5313].

[145] A. Denner, L. Hosekova, and S. Kallweit, *NLO QCD corrections to W+ W+ jj production in vector-boson fusion at the LHC*, *Phys.Rev.* **D86** (2012) 114014, [arXiv:1209.2389].

[146] B. Jaeger and G. Zanderighi, *NLO corrections to electroweak and QCD production of W+W+ plus two jets in the POWHEGBOX*, *JHEP* **1111** (2011) 055, [arXiv:1108.0864].

[147] F. Campanario, M. Kerner, L. D. Ninh, and D. Zeppenfeld, *WZ production in association with two jets at NLO in QCD*, *Phys.Rev.Lett.* **111** (2013) 052003, [arXiv:1305.1623].

[148] T. Binoth, M. Ciccolini, N. Kauer, and M. Kramer, *Gluon-induced WW background to Higgs boson searches at the LHC*, *JHEP* **0503** (2005) 065, [hep-ph/0503094].

[149] T. Binoth, M. Ciccolini, N. Kauer, and M. Kramer, *Gluon-induced W-boson pair production at the LHC*, *JHEP* **0612** (2006) 046, [hep-ph/0611170].

[150] J. M. Campbell, R. K. Ellis, and C. Williams, *Gluon-Gluon Contributions to W+ W- Production and Higgs Interference Effects*, *JHEP* **1110** (2011) 005, [arXiv:1107.5569].

[151] T. Melia, K. Melnikov, R. Rontsch, M. Schulze, and G. Zanderighi, *Gluon fusion contribution to W+W- + jet production*, *JHEP* **1208** (2012) 115, [arXiv:1205.6987].

[152] N. Kauer and G. Passarino, *Inadequacy of zero-width approximation for a light Higgs boson signal*, *JHEP* **1208** (2012) 116, [arXiv:1206.4803].

[153] **The LHC Higgs Cross Section Working Group** Collaboration, S. Heinemeyer et al., *Handbook of LHC Higgs Cross Sections: 3. Higgs Properties*, arXiv:1307.1347.

[154] A. Denner, D. Dittmaier, and L. Hofer. In preparation.

[155] S. Hoeche, F. Krauss, M. Schonherr, and F. Siegert, *W+n-jet predictions at the Large Hadron Collider at next-to-leading order matched with a parton shower*, *Phys.Rev.Lett.* **110** (2013) 052001, [arXiv:1201.5882].

[156] A. Denner et al., *Electroweak corrections to charged-current $e^+e^- \to 4$ fermion processes: Technical detail results*, *Nucl.Phys.* **B724** (2005) 247–294, [hep-ph/0505042].

[157] A. Bredenstein, A. Denner, S. Dittmaier, and S. Pozzorini, *NLO QCD Corrections to Top Anti-Top Bottom Anti-Bottom Production at the LHC: 2. full hadronic results*, *JHEP* **1003** (2010) 021, [arXiv:1001.4006].

[158] A. Denner et al., *NLO QCD corrections to off-shell top-antitop production with leptonic decays at hadron colliders*, *JHEP* **1210** (2012) 110, [arXiv:1207.5018].

[159] S. Catani, Y. L. Dokshitzer, M. Olsson, G. Turnock, and B. R. Webber, *New clustering algorithm for multijet cross sections in e^+e^- annihilation*, *Phys. Lett.* **B269** (1991) 432–438.

[160] S. Catani, B. R. Webber, and G. Marchesini, *QCD coherent branching and semiinclusive processes at large x*, *Nucl. Phys.* **B349** (1991) 635–654.

[161] I. W. Stewart and F. J. Tackmann, *Theory Uncertainties for Higgs and Other Searches Using Jet Bins*, *Phys.Rev.* **D85** (2012) 034011, [arXiv:1107.2117].

[162] S. Hoeche, S. Schumann, and F. Siegert, *Hard photon production and matrix-element parton-shower merging*, *Phys.Rev.* **D81** (2010) 034026, [arXiv:0912.3501].

[163] P. Agrawal and A. Shivaji, *Di-Vector Boson + Jet Production via Gluon Fusion at Hadron Colliders*, *Phys.Rev.* **D86** (2012) 073013, [arXiv:1207.2927].

[164] H.-L. Lai, M. Guzzi, J. Huston, Z. Li, P. M. Nadolsky, et al., *New parton distributions for collider physics*, *Phys.Rev.* **D82** (2010) 074024, [arXiv:1007.2241].

[165] J. M. Campbell and R. Ellis, *MCFM for the Tevatron and the LHC*, *Nucl.Phys.Proc.Suppl.* **205-206** (2010) 10–15, [arXiv:1007.3492].

[166] F. Krauss, R. Kuhn, and G. Soff, *AMEGIC++ 1.0: A Matrix element generator in C++*, *JHEP* **0202** (2002) 044, [hep-ph/0109036].

[167] T. Gleisberg and S. Hoeche, *Comix, a new matrix element generator*, *JHEP* **0812** (2008) 039, [arXiv:0808.3674].

[168] T. Gleisberg and F. Krauss, *Automating dipole subtraction for QCD NLO calculations*, *Eur.Phys.J.* **C53** (2008) 501–523, [arXiv:0709.2881].

[169] L. Lonnblad and S. Prestel, *Unitarising Matrix Element + Parton Shower merging*, *JHEP* **1302** (2013) 094, [arXiv:1211.4827].

[170] A. Buckley, J. Butterworth, L. Lonnblad, H. Hoeth, J. Monk, et al., *Rivet user manual*, arXiv:1003.0694.

[171] M. Cacciari, G. P. Salam, and G. Soyez, *The Anti-k(t) jet clustering algorithm*, *JHEP* **0804** (2008) 063, [arXiv:0802.1189].

[172] C. D. White, S. Frixione, E. Laenen, and F. Maltoni, *Isolating Wt production at the LHC*, *JHEP* **0911** (2009) 074, [arXiv:0908.0631].

[173] N. Kauer and D. Zeppenfeld, *Finite width effects in top quark production at hadron colliders*, *Phys.Rev.* **D65** (2002) 014021, [hep-ph/0107181].

[174] G. Bevilacqua et al., *Complete off-shell effects in top quark pair hadroproduction with leptonic decay at next-to-leading order*, *JHEP* **1102** (2011) 083, [arXiv:1012.4230].

[175] R. Frederix, *The top induced backgrounds to Higgs production in the $WW \to llvv$ decay channel at NLO in QCD*, arXiv:1311.4893.

[176] M. Jezabek and J. H. Kuhn, *QCD Corrections to Semileptonic Decays of Heavy Quarks*, *Nucl.Phys.* **B314** (1989) 1.

[177] R. D. Ball et al., *Parton distributions with LHC data*, *Nucl.Phys.* **B867** (2013) 244–289, [arXiv:1207.1303].